IMAGING ANGIOGENESIS IN BRAIN METASTASIS



Jessica Buck

Green Templeton College

Department of Oncology

Hilary Term 2019

A thesis submitted to the Medical Sciences Division of the University of Oxford in partial fulfilment of the requirements for the degree of Doctor of Philosophy in Oncology

Abstract

Brain metastasis is responsible for a large proportion of the mortality of cancer, and there are currently no effective treatments. The effect of treatments, particularly anti-angiogenic therapeutics, is difficult to ascertain using current imaging methods. Thus, the aim of this thesis is to develop methods for imaging angiogenesis using magnetic resonance imaging (MRI) in a mouse model of brain metastasis.

Arterial spin labelling (ASL) is an MRI technique that measures cerebral blood flow (CBF) non-invasively and quantitatively. The work described in this thesis optimised and validated multiphase pseudo-continuous ASL (MP pCASL) for use in mice. This sequence was then used to measure and identify areas of reduced CBF in mouse models of brain metastasis and glioma.

Integrin $\alpha_v\beta_3$ is a marker of angiogenesis expressed on tumour blood vessels, including in brain metastasis. The second major aim of the work described in this thesis was to image angiogenic blood vessels in brain metastasis *in vivo* using microparticles of iron oxide (MPIO) conjugated to an integrin $\alpha_v\beta_3$ targeting peptide (RGD-MPIO). The targeted MPIO showed some specific binding *in vivo*, but were unsuccessful at visualising angiogenesis *in vivo* owing to pre-existing hypointense voxels in the tumour, and non-specific uptake of the MPIO.

It was found that pre-existing hypointense voxels were caused by endogenous iron-laden macrophages resident in the tumour, and that non-specific contrast was a result of macrophage uptake of MPIO. It was also shown that non-specific macrophage uptake was reduced with antibody-targeted MPIO compared to peptide-targeted MPIO.

In conclusion, whilst the use of MP pCASL was successful for imaging angiogenesis in brain metastasis, the use of RGD-MPIO was precluded owing, in large part, to non-specific uptake of peptide targeted MPIO.

Acknowledgements

Firstly, to my family. None of this would have been done, none of this COULD have been done, without your support and guidance. Thank you for believing in me, and always challenging me to do more of the things I dreamed about. Dad, I may not have been dux, but hopefully this big fat thesis will help even the score. I don't really expect you to read it, but even so, it is dedicated to all of you.

To Mat, thank you for dragging yourself to the other side of the world, giving up sun and surfing and your job, just to be with me here. Thank you for the support, and the reality checks, and for bringing me wine and ice cream when I was stressed. I couldn't have done it without you. To Cass, thank you for the West End shows, the kind words and the gargantuan job of proof reading.

Thanks must also go to Dr Butler, my high school physics teacher, for inspiring me to love science, and for planting the first seed of a PhD in my mind. I remember you telling us to send you a copy if any of us ever did a PhD, and so I hope this thesis finds a place on your shelf of former students.

I also owe a huge amount to the Aurora Project, without whom I never would have been here. Thank you for taking that seed and allowing it to grow, for challenging me to study at the highest levels at one of the best universities in the world. To Aurora, to Richard, to Aunty Bronwyn and Leanne, and to the Charlie Perkins scholarship, thank you. I hope I can one day repay the inspiration and opportunities you have given me, by mentoring Indigenous STEM students to achieve their very best.

To the Charlie Perkins Scholarship, the James Fairfax Oxford Australia Scholarship, and the Green Templeton College DPhil scholarship, thank you for your support. It would not have been possible for me to come to Oxford without financial support, so I must thank you for making this dream a reality.

To GTBC, and OUWBC, I owe a lot of my fun, friends and sanity while I've been in Oxford. I never would have guessed the impact rowing would have on my life when I signed up to GTBC on my first day in town, alone and looking for a team sport to make some new friends. Thank you for welcoming me with such open arms, and introducing me to the amazing lifestyle that is rowing. To OUW, thank you for the laughter, and the tears, and being such an amazing bunch of strong women. I will miss each and every one of you, so come and visit me in Australia! To the blue boat, thanks for an amazing ride.

To the Sibson lab, these four years wouldn't have been the same without such a great group of friends. To Niki and Michael – thank you for your unending support and guidance. James – thank you for putting up with my million questions, and being the go-to guy for tools, fruit, and bank accounts. Manuel – thank you for your unending patience in teaching me surgeries and Spanglish. Manon and Nili – thank you for being great friends, and our amazing Hawaii road trip. Kevin – thank you for translating the physics talk and always encouraging our Friday afternoon pub outings. Vinton, Christina, Mario, Maria, Sarah, Claire, Vanessa, Kleo, Sasha, Nick, Paco – thank you for the lunchtime conversations, and the fun and laughter in the office.

Table of Contents

Abstract ... 3

Acknowledgements ... 5

Table of Figures ... 10

Abbreviations ... 12

Publications from this thesis ... 15

Chapter 1 – Introduction ... 17

1.1 Cancer ... 19

1.1.1 Cancer prevalence and mortality ... 19

1.1.2 Hallmarks of cancer ... 20

1.2 Angiogenesis ... 22

1.2.1 VEGF ... 25

1.2.2 Integrins ... 27

1.2.3 TIE2 ... 30

1.3 Metastasis ... 32

1.3.1 Mechanisms of metastasis ... 32

1.3.2 Brain metastasis ... 34

1.3.3 Clinical treatment ... 38

1.4 Imaging of angiogenesis and metastasis ... 40

1.4.1 Molecular imaging ... 40

1.4.2 Molecular imaging of angiogenesis ... 42

1.4.3 MRI of angiogenesis and metastasis ... 44

1.5 Aims of thesis and specific hypotheses ... 51

Aim 1 ... 51

Aim 2 ... 51

Aim 3 ... 51

Chapter 2 - Materials and methods ... 53

2.1 Chemicals and solutions ... 55

2.1.1 Chemicals ... 55

2.1.2 Substrates ... 56

2.1.3 Buffers and solutions ... 56

2.2 Cell lines and culture ... 58

2.2.1 Tumour cell lines and culture mediums ... 58

2.2.2 Cell revival ... 58

2.2.3 Cell incubation and harvesting ... 59

2.2.4 Cell storage ... 59

2.2.5 Cell preparation for injections 59
2.3 Animal models 60
2.3.1 Mouse strains 60
2.3.2 Intracerebral tumour model 60
2.3.3 Tumour harvest 62
2.3.4 Tissue storage 62
2.4 Antibodies 63
2.4.1 Immunohistochemistry 63
2.4.2 Immunofluorescence 64
2.4.3 Imaging contrast agents 64
2.5 Immunohistochemistry 65
2.5.1 Standard protocol 65
2.5.2 Mouse on mouse protocol 66
2.5.3 Perl's Prussian blue staining protocol 66
2.5.4 Histology digitisation 67
2.5 Imaging contrast agents 68
2.5.1 Cyclic RGD conjugated MPIO 68
2.5.2 Antibody conjugated MPIO 68
2.6 Imaging 70
2.6.1 T_1 weighted sequence 70
2.6.2 T_2 weighted sequence 70
2.6.3 Multiphase pseudo-continuous Arterial Spin Labelling 70
2.6.4 T_2* weighted multi-gradient echo sequence 71
2.6.5 Angiography 71
2.6.6 T_1 mapping 71
2.6.7 T_2 mapping 71
Chapter 3 - Arterial Spin Labelling to measure brain and tumour blood flow in mice 73
3.1 Introduction 75
3.2 Methods 78
3.2.1 Measurement of carotid blood flow 78
3.2.2 Simulation of labelling efficiency 78
3.2.3 Optimisation of MP pCASL sequence 80
3.2.4 Comparison with standard label-control pCASL and validation with autoradiography 84
3.2.5 Application of MP pCASL to brain tumour models 85

3.2.6 Statistics ... 86
3.3 Results ... 87
3.3.1 Measurement of carotid blood flow ... 87
3.2.2 Simulation of labelling efficiency ... 90
3.2.3 Optimisation of MP pCASL sequence ... 93
3.2.4 Comparison with standard label-control pCASL and validation with autoradiography ... 98
3.2.5 Application of MP pCASL to brain tumour models ... 101
3.4 Discussion ... 107
3.4.1 Measurement of carotid blood flow ... 107
3.4.2 Simulation of labelling efficiency ... 108
3.4.2 Optimisation of MP pCASL sequence ... 108
3.4.4 Comparison with standard label-control pCASL and validation with autoradiography ... 110
3.4.5 Application of MP pCASL to brain tumour models ... 111
3.5 Conclusions ... 116
Chapter 4 - Targeting integrin $\alpha_v\beta_3$ for *in vivo* imaging of brain metastases ... 119
4.1 Introduction ... 121
4.2 Methods ... 125
4.2.1 Expression of integrin $\alpha_v\beta_3$ in brain metastasis ... 125
4.2.2 Co-localisation of angiogenic markers with blood vessels ... 128
4.2.3 *In vitro* binding of RGD-MPIO to integrin $\alpha_v\beta_3$ ... 129
4.2.4 *In vivo* detection of angiogenic vessels using RGD-MPIO ... 130
4.2.5 Histological examination of MPIO in the brain ... 134
4.3 Results ... 135
4.3.1 Expression of integrin $\alpha_v\beta_3$ in brain metastasis ... 135
4.3.2 Co-localisation of angiogenic markers with blood vessels ... 144
4.3.3 *In vitro* binding of RGD-MPIO to integrin $\alpha_v\beta_3$ ... 147
4.3.4 *In vivo* detection of angiogenic vessels using RGD-MPIO ... 149
4.3.5 Histological examination of MPIO in the brain ... 160
4.4 Discussion ... 163
4.4.1 Expression of angiogenic markers in brain metastasis ... 163
4.4.2 *In vitro* binding of RGD peptides to integrin $\alpha_v\beta_3$ ... 166
4.4.3 *In vivo* detection of angiogenic vessels using RGD-MPIO ... 166
4.4.4 Histological examination of MPIO in the brain ... 169
4.5 Conclusion ... 170

Chapter 5 – Iron, macrophages, and the tumour microenvironment 173
5.1 Introduction 175
5.1.1 MPIO penetration of the blood-brain barrier 175
5.1.2 Retention of MPIO by tumour associated macrophages 176
5.1.3 Effect of MPIO targeting moiety 179
5.1.4 Endogenous iron-laden macrophages 181
5.1.5 Specific objectives 183
5.2 Methods 184
5.2.1 MPIO penetration of the blood-brain barrier 184
5.2.2 Retention of MPIO by tumour associated macrophages 187
5.2.3 Effect of MPIO targeting moiety 188
5.2.4 Endogenous iron-laden macrophages 190
5.3 Results 191
5.3.1 MPIO penetration of the blood-brain barrier 191
5.3.2 Retention of MPIO by tumour associated macrophages 203
5.3.3 Effect of MPIO targeting moiety 211
5.3.4 Endogenous iron-laden macrophages 222
5.4 Discussion 227
5.4.1 MPIO penetration of the blood-brain barrier 227
5.4.2 Retention of MPIO by tumour associated macrophages 230
5.4.3 Effect of MPIO targeting moiety 232
5.4.4 Endogenous iron-laden macrophages 236
5.5 Conclusion 239
Chapter 6 – Discussion and future work 243
6.1 Limitations and further work 245
6.1.1 Arterial spin labelling to measure brain and tumour blood flow in mice 245
6.1.2 Targeting integrin $\alpha_v\beta_3$ for *in vivo* imaging of brain metastasis 247
6.1.3 Iron, macrophages and the tumour microenvironment 249
6.2 Conclusions 253
References 256

Table of Figures

Figure 1.1: Hallmarks of cancer 21
Figure 1.2: Tumour growth in the brain 23
Figure 1.3: Angiogenesis signalling pathways 24
Figure 1.4: The metastatic process 32
Figure 1.5: Mechanisms of brain metastasis 36
Figure 1.6: Enhancement patterns of MRI contrast agents 48
Figure 2.1: Stereotaxic injection coordinates 61
Figure 2.2: Cyclic RGD peptide structures 69
Figure 3.1: Supervoxel processing method 83
Figure 3.2: Carotid blood flow power Doppler trace 88
Figure 3.3: Carotid artery blood flow measurement 89
Figure 3.4: Bloch simulations 90
Figure 3.5: Theoretical signal SNR 91
Figure 3.6: Inversion efficiency 92
Figure 3.7: Optimisation of EPI readout 94
Figure 3.8: Respiratory triggering method 95
Figure 3.9: Optimisation of bolus duration 96
Figure 3.10: Optimisation of post label delay 97
Figure 3.11: Cerebral blood flow maps in naïve mice 99
Figure 3.12: Microvessel density in naïve mice 100
Figure 3.13 CBF values across tumour timepoints 101
Figure 3.14: CBF values in enhancing tumours 102
Figure 3.15: CBF values in tumours with non-enhancing core 104
Figure 3.16: Correlation between CBF and microvessel density 105
Figure 3.17: CBF values in glioma 106
Figure 4.1: Immunohistochemistry quantification 127
Figure 4.2: MGE3D images and hypointense voxel segmentation 133
Figure 4.3: Angiogenic marker immunohistochemistry across timepoints 136
Figure 4.4: Angiogenic marker expression 137
Figure 4.5: Tumour size across timepoints 138
Figure 4.6: Quantification of angiogenic markers 142
Figure 4.7: Correlation of angiogenic markers with tumour size 143
Figure 4.8: Fluorescent co-localisation 145
Figure 4.9: Fluorescent co-localisation quantification 146
Figure 4.10: Binding capability of cyclic RGD peptides 148
Figure 4.11: Representative MRI images across timepoints 150
Figure 4.12: Representative MRI images across timepoints 151
Figure 4.13: Hypointense voxels in the normal striatum 152
Figure 4.14: MPIO induced hypointense voxels across timepoints 153
Figure 4.15: Respresentative MRI images in enhancing tumours 155
Figure 4.16: MPIO induced hypointense voxels in enhancing tumours 156
Figure 4.17: Representative MRI images in glioma 158
Figure 4.18: MPIO induced hypointense voxels in glioma 159
Figure 4.19: Aggregations of MPIO in tumour tissue 161
Figure 4.20: Quantification of MPIO aggregations 162
Figure 5.1: USPIO enhancement kinetics 178
Figure 5.2: Aggregation of RGD-IONPs 180

Figure 5.3: MRI imaging of BBB breakdown with CINC-1 192
Figure 5.4: Histology of BBB breakdown with CINC-1 193
Figure 5.5: Expression of MPIO targeting molecules 195
Figure 5.6: Quantification of MPIO targeting molecules 196
Figure 5.7: Representative MRI images of BBB breakdown 198
Figure 5.8: MPIO induced hypointense voxels following BBB breakdown 200
Figure 5.9: MPIO uptake in the brain following BBB breakdown 201
Figure 5.10: Quantification of iron aggregations 202
Figure 5.11: MPIO aggregations in tumours 204
Figure 5.12: MPIO aggregations inside macrophages and microglia 205
Figure 5.13: MPIO-laden macrophages are associated with blood vessels 207
Figure 5.14: Single endothelium bound MPIO 209
Figure 5.15: Quantification of endothelium bound MPIO 210
Figure 5.16: Uptake of MPIO by cells 212
Figure 5.17: Quantification of MPIO uptake by cells 213
Figure 5.18: MRI and histology of MPIO imaging in rat tumours 215
Figure 5.19: Quantification of MRI and histology in rat tumours 217
Figure 5.20: MRI and histology of antibody-targeted MPIO imaging 219
Figure 5.21: Quantification of antibody-targeted MPIO imaging 220
Figure 5.22: Histology of antibody-targeted MPIO imaging 221
Figure 5.23: Quantification of endogenous iron-laden macrophages 223
Figure 5.24: MRI images of endogenous iron-laden macrophages 224
Figure 5.25: Histology of endogenous iron-laden macrophages 225
Figure 5.26: Endogenous hypointense voxels 226

Abbreviations

ANOVA – analysis of variance

ASL – arterial spin labelling

BBB – blood-brain barrier

BOLD – blood oxygen level dependent imaging

BSA – bovine serum albumin

CAM – cell adhesion molecule

CBF – cerebral blood flow

CINC-1 – cytokine induced neutrophil chemoattractant

CNS – central nervous system

DAB - 3,3'-diaminobenzidine tetrahydrochloride hydrate

DCE-MRI – dynamic contrast enhanced magnetic resonance imaging

DMSO – di-methyl sulfoxide

DPX – mounting medium DPX

EDC - 1-Ethyl-3-(3-dimethylaminopropyl)carbodiimide hydrochloride

EDTA – Ethylenediaminetetraacetic acid

EPI – echo planar imaging

FA – flip angle

FDG-PET – fluorodeoxyglucose positron emission tomography

FOV – field of view

IONP – iron oxide nanoparticles

MES - 2-(N-morpholino)ethanesulfonic acid

MGE3D – multi-gradient echo three dimensional

MP pCASL – multiphase pseudocontinuous arterial spin labelling

MPIO – microparticles of iron oxide

MRI – magnetic resonance imaging

PBS – phosphate buffered saline

PBS-T – phosphate buffered saline with 0.01% Tween-20

pCASL – pseudocontinuous arterial spin labelling

PET – positron emission tomography

PFA – paraformaldehyde

PLD – post-label delay

PLP – periodate-lysine paraformaldehyde

RDG – arginine-aspartic acid-glycine scrambled control peptide

RF – radio frequency

RGD – arginine-glycine-aspartic acid targeted peptide

ROI – region of interest

SNR – signal to noise ratio

SPECT – single photon emission computed tomography

TE – echo time

TI – inversion time

TIE2 – angiopoietin 1 receptor

TNB – tris-NaCl buffer

TR – relaxation time

USPIO – ultrasmall superparamagnetic iron oxide

VCAM-1 – vascular cell adhesion molecule 1

VEGF – vascular endothelial growth factor

VEGFR1 – vascular endothelial growth factor receptor 1

VEGFR2 – vascular endothelial growth factor receptor 2

Publications from this thesis

Buck J, Larkin J, Khrapitchev A, Simard M, Chappell M, Sibson N. Sensitivity of multiphase pseudo-continuous arterial spin labelling magnetic resonance imaging for measuring brain tumour blood flow. *Contrast Media and Molecular Imaging*. 2018.

Buck J, Perez-Balderas F, Zarghami N, Khrapitchev A, Sibson N. Imaging angiogenesis in brain metastasis using integrin $\alpha_v\beta_3$ targeted microparticles of iron oxide. *In preparation*.

Conference abstracts and presentations from this thesis

Telethon Kids Institute research seminar, invited speaker. Imaging angiogenesis in brain metastasis. Buck J, Sibson N. 2019, Perth, WA

Department of Oncology internal seminar. Imaging angiogenesis in brain metastasis. Buck J, Sibson N. 2018, Oxford, UK

Molecular imaging of integrin αvβ3 upregulation in a mouse model of brain metastasis. Buck J, Khrapitchev A, Zarghami N, Perez-Balderas F, Sibson N. European Association for Cancer Research 25th Congress, 2018, Amsterdam, Holland.

Molecular imaging of integrin αvβ3 upregulation in a mouse model of brain metastasis. Buck J, Khrapitchev A, Zarghami N, Perez-Balderas F, Sibson N. Oxford Biomedical Imaging Festival, 2018 Oxford, UK.

Multiphase pseudo-continuous arterial spin labelling MRI enables accurate measurement of tumour blood flow in mouse models of glioma and brain metastasis. Buck J, Larkin J, Khrapitchev A, Simard M, Chappell M, Sibson N. Cancer Research UK Oxford Symposium. 2018, Oxford, UK.

Department of Oncology student symposium speaker. Multiphase pseudo-continuous ASL to image cerebral blood flow in a mouse model of brain metastasis. Buck J, Larkin J, Khrapitchev A, Simard M, Ray K, Chappell M, Sibson N. 2017, Oxford, UK

Multiphase pseudo-continuous ASL to image cerebral blood flow in a mouse model of brain metastasis. Buck J, Larkin J, Khrapitchev A, Simard M, Ray K, Chappell M, Sibson N. International Society for Magnetic Resonance in Medicine Conference. 2017, Honolulu, USA

Integrin αvβ3 as a potential target for imaging angiogenesis in brain metastases. Buck J, Sarmiento Soto M, Sibson N. British Neuro-Oncology Society Conference, 2016, Leeds, UK.

Chapter 1 – Introduction

1.1 Cancer

1.1.1 Cancer prevalence and mortality

Cancer is a disease characterised by the uncontrolled growth of abnormal cells. If untreated, cancer may interfere with the normal functioning of organs, leading to death due to organ failure. Cancer affects a huge number of people, with 14 million new cases and 12 million deaths worldwide each year[1]. In the UK, these figures are 350,000 new cases, and 160,000 deaths[2]. Of these, the most common types of cancer are breast, lung, and colorectal cancers in women; and in men prostate, lung and colorectal cancers are the most common[3]. Together, these account for more than half of all new diagnoses.

There are many different tumours that affect the brain, including both primary and secondary tumours. Primary brain tumours originate from cells in the central nervous system (CNS), of which the most common types are glioma, meningioma and pituitary tumours[4]. Primary brain tumours are responsible for around 11,000 new cases of cancer per year in the UK[4]. Secondary, or, metastatic, tumours are those that have spread to the brain from a different primary site. It is estimated that between 20 - 40% of patients with systemic cancer will develop brain metastases[1], and have a median survival of only 5 weeks without treatment[5]. Metastatic brain tumours outnumber primary brain tumours by a ratio of approximately 3:1[6], and hence represent a huge proportion of the disease burden.

Owing to these dismal statistics, it is crucially important to research and develop new therapies and early detection methods for all types of cancer, but particularly metastatic disease in the brain.

1.1.2 Hallmarks of cancer

In 2000, Hanahan and Weinberg proposed that cancer could be defined by six 'hallmarks', which are traits common to all cancers[7] (Figure 1.1). These hallmarks were defined as self-sufficiency in growth signals, insensitivity to anti-growth signals, tissue invasion and metastasis, limitless replicative potential, sustained angiogenesis, and evading apoptosis. These factors are common to all cancers, and form the cornerstone of research and treatments.

In 2011, Hanahan and Weinberg updated these hallmarks to include a further decade of cancer research[8]. The next generation of hallmarks are defined as: sustaining proliferative signalling, evading growth suppressors, avoiding immune destruction, enabling replicative immortality, tumour-promoting inflammation, activating invasion and metastasis, inducing angiogenesis, genome instability and mutations, resisting cell death, and deregulating cellular energetics.

This thesis will focus on two of the major hallmarks – angiogenesis and metastasis – and methods by which we can use imaging to understand their biology.

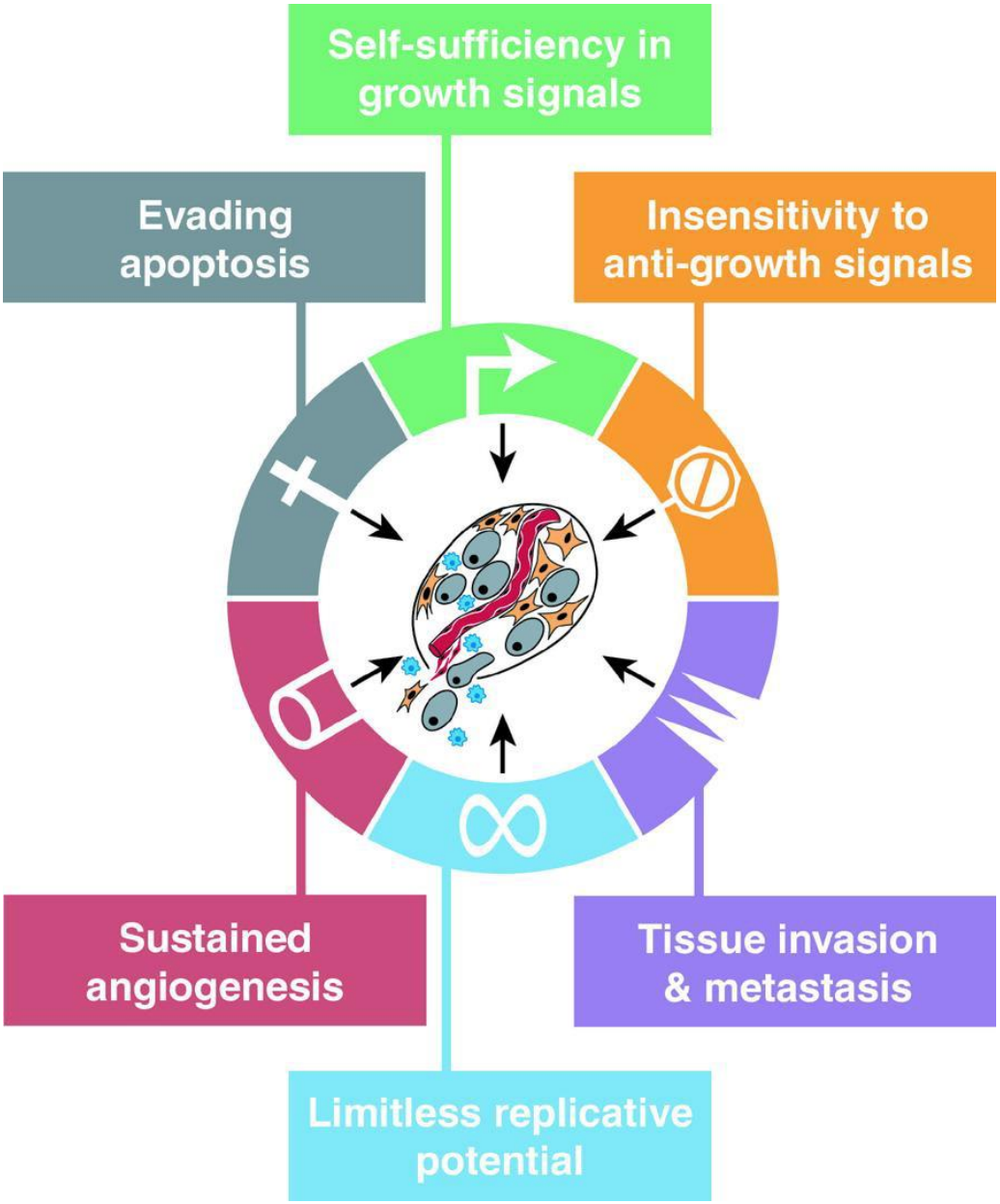


Figure 1.1: The six hallmarks of cancer, as described by Hanahan and Weinberg. Reproduced with permission from The Hallmarks of Cancer[7].

1.2 Angiogenesis

Angiogenesis is the process of new blood vessel formation from the existing vasculature, and is crucial for tumours to grow past a few millimetres in size[9]. Angiogenesis is distinct from the process of vasculogenesis, which is the de novo formation of blood vessels in embryos[10]. Angiogenesis occurs in both normal homeostatic processes, such as wound healing, and also in disease. Some diseases are characterised by excessive angiogenesis, such as cancer, psoriasis and endometriosis; whilst others are characterised by insufficient angiogenesis, such as diabetic ischemia and pre-eclampsia[11].

There are two main types of angiogenesis. The first, sprouting angiogenesis, occurs when an endothelial cell is induced to become a tip cell[12]. It then migrates towards chemotactic signals, and the endothelial cells proliferate behind it to form new vessels[13]. In contrast, intussusception occurs when an existing vessel splits into two[14]. Both of these angiogenic processes have similar cues, but rely on different molecular mechanisms. It was first suggested by Folkman that anti-angiogenic treatment strategies may be useful in preventing tumour growth in an wide range of cancer types[15].

The growth of tumours occurs via two primary mechanisms. Co-optive growth is the initial growth of tumours along the pre-existing vasculature and is followed by the 'angiogenic switch', whereby the tumour begins to produce its own vasculature[15,16], as shown in Figure 1.2. Tumour colonies must establish angiogenesis in order to grow beyond micron-millimetre size[9,17,18]. As the tumour increases in size, hypoxia occurs in the relatively avascular tumour[19]. This can induce an angiogenic switch, which is the point at which tumour cells move from growing co-optively along the existing vascular bed[16] to stimulating the growth of

their own vasculature[15]. In many tumours, a subset of cells grows in a co-optive manner whilst others are angiogenic[19-21], particularly at early timepoints. Some angiogenic cells may even revert to a non-angiogenic, dormant phenotype and back again[22]. This mixture of phenotypes demonstrates the complexity of the many molecular mechanisms that control the angiogenic switch.

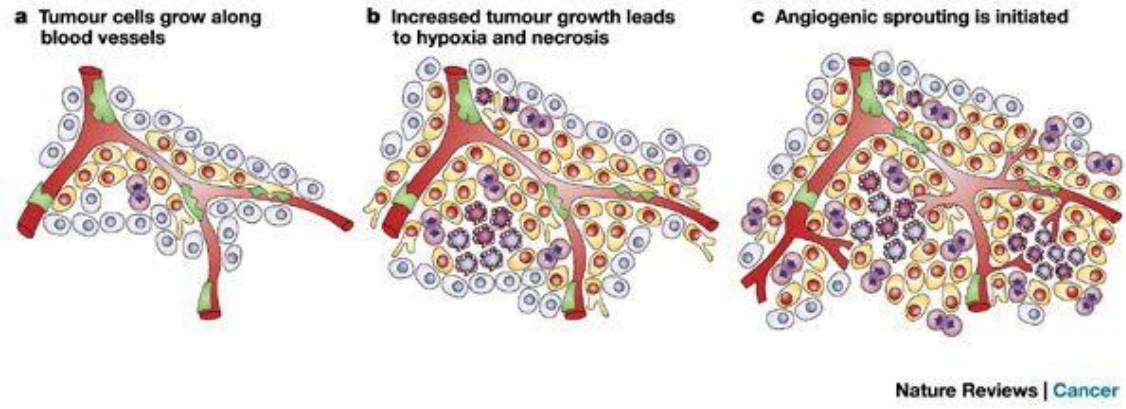


Figure 1.2: Growth of tumour cells in the brain. Tumour cells (yellow) first grow co-optively along the existing vasculature, until pressure from hypoxic cells (purple) upregulates angiogenic signalling pathways, and sprouting angiogenesis occurs. This change is known as the 'angiogenic switch'. Reproduced with permission from Bergers and Benjamin[23].

For the purposes of this thesis, this introduction will focus on angiogenesis in the context of cancer. As angiogenesis plays a large role in the growth of tumours, it is important to be able to accurately detect *in vivo*. The major signalling pathways associated with angiogenesis are shown in Figure 1.3, and are described more thoroughly in sections 1.2.1 – 1.2.3.

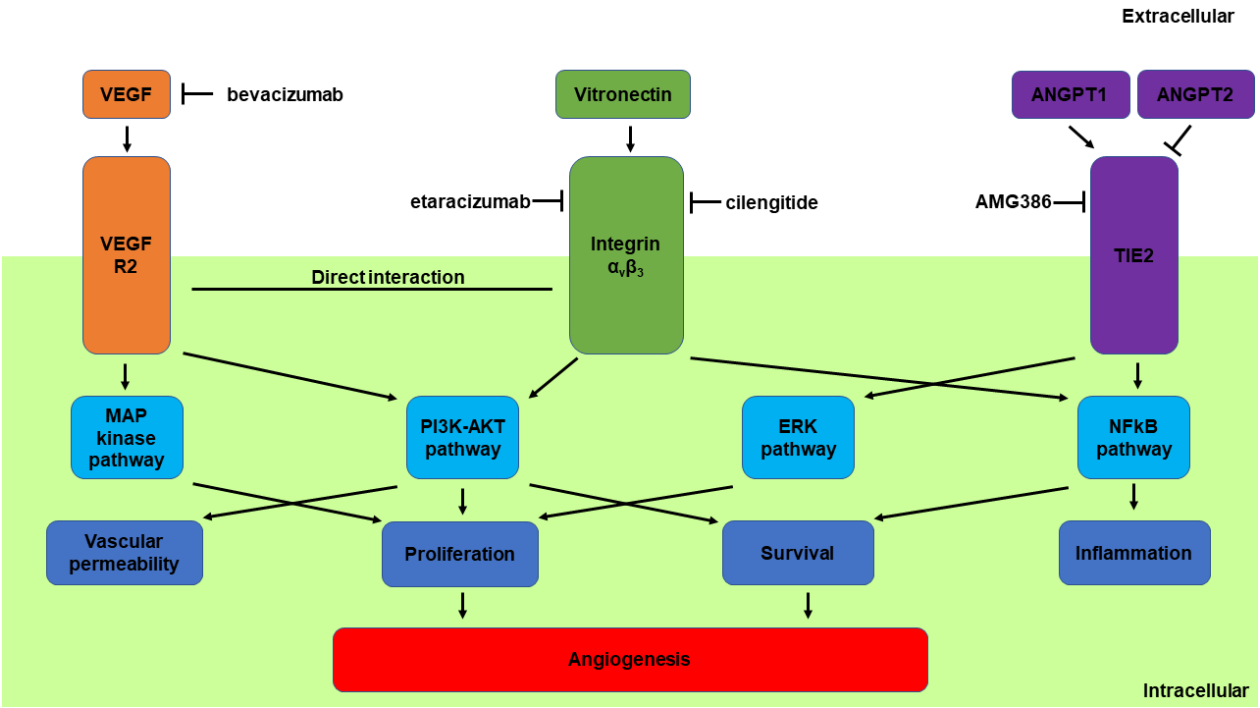


Figure 1.3: Schematic showing three of the major signalling pathways involved in angiogenesis: VEGF, integrin $\alpha_v\beta_3$ and TIE2. These receptors converge on downstream signalling pathways to mediate vascular permeability, proliferation, survival and inflammation, and ultimately mediate angiogenesis.

1.2.1 VEGF

Vascular endothelial growth factor (VEGF) and its main receptors (VEGFR1 and VEGFR2) are some of the key mediators of angiogenesis. It was recognised in the 1990's that cell associated and diffusible factors were able to induce angiogenesis, as tumour cells could be implanted onto a window in the hamster cheek pouch[24,25], or the avascular cornea[26], and induce capillary sprouting. The first of these angiogenic factors to be discovered was basic fibroblast growth factor[27], which induces the proliferation of fibroblasts and epithelial cells, and also acts as a chemoattractant for sprouting endothelial cells. VEGF was initially discovered as a vascular permeabilising factor[28], and it was subsequently discovered that it could also induce mitosis of vascular endothelial cells[29], and hence, induce angiogenesis.

VEGF has been found to have a number of isoforms of different lengths, with the 121 amino acid isoform being freely diffusible[30] and found in a number of bodily fluids[31]. Mouse[32], rat[33], and guinea pig[34] homologues were also discovered, suggesting that VEGF was an important and highly conserved factor in angiogenesis. Despite having been characterised in tumour cell lines, the first evidence for the role of VEGF in tumour angiogenesis *in vivo* was the discovery that it was expressed in glioblastoma multiforme[35], particularly in hypoxic regions of the tumour. It was also shown that VEGF secretion could be induced by hypoxia in *in vitro* cell cultures[36], and hence is a modulator of hypoxia induced angiogenesis.

VEGF mediates angiogenesis by binding to its receptors[37], causing receptor dimerization, and activation of a tyrosine kinase signalling pathway[38], as shown in Figure 1.3. Binding to VEGF receptor 2 (VEGFR2) activates the MAP kinase signalling pathway[39] and PI3K-AKT-mTOR pathway[40], which induces mitosis of the endothelial cells, as shown in Figure 1.3.

Since these discoveries, it has been widely reported that VEGFR2 is overexpressed on angiogenic endothelial cells in many types of tumour[41-43], including primary brain tumours and metastases[44], and is expressed on the luminal surface of these cells, which allows targeting by blood-based imaging contrast agents. With these mechanisms, expression of VEGF and its receptors has been correlated with increased microvessel density[45-47], metastasis[46-49], and poor survival rates[45,50-53] in a number of different tumour types. *In vivo* blocking of VEGF activity leads to reduced tumour growth and blood vessel density[54-56], and has contributed to the development of anti-angiogenic therapeutics in clinical use such as bevacizumab (Avastin)[57,58]. Bevacizumab is approved for the treatment of colorectal, renal, lung, breast and ovarian cancers[59]. Other anti-angiogenic drugs targeting the VEGF pathway are approved for the clinical treatment of cancer, including sorafenib, sunitinib and ramucirumab, amongst others[59].

Thus, VEGF, and its receptor VEGFR2, are important factors in the induction and maintenance of angiogenesis in the tumour environment.

1.2.2 Integrins

Integrins are a family of transmembrane glycoproteins that act as adhesion molecules. They are heterodimers consisting of an alpha and a beta subunit, of which there are more than 24 combinations[60]. Of these heterodimers, a number are involved in angiogenesis, including $\alpha_v\beta_3$, $\alpha_v\beta_5$, $\alpha_1\beta_1$, $\alpha_2\beta_1$, $\alpha_4\beta_1$, and $\alpha_5\beta_1$, which are all upregulated during angiogenesis. Integrin $\alpha_v\beta_3$ is one of the most widely expressed integrins in angiogenesis and, as such, this thesis will focus on integrin $\alpha_v\beta_3$ in angiogenesis, its expression in brain metastases, and targeting it using molecular imaging.

Integrin $\alpha_v\beta_3$, also known as the vitronectin receptor, is expressed at high levels on angiogenic endothelial cells[61,62], along with osteoclasts[63], and some types of tumour cells[63-65]. At low levels, it is expressed in the kidney[63] and on circulating monocytes[66]. Its main signalling pathways are shown in Figure 1.3.

Along with a number of other integrins, integrin $\alpha_v\beta_3$ has a specific binding site in the peptide motif Arg-Gly-Asp (RGD). This motif was first discovered in 1984 by Pierschbacher and Ruoslahti, as a peptide sequence that accounted for the ability of fibronectin to bind to the cellular membrane[67]. This sequence was later found in other cell adhesion molecules, including the integrin $\alpha_v\beta_3$ ligand vitronectin[68,69]. Different integrins have a preference for binding different RGD containing extracellular matrix proteins, and these recognition mechanisms are reviewed comprehensively by Ruoslahti[70]. More recently, a large array of RGD containing peptides and peptidomimetics with varying binding abilities and specificity for each integrin heterodimer have been created, and their IC50 values measured[71,72]. These RGD peptides are used in a wide range of blocking and

targeting applications, including small molecule drugs and molecular imaging (reviewed in section 1.4.3).

Integrin $\alpha_v\beta_3$ plays a prominent role in both developmental and pathological angiogenesis. Knockout of the α_v subunit results in embryonic lethality[73,74], although the vasculature does develop if the knockout is confined to endothelial cells[75]. Similarly, blockade of the α_v subunit *in vivo* results in reduced tumour growth in several pre-clinical models[76,77]. The β_3 subunit (CD61), however, can be compensated for in some knockout models, as the vasculature develops normally[78,79], although pathological angiogenesis is reduced when the subunit is unable to undergo phosphorylation[80]. *In vivo* blockade of integrin $\alpha_v\beta_3$ also results in reduced tumour growth pre-clinically in models of breast cancer[81], Kaposi's sarcoma[82], melanoma[83,84], and glioblastoma[85,86].

In combination, expression of integrin $\alpha_v\beta_3$ was detected in many human tumour samples, on the vasculature[62,87] as well as on the tumour cells themselves[62]. Expression of integrin $\alpha_v\beta_3$ was found to correlate with relapse-free survival[87]. As a result, inhibition of integrin $\alpha_v\beta_3$ became an important target for anti-angiogenic chemotherapeutic agents. It was first demonstrated in 1994 that inhibition of integrin $\alpha_v\beta_3$ with RGD peptides or antagonistic antibodies caused apoptosis of angiogenic vessels followed by tumour regression[88]. This finding has been replicated in many other pre-clinical tumour models[83,89], and has also been useful in the treatment of proliferative retinopathy[90-92]. Integrin $\alpha_v\beta_3$ also shows cross-talk with other angiogenic signalling pathways, in particular, the VEGF pathway. Integrin $\alpha_v\beta_3$ interacts directly with VEGFR2[93], and also shares downstream effector pathways that mediate angiogenesis[94-96] and vessel permeability[97] (Figure 1.3).

Because of these effects on angiogenesis, inhibitors of integrin $\alpha_v\beta_3$ have been investigated as a possible strategy for cancer treatment. Many RGD based peptides have shown promising anti-angiogenic activity in preclinical studies[98,99]. Nevertheless, clinical trials of integrin $\alpha_v\beta_3$ antagonists have had mixed results. Cilengitide, an RGD-based peptide, has shown an ability to reduce tumour growth in preclinical models of melanoma[100] and glioblastoma[85,86], and showed promising early-phase clinical results against solid tumours[101,102], head and neck tumours[103], and glioblastoma[104-107]. However, it showed no benefit over gold standard treatment for pancreatic cancer[108], or against glioblastoma in Phase II and III trials[109,110], and is not currently recommended for clinical use. In fact, some studies showed that at low concentrations, Cilengitide was found to increase integrin $\alpha_v\beta_3$ mediated angiogenesis[111,112]. Despite this finding, the drug still shows some promise for vascular normalisation therapy[113], and may show synergistic effects in combination with radiotherapy[114,115] and other chemotherapeutics. At present, however, no clinical trials are ongoing.

Etaracizumab, (Vitaxin, Abegrin[116]), a humanised anti-$\alpha_v\beta_3$ antibody, based on the LM609 antibody, which showed good anti-angiogenic efficacy in pre-clinical studies[89], has also shown some efficacy against cancer in early-phase clinical trials[117]. However, it has shown no benefit in metastatic cancer[118,119] or leiomyosarcoma[120]. No clinical trials are currently ongoing.

It must be stated that none of these clinical trials have attempted to stratify patients by integrin $\alpha_v\beta_3$ expression levels, which may predict response. In the only trial that attempted to image integrin $\alpha_v\beta_3$ using radiolabelled Vitaxin, the imaging was unsuccessful[118]. This lack of stratification highlights the need for sensitive, specific, and reproducible clinical imaging of the angiogenic vasculature in tumours, the

development of which is the major aim of this thesis. As the expression of integrin $\alpha_v\beta_3$ on the vasculature of metastatic brain tumours in murine models has not previously been established, the first aim of this thesis will be to quantify the expression over time of integrin $\alpha_v\beta_3$ in a mouse model of brain metastasis.

1.2.3 TIE2

TIE2 (angiopoietin 1 receptor, TEK, CD202b) is an endothelial tyrosine kinase receptor, which mediates angiogenic pathways through its ligands angiopoietin 1 and 2, as shown in Figure 1.3. The effects of these ligands depends on a number of upstream and downstream factors, but angiopoietin 1 usually acts as a receptor agonist[121] resulting in survival signals and quiescent vasculature, whilst angiopoietin 2 usually acts as an antagonist[122] or partial agonist[123], resulting in increased endothelial permeability and priming of the vasculature for angiogenesis. The TIE2 pathway also provides a link between angiogenesis and inflammation, via crosstalk with the NF-κB pathways, as shown in Figure 1.3. TIE2 is expressed on endothelial cells, as well as on some tumour cells[124], monocytes[125], and tumour-associated macrophages[126,127].

Studies have shown that overexpression of angiopoietin 2, and hence increased angiogenic signalling through TIE2, correlates with poor prognosis in breast[128] and colorectal cancer[129], as well as correlating with invasion and metastasis in breast cancer[130] and melanoma[124]. Similarly, in angiopoietin 2 deficient mice, initial tumour growth is impaired[131]. Knockdown of angiopoietin 2 also results in decreased metastatic potential[132]. In some tumour models, including glioma, the TIE2/angiopoietin 2 axis was found to mediate co-option of the existing host

vasculature by tumour cells in early invasive stages, along with angiogenesis in later stages[19].

Antibody inhibition of the angiopoietin 2/TIE2 axis has also shown good results in preclinical studies[133,134], and a synergistic effect in combination with VEGF inhibition[135,136]. Gene therapy using a vector to produce a soluble TIE2 blocking protein has also been used in mice to reduce angiogenesis, tumour growth and metastasis in the 4T1 metastatic murine mammary carcinoma model[137]. Clinically, drugs inhibiting the TIE2 pathway have also been studied in early phase trials. AMG386, a peptide-antibody fusion protein that blocks interaction with the TIE2 receptor has shown anti-angiogenic and anti-tumour activity in patients with solid tumours[138].

As it is believed that the balance of angiopoietin 1 and 2 may act as a molecular angiogenic switch[139], molecular imaging of TIE2 is an attractive target for the *in vivo* visualisation of angiogenesis, and as such, this thesis aims to characterise the expression of TIE2 on the brain vasculature in a mouse model of brain metastasis.

1.3 Metastasis

1.3.1 Mechanisms of metastasis

One of the enduring challenges in the treatment of cancer is metastasis, which is the spread from the primary tumour to distant sites. In order for metastasis to occur, cells must invade surrounding tissue, detach from the primary tumour, intravasate into blood or lymphatic vessels, extravasate into the tissue at distant sites, and establish a new tumour colony. Each of these steps, as shown in Figure 1.4 has separate mechanisms, signalling pathways and processes, which are reviewed in detail by Geiger and Peeper[140].

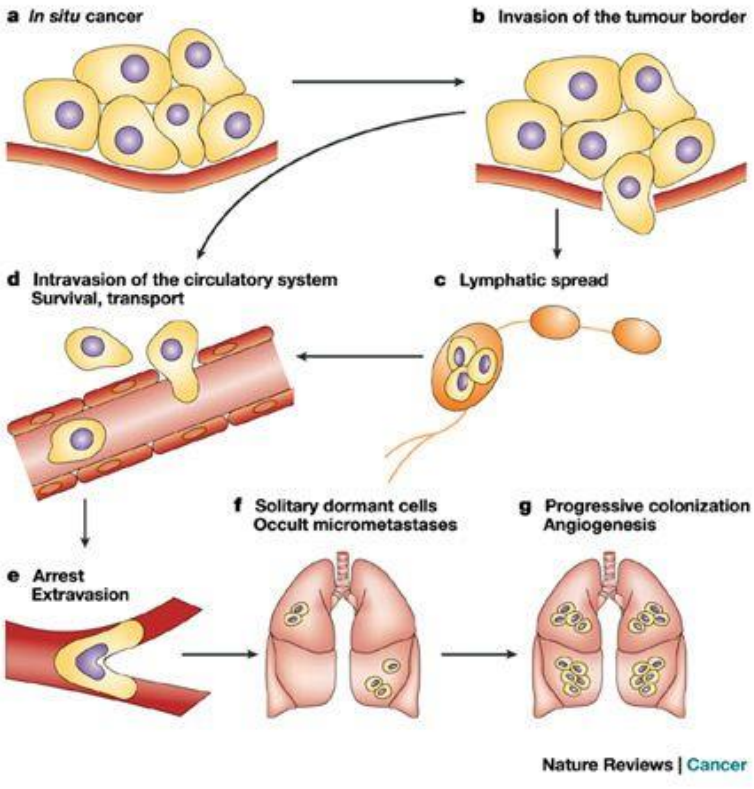


Figure 1.4: Steps involved in the metastatic spread of tumour cells. Tumour cells *in situ* must first invade through the basement membrane. Following this, they must invade the lymphatic system, or intravasate into the circulation. They then arrest in small vessels at a distant site, and extravasate. At the secondary site, some cells become dormant, while others grow to form macrometastatic tumours. Reproduced with permission from Steeg, 2003[141].

Integrins are also involved in many of the steps of the metastatic cascade. As important cell adhesion molecules, many different integrins regulate the adhesion of cancer cells to the extracellular matrix, and by signalling the upregulation of matrix metalloproteases they contribute to the breakdown of the basement membrane and local invasion[142,143]. Integrin $\alpha_v\beta_3$ in particular, along with integrin $\alpha_5\beta_1$, is associated with the remodelling of fibronectin in the extracellular matrix, allowing cancer cell migration and invasion[144,145].

Integrins are also involved in providing adhesion independent cell survival signals through their bi-directional signalling ability[146,147], which is crucial for the survival of circulating tumour cells. Integrin $\alpha_v\beta_3$ is also able to promote metastasis to the lung by mediating the ability of tumour cells to bind to fibronectin-enriched blood clots, and hence arrest in the lungs[148]. As a result, nanoparticles encapsulating the chemotherapeutic agent doxorubicin, when targeted to integrin $\alpha_v\beta_3$, can both reduce the angiogenic vasculature of tumours and also reduce the incidence of metastatic spread[149,150]. Tumour extravasation pathways are also mediated by integrins, particularly the β_5 subunit in conjunction with the TIE2/angiopoietin 2 axis[151], and the β_1 integrins[152].

It is currently unknown whether integrin $\alpha_v\beta_3$ contributes to the seeding of brain metastasis, however a role for integrin β_1 has been shown[16,153]. Integrin $\alpha_v\beta_3$ does, however, contribute to the intracranial growth and angiogenesis of metastatic tumour cells in the brain once they are established[154], and is expressed in the brain metastases of a number of different primary tumour types[155]. It has also been established that expression of integrin $\alpha_v\beta_3$ contributes to breast cancer bone

metastasis[156,157], and many other integrins contribute to seeding in other organs[158]. For this reason, it is important to evaluate expression of integrin $\alpha_v\beta_3$ in brain metastasis models in the context of both early metastatic seeding and angiogenesis.

1.3.2 Brain metastasis

Metastasis to the brain has a distinct pathophysiology, epidemiology and prognosis to metastasis in other sites. These aspects, along with diagnosis and clinical management, are reviewed extensively in the recent Nature Reviews Disease Primer by Achrol et al[159], which provides an excellent overview of brain metastasis beyond the scope of what can be described in this thesis.

The detection and treatment of brain metastasis remains an important clinical challenge. Most brain metastases are not detectable by the clinical gold standard of gadolinium contrast-enhanced imaging until they are approximately 0.5 cm in diameter or larger[160-162]. In mice, despite evidence for increased passive permeability at metastasis sites[163], metastases usually do not show gadolinium enhancement below 0.5 mm in diameter[164-166]. Above this size, metastases may have leaky, and hence detectable, vasculature. The low sensitivity of gadolinium contrast-enhanced imaging reflects the necessity for blood-brain barrier (BBB) breakdown to have occurred in order for contrast agents to penetrate the tumour. However, BBB breakdown occurs mostly in the later stages of metastasis[167]. The ability to detect brain metastases at early timepoints may increase the treatment options available, potentially improving prognosis. Similarly, the ability to image features of the tumour microenvironment, including angiogenesis, allows mapping and quantitation of metabolic parameters, monitoring of treatment response, and

patient risk stratification or selection for therapies, which may also contribute to improving prognosis[168,169].

It has been shown using intravital microscopy that less than 10% of injected metastatic cells arrest in the brain vasculature and, of these, only a small percentage go on to extravasate[170]. This process takes place in the first 9 days after injection. Following extravasation, some metastatic cells form dormant micrometastases, while others form active micrometastases which go on to form macrometastatic tumour colonies, co-opting existing blood vessels, then eventually becoming angiogenic[170-173], as shown in Figure 1.5.

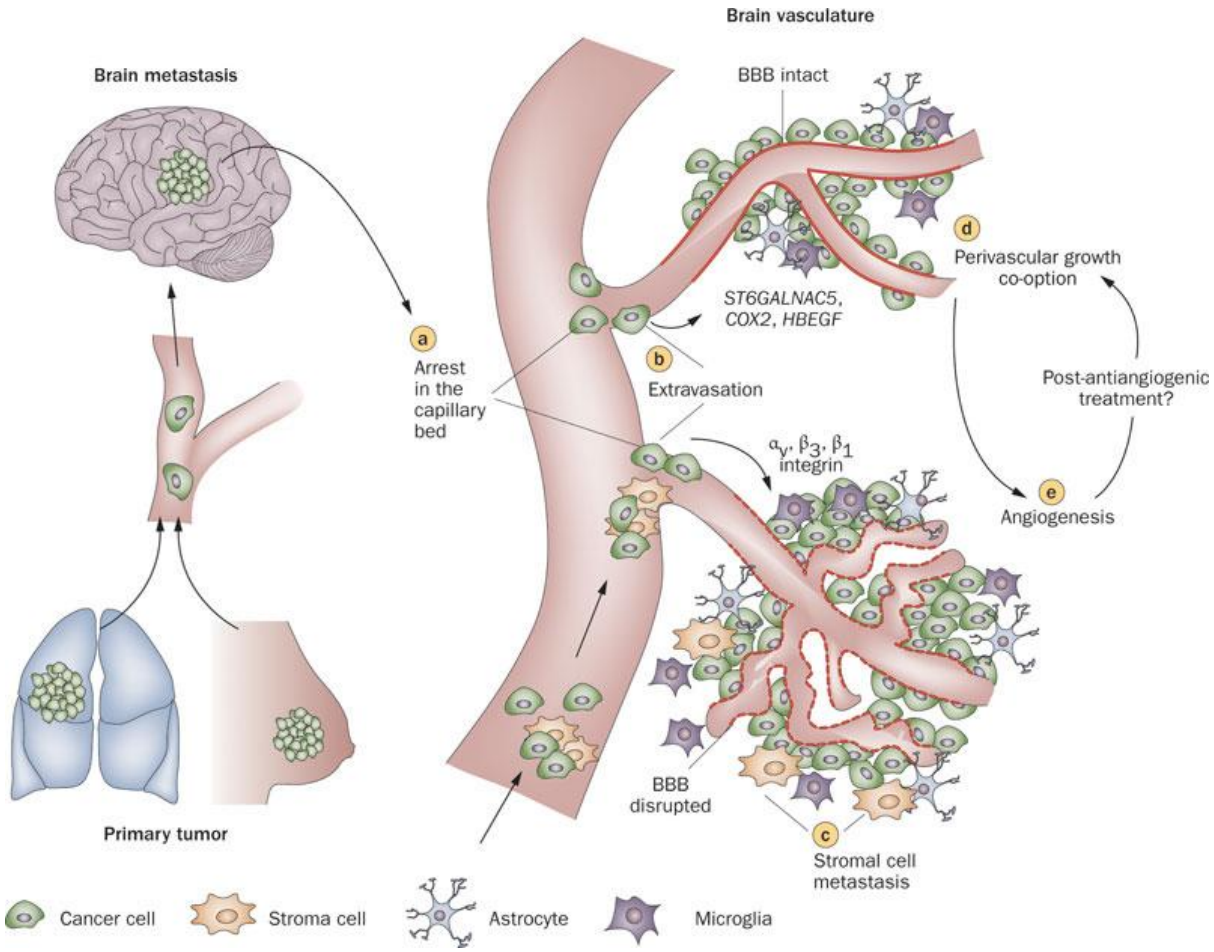


Figure 1.5: Mechanisms of metastasis from the primary tumour to the brain. Tumour cells first arrest in the capillary bed of the brain, then extravasate into the parenchyma. Initially, they grow co-optively along the pre-existing vasculature, behind an intact BBB, and at this stage are very difficult to detect. The tumour may then initiate angiogenic pathways, and recruit stromal cells to the site, resulting in a compromised BBB. Reproduced with permission from Eichler et al. 2011[174].

The mouse model of brain metastasis used in this study is the 4T1 murine metastatic breast cancer cell line[175], which has been stably transfected to express EGFP[176] (4T1-GFP). This cell line closely mimics the characteristics of human metastatic breast cancer, as it is 'triple negative' (HER2, oestrogen receptor and progesterone receptor negative). When the primary tumour is established in the mammary fat pad, cells spontaneously metastasise to the draining lymphatics and eventually to the brain, bone, liver and lungs[175,177]. One

of the advantages of this model is that the primary tumour can be surgically removed to study metastatic disease in the context of clinical surgical management[175]. To establish brain metastasis without a primary tumour, cells can be seeded via intracardiac injection to study the early phases of vascular dissemination, or injected intracerebrally to study established macrometastatic growth. In the intracerebral 4T1 model, a co-optive growth phase occurs in the majority of metastatic colonies from day 3-14, with the BBB remaining intact over this time period, followed by a switch to a permeable BBB and angiogenic growth in macrometastatic colonies thereafter[16]. In the intracardiac model, some permeability of the blood-tumour barrier is seen in most metastatic lesions at 2-6 weeks following induction, but at this point the mice show neurological symptoms[163].

In the clinic, breast cancer brain metastases are very difficult to detect with gold-standard gadolinium enhanced MRI prior to BBB breakdown, and hence the macrometastatic tumours in the intracerebral injection model are representative of brain metastases at the time of diagnosis. Clinically however, the radiological presentation of breast cancer brain metastases is likely to include multiple metastatic lesions, with at least 40% of patients presenting with 3 or more at the time of diagnosis[178,179]. Patients with a triple negative primary tumour are also more likely to present with leptomeningeal metastases[178,180]. Intracardiac injection of the 4T1 cells does produce multiple metastatic lesions with some leptomeningeal involvement, however by the time these lesions become angiogenic with BBB breakdown, the mouse is likely to be moribund. While the intracerebral model does not recapitulate the features of either multiple or leptomeningeal metastases, in

this case it is the most appropriate model for studying angiogenic, macrometastatic lesions.

A primary brain tumour model, U87 glioma, which is highly angiogenic[64,181], will be used as a positive control for the metastasis model.

1.3.3 Clinical treatment

Clinical treatment of brain metastasis is difficult. There are currently no targeted chemotherapeutic agents approved by the USA Food and Drug Administration, nor the European Medicines Agency, for the treatment of brain metastasis from solid tumours[182], however treatment of systemic disease can improve survival. The current National Institute for Health and Care Excellence (NICE) guidelines recommend a combination of surgery and stereotactic radiotherapy/ radiosurgery for patients who have one to three small intracranial metastases[183]. Whole brain radiotherapy is only recommended in patients with multiple, unresectable metastases after consultation with patients[183]. Systemic chemotherapy is only recommended in specific cases where the primary tumour is known and is likely to respond to a particular therapy[183].

For primary brain tumours, such as glioma, the treatment options are similarly bleak. The standard of care is surgery, radiotherapy with temozolomide, and also adjuvant chemotherapy[184,185]. However, adjuvant drugs such as bevacizumab have not been shown to improve overall survival, although they may improve progression free survival[184]. For recurrent glioma, there is no established standard of care[185].

There are many reasons why clinical trials of adjuvant therapies fail, in both primary and secondary brain tumours. These include heterogeneous patient groups, small sample sizes, and insufficient control groups[186]. Another reason is the inability to accurately predict treatment response from standard imaging, due to issues including pseudo-progression. 'Pseudo-progression' is an issue that affects MR imaging, particularly in the brain[187,188]. Typically, if an MRI scan mid-way through treatment shows a gadolinium-enhancing tumour area that is larger than the baseline pre-treatment scan, it is concluded that the treatment is not working. However, in some patients, a further scan at a later timepoint shows a marked reduction in tumour volume, suggesting that the earlier pseudo-progression was related to inflammation or post-surgical lesions indistinguishable from tumour. In rare cases, a pseudo-response may also be observed, where imaging shows an early reduction in tumour volume followed by rapid growth. Although the response assessment criteria for clinical trials have been updated to reflect this, there is still no good way to measure treatment response[189]. Because of this, more sophisticated imaging techniques need to be developed in order to more accurately assess treatment response.

Both the NICE and European Association of Neuro-oncology (EANO) guidelines recommend anatomical MRI imaging (T_2 weighted, FLAIR, DWI and pre- and post-gadolinium contrast enhanced T_1 weighted sequences) as the standard of care for brain metastasis diagnosis[182,183]. However, both recommend against the use of advanced MRI techniques, as there is not currently enough high-quality evidence on the sensitivity and specificity of individual methods. Because of this, it is important that molecular imaging methods are developed in line with the recommendations for imaging biomarkers in cancer[190].

1.4 Imaging of angiogenesis and metastasis

1.4.1 Molecular imaging

Imaging allows the visualisation of anatomical structures. In some modalities, specific imaging types or contrast agents allow for molecular imaging, which visualises molecular and cellular structures. Molecular imaging is of particular benefit in the context of disease in the brain, as it allows the visualisation of pathology that cannot be easily biopsied. There are many modalities that lend themselves to molecular imaging, and each have advantages and disadvantages that make them more suitable for some applications.

Positron emission tomography (PET) and single photon emission tomography (SPECT) are two of the most widely used clinical molecular imaging modalities. A targeting ligand, such as a small molecule, peptide, protein or antibody, is labelled with a radioisotope. Common PET radioisotopes include ^{11}C, ^{13}N, ^{15}O, and ^{18}F, which are produced in onsite or local cyclotrons due to their short half-lives. By far the most common PET tracer, both in oncology and neuroimaging applications, is fluorodeoxyglucose (FDG-PET). This is a modified glucose molecule with an ^{18}F label, which accumulates in cells and can provide a readout of metabolic activity. Similarly, common SPECT radioisotopes include ^{99m}Tc, ^{111}In, ^{123}I and ^{201}Tl.

PET and SPECT have good sensitivity, and a wide range of molecularly targeted tracers are available. Relatively few are approved for clinical diagnostic use, but tracers for hundreds of ligands have been created for pre-clinical research. However, these scans require exposure to ionising radiation, and the resolution is relatively poor. For clinical systems, the resolution for PET is approximately 5 mm

and for SPECT approximately 10 mm. For pre-clinical systems, this is approximately 1 mm for both modalities. This low resolution limits the utility of PET and SPECT for measuring intra-tumoral variation, for example angiogenic hotspots, as the resolution is such that the tumour may only comprise a few voxels.

Ultrasound is another modality that is being developed for molecular imaging. Gaseous microbubbles that are sensitive to ultrasound can be targeted to molecular features using peptides, proteins, antibodies and small molecules, and in this way can image molecular targets. These microbubbles can also be engineered to release substances, for example a chemotherapeutic drug, at the target site upon induction with ultrasound waves. This makes it a promising modality for 'theranostic' agents – contrast agents with a dual purpose of diagnosis and therapy[191]. Ultrasound is inexpensive, portable, and involves no radiation exposure. However, the images suffer from poor penetration depth, and current contrast agents are limited to intravascular targets[192].

More recently, the use of MRI for molecular imaging has been proposed, although this is much less widespread. MRI is widely used in the clinic for standard anatomical imaging, because it has high spatial resolution, involves no ionising radiation, and is multi-parametric. Multi-parametric means that a number of different types of images can be collected in a single imaging session, with different MRI sequences showing different features. In this way, information on tumour anatomy, tumour margins, oxygenation, perfusion, oedema, and cellularity can potentially be collected within a single imaging session using a single modality.

Molecular imaging using MRI can be performed in several ways. The most frequently used method is to conjugate commonly used MR contrast agents, such

as gadolinium or iron oxide, to targeting antibodies[166,193,194], proteins, peptides[195] or small molecules. These contrast agents allow the visualisation of specific molecular targets *in vivo*. The challenge of molecular MRI in the brain is the difficulty in getting molecular imaging contrast agents across the BBB, particularly in small or diffuse tumours where BBB breakdown may not be apparent. For this reason, molecular targets that are exposed on the luminal side of endothelial cells are an attractive target as BBB breakdown is not necessary. In the case of angiogenesis, luminal targets include VEGFR2, integrin $\alpha_v\beta_3$, and TIE2. Using targeted MRI contrast agents, the spatial resolution achieved is considerably superior to PET and SPECT imaging, although the sensitivity is in the micromolar range and is, therefore, only possible for highly expressed targets[196].

Magnetic resonance spectroscopic imaging (MRSI) can also be used to semi-quantitatively image the chemistry of tissues, and chemical exchange saturation transfer (CEST) can be used to map tissue pH and protein content[197]. The greatest benefit of MRI is that all of these molecular imaging techniques can be used to collect multi-parametric information in a single scanning session, which cannot be achieved with other modalities such as PET and SPECT. It is for this reason we believe that MRI has excellent, as yet unrealised potential for the *in vivo* imaging of angiogenesis, and this thesis will focus on molecular MRI methods.

1.4.2 Molecular imaging of angiogenesis

A number of different methods have been used for molecular imaging of angiogenesis *in vivo*. The molecular mechanisms mediating angiogenesis are well-characterised, and have allowed appropriate targets to be developed[198,199]. The

vessel density and angiogenic phenotype of tumours is very heterogeneous[200], including between core and rim regions[201], so molecular imaging is very useful to examine these parameters *in vivo*. However, most molecular imaging studies have been performed in solid, subcutaneous tumours, with very few studies examining intracerebral tumours or metastases.

One useful molecular imaging target is integrin $\alpha_v\beta_3$, which plays an important role in angiogenesis, as described in Chapter 1.2.2. This integrin is present on normal endothelial cells at low levels, but is highly upregulated on angiogenic vessels[62,87,202-205], making it an attractive target to visualise. Molecular imaging of integrin $\alpha_v\beta_3$ has been possible for many years owing to its binding to the extracellular matrix via a conserved amino acid sequence, arginine-glycine-aspartic acid (RGD), in extracellular matrix proteins[206]. This has allowed a number of different radio-labelled RGD peptides to be developed for integrin $\alpha_v\beta_3$-targeted PET and SPECT imaging[207-211]. Novel RGD targeted agents for optical and fluorescence based imaging have also been developed[212,213], however these modalities have limited depth penetration in the brain. Molecular imaging of VEGFR2 *in vitro* has also been carried out using fluorescent imaging[214,215], but this has limited applications *in vivo*, again due to limited depth penetration. Pre-clinical PET and SPECT based studies targeting VEGFR2 are also being undertaken[215-220], but are invasive and are limited by relatively poor resolution. Some pre-clinical studies using ultrasound of microbubbles targeted to VEGFR2 using a lipopeptide[221-223] or antibodies[224-228] have been reported, along with early clinical studies in humans[229,230].

However, many of these agents have not progressed to clinical trials, and very few are in widespread clinical use. A ^{99m}Tc labelled RGD peptide, known as

Maraciclatide (GE Healthcare), has progressed to clinical studies in breast cancer[231,232] and skeletal metastases[233], following promising pre-clinical results in mouse models of glioma[234,235], but is not yet in widespread clinical use. Despite poor results of RGD-based $\alpha_v\beta_3$ antagonists such as Cilengitide in clinical trials[110,236], RGD peptides remain a viable target for imaging as they have a high affinity for the integrin, and as a targeting agent are not required to have functional activity.

Studies using integrin $\alpha_v\beta_3$ targeted microbubbles to image angiogenic vasculature have also been reported in pre-clinical models of glioma[237], ovarian adenocarcinoma[225,238,239], breast[225,240], and pancreatic cancer[225]. Dual targeting of both integrin $\alpha_v\beta_3$ and VEGRF2 has also been shown to increase the visualisation of angiogenic vasculature in tumour models[239], as has triple targeting including p-selectin[241,242]. However, ultrasound is not an ideal medium for molecular imaging of the brain owing to limited signal penetration and distortion difficulties posed by the skull.

1.4.3 MRI of angiogenesis and metastasis

There are many different MRI methods available for the characterisation of tumours, and these are routinely used for clinical diagnosis and for monitoring of treatment response. MRI is a preferred modality for the investigation of many tumours, owing to superior resolution and soft tissue contrast, lack of ionising radiation, and the ability to perform multi-parametric scans to characterise different aspects of the tumour microenvironment. For an excellent overview of the methods used in the clinic for imaging brain metastasis, please see the review by Fink and Fink[243].

The primary MRI method used for the clinical detection of tumours, along with the monitoring of treatment response, is gadolinium enhanced T_1 weighted scans. Gadolinium-based contrast agents are paramagnetic, which lengthens T_1 relaxation times, and allows changes in signal intensity to be detected. As a small molecule, it is able to move out of the vasculature and into the tissue from permeable blood vessels, such as angiogenic tumour vessels. Vessels in metastatic tumours have been shown to have increased permeability when compared to the vasculature of the primary tumour[244]. However, in the brain, the presence of the BBB prevents the entry of gadolinium-based contrast agents into the brain parenchyma under normal circumstances. It is only when the BBB is permeable, for example in the presence of tumour or inflammation, that gadolinium can cause contrast enhancement in the brain.

The kinetics of gadolinium enhancement, as measured by a Dynamic Contrast Enhanced (DCE-MRI) scan gives semi-quantitative or quantitative information on vessel permeability, tumour blood volume and perfusion[245,246]. In many cases this correlates with microvessel density on histology[247-249]. This contrast is particularly apparent in the brain, where in normal vasculature the BBB prevents gadolinium from diffusing into the tissue. DCE-MRI is also widely used to measure the response of the tumour vasculature to anti-angiogenic drugs, in both clinical[250] and pre-clinical[251-254] studies. However, in some preclinical models of brain metastasis, particularly those not expressing high levels of VEGF-A, peritumoural blood vessels are not permeable to gadolinium, and vascular changes can only be detected using USPIO[255]. Similarly, blockade of VEGF-A in angiogenic tumours can also result in reduced permeability of gadolinium, and hence the inability to detect tumours[173]. With widespread clinical adoption of gadolinium-based contrast

agents in recent years, the high sensitivity of gadolinium for tumour detection, along with improved management of primary tumours, has resulted in a huge increase in the incidence of brain metastases[256,257].

As DCE-MRI is limited in the parameters it can measure, many alternative methods have been developed for MRI that are able to quantitatively assess vasculature in tumours. These include measurements of perfusion using Arterial Spin Labelling (ASL), and oxygenation using Blood Oxygen Level Dependent (BOLD) imaging, which are unique in that they do not require the use of exogenous contrast agents. BOLD is able to image tumour hypoxia, and can distinguish between viable and necrotic areas of tumours when combined with a carbogen challenge[258]. Angiogenic vessels can also be identified using BOLD, as they are less reactive to a hypercarbia challenge[259]. Similarly, areas with mature vascular can be distinguished from the immature angiogenic vasculature using BOLD imaging[260,261]. Oxygen enhanced MRI can also be used to quantify tumour hypoxia without the use of exogenous contrast agents[262].

ASL has been used successfully to measure blood flow in angiogenic tumour vessels, both clinically and pre-clinically, and is an important technique as it requires no exogenous contrast agent. However, it is difficult to implement in a pre-clinical setting, and is most often used for clinical research. MRI methods measuring perfusion are important for the study of anti-angiogenic therapies, and have been used to successfully evaluate treatment response in clinical trials, including Cilengitide[104]. In this context, quantitative measurements of blood flow represent an important imaging biomarker, as they can be used to quantitatively assess treatment response to anti-angiogenic drugs.

Imaging of the tumour vasculature can also be performed using iron oxide contrast agents. Untargeted iron oxide nanoparticles have been found to be intravascular agents during a first pass through the vasculature, and thus can be used to image vascular morphology in intracerebral tumours[263]. The enhancement kinetics of untargeted ultrasmall superparamagnetic iron oxide (USPIO) nanoparticles, described in Figure 1.6, have been found to correlate with microvessel density, and can be used to delineate permeability hotspots along with blood volume hotspots[264]. Untargeted USPIO have also been used clinically to delineate tumour margins more sharply than gadolinium due to reduced extravasation from the vasculature[265]. USPIO can also be used to measure tumour blood volume[247,266], and changes in blood volume can be used to predict a vascular response to anti-angiogenic drugs[267].

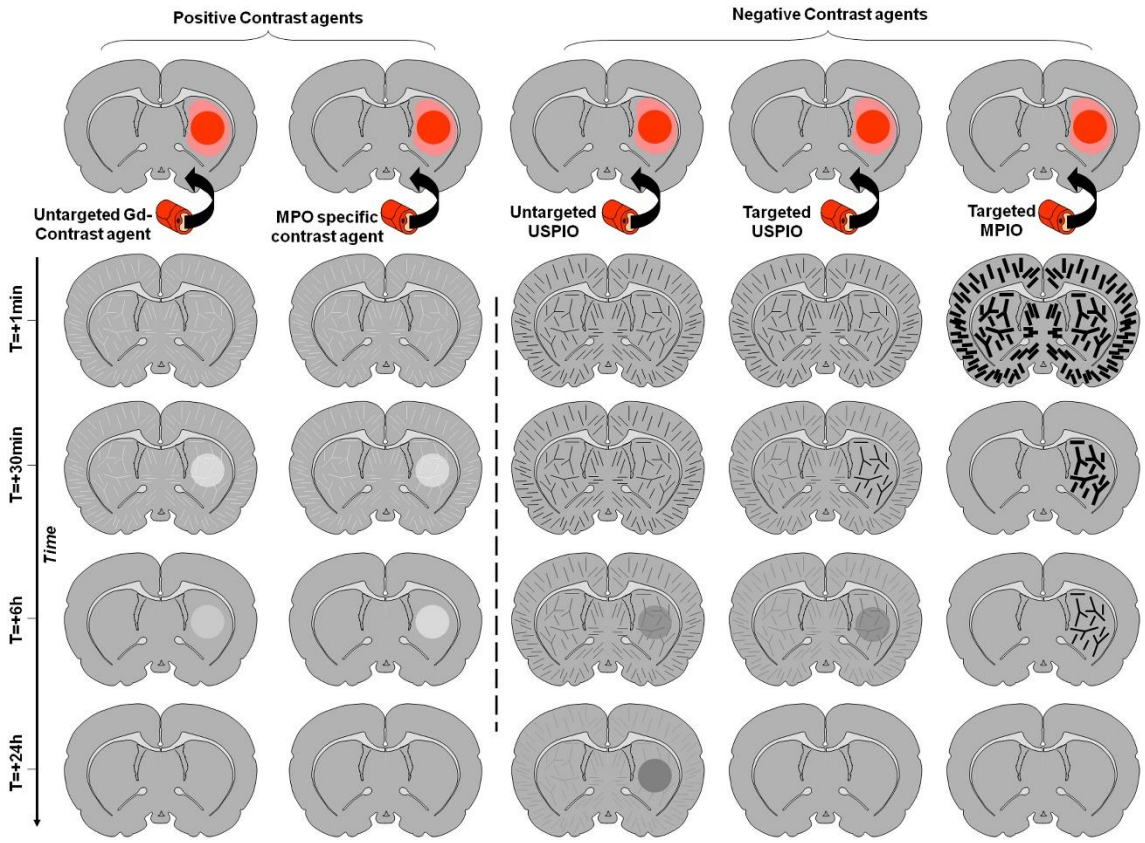


Figure 1.6: Enhancement kinetics of MRI contrast agent for imaging brain tumour vasculature. Gadolinium (Gd) based contrast agents produce short-term positive contrast on T_1-weighted imaging, and are often used to assess dynamic enhancement kinetics and BBB breakdown. Iron oxide contrast agents produce negative contrast on T_2- and T_2*-weighted images. Untargeted USPIO can be used to image the vasculature in the minutes following injection, and can image the tumour parenchyma through passive extravasation, and macrophage infiltration through phagocytosis in the hours to days following injection. Targeted USPIO can still be used in a similar way to untargeted USPIO, although accumulation in the tumour is faster and non-specific signal is reduced. Targeted MPIO can be visualised in the vasculature in the first seconds to minutes following injection, but with a short blood half-life this effect does not last long, and specific imaging of the target is possible in the minutes following injection. Due to the higher iron content of MPIO, a more intense contrast is produced compared to USPIO. Reproduced with permission from Gauberti et al.[268]

Molecular targeting of USPIO has been used successfully in a range of preclinical models, with the addition of antibodies or peptides to target specific molecular markers. These include the imaging of hepatic fibrosis, atherosclerotic plaques, and tumour imaging among many applications, which are reviewed by Thorek et al[269]. However, USPIO are able to passively extravasate from the vasculature, and, hence, present the problem of non-specific signal[193]. Because of this extravasation, micron-sized iron oxide particles (MPIO, 1 μm in diameter), an order of magnitude larger, have been used for molecular targeting. Because they are so large, these particles are obligate intravascular agents and do not passively extravasate. However, the downside of this approach is that they can therefore only target intravascular molecules. There are a wide range of cell adhesion molecules and receptors involved in angiogenesis that are expressed on the luminal surface of the angiogenic vasculature, and this makes MPIO an ideal medium for molecular imaging of angiogenesis.

Targeted MPIO have been used in a number of applications, including to image tumour angiogenesis[195], cerebral malaria[270], cerebral ischemia[271-273], inflammation[274], multiple sclerosis[275], vascular dementia[276], and brain metastasis[166,194]. Targeted MPIO have also been used as a theranostic agent, with conjugation to cetuximab, allowing both MR imaging and treatment with a single agent[277]. Targeted MPIO represent a promising avenue for the molecular imaging of angiogenesis *in vivo*.

Molecular imaging of angiogenesis has become a growth area in imaging with the rise in clinical use of anti-angiogenic drugs. As yet, a consensus on the best method of monitoring treatment efficacy, particularly for anti-angiogenic treatments, has not been decided, although Response Assessment in Neuro-

Oncology (RANO) guidelines exist for brain tumours[278] and brain metastases[279]. The normal method of measuring tumour shrinkage and categorising a complete or partial response, or a progression, is not optimal as anti-angiogenic drugs often do not measurably reduce tumour size despite having a metabolic or physiologic effect[280]. For this reason, quantitative imaging biomarkers that can be used to monitor clinical trials are necessary. Similarly, a biopsy often does not detect angiogenic hotspots in tumours[281], so molecular imaging is also well placed to help identify and stratify patients who would benefit from anti-angiogenic treatments.

As there are no sensitive or specific methods for the molecular imaging of angiogenesis *in vivo*, and nothing widely used in the clinic, this thesis will focus on the development of quantitative and qualitative angiogenic imaging biomarkers in order to fulfil this unmet need.

1.5 Aims of thesis and specific hypotheses

The overarching aim of this thesis is to develop and validate effective imaging techniques for the *in vivo* visualisation of angiogenesis in brain metastasis. Specifically, arterial spin labelling techniques for measuring tumour blood flow will be developed in parallel with molecular imaging with targeted microparticles of iron oxide.

Aim 1 – Develop and validate arterial spin labelling for quantitative measurement of tumour blood flow in a mouse model of brain metastasis.

Aim 2 – Develop and validate targeted microparticles of iron oxide (MPIO) for visualisation of angiogenesis by MRI.

Aim 3 – Investigate the retention of peptide- and antibody-conjugated microparticles of iron oxide by macrophages, both *in vitro* and *in vivo*.

Chapter 2 - Materials and methods

2.1 Chemicals and solutions

2.1.1 Chemicals

Di-sodium hydrogen orthophosphate (Sorenson's salt, S/4440/60), DPX mounting medium (10050080), ethanol (99.8%) (E/0650DF/17), hydrochloric acid (H/1200/PB17), iso-pentane (99+%) (P/1030/08), methanol (99.9%) (M/4000/17), phosphorous pentoxide (P296048), sodium chloride (BP358-212), sodium dihydrogen orthophosphate dihydrate (S/3760/53), sucrose (S/8600/60), and tris-hydrochloride (BPE153-1) were obtained from Fisher Scientific (Loughborough, UK).

Aluminium sulphate (202614), ammonium nickel sulphate (A1827), bovine serum albumin (BSA, A3059), cobalt (II) chloride (232696), di-methyl sulfoxide (DMSO, C6164) ethylenediaminetetraacetic acid (EDTA, E5134), glutaraldehyde (G5882), hydrogen peroxide (H1009-500ML), L-lysine monohydrochloride (L5626), nuclear fast red (N8002), o-xylene (95662), paraformaldehyde (PFA, 15,812-7), phenylenediamine (P6001), potassium ferrocyanide (P3289), pyrocatechol (C9510), sodium cacodylate (C0250), sodium hydroxide (7169-500G), sodium phosphate monobasic dihydrate (71-500), TEGOPS/DIPEA (387649), and tween-20 (P9416) were obtained from Sigma-Aldrich (Gillingham, UK).

Mounting medium (H-1000), and mounting medium with DAPI (H-1200), were obtained from Vector Laboratories (Peterborough, UK)

Phosphate buffered saline (Dulbecco A) tablets (PBS, BR0014G) were obtained from Oxoid (Basingstoke, UK).

Ethanolamine (8.00849.0100), and sodium metaperiodate (27986.235) were obtained from VWR International (Lutterworth, UK).

1-Ethyl-3-(3-dimethylaminopropyl)carbodiimide hydrochloride (EDC, 24810) was obtained from Fluorochem (Hadfield, UK)

Cresyl violet acetate was obtained from ACROS Organics (Sigma Aldrich, Gillingham, UK)

2.1.2 Substrates

3,3'-diaminobenzidine tetrahydrochloride hydrate (97%) (DAB, 11209-0050) was purchased from ACROS Organics (Sigma Aldrich, UK)

Vectorstain Avidin-Biotin Complex Horseradish Peroxidase (ABC-HRP) Kit (PK-4000); and Mouse on Mouse (MOM) Basic Kit (BMK-2202) were obtained from Vector Laboratories (Peterborough, UK)

2.1.3 Buffers and solutions

MES buffer: 15 mM 2-(N-morpholino)ethanesulfonic acid

Phosphate buffered saline (PBS): 10 mM Na_2HPO_4 pH 7.5, 150 mM NaCl

Phosphate buffered saline with tween-20 (PBS-T): 10 mM Na_2HPO_4 pH 7.5, 150 mM NaCl, and 0.01% tween-20.

Periodate-lysine paraformaldehyde (PLP-light): 2% paraformaldehyde, 0.075 M L-lysine monohydrochloride, 0.37 M sodium phosphate, 0.01 M sodium metaperiodate, adjusted to pH 7.4, with 0.1% glutaraldehyde.

Tris-NaCl buffer (TNB): 1 M Tris-Cl (pH 7.5), 5 M NaCl.

0.1M Phosphate buffer: 0.1 M Na_2HPO4, 0.2 M NaH_2PO_4, pH 7.4

Hanker–Yates base solution: 0.2 M sodium cacodylate (pH 5.2), 0.2% w/w p-phenylenediamine, 0.4% w/w catechol.

Hanker-Yates Metal solution: 48 mL of 1% cobalt (II) chloride solution in water, 32 mL of 1% ammonium nickel sulphate solution in water and 40 mL Hanker-Yates base solution.

Hanker-Yates developing solution: 120 mL Hanker-Yates solution with 200 µL 30% w/v hydrogen peroxide.

Hank's balanced salt solution (HBSS) with sodium bicarbonate, without phenol red (H8264, Sigma Aldrich, UK)

Karnovsky's fixative: 1.25% paraformaldehyde, 2.5% glutaraldehyde, in 0.1 M phosphate buffer at pH 7.3.

2.2 Cell lines and culture

2.2.1 Tumour cell lines and culture mediums

4T1 murine metastatic mammary carcinoma cells[177,282], transfected with a plasmid promoting the expression of EGFP[283] (4T1-GFP), were used as a secondary brain tumour model. These cells were kindly provided by Professor Ruth Muschel (University of Oxford, UK).

U87 human glioma cells[284,285] were used as a primary brain tumour model. These cells were kindly provided by Professor Adrian Harris (University of Oxford, UK).

RAW 264.7[286] cells were used as a murine macrophage model. These cells were kindly provided by Dr Wang from Professor Xin Lu's laboratory (University of Oxford, UK).

The above cell lines were cultured in Dulbecco's Modified Eagle Medium (DMEM, D5796, Sigma Aldrich) containing 10% v/v (25 mM/L) glucose and supplemented with 1% v/v (200 mM/L) L-glutamine (G7513, Sigma Aldrich) and 10% v/v foetal bovine serum (FBS, FCS-SA/500H, BioSera, Heathfield, UK).

2.2.2 Cell revival

Cells were thawed from storage and immediately diluted in 5 mL pre-warmed complete medium. The suspension solution was centrifuged and supernatant discarded to remove DMSO (5 min at 1200 rpm, 4°C). Cells were re-suspended in complete medium, before seeding into appropriate flasks.

2.2.3 Cell incubation and harvesting

Cells were seeded in tissue culture flasks of 25 cm^3 or 75 cm^3 (Corning Life Sciences, UK) in complete medium. Cells were grown in an incubator at 37ºC in 5% CO_2. The cells were grown until 90% confluent. Prior to passaging or harvesting for injection, cell culture flasks were first washed with pre-warmed PBS buffer and then incubated for 2-5 min with Trypsin 0.05% with EDTA (T3924, Sigma Aldrich). The cell suspension was then diluted in pre-warmed complete medium and centrifuged (4 min at 1200 rpm, 4°C).

2.2.4 Cell storage

Following harvesting as described above, 1 x 10^7 cells were re-suspended in 1 mL of 90% FBS and 10% DMSO and aseptically sealed in cryo-vials (Sigma Aldrich). For long-term storage, cryo-vials were stored in liquid nitrogen vapour phase at -180°C.

2.2.5 Cell preparation for injections

Following harvesting as described above, cells were re-suspended in 100 µL pre-warmed PBS. The cell concentration was measured using the Countess II Automated Cell Counter (Fisher Scientific) as per manufacturer's instructions. The appropriate dilution was calculated for the live cell fraction and cell suspensions for injection were prepared in sterile PBS buffer.

2.3 Animal models

2.3.1 Mouse strains

All mice were housed in individually ventilated cages with food and water provided *ad libitum.* All experiments were performed in accordance with UK legal requirements under the "Animals (Scientific Procedures) Act 1986" and ethical guidelines of the University of Oxford. Female BALB/c and SCID mice between the ages of 6-10 weeks were purchased from Charles River Laboratories, UK.

2.3.2 Intracerebral tumour model

BALB/c (for 4T1-GFP cells) or SCID mice (for U87 cells) were anaesthetised in an induction chamber in 3% isoflurane (IsoFlo) vaporised in 30% oxygen and 70% nitrous oxide. Mice were then transferred to a stereotaxic frame and anaesthesia maintained at 1.5-2% isoflurane. Core temperature was monitored using a rectal probe and maintained at 37°C with a homoeothermic system (Harvard Instruments, Edenbridge, UK). An incision was made along the scalp to expose Bregma, and a burr hole drilled in the skull at coordinates +0.5 mm (rostral-caudal), +2.0 mm (lateral) relative to Bregma, as shown in Figure 2.1. A pulled glass capillary with outer diameter approximately 75 µm was inserted to coordinates of -2.5 mm relative to the dura mater, and 0.5 µL of cell suspension containing 5×10^3 cells was injected at a rate of 0.1 µL/min. The scalp was then closed with non-absorbable sutures (Mersilk) and the mouse allowed to recover.

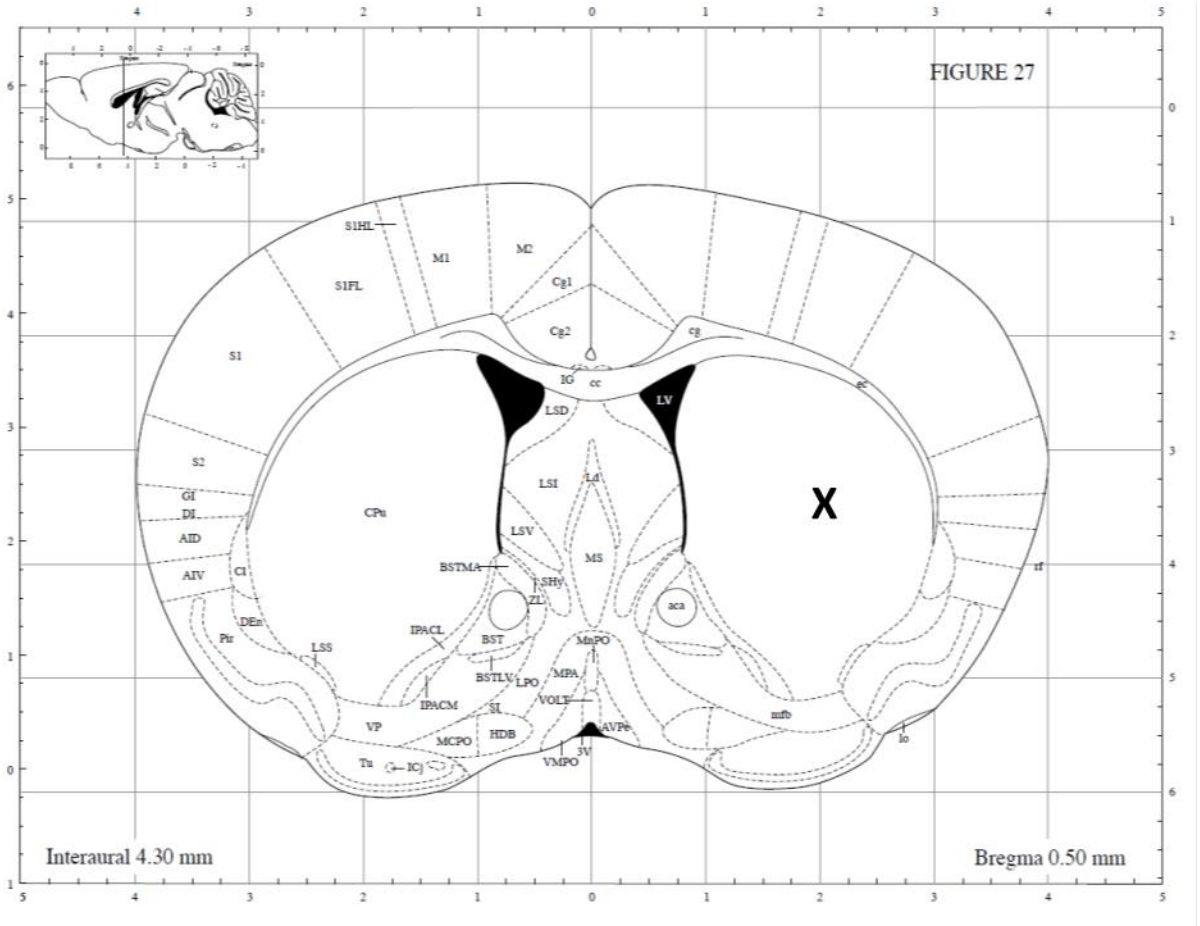


Figure 2.1: Location of the intracerebral injection of cells in the left striatum, indicated by the X. Stereotaxic coordinates used are: +0.5 mm (rostral-caudal) and +2.0 mm (lateral) relative to Bregma, and -2.5 mm (vertical) relative to the dura mater. Image modified from The Mouse Brain in Stereotaxic Coordinates with permission[287]

2.3.3 Tumour harvest

At specified timepoints, mice underwent transcardial perfusion-fixation with 20 mL of 0.9% heparinised saline, followed by 20 mL of periodate lysine paraformaldehyde containing 0.1% glutaraldehyde (PLP-light). Brains were extracted and stored in PLP-light for 4 hours at 4°C. Brains were then incubated with 30% w/v sucrose at 4°C for at least 24 hours for cryoprotection.

2.3.4 Tissue storage

Brains were embedded in OCT-Tissue Tek (VWR International Ltd, Lutterworth, UK) and rapidly frozen in isopentane on dry ice. 10 µm sections were collected through the striatum using a cryostat, in parallel, onto groups of 5 glass slides. Slides were dried at room temperature overnight, and stored long-term at -20°C.

2.4 Antibodies

2.4.1 Immunohistochemistry

Mouse monoclonal to integrin $\alpha_v\beta_3$ primary (ab78289, Abcam, Cambridge, UK), with mouse-on-mouse basic kit biotinylated anti-mouse IgG (BMK-2202, Vector Laboratories, Peterborough, UK)

Mouse monoclonal to TIE2 primary (ab24859, Abcam, Cambridge, UK), with biotinylated horse anti-mouse IgG (BA-2001, Vector Laboratories, Peterborough, UK)

Goat polyclonal to CD31 primary (AF3628, R&D Systems, Abingdon, UK), with biotinylated horse anti-goat IgG secondary (BA-9500, Vector Laboratories, Peterborough, UK)

Rat monoclonal to VCAM-1 primary (1510-14, Southern Biotech, Birmingham, USA), with biotinylated goat anti-rat IgG (BA-9401, Vector Laboratories, Peterborough, UK)

Goat polyclonal to Iba-1 primary (ab5076, Abcam, Cambridge, UK), with biotinylated horse anti-goat IgG secondary (BA-9500, Vector Laboratories, Peterborough, UK)

2.4.2 Immunofluorescence

Mouse monoclonal to integrin $\alpha_v\beta_3$ primary (ab78289, Abcam, Cambridge, UK), with Texas red conjugated horse anti-mouse IgG (TI-2000, Vector Laboratories, Peterborough, UK).

Mouse monoclonal to TIE2 primary (ab24859, Abcam, Cambridge, UK), with Texas red conjugated horse anti-mouse IgG (TI-2000, Vector Laboratories, Peterborough, UK).

Goat polyclonal to CD31 primary (AF3628, R&D Systems, Abingdon, UK) with biotinylated horse anti-goat IgG secondary (BA-9500, Vector Laboratories, Peterborough, UK) and streptavidin-dylight 405, 1:200 (21831, Thermo Fisher Scientific, Loughborough, UK) for 4T1-GFP tumours

Goat polyclonal to CD31 primary (AF3628, R&D Systems, Abingdon, UK) with dylight 488 conjugated horse anti-goat IgG (DI-3088, Vector Laboratories, Peterborough, UK) for U87 tumours.

2.4.3 Imaging contrast agents

Rat monoclonal to VCAM-1 (1510-14, Southern Biotech, Birmingham, USA)

Rat IgG isotype control (0116-14, Southern Biotech, Birmingham, USA)

2.5 Immunohistochemistry

2.5.1 Standard protocol

For immunohistochemistry, frozen sections were thawed for 20 min at room temperature and washed with PBS containing 0.01% tween-20 (PBS-T). Sections were then quenched with 1% v/v of 30% w/v hydrogen peroxide in PBS for 30 mins. The sections were then blocked with 10% serum in PBS for 1 hour, with the serum derived from the host species of the secondary antibody (i.e. where secondary antibody is horse anti-goat, horse serum is used for blocking). Sections were incubated with primary antibody and 1% serum in PBS at 4ºC overnight. Sections were then washed with PBS-T and incubated with biotinylated secondary antibody for 45 min. Slides were washed with PBS-T and then incubated with the Vectorstain Elite ABC kit 1(A):1(B):100(PBS), for 30 min. The peroxidase was visualised by DAB for 30-90 seconds. Sections were counterstained with cresyl violet for 30 sec, and rinsed briefly in water before dehydration in increasing concentrations of ethanol (75%, 95%, 100%, 100%, 30 sec each), clearing in xylene (3 x 5 min), and coverslips mounted using DPX.

Positive and negative control slides for each antibody were also stained concurrently under the same protocol. The positive control consisted of mouse kidney sections, as the kidney is a highly vascular organ which expresses many angiogenic markers on its vessels. The negative control consisted of a slide incubated with secondary antibody, but with the primary antibody omitted.

2.5.2 Mouse on mouse protocol

For primary antibodies raised in mouse, the Mouse on Mouse Basic Kit from Vector Laboratories was used in order to reduce background staining from endogenous mouse IgG. Staining was performed as per manufacturer protocols, followed by the Vectorstain Elite ABC kit (1(A):1(B):100(PBS), Vector Laboratories) for 30 min. The peroxidase was visualised DAB, and counterstained, dehydrated and mounted as described in Chapter 2.5.1 above.

2.5.3 Perl's Prussian blue staining protocol

Before use, all glassware was cleaned with dilute (1 M) HCl, then rinsed with iron-free distilled water. Tissue sections were washed in PBS for 5 minutes, followed by iron-free distilled water for 5 min. While sections were in distilled water, Perl's solutions A and B were prepared separately. Perl's solution A was prepared by dissolving 4 g potassium ferrocyanide in 200 mL iron-free distilled water. Perl's solution B was prepared by adding 4 mL 37% HCl (12 M) to 196 mL iron-free distilled water. Solutions A and B were mixed just prior to use, and the sections incubated in the mixture for 15 mins.

Nuclear fast red stain was prepared by adding 0.2 g nuclear fast red dye to 100 mL distilled water with 5 g aluminium sulphate as a mordant. The solution was boiled for 5 mins with stirring, then filtered and allowed to cool before use. Following Prussian blue staining, sections were counterstained in nuclear fast red for 2 mins. Sections were rinsed briefly in water before dehydration in increasing concentrations of ethanol (75%, 95%, 100%, 100%, 30 sec each), clearing in xylene (3 x 5 min), and coverslips mounted using DPX.

2.5.4 Histology digitisation

Slides were scanned with a Leica Biosystem ScanScope CS2 (Aperio, ePathology Solutions, Milton Keynes, UK), with 20x or 40x magnification images acquired. Images were analysed using Image Scope software (ePathology Solutions).

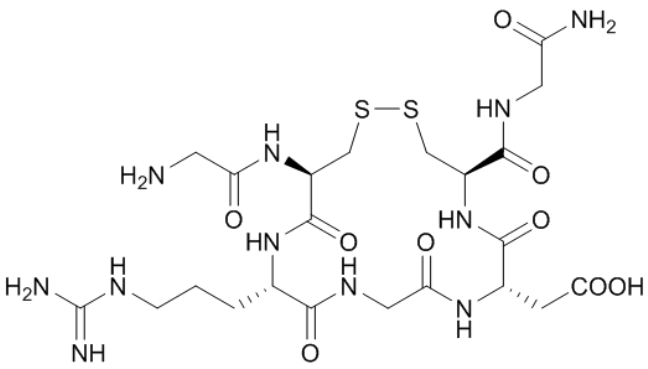
2.5 Imaging contrast agents

2.5.1 Cyclic RGD conjugated MPIO

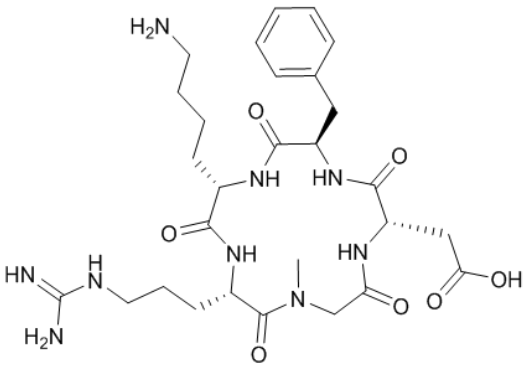
Cyclic RGD conjugated MPIO were prepared using 1 µm diameter Dynabead MyOne carboxylic acid beads (65011, Fisher Scientific). Beads were washed twice in 15 mM MES buffer at pH 6.0 and resuspended. EDC was added to functionalise the beads, and were incubated in a shaker at 1000 rpm for 30 mins. The beads were washed twice with MES buffer, and were incubated for 24 hours in a shaker at 1000 rpm for 30 mins with 10 µL of 10 mM cyclic RGD peptides (for chemical structures see Figure 2.2). The beads were then washed four times in PBS-T and stored in sterile PBS at 4°C on a shaking platform.

2.5.2 Antibody conjugated MPIO

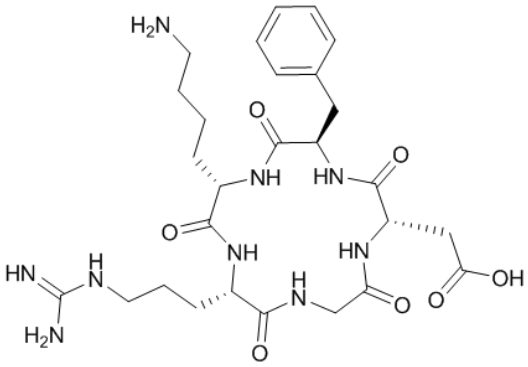
Antibody conjugated MPIO were prepared using 1 µm diameter ProMag carboxylic acid beads (PMC1N, Stratech, Ely, UK). Beads were washed twice in 15 mM MES buffer at pH 6.0 and resuspended. EDC was added to functionalise the beads, and were incubated in a shaker at 1000 rpm for 30 mins. The beads were washed twice with MES buffer, and were incubated for 24 hours in a shaker at 1000 rpm for 30 mins with 40 µg VCAM-1 or IgG antibody. The beads were then washed four times in PBS-T and stored in sterile PBS at 4°C on a shaking platform.



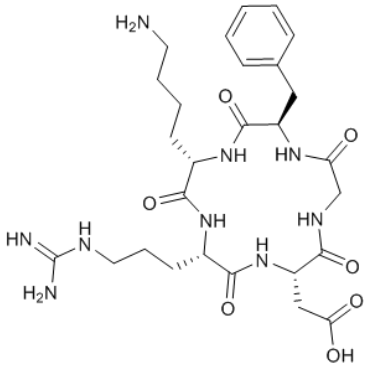
PP001: H-<u>Gly</u>-Cys*-Arg-Gly-Asp-Cys*-Gly-NH_2



PP785: Arg*-Sar-Asp-*Phe*-<u>Lys</u>*



PP786: Arg*-Gly-Asp-*Phe*-<u>Lys</u>*



PP787: Arg*-Asp-Gly-*Phe*-<u>Lys</u>*

Figure 2.2: Chemical structures of the cyclic RGD peptides used in this study. The amino acid underlined is the free amine that binds to the MPIO, those with asterisks indicate the cyclic part of the structure, and those in italics indicate D-amino acids. PP001, PP785 and PP786 are cyclic-RGD structures, while PP787 is a scrambled peptide with sequence RDG which is used as a negative control. Gly – glycine, Cys – cysteine, Arg – arginine, Asp – aspartic acid, Sar – sarcosine (N-methyl-glycine), Phe – phenylalanine, Lys – lysine.

2.6 Imaging

Zero and first order shimming was conducted at the beginning of each imaging session. Using a PRESS sequence with a voxel encompassing the brain, manual shimming was conducted until the full width half maximum linewidth was less than 125 Hz.

2.6.1 T_1 weighted sequence

T_1 weighted spin-echo multi-slice anatomical scans were acquired with TR = 0.5 s, TE = 20 ms, number of averages = 2, matrix size = 256 x 256, FOV = 20 x 20 mm, in plane resolution = 78.125 µm isotropic, slice thickness 1 mm, number of slices = 8

2.6.2 T_2 weighted sequence

T_2 weighted fast spin-echo multi-slice anatomical scans were acquired with TR = 3.5 s, echo spacing = 15 ms, effective TE = 60 ms, number of segments = 4, matrix size = 256 x 256, FOV = 20 x 20 mm, in plane resolution = 78.125 µm isotropic, slice thickness 1 mm, number of slices = 8

2.6.3 Multiphase pseudo-continuous Arterial Spin Labelling

2-shot spin-echo echo-planar imaging, TR = 4.0 s, TE = 18.32 ms, spectral width = 250 kHz, FOV = 20 x 20 mm, matrix size = 64 x 64, in plane resolution = 312.5 µm isotropic, slice thickness = 1mm, number of slices = 8, MP pCASL labelling (RF pulse duration 600 µs, Hanning shape with effective flip angle (FA) = 40°, slice refocusing gradient pulse duration 600 µs), duration 0.9s, phase increment

between 0˚ and 315˚ (steps of 45˚), labelling plane -10° relative to the axial plane, post-label delay (PLD) = 0.4s

2.6.4 T_2* weighted multi-gradient echo sequence

A T_2* weighted three dimensional multi-gradient echo (MGE3D) sequence was used to detect MPIO, with parameters TR = 32.55 ms, TE = 2.5 ms, TE_2 = 4 ms, number of echoes = 6, FA = 13°, matrix = 256 x 192 x 192 (zero-filled to 256 x 256 x 256), FOV = 22.5 x 22.5 x 22.5 mm, resolution = 87.89 µm isotropic

2.6.5 Angiography

Time of flight angiography was acquired with TR = 30 ms, TE = 1.78 ms, FA = 30°, matrix size = 128 x 128 x 192, FOV = 20 x 20 x 30 mm, in plane resolution = 156.5 µm isotropic

2.6.6 T_1 mapping

An EPI inversion recovery T_1 map was acquired with TR = 10s, TE = 14.54 ms, TI = 13.14 – 8000 ms with 9 TIs, matrix size = 64 x 64, FOV = 20 x 20 mm, in plane resolution = 312.5 µm isotropic, slice thickness 1 mm, number of slices = 8

2.6.7 T_2 mapping

An EPI T_2 map was acquired with TR = 5s, TE arrayed between 10 – 3000 ms with 8 TIs, matrix size = 64 x 64, FOV = 20 x 20 mm, in plane resolution = 312.5 µm isotropic, slice thickness 1 mm, number of slices = 8

Chapter 3 - Arterial Spin Labelling to measure brain and tumour blood flow in mice

3.1 Introduction

Tumour perfusion measurements are widely used in clinical imaging as an indicator of tumour microenvironment, physiology, stage, and progression. Clinical studies have shown that tumour perfusion, and consequently, oxygenation, are highly correlated with clinical outcome[288-290], and often resistance to radiotherapy[288]. Similarly, many tumours are highly angiogenic and show altered vasculature and blood flow patterns[291]. Critically, the increased use of anti-angiogenic and vascular normalising therapies has resulted in a need for improved quantitative measures of vascular parameters in order to monitor treatment response.

The MRI method arterial spin labelling (ASL) is often used as a preferred method of imaging cerebral blood flow (CBF), as it requires no exogenous contrast agent and is readily implemented on clinical scanners. Moreover, this method can provide absolute quantitative measures of blood flow, which are not readily obtained by other modalities. Pseudo-continuous arterial spin labelling (pCASL), in particular, has been recommended as the methodology of choice for clinical ASL[292], but no such recommendations currently exist for rodents. Importantly, many potential therapeutic strategies for brain tumours are initially tested in rodent models. Consequently, there is a need for accurate methods for measuring brain and tumour blood flow in rodents, reflecting those used in the clinic, to enable assessment of likely therapeutic efficacy.

Despite initial reports developing ASL in rodents[293,294], most implementations have focussed on clinical ASL. Many challenges exist in the adaptation of ASL for use in preclinical models, including higher blood flow velocities in the feeding arteries, smaller brain size, close proximity of blood vessels, susceptibility artefacts from neighbouring air spaces and B_0 inhomogeneities in high field preclinical systems.

Implementations of ASL in mice have historically produced CBF values that are semi-quantitative[295-297], single-slice[298], or vary with the sequence[299-301] and body position[302] used. Even studies from within a single research group in the same mouse model have shown three-fold differences in CBF values using different ASL-based sequences, demonstrating a need for improvement and standardisation[303,304]. These values may be influenced by the use of anaesthetics, which at high concentrations can increase CBF dramatically[305,306]. Moreover, the mean brain CBF values obtained are often unphysiologically high (>200 mL/100 g/min)[299,307-309] and show little concordance with gold-standard autoradiography measurements (*ca.* 100 mL/100 g/min) in normal mouse brain[310-314]. Whilst some preclinical studies have validated their ASL measurements using autoradiography[315-317] or microspheres[318], pCASL has not yet been validated in the mouse brain.

A previous implementation of pCASL to measure CBF in mice showed clear advantages over pulsed ASL sequences, but also showed a loss of inversion efficiency stemming from phase offsets in the label-control acquisitions[300]. The use of multiphase pCASL (MP pCASL) has been shown to reduce these errors in both humans[319] and rats[317], but this sequence has not yet been implemented in mice. We have recently implemented a multiphase pCASL method for use in the rat brain, which shows high reliability, reproducibility, and accuracy for CBF measurements that are in concordance with gold-standard autoradiography[317]. However, given the even smaller size of the mouse brain, implementing this sequence in mice remains challenging. Movement artefacts from respiration affect the signal at the base of the brain in particular, and air spaces surrounding the brain produce distortions. Nevertheless, the majority of preclinical models of brain

metastasis are established in mice rather than rats and, therefore, developing this method further for robust and reliable application in mice is essential.

Thus, the aim of this study was to optimise and validate MP pCASL for measuring CBF in naïve mice and, subsequently, to assess the sensitivity of the optimised MP pCASL sequence to changes in blood flow in mouse models of secondary brain cancer (metastasis) and primary glioma. The specific objectives for this chapter are:

1. Optimise arterial spin labelling for use in mice.
2. Validate quantitative arterial spin labelling measurements against gold-standard autoradiography measurements.
3. Use arterial spin labelling to measure perfusion changes correlating with angiogenesis in brain metastases. The specific hypothesis is that cerebral blood flow will decrease in angiogenic tumours.

3.2 Methods

3.2.1 Measurement of carotid blood flow

Mice (n = 4) were anaesthetised with 3% isoflurane in O_2. Temperature was monitored and maintained at 37 ± 0.5°C throughout with a heating feedback system. Respiration was monitored and maintained between 30 and 80 breaths per minute, and an electrocardiogram was also acquired. Using a Vevo 3100 ultrasound (Visualsonics, Amsterdam, Netherlands) and a mouse cardiology probe (MX550D), a respiration-gated 3D ultrasound image was acquired across the whole neck. The left carotid artery was located, and 10 Power Doppler blood flow clips of 30 s duration were acquired per mouse at respiration rates across the range of 30-80 breaths per minute, achieved by varying the concentration of isoflurane between 3 and 1%. Carotid blood flow values from the Power Doppler trace were extracted using an open source plot digitiser[317], and values representing the systolic and diastolic flow velocities were determined, in order to be used in pCASL simulations.

3.2.2 Simulation of labelling efficiency

Bloch simulations were carried out to simulate labelling efficiency over a range of different gradient strengths, radio frequency (RF) powers, labelling plane thicknesses, and blood flow velocities, as described by Okell[320]. We conducted Bloch simulations whilst varying G_{max} and G_{mean} (G_{mean} = 0.05 x G_{max} in our MP pCASL sequence) gradient strengths, equivalent to converted labelling plane thicknesses of 1-10 mm in 0.5 mm steps. Blood flow velocities of between 1-20

cm/s with steps of 1cm/s were modelled with T_{1blood} = 2.1s, T_{2blood} = 0.033s (based on ex vivo rat blood measurements at 9.4 T[317]), RF pulse amplitudes of 1-10 μT with steps of 0.5 μT for a train of 600 μs Hanning-shaped pulses, beginning every 1.2 ms.

Simulations to estimate the effect of label duration on the net magnetisation signal were carried out. Saturation recovery of labelled water in the brain was modelled by assuming full saturation of the in-flowing blood from the labelling plane, an instant transfer of labelled water to the imaging region and relaxation according to the blood T_1. Under such conditions, tissue saturation increases as a function of label duration, eventually reaching a plateau whose level is dictated by the T_1 recovery equation:

$$M = M_0 \left(1 - e^{-t/T1}\right)$$

Using these theoretical maximum signal change values, and the SNR data from respiration triggered MP pCASL, SNR values with 95% confidence intervals were calculated for label durations of 0.1 – 5 seconds.

A non-quantitative readout of the MP pCASL inversion was also acquired. MP pCASL labelling was implemented with a 0.9 s labelling train consisting of a set of slice selective RF/gradient pulse pairs (RF pulse duration 600 μs, Hanning shape with effective flip angle (FA) =40°, slice refocusing gradient pulse duration 600 μs). Following this, an imaging readout was acquired which consisted of a single 2 mm midline sagittal slice of the brain using a fast spin-echo readout. The imaging readout was acquired both with and without the labelling pulse, and a subtraction was performed to obtain a non-quantitative map of signal inversion.

3.2.3 Optimisation of MP pCASL sequence

MP pCASL optimisation experiments were performed on a separate cohort of mice (n = 4) using a 9.4 T MRI spectrometer (Agilent Technologies Inc., Yarnton, UK) with a 26 mm volume transmit-receive birdcage RF coil (Rapid Biomedical GmbH, Rimpar, Germany). Mice were anaesthetised with 3% isoflurane in 30% O_2 : 70% N_2, and positioned in a custom built cradle in the volume coil. Mouse temperature was monitored and maintained at 37 ± 0.5°C with a rectal probe and heating blanket feedback system. Respiration was monitored using a pressure balloon, and breathing rate was maintained at approximately 60 breaths per minute by adjusting isoflurane concentration; stable breathing was typically maintained with an isoflurane concentration of 1.2 – 1.5%. The respiration trace was recorded and used to inform respiratory triggering.

The EPI readout was first optimized to increase tissue contrast and reduce artefacts by varying repetition time (TR) = 1-4 s, number of shots = 1-8, respiratory triggering (with an associated variable post-trigger delay), and comparing spin-echo and gradient-echo encoding. The final EPI readout images were acquired with the following parameters: 2-shot spin-echo encoding, TR = 4.0 s, echo time (TE) = 18.32 ms, spectral width (SW) = 250 kHz, Field of View (FOV) = 20 x 20 mm, matrix size = 64 x 64, slice thickness = 1 mm, number of slices = 8, with the anterior slice positioned just posterior to the olfactory sulcus. The full triple reference acquisition algorithm was employed to reduce possible EPI artefacts. Respiratory triggering (with an associated variable post-trigger delay) was also employed to reduce signal fluctuation at the base of the brain caused by respiratory motion.

Subsequently, the MP pCASL parameters were optimized for use in mice. The MP pCASL labelling was implemented with a labelling train consisting of a set of slice selective RF/gradient pulse pairs, followed by a slice refocusing gradient pulse (RF pulse duration 600 μs, Hanning shape with effective flip angle (FA) = 40°, slice refocusing gradient pulse duration 600 μs). The phase of these RF pulses was arrayed between 0˚ and 315˚ with incremental steps of 45˚: 0°, 45°, 90°, 135°, 180°, 225°, 270° and 315°. The labelling plane was oriented at -10° relative to the axial plane in order to be perpendicular to the carotid and vertebral arteries. The labelling pulse train was followed by a gradient crusher to remove residual transverse magnetisation, a post-label delay (PLD) to enable labelled blood water spins to travel to the brain, and the EPI readout. Labelling train duration was varied between 0.4-5.0 s (TR increased accordingly from 4-7.6 s) and between 10-1000 ms, respectively, to optimise MP pCASL signal. Using these parameters and the variable respiration trigger, the duration of the scan varied from 3 minutes 12 seconds to a maximum of approximately 5 minutes. A standard label-control pCASL sequence (phases of 0º and º180 only) was also acquired for comparison with the multiphase sequence.

ASL data analysis and perfusion quantification was performed using a custom version of the BASIL toolbox from the FMRIB Software Library (www.fmrib.ox.ac.uk/fsl/BASIL). Firstly, a modified Fermi function[321] (α = 7, β = 19) was fit to the MP pCASL data, using supervoxel clustering[322] to produce high precision phase priors. The raw multiphase data were then fitted with unconstrained priors, producing voxel-wise estimates of phase, magnitude and offset. The phase maps were clustered using a supervoxel approach[321] with four supervoxels per phase map, a smoothing (σ) of 0.8 and a compactness of 0.1. This

was used to define ROIs from the data that represent individual flow territories, as indicated by their phase value arising from the phase offset present in the feeding artery. For each supervoxel region, the original multiphase data were averaged for all voxels across each phase, yielding a new higher SNR multiphase dataset. This dataset was fitted to the Fermi function, estimating a single phase value for each supervoxel ROI. These final phase values were used as a high precision prior for the final fitting of the original raw multiphase data, yielding a voxel-wise map of magnitude and offset. Figure 3.1 shows a flow chart of this methodology, including example images derived by the process. The resultant maps of the magnitude of the fitted function, representing the presence of labelled water in each voxel, and equivalent to the subtracted label-control images from traditional pCASL, were processed according to the kinetic model of Buxton et al.[323] and calibration with oxford_asl[324]. Reference scans acquired without labelling were used for absolute quantitation of CBF. Standard label-control pCASL images were obtained by using phases of 0° and 180°, for comparison.

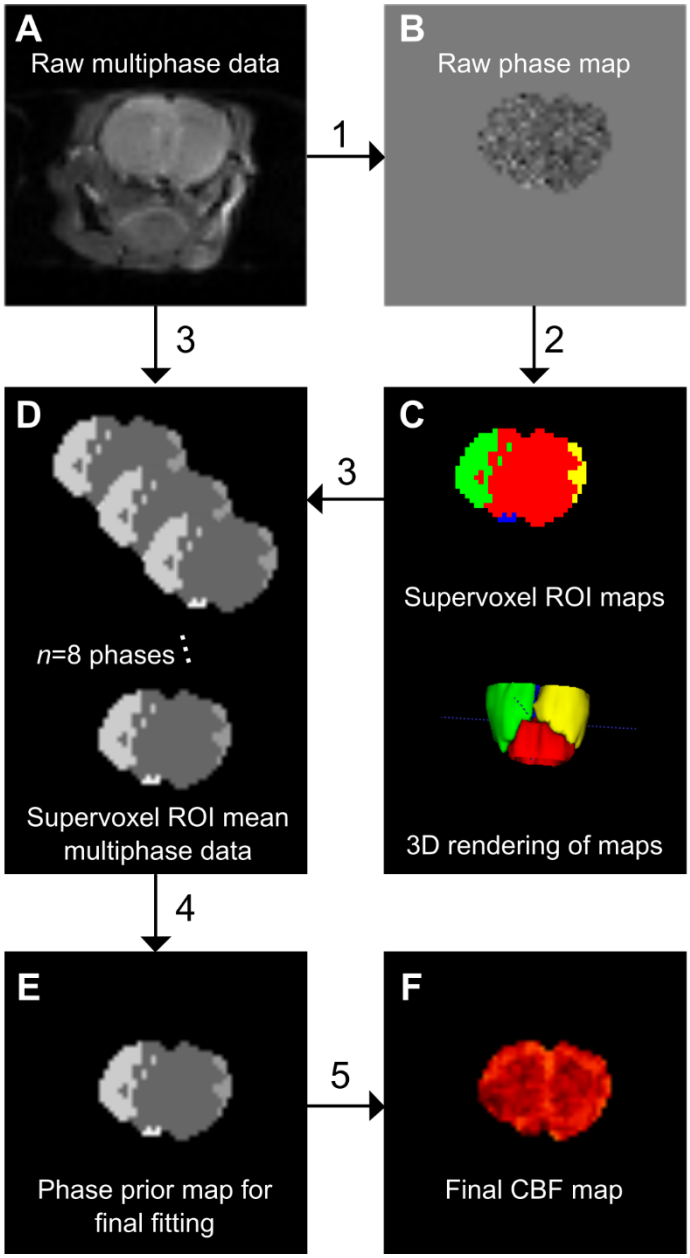


Figure 3.1: Diagram showing the use of supervoxels in preparing high precision phase map priors. The raw multiphase data (A) are initially fitted to the Fermi function with low precision priors (1) to yield a raw phase map (B). This raw phase map contains good spatial information but the phase values themselves are overestimated. The data are smoothed and clustered using supervoxels (2) to yield ROIs for each supervoxel phase cluster present (C). The raw multiphase data are then combined with the supervoxel ROIs (3) to yield high SNR supervoxel-ROI means of the multiphase data (D). This high SNR multiphase dataset is then fitted again (4) yielding a high precision phase map (E) which can be used to generate the final CBF maps (F), in combination with the raw data (5). Modified from Larkin *et al.* with permission[317].

In addition to MP pCASL acquisitions, T_1 and T_2 maps, angiography, and T_1 and T_2 weighted anatomical scans were acquired for each mouse, with parameters described in Chapter 2.6. In tumour-bearing animals, a contrast-enhanced scan was obtained 5 minutes post intravenous injection of 30 µL (15 µmol, approximately 0.75 mmol/kg based on a 20 g mouse) Gadodiamide (Omniscan, GE Healthcare) using the T_1 weighted scan parameters described above.

3.2.4 Comparison with standard label-control pCASL and validation with autoradiography

For comparison of MP pCASL data with gold-standard autoradiography CBF measurements, naïve mice (n = 4) were anaesthetised as for MRI above, with care taken to use the same isoflurane concentration and anaesthetic depth. MP pCASL was performed on each animal the day prior to autoradiography, owing to institutional restrictions concerning the use of radioisotopes in certain rooms. Care was taken to ensure breathing rate, isoflurane concentration and duration of anaesthesia prior to measurements were as similar as possible between the ASL and autoradiography sessions. For the MP pCASL MRI, a labelling pulse duration of 0.9 s and a post-label delay of 0.4 s were used with the parameters described above.

Autoradiography was performed the following day using the method described by Maeda *et al*.[311]. Briefly, mice were injected intraperitoneally with 0.15 µCi of 4-iodo-*N*-methyl-[^{14}C]antipyrine (Hartmann Analytic, Germany, specific activity 55 mCi/mmol) in 150 µL saline. 2 minutes after injection, mice were terminally anaesthetised with an overdose of pentobarbitone injected intraperitoneally, then

immersed in isopentane on dry ice until frozen. The frozen brain was extracted quickly, and 20 µm sections were collected at 200 µm intervals and dried at 60°C for 10 min. These sections were exposed to film for 24 hours alongside calibrated radioactive standards, and films were scanned. (Carestream Kodak BioMax MR Film; standards: 0-35 µCi/g, ARC; Expression 10000XL transmittance scanner, Epson, UK). Scanned films were background subtracted and calibrated against the standards. Absolute CBF was then calculated using the equation as described by Sakurada *et al*.[325]. Blood sampled from the frozen heart at end-point was used to calculate the final arterial tracer concentration using autoradiography.

For calculation of regional CBF values, the autoradiography images were perspective transformed, aligned to the MR images and down-sampled to the same resolution as the MP pCASL images (64 x 64 pixels). Subsequently, regional masks were created.

3.2.5 Application of MP pCASL to brain tumour models

Mice underwent intracranial injection of 4T1-GFP and U87 tumours as described in Chapter 2.3.2. At timepoints of day 7 (n = 3), 14 (n = 5), 21 (n = 6), 28 (n = 8) or 35 (n = 6) for 4T1-GFP tumours; and day 14 (n = 10) or day 28 (n = 6) for U87 glioma; and day 7 (n = 4) for a sterile saline control group. Mice underwent an imaging session which consisted of T_1 and T_2 weighted anatomical imaging, MP pCASL, pre- and post-RGD-MPIO injection MGE3D scans, and a gadolinium enhanced T_1 weighted scan. Following imaging, brains were harvested and prepared for histology as described in Chapter 2.3. Immunohistochemical analysis of blood vessel density (CD31) was performed as described in Chapter 4.2.1.

3.2.6 Statistics

All data are reported as group mean ± group standard deviation. Differences between groups were determined using two-tailed paired t-tests or one-way ANOVA (regional and histology analysis); or two-way repeated measures (paired) ANOVA (time-course analysis), followed *post hoc* by Bonferroni multiple test correction. An f-test was used to assess heterogeneity between groups.

3.3 Results

3.3.1 Measurement of carotid blood flow

Blood velocity in the carotid artery was measured using Doppler ultrasound (Figure 3.2) to inform Bloch simulations of pCASL. The mean blood velocity in the carotid artery was found to be 124 ± 17 mm/sec, and the maximum blood velocity was found to be 275 ± 58 mm/sec. Mean blood velocity was consistent between animals (Figure 3.3), but varied with respiration rate in 3 of 4 animals (linear regression, slope = 0.3 – 1.4). Maximum systolic blood velocity varied between animals (range = 214 – 556 mm/sec, Figure 3.3), and also varied with respiration rate in 3 of 4 animals (linear regression, slope = 2.0 – 7.6).

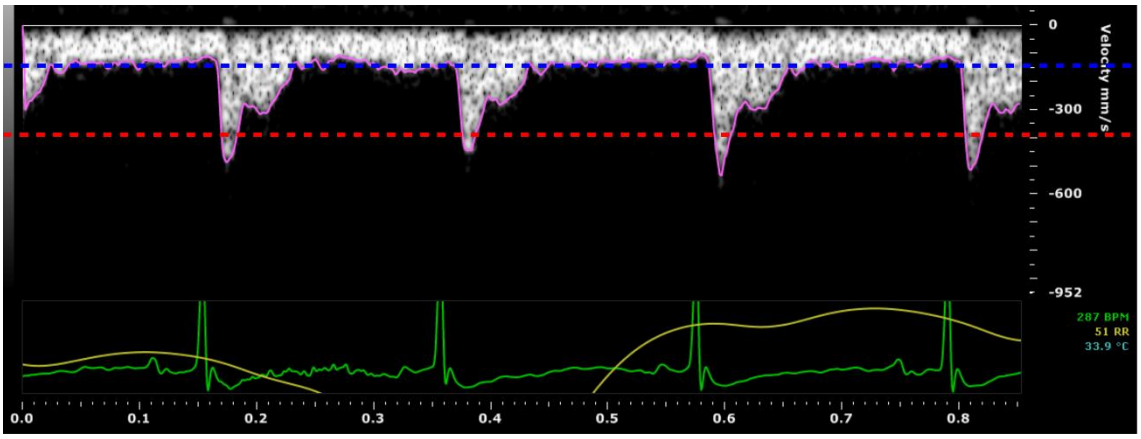


Figure 3.2: Power Doppler image of blood flow through the carotid artery. The pink trace is digitised and used to extract systolic and diastolic blood flow velocities. The green trace is the electrocardiogram, and the yellow trace represents respiration. The dotted blue line represents the mean carotid blood flow velocity, and the dotted red line represents the maximum carotid blood flow velocity for this animal.

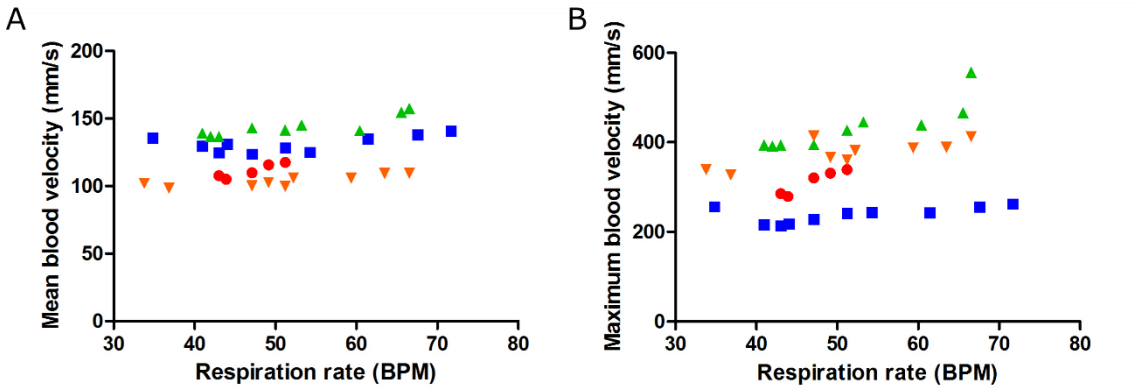


Figure 3.3: Carotid artery blood flow velocity in mice measured using Power Doppler ultrasound. (A) Mean blood velocity, and (B) Maximum blood velocity. Each symbol represents one individual animal (n = 4), and each data point represents a separate blood velocity measurement.

3.2.2 Simulation of labelling efficiency

Using the carotid blood flow values to inform the Bloch simulations, a 2mm label thickness was chosen as it provided sufficient theoretical inversion (labelling) efficiency (78.5%, Figure 3.4) at the RF pulse amplitude used in our system (5 µT) and mean blood velocity of 124 mm/s, and lies within the linear portion of the feeding arteries in the neck.

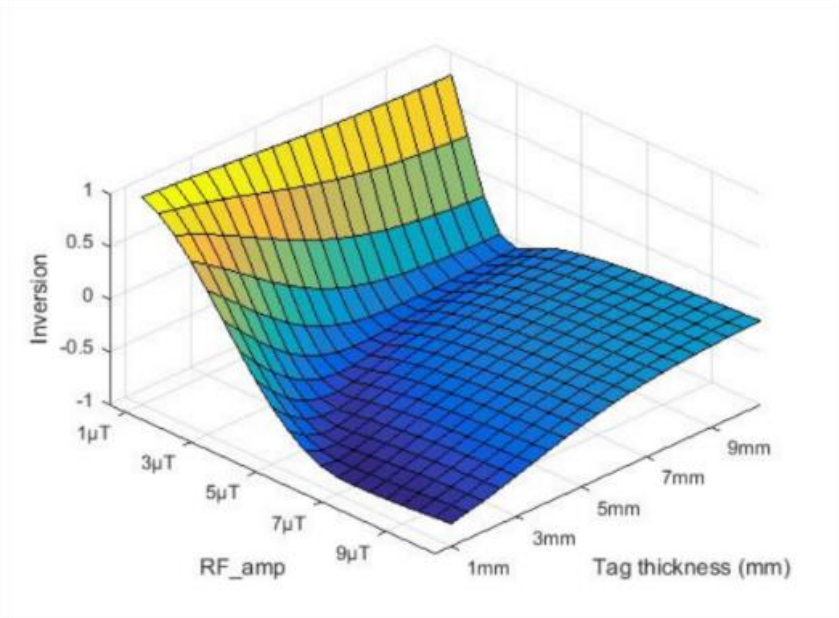


Figure 3.4: Labelling efficiency measurements of the MP-pCASL sequence. Bloch simulations using an average blood velocity of 124 mm/s, as measured previously, show a maximum theoretical labelling efficiency of 78.5% for a 2 mm labelling plane thickness, and 5 µT RF pulse amplitude.

Simulations to estimate the effect of label duration on the net magnetisation signal were carried out, and are shown in Figure 3.5. A tag duration of 0.9 s was the lowest duration tested with a 95% confidence interval of an SNR above zero. From these SNR simulations, label durations of 0.4, 0.9, 1.4, 2.4, 3.7 and 5 s were chosen for *in vivo* optimisation in order to test across a wide range of values.

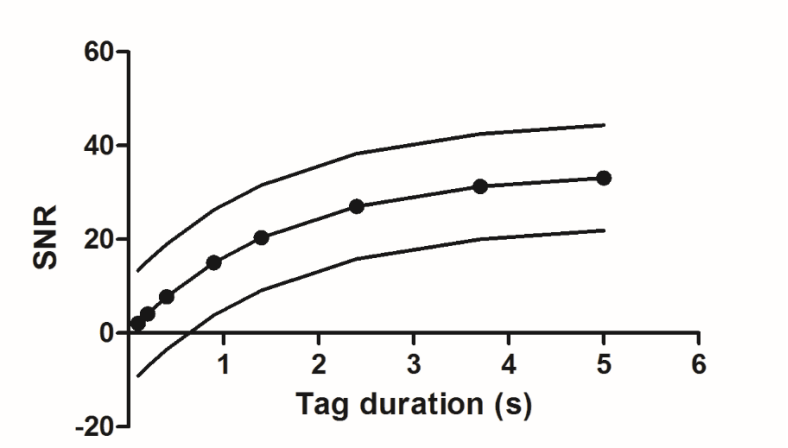


Figure 3.5: Change in theoretical signal saturation over a range of label durations.

Using a label duration of 0.9 s, a non-quantitative readout of blood saturation using the MP pCASL labelling pulse was obtained. These images, shown in Figure 3.6, showed clear inversion of the blood signal both in the labelling plane and in the carotid arteries.

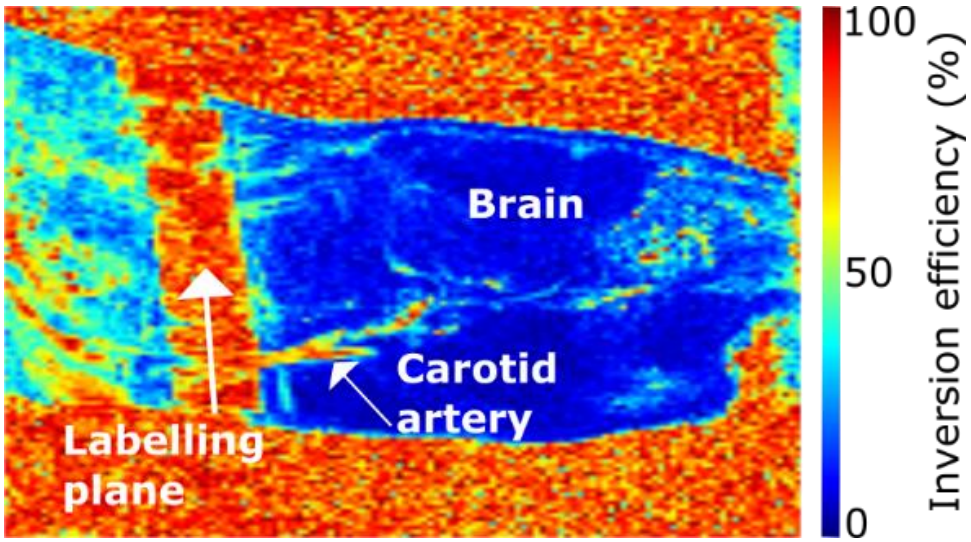


Figure 3.6: Non-quantitative imaging of signal inversion using the MP pCASL sequence with a fast spin-echo readout. The inversion of the signal in both the labelling plane, and also the outflowing blood in the carotid arteries, can be clearly seen.

3.2.3 Optimisation of MP pCASL sequence

The EPI readout was optimised from system default parameters (Figure 3.7A) as a spin-echo scan with a TR of 4 s to maximise SNR and tissue contrast (Figure 3.7B). A 2-shot sequence was determined to be optimal with regards to reducing image distortion within a reasonable scan time.

Respiratory triggering, whereby the imaging readout was acquired during the plateau phase of respiration, was found to reduce signal fluctuation at the base of the brain (Supplementary Video 1, available at https://www.hindawi.com/journals/cmmi/2018/4580919/#supplementary-material-1). A variable post-trigger delay was encoded in the sequence to allow adjustment for changing respiration rates in subsequent scans (Figure 3.7C). The respiratory triggering also significantly increased the signal-to-noise ratio (SNR) of the MP pCASL data (15.1 ± 5.9) compared to the untriggered sequence (6.5 ± 1.5, $p < 0.05$; Figure 3.8).

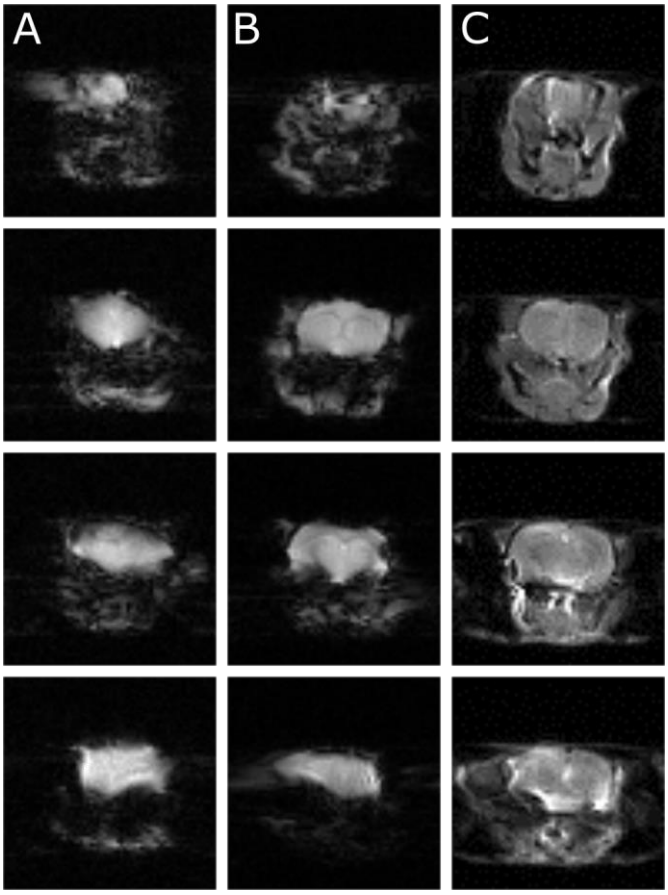


Figure 3.7: Optimisation of EPI readout. (A) Representative images obtained using the standard system-set EPI parameters of TR = 1 s, single shot, no triggering, and standard gradient echo encoding, showing high levels of distortion and poor contrast. (B) Images obtained with TR = 4 s, single shot, no triggering, and showing high levels of distortion and poor contrast. (C) Images obtained using the optimised EPI readout with respiratory triggering, TR = 4 s, 2-shot, and spin echo encoding showing substantially reduced image distortion and increased tissue contrast.

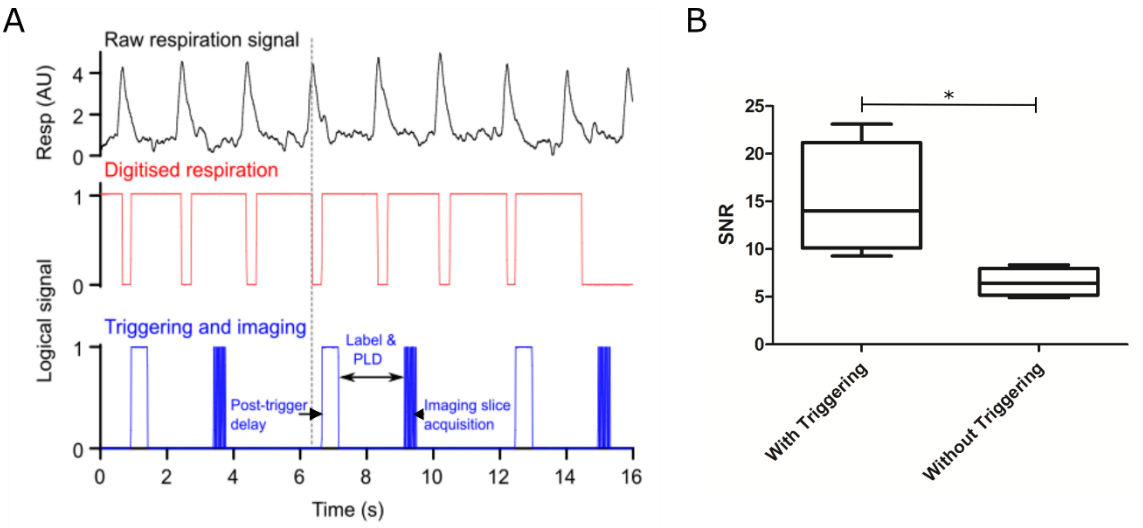


Figure 3.8: Respiratory triggering in the MP pCASL sequence. (A) Schematic of the respiratory triggering method used to acquire the imaging readout during the plateau phase of respiration, reducing signal fluctuation at the base of the brain. Black trace = raw respiration trace; red trace = digitised respiration trace which acts as the trigger signal; blue trace = readout of the post-trigger delay period, followed by the imaging slice acquisition. A variable encoding the post-trigger delay was implemented in the sequence to allow adjustment for changing respiration rates. (B) Box and whisker plot showing signal-to-noise ratio (SNR) of the MP pCASL sequence with and without respiratory triggering ($n = 4$, $^*p < 0.05$). Boxes represent median and interquartile range, and whiskers represent minimum and maximum values.

Following angiography, a labelling plane positioned at -10° relative to the axial plane was found to be perpendicular to the carotid and vertebral arteries. Label placement just posterior to the medulla oblongata enabled consistent labelling plane placement between animals using a distinct anatomical landmark, and is posterior to the vertebral flexure of the carotid arteries (Figure 3.9A).

All labelling pulse train durations tested yielded CBF values close to the physiological range expected from the literature (Figure 3.9B), and no significant differences in calculated CBF values were found between the different durations. Similarly, phase maps were stable across labelling durations. Thus, as a compromise between ensuring sufficient labelling and keeping scan time as short as possible, a label duration of 0.9 s was chosen.

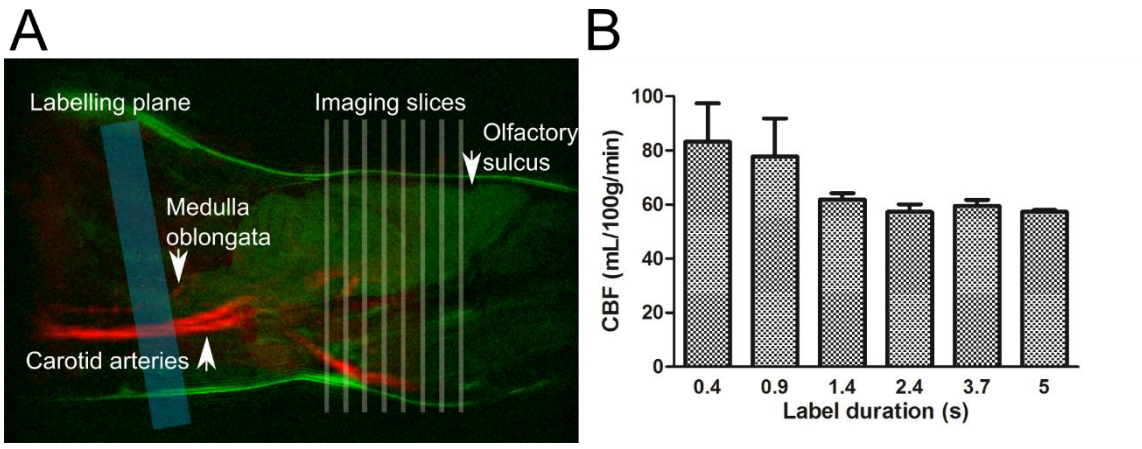


Figure 3.9: Optimisation of MP pCASL bolus duration. (A) A -10° labelling plane (blue) relative to the axial imaging plane (yellow) was optimal, as this was perpendicular to the carotid and vertebral arteries visible by angiography (red). Label plane placement posterior to the medulla oblongata, visible on a sagittal T_2 weighted anatomical image (green), enabled consistent label plane location between animals, while not interfering with imaging slices (yellow). (B) No significant differences were found in calculated CBF across the range of label duration times tested (n = 3). Graph represent mean ± standard deviation.

To allow measurement of arterial transit time, 12 PLDs from 10 to 1000 ms were acquired, each with 8 phases of labelling RF pulses. Arrival maps showed that the bolus arrived at over 95% of voxels in the most anterior slice, and at 99% of voxels in the most posterior slice within 0.4 s (Figure 3.10). Thus, 0.4 s was chosen as the optimal PLD to reduce signal loss from relaxation.

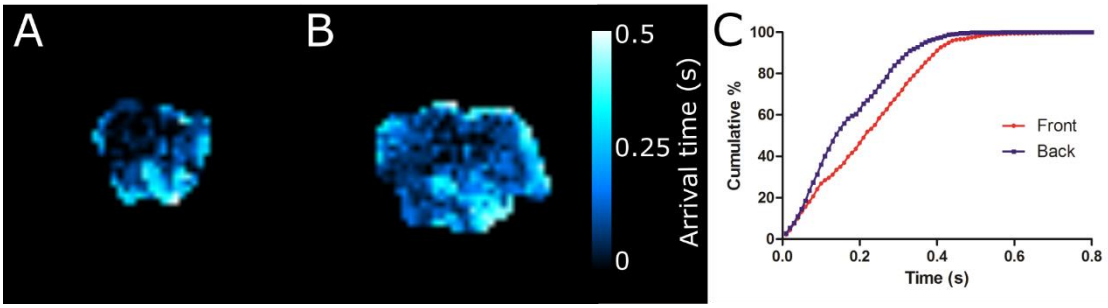


Figure 3.10: Optimisation of post label delay. (A-B) Multi-PLD scans were acquired to measure arterial transit time at the front and back of the brain. Example maps of bolus arrival time in (A) anterior and (B) posterior slices. (C) Arrival maps showed bolus arrival in over 95% of voxels in the anterior slice and 99% of voxels in the posterior slice within 0.4 s (n = 4).

3.2.4 Comparison with standard label-control pCASL and validation with autoradiography

Use of the non-multiphase, label-control pCASL yielded poor quality CBF maps with many voxels showing CBF values of zero (Figure 3.11A). The measured CBF values were 115 ± 88 mL/100 g/min on average across the brain (Figure 3.11B). Use of the optimised MP pCASL parameters in naïve mice resulted in measured CBF values of 96 ± 18 mL/100 g/min on average across the brain (Figure 3.11B). Average CBF values were 103 ± 23 mL/100 g/min in the cortex, 90 ± 24 mL/100 g/min in the striatum, and 77 ± 21 mL/100 g/min in the corpus callosum (Figure 3.11C). A comparison with regional CBF values obtained using label-control pCASL was not carried out as we were unable to obtain results of sufficient quality using this method. Whilst on average, the whole brain values using the label-control pCASL sequence were not significantly different to the MP pCASL values, the voxel to voxel variance was significantly lower using the MP pCASL sequence (F test, $p < 0.0001$).

Using the gold-standard autoradiography method, CBF was measured at 101 ± 32 mL/100g/min across the whole brain (Figure 3.11B), a difference of <6% when compared to MP pCASL results across the same region. Average CBF values were 102 ± 32 mL/100 g/min in the cortex, 95 ± 25 mL/100 g/min in the striatum, and 87 ± 28 mL/100 g/min in the corpus callosum (Figure 3.11C). No significant differences were evident between MP pCASL and autoradiography CBF measurements (Figure 3.11B).

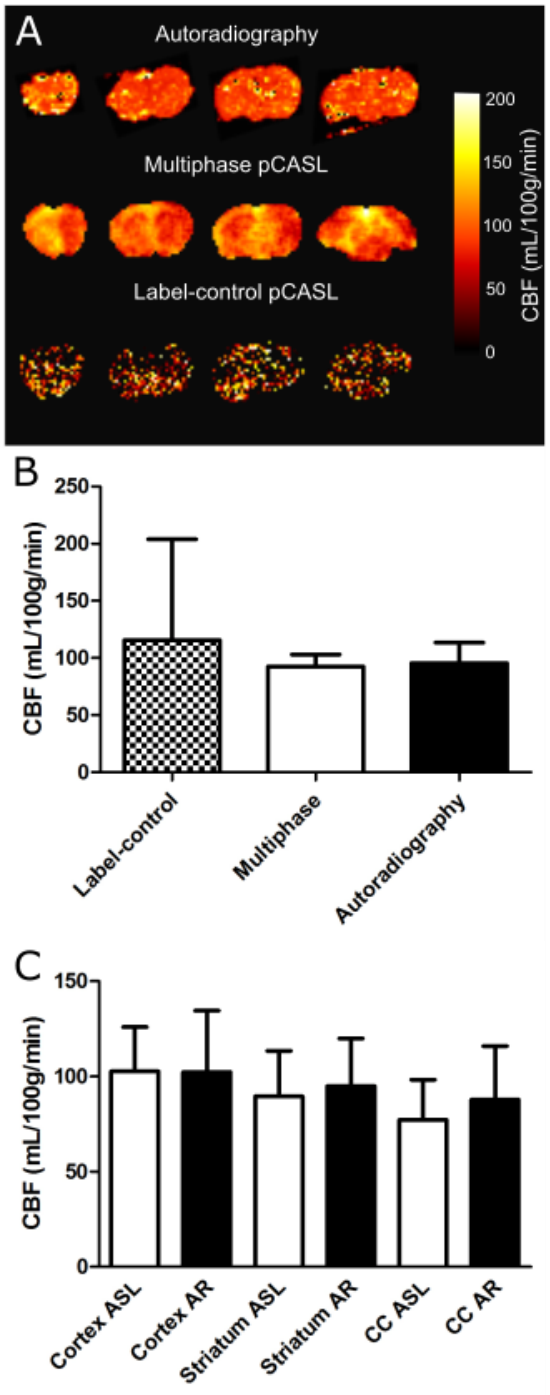


Figure 3.11: Cerebral blood flow maps and regional values. (A) Representative CBF maps produced using gold-standard autoradiography (top row), the optimised MP pCASL sequence (middle row) and label-control pCASL (bottom row). (B) Graph showing whole brain average CBF values obtained using label control pCASL, MP pCASL, and autoradiography, shown as mean ± standard deviation. (C) Graph showing regional CBF values as measured by MP pCASL (white columns) and autoradiography (black columns), shown as mean ± standard deviation. No significant differences were found between MP pCASL and autoradiography CBF measurements for any of the brain regions tested.

Blood vessel density was also calculated from histological sections stained for CD31 in these animals, yielding values of 3.0 ± 0.6%, 2.2 ± 0.8% and 0.8 ± 0.3% for the cortex, striatum and corpus callosum, respectively (Figure 3.12). Although both CBF and vessel density appeared to decrease across the three regions studied (cortex > striatum > corpus callosum), no significant correlation between vessel density and CBF was found.

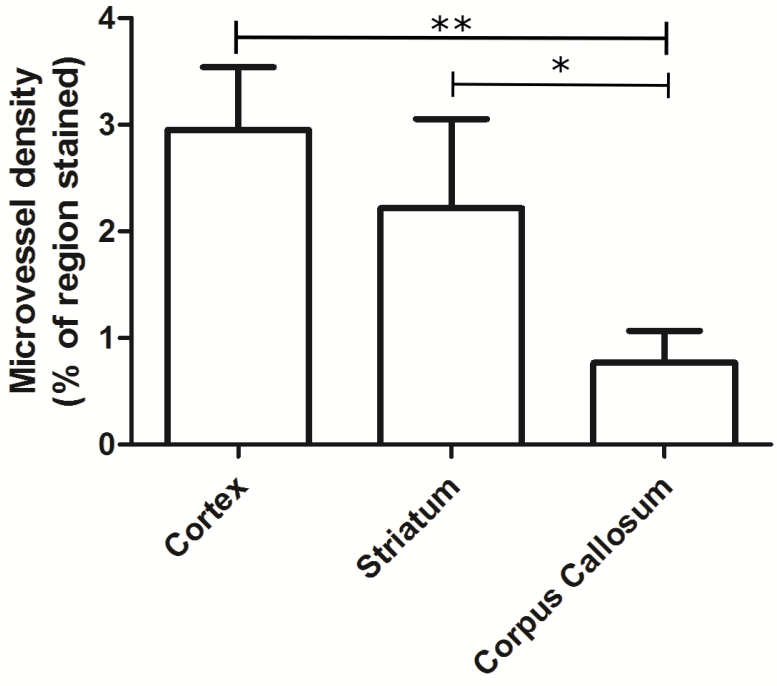


Figure 3.12: Graph showing microvessel density of brain regions in naïve animals used for autoradiography (n = 4), shown as mean ± standard deviation. * $p < 0.05$; ** $p < 0.01$

3.2.5 Application of MP pCASL to brain tumour models

Application of the MP pCASL sequence to mice with intracerebral metastases showed a significant, 16% decrease in CBF in the tumour-bearing striatum (84 ± 16 mL/100 g/min) compared to the contralateral (normal) striatum (99 ± 24 mL/100 g/min) at day 35 (ANOVA $p < 0.05$, post hoc Bonferroni test $p < 0.05$; Figure 3.13). No differences were found between hemispheres at other time-points. All tumours were confirmed histologically, and the mean tumour diameter measured by histology at day 35 was 2.14 ± 0.53 mm.

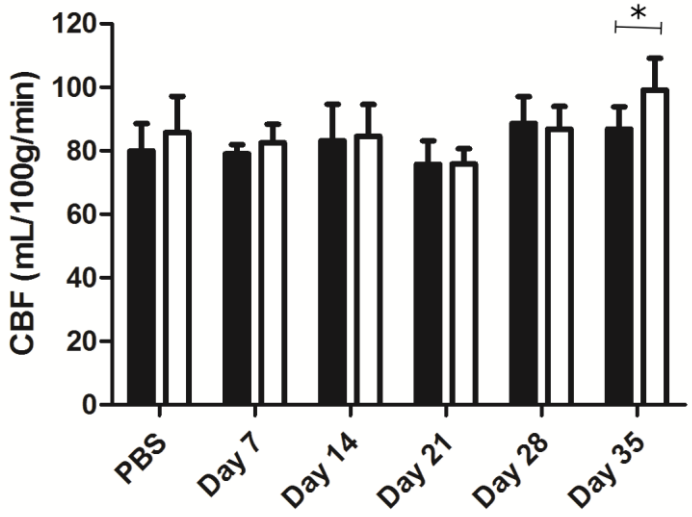


Figure 3.13: Graph showing cerebral blood flow in a mouse model of brain metastasis. Cerebral blood flow in the tumour-bearing striatum (black) was significantly reduced compared to the contralateral striatum (white) at the day 35 time-point (ANOVA $p = 0.04$, *post hoc* $p < 0.05$). Bars represent mean ± standard deviation, at day 7 (n = 3), 14 (n = 5), 21 (n = 6), 28 (n = 8) and 35 (n = 6).

In a subset of animals (n = 7 from days 21-35), the striatum exhibited gadolinium enhancement throughout the area of metastatic foci, and in these animals, no difference in CBF was evident between the tumour bearing striatum (86 ± 26 mL/100 g/min) and contralateral striatum (92 ± 24 mL/100 g/min; Figure 3.14A-C). Analysis of microvessel density within the metastatic foci showed an increased vessel area fraction (7.7 ± 2.2%; Figure 3.14D-F) in the non-enhancing tumour core compared to normal tissue in the contralateral striatum (0.9 ± 0.4%, $p < 0.0005$, Figure 3.14D-F).

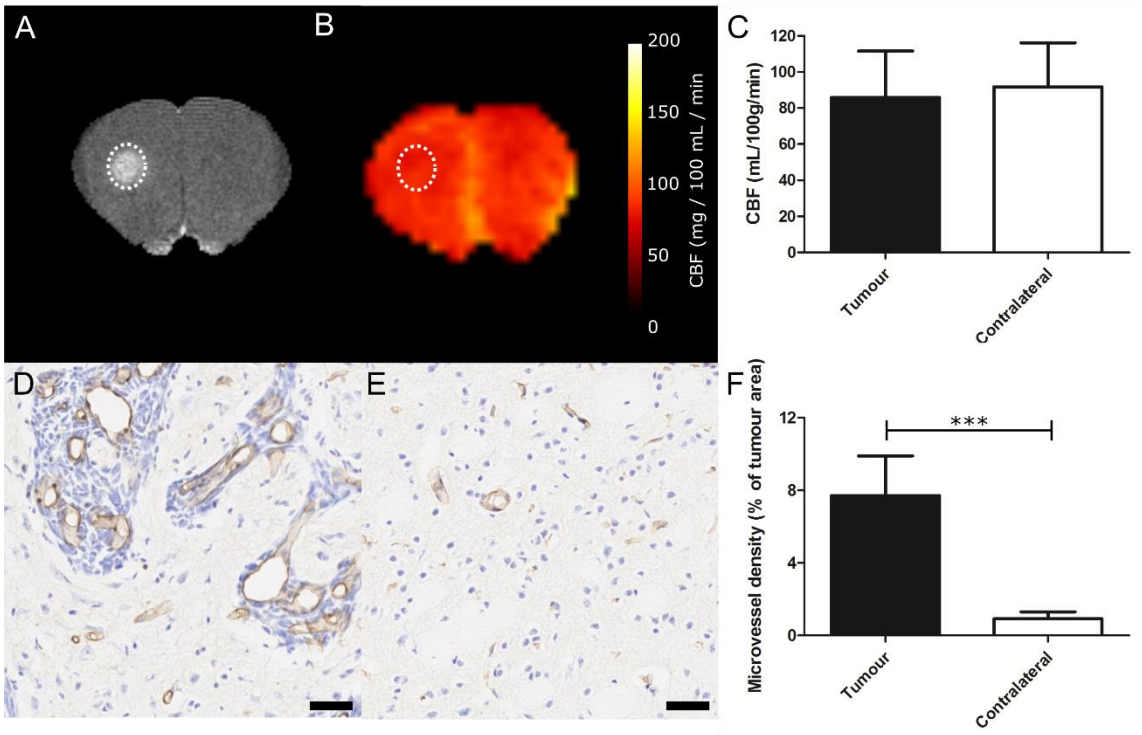


Figure 3.14: Application of the MP-pCASL sequence in mice with intracerebral 4T1-GFP metastatic tumours showing gadolinium enhancement. (A) T_1 weighted image showing enhancement (dotted outline) of metastatic foci. (B) CBF maps with the same ROI indicated. (C) Graph showing CBF values in tumour and contralateral regions; no significant decrease in perfusion is evident. (D-E) Histological comparison of microvessel area fraction in tumour (D), and contralateral (E) regions. Scale bars represent 20 µm. (F) Graph showing quantitation of microvessel area fraction in tumour and contralateral striatum regions; a significant increase in microvessel area fraction is evident in tumour compared to normal tissue in the contralateral striatum. Bars represent mean ± standard deviation (n = 7). ***$p < 0.001$

However, in a further, distinct, subset of animals from days 28 and 35 (n = 6), a gadolinium-enhancing tumour rim was evident surrounding a non-enhancing tumour core. Analysis of these animals showed a significant reduction in blood flow in the core of the tumour region (69 ± 14 mL/100 g/min) compared to the rim (83 ± 10 mL/100 g/min; $p < 0.05$; Figure 3.15A-C). No difference was found between the enhancing rim of the tumour and normal tissue in the contralateral striatum (82 ± 13 mL/100 g/min; Figure 3.15C). The mean absolute reduction in CBF in the tumour core compared to the tumour rim was 13.4 mL/100 g/min. The tumour voxels (including core and rim) showed significantly greater heterogeneity, as demonstrated by higher intra-ROI voxel variance, than the contralateral striatum (F-test, $p < 0.001$).

Analysis of microvessel density within the metastatic foci showed a greatly increased vessel area fraction (13.5 ± 2.5%) in the non-enhancing tumour core compared to the tumour rim (6.6 ± 2.5%, $p < 0.0001$; Figure 3.15D-F), which in turn showed greater vessel area fraction than the normal tissue in the contralateral striatum (1.2 ± 0.7%, $p < 0.0001$; Figure 3.15F). Correlation analysis revealed a trend towards negative correlation between microvessel density and CBF measured by MP pCASL MRI in the tumour core region, but this did not reach significance (Figure 3.16, $R^2 = 0.61$, $p = 0.066$).

In the remaining subset of non-enhancing tumours from days 28 and 35, no difference was found between the tumour-bearing and contralateral striatum (paired t-test, n = 5).

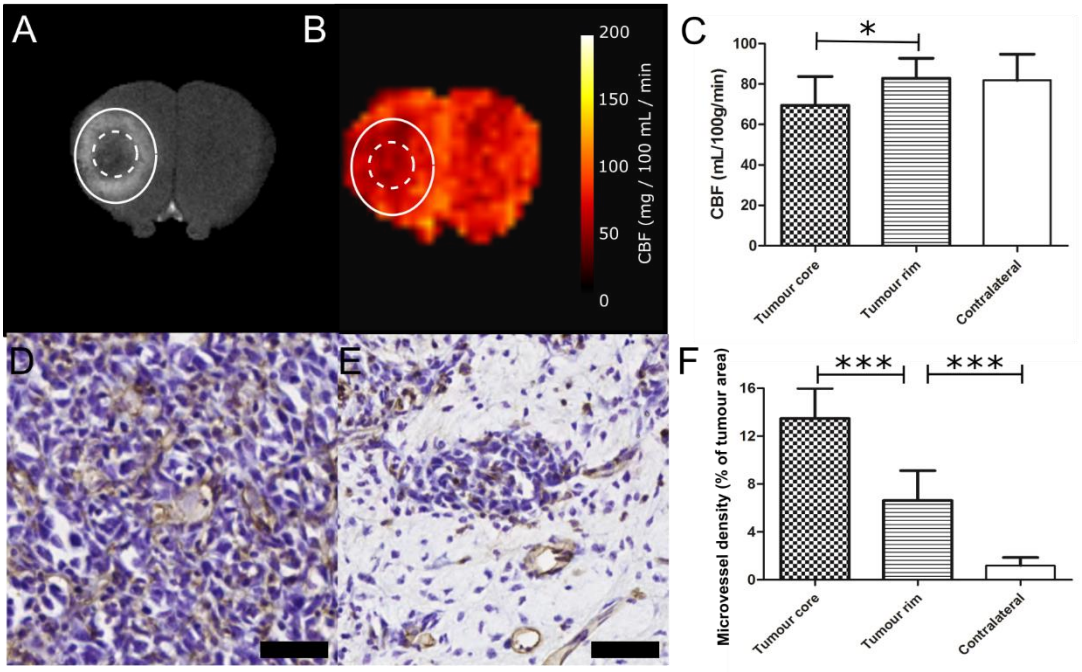


Figure 3.15: Application of the MP-pCASL sequence in mice with intracerebral 4T1-GFP metastatic tumours showing a gadolinium enhancing rim and a non-enhancing core region. (A) T_1 weighted image showing core (non-gadolinium enhancing central regions; dotted outline) and rim (gadolinium enhancing regions; solid outline) of metastatic foci. (B) CBF maps with the same ROIs indicated. (C) Graph showing CBF values in core, rim and contralateral regions; a significant decrease ($n = 6$, $p < 0.05$) in perfusion is evident between the core and rim regions of tumours. (D-E) Histological comparison of microvessel area fraction in core (D), and rim (E) regions. Scale bars represent 20 µm. (F) Graph showing quantitation of microvessel area fraction in core, rim and contralateral striatum regions; a significant increase in vessel area fraction is evident in core regions compared to both the rim regions ($p < 0.0001$) and normal tissue in the contralateral striatum ($p < 0.0001$). Bars represent mean ± standard deviation ($n = 6$). *$p < 0.05$; ***$p < 0.0001$

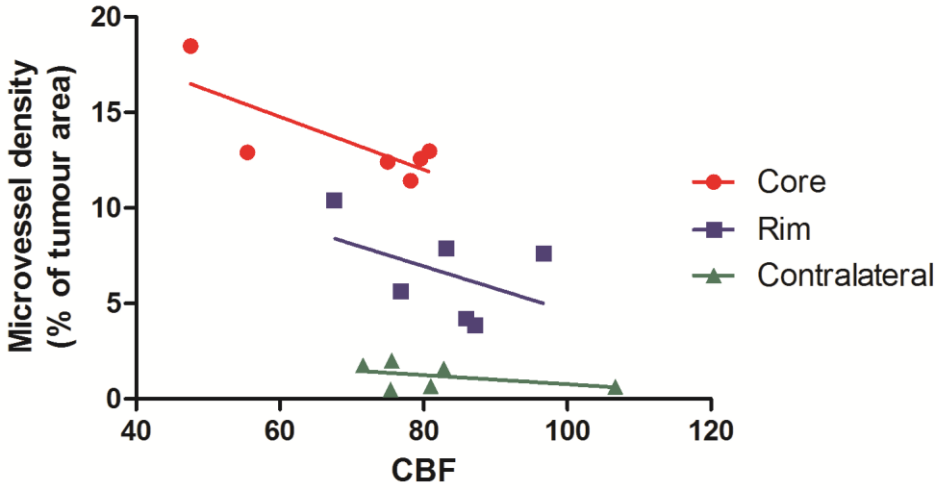


Figure 3.16: Plot showing correlation analysis between CBF and microvessel density in a subset of animals (n = 6) with a gadolinium enhancing rim and non-enhancing core structure. Linear regression lines for each dataset are plotted, showing a trend towards an inverse correlation between CBF and microvessel density in the core region ($R^2 = 0.61$, $p = 0.066$).

Application of the MP-pCASL sequence to mice injected intracerebrally with U87 glioma cells showed a significant, 19% reduction in CBF in the tumour-bearing striatum (61 ± 12 mL/100 g/min) compared to the contralateral striatum at day 28 (74 ± 10 mL/100 g/min; $p < 0.05$; Figure 3.17). Only two tumours were found to have gadolinium enhancement, and no tumours showed non-enhancing core regions. As for the metastasis model, analysis of microvessel density within the day 28 tumours showed an increased vessel area fraction (10.7 ± 2.9%) in the tumour compared to normal tissue in the contralateral striatum (3.6 ± 0.5%, $p < 0.05$, Figure 3.17D-E). All tumours were confirmed histologically, and the mean tumour diameter measured by histology at day 28 was 1.20 ± 0.52 mm.

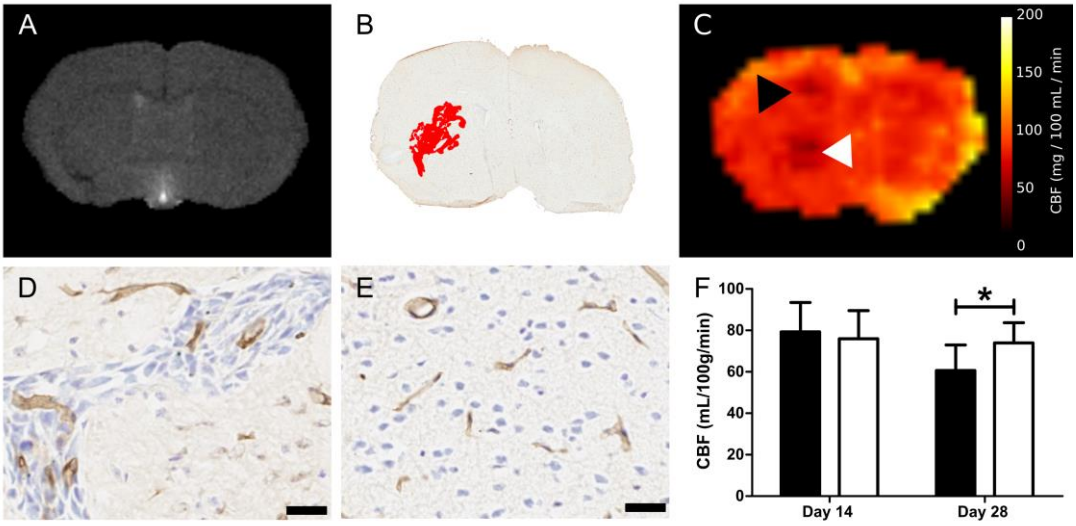


Figure 3.17: Application of the MP pCASL sequence in mice with intracerebral U87 glioma at the day 28 timepoint. (A) T_1 weighted image showing no evidence of gadolinium enhancement in the tumour injected (left) hemisphere. (B) Immunohistochemical image showing an overlay of tumour area (red) combined from tissue sections spanning 500 µm corresponding to the MRI slice in (A). (C) CBF maps showing reduction in local CBF (arrowheads). (D-E) Immunohistochemical image showing CD31 staining of vessels (brown) in tumour injected striatum (D) and contralateral striatum (E). (F) Graph showing CBF values in the tumour-bearing (black) and contralateral (white) striatum. CBF is reduced in the tumour-bearing compared to the contralateral striatum at the day 28 time-point ($p < 0.05$). Scale bars indicate 20 µm, graph bars represent mean ± standard deviation (n = 3).

3.4 Discussion

Pseudo-continuous ASL is the recommended MRI sequence for clinical measurements of cerebral blood flow, and multiphase ASL sequences have many advantages in compensating for off-resonance effects that alter labelling efficiency, thus improving the quality and reliability of CBF maps produced. Despite these advantages, no studies have been published implementing multiphase pCASL in mice. I have now demonstrated that our optimised MP pCASL sequence provides reliable and accurate measures of CBF in naïve mice *in vivo*, and is sensitive to changes in tumour blood flow.

3.4.1 Measurement of carotid blood flow

The MP pCASL sequence was first optimised for use in mice. The carotid ultrasound showed a modest increase in both mean and maximum blood flow velocity as respiration increased. As this has the potential to influence the labelling of the blood, care was taken during MRI sessions to keep the breathing rate as stable as possible at approximately 60 breaths per minute. At these blood flow velocities, simulation of the Bloch equations showed an optimum labelling plane thickness of 2 mm, which was taken forward for use in all subsequent experiments.

It has been shown in previous studies that a labelling plane perpendicular to the feeding arteries is important to ensure homogenous blood labelling[292,317], so for this reason our sequence used a labelling plane oriented at -10° relative to the axial plane, in order to be perpendicular to the common carotid artery. Similarly, the anatomical landmark of the medulla oblongata was chosen for consistency of positioning of the labelling plane, as the 2mm labelling plane could be placed there

in such a way so as not to interfere with the imaging slices, whilst also lying posterior to the vertebral flexure of the carotid artery.

3.4.2 Simulation of labelling efficiency

Labelling efficiency is difficult to measure directly. Imaging of inverted/saturated blood in the arteries can be performed, however as each voxel contains a mixture of static tissue and blood, quantifying the absolute signal change compared to 100% inversion is not possible. For this reason, direct measurement of labelling efficiency has not been included in this study. However, using the 2 mm labelling plane positioned as described above, a non-quantitative visualisation of blood saturation was performed. This confirmed labelling (inversion) of the blood in the carotid arteries adjacent to the labelling plane. Following this confirmation, the parameters of the MP pCASL sequence itself were optimised.

3.4.2 Optimisation of MP pCASL sequence

The use of a 2-shot EPI sequence, whilst doubling the required scan time, enabled a reduction in distortions so that anatomical details could be resolved. The inclusion of a respiration trigger in the sequence reduced signal fluctuation at the base of the brain and improved image quality. However, this technique does result in a variable TR between phase acquisitions. As the TR becomes longer than the minimum with triggering, it is expected that there will be no effect on the subsequent phase acquisition. Extended TR values of up to 20 s have been tested with this sequence and have shown no effect on data quality. The use of respiratory triggering also relies on a reasonably stable respiratory cycle, which was reliably

achieved at ~60 breaths per minute with 1.2 - 1.5% isoflurane concentrations for up to two hours.

In the optimisation of MP pCASL parameters, the optimal post-label delay found here (0.4 s) was in accord with the bolus arrival times seen in previous implementations of ASL in mice[300,326] and rats[317]. To determine an optimised labelling duration, modelling of the theoretical signal from each labelling pulse was conducted for labelling durations ranging from 0.1-15 seconds. Labelling pulse trains of less than 0.9 s were found to have a scaled SNR with a 95% confidence interval of less than zero, and therefore much shorter durations were not tested. No significant differences in calculated CBF values were found between the different pulse durations, and all pulse durations tested yielded CBF values close to the physiological range expected from the literature. Phase maps were also stable across labelling durations. Thus, as a compromise between ensuring sufficient labelling and keeping scan time as short as possible, a label duration of 0.9 s was chosen.

Using these optimised parameters, the MP pCASL approach yields substantially higher quality CBF maps than conventional label-control subtraction ASL methods, resulting in a more robust and reliable method of quantitatively measuring CBF than non-multiphase ASL methods. The MP pCASL total acquisition time is 3-4 minutes (allowing for variable respiratory triggering) as compared to 1.5 minutes for a standard label-control scan, which is still reasonable for a pre-clinical scan. It is unlikely that an increase in the number of averages per label-control acquisition to bring the total scan time into line with the MP pCASL sequence would result in a substantial increase in SNR, as data collected in rats suggests that label-control acquisitions have reduced SNR, even with identical scan times[317]. Similarly, it has

been shown that there is no difference in CBF measurements using this sequence when analysed using either a one or two-compartment model[317]. Therefore, it is reasonable to employ the simplest, single compartment model.

3.4.4 Comparison with standard label-control pCASL and validation with autoradiography

In this study, our aim was to produce MP pCASL measurements that can be used to obtain CBF maps in mice that replicate blood flow values obtained using the gold-standard approach of autoradiography. Our results showed good concordance with autoradiography, and were in accord with previous autoradiography findings[310-312], including those comparing ASL with autoradiography[314,317]. Moreover, direct comparison of MP pCASL and autoradiography CBF maps in the same animals in the current study showed no statistically significant differences between brain regions, and measurements varied by <6% between the two techniques, allowing us to conclude that the MP pCASL sequence produces accurate quantitative CBF values in the naïve mouse brain. As anticipated, the use of multiphase pCASL reduced the errors seen in the previous implementation of label-control pCASL in mice owing to loss of inversion efficiency[300]. As an alternative to the MP pCASL approach described here, phase correction can also be applied using pre-scans[327,328]. However, this method requires processing during scan time rather than post-hoc. For this reason, the MP pCASL approach offers an easier implementation, and a potentially more time efficient approach for the measurement of CBF. Whilst other ASL sequences have been validated preclinically, to our knowledge, this is the first pCASL study in mice that has been directly validated by autoradiography.

Our data show less regional variation in CBF than other autoradiography studies in mice, which may, at least in part, reflect differences in mouse strain and anaesthetic regime used[311,313,329]. Gaseous anaesthesia, in particular, is known to have region specific effects on CBF, and in rats the caudate/putamen shows a much greater (~70%) increase in CBF than the cortex (~20%) under isoflurane anaesthetised conditions compared to awake animals[305]. Consequently, regional differences in CBF under isoflurane anaesthesia are greatly reduced[305], and it is likely that this underlies the reduced regional variation in CBF observed in the current study. The reduced regional variation was observed in both MP pCASL and autoradiography data, supporting the above conclusion. To reduce the effects on our CBF measurements, we used the lowest possible concentration of isoflurane in order to achieve a stable breathing rate of ~60 breaths per minute. It is also possible that the time taken to extract the frozen brain from the skull has affected the autoradiography results. As shown in the Maeda *et al*. paper describing this methodology, an extraction time of 60 sec compared to 30 sec results in passive diffusion of the radiotracer, and hence blurring of regional boundaries and reduced differences in regional CBF[311]. Although this artefact could have affected our autoradiography results, they are consistent with the regional CBF measurements as determined by MP pCASL, suggesting that this isn't the case.

3.4.5 Application of MP pCASL to brain tumour models

The MP pCASL technique was then used to assess CBF in two mouse brain tumour models. MP pCASL was found to be sensitive to changes in tumour perfusion in a mouse model of brain metastasis at later time-points. It appeared there may be an effect of increased CBF in the contralateral hemisphere at the day

35 timepoint, however the CBF of the contralateral striatum at this timepoint was not significantly different from the CBF of the contralateral striatum in the PBS control group, or the contralateral striatum at other timepoints. This may be due to co-incidental natural variation in CBF between mice, or may reflect a real increase in contralateral CBF due to the tumour pathology. Similarly, in the glioma model, a reduced perfusion was observed at the late timepoint, even where no contrast enhancement was evident. This finding is consistent with the work of Vallatos et al[330], who have found that perfusion weighted imaging can detect infiltrative tumour margins in the absence of contrast enhancement in a mouse model of glioblastoma.

The MP pCASL technique was also sensitive to perfusion heterogeneity within metastatic tumours, showing significantly reduced (but not absent) perfusion in the non-enhancing tumour core compared to normal tissue in the contralateral striatum, and increased heterogeneity in perfusion compared to the contralateral striatum. However, no differences in CBF were seen in late timepoint mice with either fully enhancing or non-enhancing tumours. As autoradiography has only been used to validate CBF measurements in the naïve brain, it is possible that differences in tumour arterial transit time or tissue relaxation time may affect the CBF quantification from MP pCASL data in these tumour-bearing animals. However, these results are in line with other preclinical primary brain tumour perfusion studies, which showed reduced perfusion in the tumour core[295,331-333].

The CBF reduction in tumour blood flow observed in the current study was considerably smaller than other (primary) tumour perfusion studies. The majority of previous studies have investigated large tumours (> 5 mm diameter in mice) [295,297,331,333], which often have a large necrotic core with few blood vessels[295,334]

resulting in a substantial perfusion deficit. In contrast, in both the metastasis and glioma models used here, the tumour foci were considerably smaller (1-2mm diameter) and more diffusely growing. Moreover, histological analysis demonstrated that the core regions, rather than being necrotic and devoid of vessels, in fact contained large numbers of blood vessels. Such tumours would be ideal clinical candidates for treatment with vascular modifying agents, and the ability to quantitatively measure changes in blood flow in such small tumours could be of considerable use in pre-clinical testing.

Tumours have a number of distinct vascular phenotypes, each of which may confer changes in blood flow. One such phenotype, which is present in our model, is that of a highly branched network of non-functional angiogenic vessels. In this case, despite an increase in the density of vessels, a decrease in CBF may be observed in this region owing their highly branched and dysfunctional nature. Another vascular phenotype often seen in solid tumours[295], is the rapid growth of the tumour faster than the vasculature can keep up, resulting in a tumour core with low vascularity, and hence a decreased CBF. Both of these phenotypes are characterised by a decrease in CBF, despite the differences in tumour vascularity.

Interestingly, the rim of the metastatic tumour area also showed an increased microvessel area fraction histologically compared to normal tissue in the contralateral striatum, but in this region CBF measured by MP-pCASL was normal. Similarly, in those tumours showing enhancement but no core region, microvessel density was increased despite no change in CBF. These findings indicate that MP-pCASL identifies changes in tumour blood flow that could not be predicted from histological assessment of vascularity alone. Taking all of the above findings together, by identifying areas of reduced (but not absent) flow, MP pCASL MRI

may enable identification of brain tumours in which vascular normalising therapy or anti-angiogenic therapy could be beneficial prior to, or in conjunction with, radiotherapy.

There are small differences in blood vessel density measurements across the ‘normal control’ groups in our study. This may reflect differences in tissue processing between individual experiments; in particular, in the naïve mice used for autoradiography, tissue preparation and fixation protocols were different to those used in the tumour models for immunohistochemical analysis. These differences in tissue processing (fixation method, cryoprotection, thicker sections) may result in differences in antibody hybridisation and, hence, variation in measured blood vessel density. Similarly, the metastasis model and the glioma model were studied in different strains of mice, in which the underlying ‘normal’ vessel density may differ. The only comparison in which all conditions are the same is that for the normal striatum in mice with wholly-enhancing tumours compared to mice with a core/edge structure, and in this case the difference in vessel density measurements is within one standard deviation of the mean for either condition. Moreover, where comparisons of vessel density are being made between brain/tumour regions, these are all performed within group. So even if the absolute numbers are, to some extent, dependent on tissue processing/fixation/staining methods, the comparison between different brain/tumour regions is valid as these are all subject to the same conditions.

Gadolinium contrast enhancement on MRI reports on a combination of vessel permeability and blood flow, and a lack of gadolinium enhancement in tumour core regions is typically taken to reflect tissue necrosis and complete absence of vessels. In contrast, blood vessel density measurements provide no information on

whether vessels are perfused, but only whether they are present. However, in both models used in the current study, although core tumour areas showed significant reductions in blood flow in areas devoid of gadolinium enhancement, histological assessment revealed a significant increase in microvessel density and only very small areas of necrosis. Together, these findings suggest that these core vessels are either structurally abnormal or have abnormal flow patterns, as is common in angiogenic tumour vessels[335-337], and that MP pCASL measurements may complement histology and contrast-enhanced MRI to provide useful insights into vessel patency and tumour blood flow.

Optimisation and standardisation of parameters in mice will also ensure that measurements and imaging biomarkers developed in mouse models are translatable to the clinic. It is important, as highlighted by the clinical ASL white paper[292], that imaging biomarkers, including ASL measurements, are quantitative, so that measurements can be compared across groups and experimental conditions. Similarly, there are a number of further recommendations in the white paper that could be implemented pre-clinically to move further in line with clinical recommendations. These include the addition of background suppression, and the use of a 3D readout for pCASL sequences[338]. As stated in the imaging biomarker roadmap, single- and multi-centre repeatability studies are also essential for imaging biomarker translation, along with biological validation[190]. To achieve this, further repeatability studies could be carried out, along with validation of tumour blood flow measurements using gold-standard autoradiography.

These possible future developments notwithstanding, I have demonstrated that MP pCASL is an important and useful technique for measure cerebral blood flow in pre-clinical rodent models of disease.

3.5 Conclusions

Multiphase pCASL MRI has been successfully optimised and validated for imaging cerebral blood flow in naïve mice, and has been shown to overcome the limitations inherent in standard non-multiphase ASL methods. The data show high reproducibility in CBF measurements between animals and concordance with gold standard autoradiography measurements in naïve mice. Further, this imaging approach is sensitive to changes in perfusion in mouse models of both primary and secondary brain tumours, even in relatively small tumours, and provides insight into tissue blood flow dynamics that complements vessel density measurements and contrast-enhanced MRI. This method could be of high value for non-invasive measurement of brain tumour blood flow prior to and following therapy, increasing the potential for clinical translation.

Chapter 4 - Targeting integrin $\alpha_v\beta_3$ for *in vivo* imaging of brain metastases

4.1 Introduction

Integrin $\alpha_v\beta_3$, targeted by the peptide ligand RGD, is an attractive target for the molecular imaging of angiogenesis, as discussed in Chapter 1.2.2. There are currently no molecular imaging techniques for imaging integrin $\alpha_v\beta_3$ in widespread clinical use, and this has implications for clinical trials of integrin inhibitors in the context of both anti-angiogenic therapy and also vascular normalisation. Therapies that perform well in homogenous tumour models often fail in heterogeneous patient groups. Where patients cannot be accurately stratified based on integrin expression levels, it is difficult to determine which patients are good candidates for therapy. Similarly, it is difficult to measure the effect of such drugs, particularly in the context of the brain. These issues highlight the need for sensitive, specific, and reproducible imaging of the angiogenic vasculature in tumours.

To facilitate molecular imaging, whilst allowing for multi-parametric imaging in a limited clinical imaging appointment, a number of integrin $\alpha_v\beta_3$ targeted MRI contrast agents have been developed[339]. MRI has the advantage of enabling spatially localised data on tumour structure, diffusion, metabolism and angiogenesis to be collected in a single session. Molecular MRI strategies that have previously been used to image angiogenesis include the conjugation of integrin $\alpha_v\beta_3$ antibodies or various RGD peptides to paramagnetic gadolinium containing liposomes[198,340-343], perfluorocarbon based nanoparticles[344-347], or lipoprotein cores[348]. However, the clearance rates, specificity, and SNR of these particles remained low, so focus has turned to alternative approaches.

Currently, a large amount of research is focussed on the development of super-paramagnetic iron oxide nanoparticles (SPIONs) and ultra-small particles of iron oxide (USPIO), which are already in use for non-molecular applications such as

cerebral blood volume imaging, both clinically[349] and pre-clinically[350]. USPIO have also been used to measure tumour blood volume, and can detect angiogenic hotspots in preclinical models[266,351]. Dual-contrast imaging, using both gadolinium and USPIO, can also be used to detect mismatch between perfusion and blood volume in brain tumours[352]. Integrin $\alpha_v\beta_3$ targeting of USPIO has been achieved[353-357], and in some studies with sufficient SNR to be detected on a clinical scanner[358,359]. In preclinical studies, this approach has enabled differentiation between integrin $\alpha_v\beta_3$ expressing angiogenic blood vessels and integrin $\alpha_v\beta_3$ overexpressing tumour cells[358], and prediction or measurement of response to treatment[355,360]. Genetically tailored nanoparticle sized magnetoliposomes produced in bacteria have also been reported with RGD targeting to successfully image angiogenesis in glioma[361], although the complicated production method does not lend itself well to clinical translation. Despite the increased sensitivity compared to gadolinium-based molecular imaging agents, the small size of USPIO means that they are able to extravasate into the extracellular space, and also have a long half-life in the blood (~16.5 hours)[193], both of which increase non-specific signal and decrease sensitivity[362-364].

For this reason, cyclic-RGD conjugated microparticles of iron oxide (MPIO) are being developed. The size of the particles (1 μm diameter) is larger by orders of magnitude than USPIO, which confers a shorter half-life in the blood of ~1 min[193,195,365] and prevents extravasation[366,367], thereby increasing specificity. It has been shown, using well-characterised molecularly targeted iron oxide particles, that micron sized particles show more specific and sensitive binding than the equivalent USPIO (~5-50 nm)[193]. Because of this increased sensitivity and specificity, MPIO are used in preference to USPIO in the current study.

MPIO have been used successfully in pre-clinical studies to image a variety of different disease states. The use of vascular cell adhesion molecule 1 (VCAM-1) antibodies, conjugated to MPIO, has enabled imaging of atherosclerosis[368], acute neuro-inflammation[193,366], vascular dementia[276], cerebral ischemia[272], multiple sclerosis[275], brain metastasis[166], and other neurological conditions. A similar study using VCAM-1 targeted MPIO has shown that brain metastases are closely associated with the brain vasculature, and that micrometastases can be detected using targeted MPIO contrast agents[166]. MPIO targeted with antibodies to other cell adhesion molecules (CAMs) including p-selectin[273,368,369] and ICAM-1[271] have also been developed. As MPIO contain a higher payload of iron than USPIO, they produce a larger dephasing effect[370,371]. It has been shown that a single microparticle of iron oxide or a single MPIO labelled cell can be detected at relevant pre-clinical field strengths[276,371], which makes them ideal for detecting small amounts of endothelial target expression. The recent development of peptidase-degradable MPIO[372] also allows for molecular imaging using MPIO to be translated clinically, where preclinical studies are successful.

Recently, it has been shown that using the integrin $\alpha_v\beta_3$ targeting peptide RGD, RGD-MPIO can be used successfully to detect integrin $\alpha_v\beta_3$ expression in subcutaneous models of melanoma and colon cancer[195]. The RGD-MPIO were found to bind specifically to endothelial cells, and were highly correlated with integrin $\alpha_v\beta_3$ expression. In the brain, it has been shown that integrin $\alpha_v\beta_3$ is expressed on angiogenic blood vessels, but not on normal quiescent brain vasculature[204].

On the basis of the above findings, the aim of the current study was to determine the potential for targeting integrin $\alpha_v\beta_3$ expression in brain metastasis in order to

image angiogenesis. The development of imaging biomarkers, including new molecular contrast agents, should follow the CRUK/EORTC recommendations[190], including biological validation through correlation of imaging and pathology. The use of 3D imaging is also recommended, so as to examine the entirety of the tumour. Thus, the major aim of this chapter was to develop and validate targeted microparticles of iron oxide (MPIO) for visualisation of angiogenesis by MRI.

Therefore, the specific objectives of this chapter are:

1. To assess the expression of integrin $\alpha_v\beta_3$ in a mouse model of brain metastasis, and to determine the extent of expression on the neovasculature. The specific hypothesis is that integrin $\alpha_v\beta_3$ expression will increase at later timepoints and in larger tumours.
2. Measure the binding efficacy of various cyclic-RGD conjugated MPIO *in vitro* under physiological flow conditions to ensure adequate integrin $\alpha_v\beta_3$ binding and selectivity, and to determine the optimal peptide configuration for use in mice.
3. To determine whether RGD-MPIO enable detection of the switch from co-optive to angiogenic tumour growth in brain metastasis *in vivo*. The specific hypothesis is that RGD-MPIO will bind to angiogenic blood vessels at later timepoints, and this will correlate with integrin $\alpha_v\beta_3$ expression as measured by histology.

4.2 Methods

4.2.1 Expression of integrin $\alpha_v\beta_3$ in brain metastasis

In order to quantify angiogenic marker expression, 4T1-GFP experimental brain metastases were induced as described in Chapter 2.3.2, and tumour-bearing brains were harvested at days 7 (n = 4), 14 (n = 6), 21 (n = 3), 28 (n = 4), or 35 (n = 4). A primary brain tumour model, U87 glioma, which is highly angiogenic[64,181], was used as a positive control, at day 28 (n = 3). As a control group, mice (n = 3) underwent intracerebral injection of 0.5 µL sterile PBS, and brains were harvested at day 7.

Consecutive sections were stained for integrin $\alpha_v\beta_3$ as an angiogenic marker, CD31 as a marker of blood vessels, and TIE2 as a further marker of angiogenesis. Primary and secondary antibody combinations used for immunohistochemistry are described in Chapter 2.4.1. For integrin $\alpha_v\beta_3$, the mouse on mouse protocol described in Chapter 2.5.2 was used. For CD31 and TIE2 immunohistochemistry, the standard protocol described in Chapter 2.5.1 was used.

Slides were scanned with a Leica Biosystem ScanScope CS2 (Aperio, ePathology Solutions, Milton Keynes, UK), with 20x magnification images acquired. Images were analysed using Image Scope software (ePathology Solutions, Milton Keynes, UK). For each section on the slide, the tumour (or ipsilateral striatum for control animals) was manually segmented (Figure 4.1A) and the 'Positive Pixel Count 2004-08-11' algorithm run to return the number of positive pixels that were moderately or strongly stained (Figure 4.1B-C). For CD31, the contralateral striatum was also analysed so the number of blood vessels could be compared.

An automated algorithm was used to identify stained pixels. For integrin $\alpha_v\beta_3$ and CD31 the parameters used were: moderately stained pixel intensity between 202 and 185, and strongly stained pixel intensity lower than 10. For TIE2 the parameters used were: moderately stained pixel intensity between 101 and 51, and strongly stained pixel intensity lower than 51.

Group-wise differences in immunohistochemistry were assessed statistically using the Kruskal-Wallis one-way ANOVA, with Dunn's multiple comparison test post-hoc. For CD31, differences between the tumour and contralateral hemispheres were assessed using a two-way paired ANOVA with factors of timepoint and hemisphere, and Bonferroni's multiple comparison tests post-hoc.

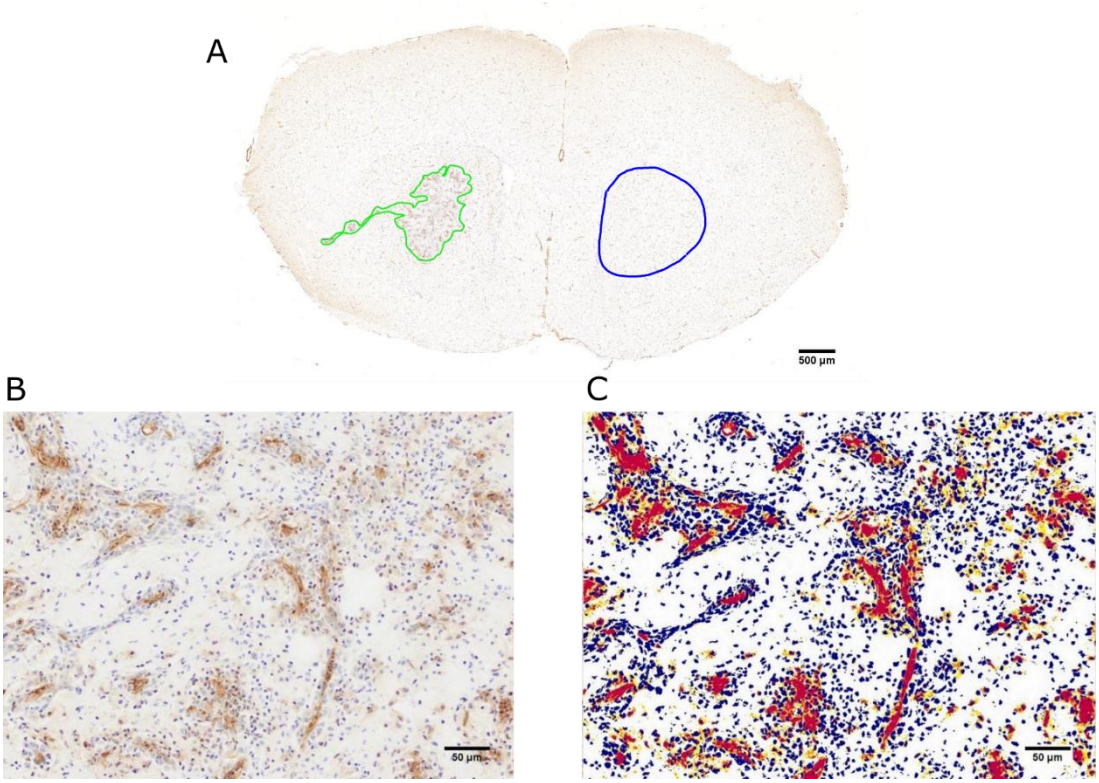


Figure 4.1: Example of quantification of immunohistochemistry in a CD31 stained section. (A) Whole brain section at the level of the striatum. Cell nuclei are stained purple with Cresyl Violet, and CD31 is stained brown with DAB. The tumour is manually segmented (green) to allow measurement of the area, and the contralateral striatum is also manually segmented and analysed as an internal control. (B) Inset of tumour area at 20x magnification. Cell nuclei are stained purple with Cresyl Violet, and CD31 is stained brown with DAB. (C) Output of the 'Positive Pixel Count 2004-08-11' quantification algorithm on the tissue section shown in (B). Red indicates strongly stained pixels, yellow indicates moderately stained pixels, and purple indicates Cresyl violet stained (negatively stained) pixels. The areas of each colour are compared between groups.

4.2.2 Co-localisation of angiogenic markers with blood vessels

Sections were co-stained for integrin $\alpha_v\beta_3$ and CD31 to determine the percentage of blood vessels that are angiogenic. Consecutive sections were also co-stained for TIE2 and CD31. Primary and secondary antibody combinations and the fluorophores used are described in Chapter 2.5.2.

Frozen sections were thawed for 20 min at room temperature and washed with PBS. Sections were then quenched with 1% v/v of 30% w/v hydrogen peroxide in PBS and blocked with Tris-NaCl Blocking buffer (TNB) for 1 hour. Sections were incubated with primary antibodies in PBS at 4ºC overnight. Sections were then washed with PBS and incubated with secondary antibodies for 45 min. All steps after this point were performed in darkness. Slides were washed and then incubated in fluorophore. Slides were washed again, then mounted and cover-slipped in DAPI-free Vectorshield mounting medium for 4T1-GFP cells, or in Vectorshield mounting medium with DAPI for U87 cells. Positive and negative control slides for each antibody were also stained concurrently.

Slides were examined using a confocal microscope (Leica SP8) at 20x magnification, and three areas of tumour were examined per animal. A z-stack image was acquired through the entire focal plane (approximately 10 µm) using lasers at wavelengths 405 nm (blue), 448 nm (green) and 552 nm (red). Images were acquired with a resolution of 0.57 µm in a 581.25 μm^2 FOV, using a line-sequential sequence, bi-directional acquisition and 4 line averages.

The acquired images were loaded into ImageJ, and an in-house plug-in was used to analyse the co-localisation of pixels in each channel. The threshold used for each channel was 30.

Group-wise differences were assessed statistically using the Kruskal-Wallis one-way ANOVA, with Dunn's multiple comparison test post-hoc.

4.2.3 *In vitro* binding of RGD-MPIO to integrin $\alpha_v\beta_3$

To measure the binding of RGD-MPIO to integrin $\alpha_v\beta_3$ under flow conditions, glass capillaries were mounted onto a narrow-gauge syringe with dry-cure glue. Each glass capillary was functionalised by firstly filling and incubating with a mixture of o-Xylene/TEGOPS/DIPEA at 1000:320:10 for 17 hours at 80° with phosphorous pentoxide. Capillaries were then washed with o-xylene and methanol, and dried for 4 hours at room temperature under vacuum conditions. Subsequently, capillaries were filled with a solution of PBS containing 200 ng/mL mouse integrin $\alpha_v\beta_3$ (7889-AV-050, R&D Systems, Abingdon, UK) and incubated at room temperature for 24 hours. Remaining functional groups were quenched with 10 mM ethanolamine for 24 hours at room temperature. Control capillaries were filled with 200 ng/mL BSA and incubated as above. Capillaries were then washed with PBS-T and PBS, and stored filled with PBS at 4°C.

The binding efficiency of various RGD peptides has been measured previously for human integrin $\alpha_v\beta_3$, but not for mouse integrin $\alpha_v\beta_3$. Thus, we tested the binding of three different RGD cyclic peptides, and one control scrambled RDG peptide (structures described in Chapter 2.5), to mouse integrin $\alpha_v\beta_3$. These peptides were conjugated separately to MPIO as described in Chapter 2.5.1.

Capillaries were mounted under a Nikon TE 2000-U microscope, and 5 µL of RGD-MPIO or control RDG-MPIO was resuspended in 200 µL of 30% sucrose in PBS to mimic the viscosity of blood. The sucrose-MPIO solution was infused, using a syringe pump, at 14 rpm to mimic shear conditions in blood vessels. The volume

of solution and infusion time were recorded in order to calculate flow rates retrospectively. Photomicrographs were taken across 8 separate FOV along the capillary, and the number of bound MPIO per FOV was counted.

Group-wise differences were assessed statistically using a two-way ANOVA with factors of MPIO and capillary coating, and Bonferroni's multiple comparison tests were carried out post-hoc.

4.2.4 *In vivo* detection of angiogenic vessels using RGD-MPIO

In order to detect angiogenic vessels *in vivo* in brain metastases, experimental 4T1-GFP brain metastases were induced as described in Chapter 2.3.2, and each mouse was imaged once using RGD-MPIO (peptide PP785) at day 7 (n = 3), 14 (n = 3), 21 (n = 3), 28 (n = 3), or 35 (n = 3). Further mice were also imaged using a control RDG-MPIO (peptide PP787) at day 7 (n = 3), 14 (n = 3), 21 (n = 2), 28 (n = 3), or 35 (n = 2).

Mice injected with U87 glioma cells as a positive control were imaged at day 28 with the RGD-MPIO (n = 3), or the control RDG-MPIO (n = 3). Mice injected with 0.5 µL sterile PBS as a negative control were imaged at day 7 using RGD-MPIO (n = 3).

Experiments were performed using a 9.4 T MRI spectrometer (Agilent Technologies, Yarnton, UK) with a 26 mm internal diameter volume transmit-receive birdcage RF coil (Rapid Biomedical GmbH, Rimpar, Germany). Mice were anaesthetised with 3% isoflurane in 30% O_2 : 70% N_2, and had a cannula implanted in the lateral tail vein and flushed with 0.9% heparinised saline prior to positioning in the volume coil. Mouse temperature was monitored and maintained at 37 ± 0.5°C

with a rectal probe and heating blanket feedback system. Respiration was monitored using a pressure balloon, and breathing rate was maintained at approximately 60 breaths per minute by adjusting isoflurane concentration; stable breathing was typically maintained with an isoflurane concentration of 1.2 – 1.5%. The imaging session consisted of T_1- and T_2-weighted anatomical imaging, pre- and post-MPIO injection MGE3D scans, and a gadolinium-enhanced T_1-weighted scan.

A pre-contrast MGE3D scan was performed as described in Chapter 2.6.3. During this time, the RGD- or control RDG-MPIO, as appropriate, were prepared for injection at a dose of 4 mg/kg Fe in 100 µL sterile saline. Immediately prior to injection, the MPIO were vortexed for 2 min and sonicated for 2 min to reduce particle clumping. The mouse was removed from the magnetic field, but remained anaesthetised and positioned inside the volume coil. The particles were injected through the tail vein cannula, with the mouse remaining outside the magnetic field to prevent particles clumping in the needle hub or dropping out of solution in the cannula. A 20 min dummy scan was run during this time to prevent field drift from gradient cooling. The mouse was then repositioned back in the magnetic field, and a post-contrast MGE3D scan carried out. Subsequently, with the mouse remaining inside the magnet, 30 µL of Gadodiamide (Omniscan, GE Healthcare) was injected through the cannula, and after 5 min a post-gadolinium T_1 weighted scan was acquired to assess blood-brain barrier (BBB) breakdown. Following the imaging session, brains were harvested and tissue stored as described in Chapter 2.3.3.

The MGE3D raw images were processed using in-house Matlab code. Magnitude images were reconstructed for each echo, and the final MGE3D images were reconstructed using the square root of sum of squares (SqrtSOS) algorithm for

individual echoes. A segmentation mask for the striatum was created for each mouse. Pre- and post-contrast masks were created for each animal as the movement out of the magnetic field to facilitate the injection may result in a slight discrepancy of positioning between scans, resulting in a lack of co-registration.

For the contralateral (normal) striatum, the mean signal intensity and standard deviation were calculated in Matlab. Any voxel with a signal intensity of more than 3 standard deviations below the mean was designated as hypointense, as shown in Figure 4.2. The volume of hypointense voxels in both the tumour-bearing and contralateral striatum was recorded. As the tumours contained naturally hypointense areas in the pre-injection datasets, all data are reported as the difference in hypointense voxels between the post- and pre-contrast scans (MPIO induced hypointense voxels).

In a number of tumours from both targeted and control groups (n = 3 RGD, n = 5 control RDG), the hypointense voxels in the tumour-bearing striatum of the pre-contrast image were more numerous than those in the post-contrast image. This resulted in a negative difference in post- minus pre-contrast hypointense voxels. Images were inspected to ensure no artefacts were present that would affect image quality, or any differences in SNR. In the absence of any technical basis for this observation, it was concluded that MPIO-induced hypointense voxels in these mice fall within the noise range of this technique, which has been calculated and reported in Chapter 4.3.4. Consequently, for further analysis those animals were assigned a value of zero MPIO-induced hypointense voxels rather than a negative value, which is impossible. For the positive control glioma model, three animals (n = 1 RGD-MPIO, n = 2 control RDG-MPIO) had a negative post- minus pre-contrast hypointensity value, and were allocated a zero value for analysis.

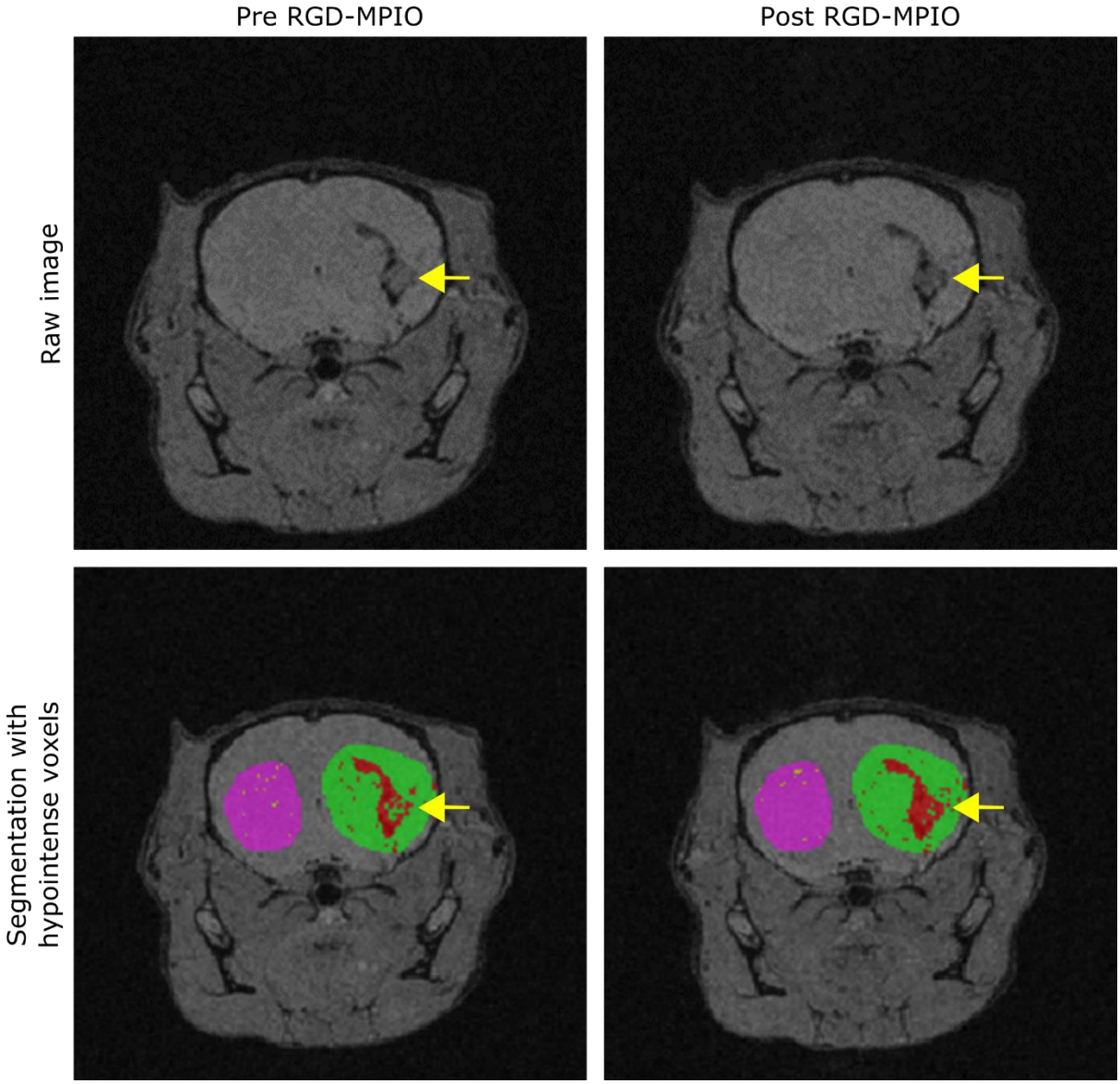


Figure 4.2: Representative pre- and post- RGD-MPIO injection images acquired at day 35. Arrows denote the core tumour area. Segmentation shows the contralateral striatum in pink, and the tumour bearing striatum in green. Hypointense voxels with signal intensity more than 3 standard deviations below the mean of the contralateral striatum are highlighted in red.

Group-wise differences between the tumour and contralateral hemispheres were assessed statistically using a two-way paired ANOVA with factors of timepoint and hemisphere, and Bonferroni's multiple comparison tests post-hoc. Group-wise differences between enhancing and non-enhancing tumours were assessed using a one-way ANOVA with Tukey's multiple comparison tests post-hoc.

4.2.5 Histological examination of MPIO in the brain

In order to visualise MPIO in the tumour tissue, Perl's Prussian blue staining was conducted as per the protocol described in Chapter 2.5.3 on tumour sections prepared as described in Chapter 2.3.4. The amount of Prussian blue was quantified by manual counting of the blue beads in each tumour area.

4.3 Results

4.3.1 Expression of integrin $\alpha_v\beta_3$ in brain metastasis

Immunohistochemical staining was carried out to assess for the presence and quantity of integrin $\alpha_v\beta_3$ in metastatic tumours. A second angiogenic marker, TIE2, was used to confirm the presence of angiogenic vessels, and microvessel density was also examined as a further marker of angiogenesis. Examples of immunohistochemical staining of tumour sections at each timepoint are shown in Figure 4.3, along with immunofluorescence in Figure 4.4.

The tumour area was measured from the manual segmentation of the infiltrating tumour margins on the CD31 stained slides, and is shown in Figure 4.5. The tumour area was measured as an average of the area of all tumour containing sections out of the 10 sections on the slide, spanning approximately 500 µm of the brain. In smaller tumours, this encompassed the entire tumour, whilst in larger tumours the approximate midpoint of the tumour (anterior-posterior) was analysed. The average tumour area per section was 0.42 ± 0.31 mm^2 at day 7, 0.37 ± 0.31 mm^2 at day 14, 0.51 ± 0.42 mm^2 at day 21, 0.76 ± 0.96 mm^2 at day 28, and 1.30 ± 1.52 mm^2 at day 35.

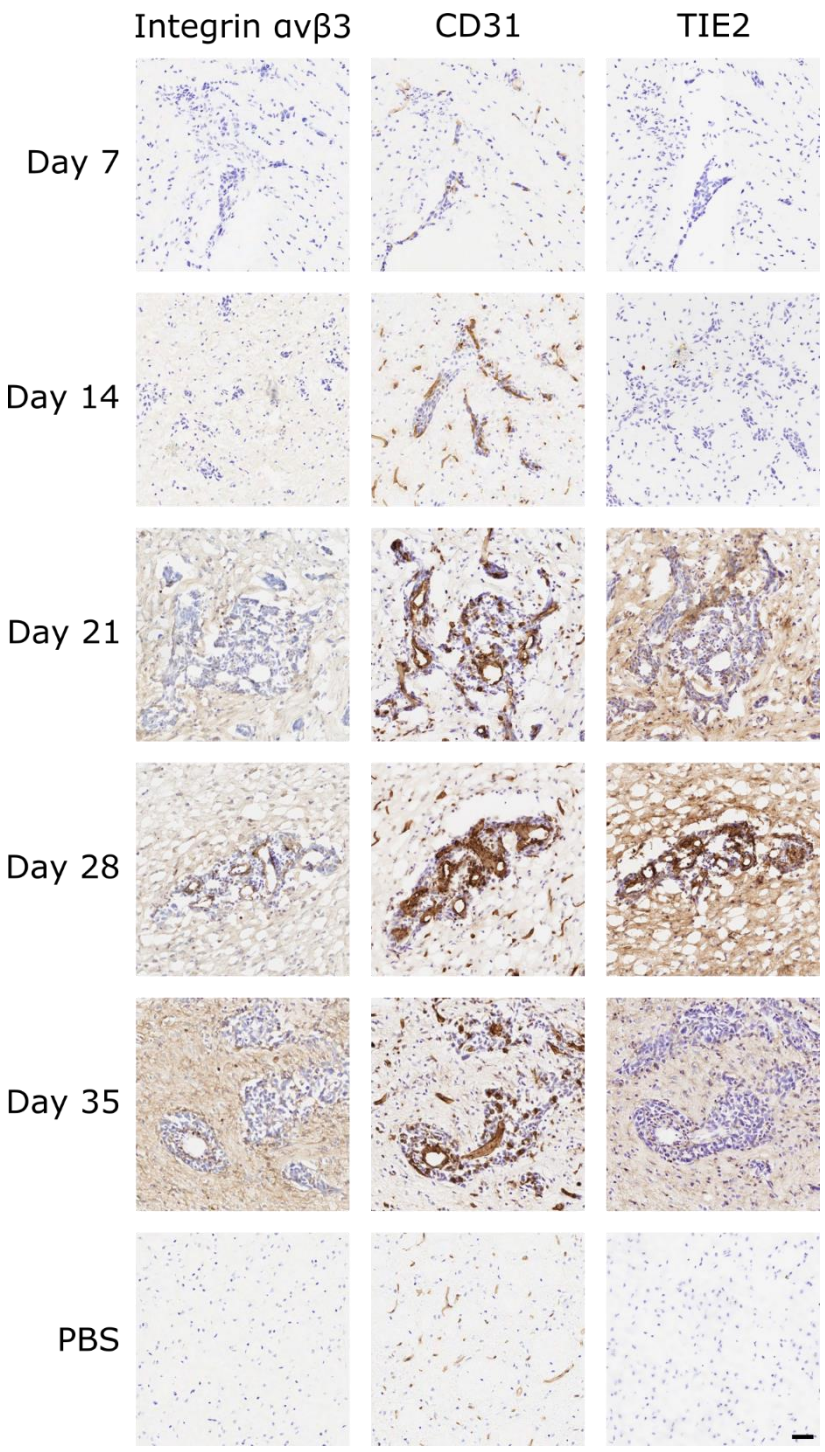


Figure 4.3: Example histology of angiogenic markers integrin $\alpha_v\beta_3$, CD31, and TIE2 at each timepoint in the 4T1-GFP metastasis model. Each marker is visualised on consecutive sections with DAB (brown), and nuclei are counterstained with cresyl violet (purple). Scale bar indicates 15 µm in all images.

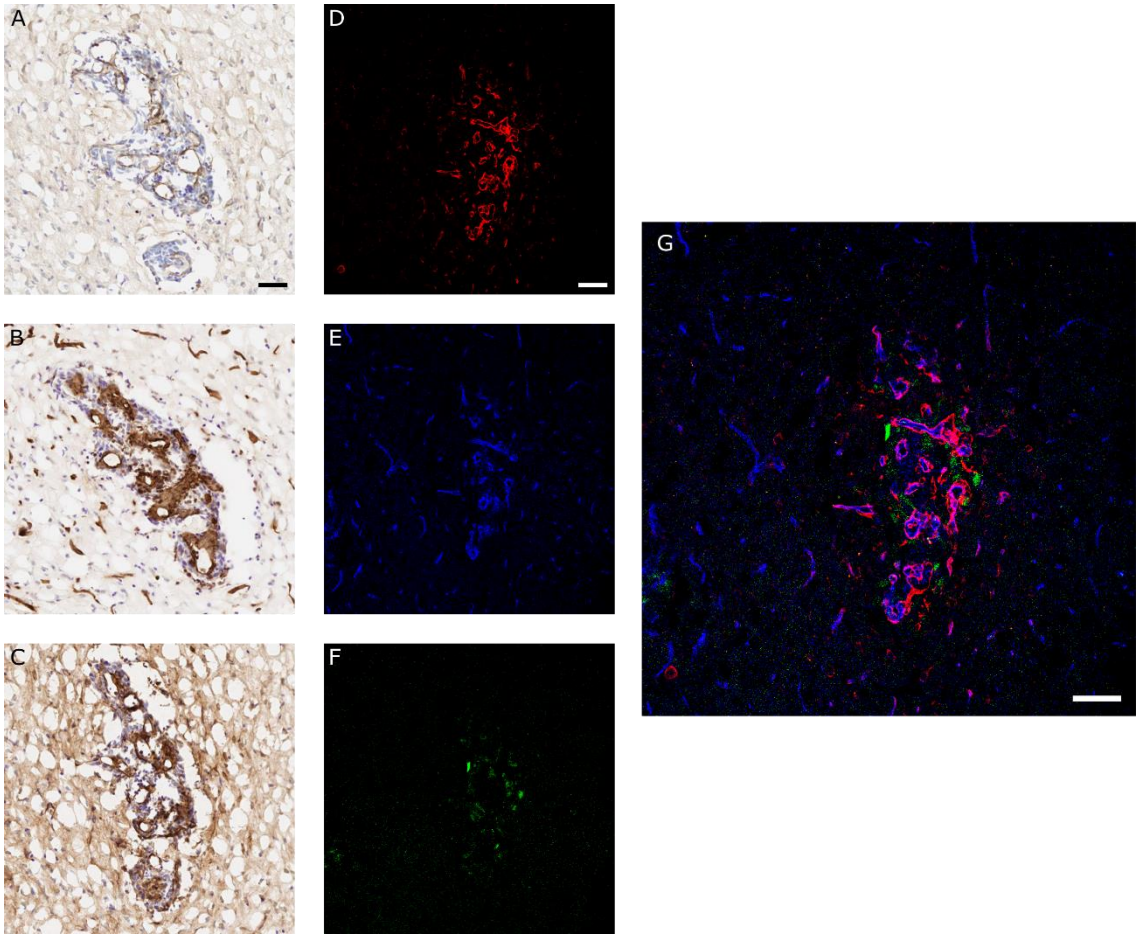


Figure 4.4: Consecutive sections of 4T1-GFP tumour at the day 28 timepoint. Immunohistochemistry is visualised on consecutive sections with DAB (brown), and nuclei are counterstained with cresyl violet (purple). Sections are stained for (A) integrin $\alpha_v\beta_3$, (B) blood vessel marker CD31, and (C) TIE2. Immunofluorescence is visualised for (D) integrin $\alpha_v\beta_3$ (red channel), (E) blood vessel marker CD31 (blue channel), and (F) GFP positive 4T1 metastatic murine mammary carcinoma tumour cells. (G) Merged channels showing co-localisation of integrin $\alpha_v\beta_3$ with blood vessels.

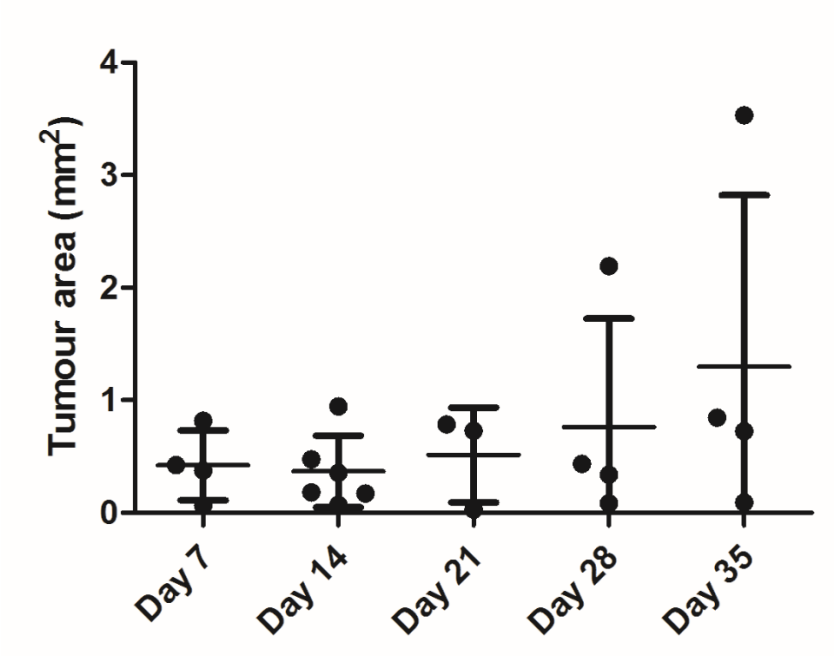


Figure 4.5: Graph showing average tumour area at each timepoint, as measured by manual segmentation of tumour margins. Day 7 (n = 4), 14 (n = 6), 21 (n = 3), 28 (n = 4), and 35 (n = 4) timepoints are shown. Error bars indicate mean ± standard deviation, and each data point indicates the average tumour area for one animal.

Expression of integrin $\alpha_v\beta_3$ as a percentage of tumour area was 0.0050 ± 0.0032% in the PBS injected control group, 0.22 ± 0.13% at day 7, 0.38 ± 0.46% at day 14, 4.50 ± 2.04% at day 21, 5.16 ± 6.84% at day 28, and 9.05 ± 9.00% at day 35. A significant increase in integrin $\alpha_v\beta_3$ total stained area as a percentage of tumour area, compared to control PBS injected animals, was evident at days 21, 28 and 35 (Kruskal-Wallis test $p < 0.01$, post-hoc $p < 0.05$, Figure 4.6A).

For integrin $\alpha_v\beta_3$, the positive vessel count was 0.72 ± 0.46 in the PBS injected control group, 20.94 ± 14.10 at day 7, 8.52 ± 7.30 at day 14, 12.50 ± 9.36 at day 21, 28.54 ± 26.50 at day 28, and 66.69 ± 85.10 at day 35. A significant increase in integrin $\alpha_v\beta_3$ positive vessels, compared to control PBS injected animals, was evident at days 28 and 35 (Kruskal-Wallis test $p < 0.05$, post-hoc $p < 0.05$, Figure

4.6B). Analysis of integrin $\alpha_v\beta_3$ positive vessels compared to tumour size showed a significant positive correlation ($p < 0.0001$, $R^2 = 0.88$, Pearson's coefficient, Figure 4.7A). Comparison of integrin $\alpha_v\beta_3$ positive vessels with CD31 positive vessels also showed a significant positive correlation ($p < 0.001$, $R^2 = 0.46$, Pearson's coefficient, Figure 4.7B).

Expression of integrin $\alpha_v\beta_3$ was also significantly increased in the positive control U87 glioma tumours (5.64 ± 2.82%), for total stained area (t-test, $p < 0.01$, Figure 4.6A) when compared to PBS.

Expression of TIE2 as a percentage of tumour area was 0.0035 ± 0.0013% in the PBS injected control group, 0.30 ± 0.33% at day 7, 0.74 ± 0.66% at day 14, 0.51 ± 0.12% at day 21, 4.52 ± 4.06% at day 28, and 3.53 ± 6.52% at day 35. A trend towards an increase in TIE2 total stained area as a percentage of tumour area, compared to control PBS injected animals, was evident at later timepoints, but was not statistically significant (Kruskal-Wallis test $p = 0.07$, Figure 4.6C).

For TIE2, the positive vessel count was 1.89 ± 0.19 in the PBS injected control group, 20.04 ± 13.53 at day 7, 21.09 ± 26.90 at day 14, 37.23 ± 29.84 at day 21, 90.23 ± 101.00 at day 28, and 116.10 ± 107.20 at day 35. A significant increase in TIE2 positive vessels, compared to control PBS injected animals, was evident at day 28 and 35 (Kruskal-Wallis test $p < 0.05$, post-hoc $p < 0.05$, Figure 4.6D). Analysis of TIE2 positive vessels compared to tumour size showed a significant positive correlation ($p < 0.0001$, $R^2 = 0.85$, Pearson's coefficient, Figure 4.7C). Comparison of TIE2 positive vessels with CD31 positive vessels also showed a significant positive correlation ($p < 0.005$, $R^2 = 0.41$, Pearson's coefficient, Figure 4.7D). Similarly, comparison of integrin $\alpha_v\beta_3$ positive vessels with TIE2 positive

vessels also showed a significant positive correlation ($p < 0.0001$, $R^2 = 0.75$, Pearson's coefficient, Figure 4.7E).

Expression of TIE2 was also significantly increased in the positive control U87 glioma tumours (4.99 ± 1.55%), for total stained area (t-test, $p < 0.001$, Figure 4.6C) when compared to PBS.

For CD31, in the control PBS injected animals, 1.55 ± 0.67% of the ipsilateral striatum was positively stained, compared to 1.50 ± 0.8% of the contralateral striatum. In the tumour model, 5.64 ± 1.56% of the tumour was stained at day 7, 7.74 ± 2.99% of the tumour was stained at day 14, 17.14 ± 6.61% of the tumour was stained at day 21, 24.16 ± 14.54% of the tumour was stained at day 28, and 12.78 ± 6.88% of the tumour was stained at day 35. Analysis of the stained area as a percentage of tumour area, compared to the percentage of stained area in the contralateral striatum, showed a significant effect of both hemisphere (2-way paired ANOVA, $p < 0.0001$) and timepoint (2-way paired ANOVA, $p < 0.01$, Figure 4.6G). Bonferroni multiple comparison post-hoc tests showed significant differences between ipsi- and contralateral hemispheres at days 21 ($p < 0.05$), 28 ($p < 0.001$) and 35 ($p < 0.05$).

For CD31 vessel counts, in the control PBS injected animals, there were 322.5 ± 62.9 vessels per mm^2 in the ipsilateral striatum, compared to 322.8 ± 44.1 vessels in the contralateral striatum. In the tumour model, there were 468.7 ± 91.6 vessels per mm^2 in the tumour at day 7, 408.9 ± 76.2 vessels per mm^2 in the tumour at day 14, 704.2 ± 103.8 vessels per mm^2 in the tumour at day 21, 605.9 ± 139.5 vessels per mm^2 in the tumour at day 28, and 671.6 ± 353.8 vessels per mm^2 in the tumour at day 35. Analysis of these results showed a significant effect of both hemisphere

(2-way paired ANOVA, $p < 0.0001$) and timepoint (2-way paired ANOVA, $p < 0.05$, Figure 4.6H). Bonferroni multiple comparison post-hoc tests showed significant differences between ipsi- and contralateral hemispheres at days 21 ($p < 0.05$) and 35 ($p < 0.05$).

Expression of CD31 was also significantly increased in the U87 glioma tumours, in both total stained area (11.19 ± 4.32%) compared to contralateral hemisphere (2.34 ± 1.13%, paired t-test, $p < 0.05$, Figure 4.6G); and vessel counts per mm^2 (777.3 ± 165.6) when compared to the contralateral hemisphere (331.0 ± 50.1, paired t-test, $p < 0.05$, Figure 4.6H).

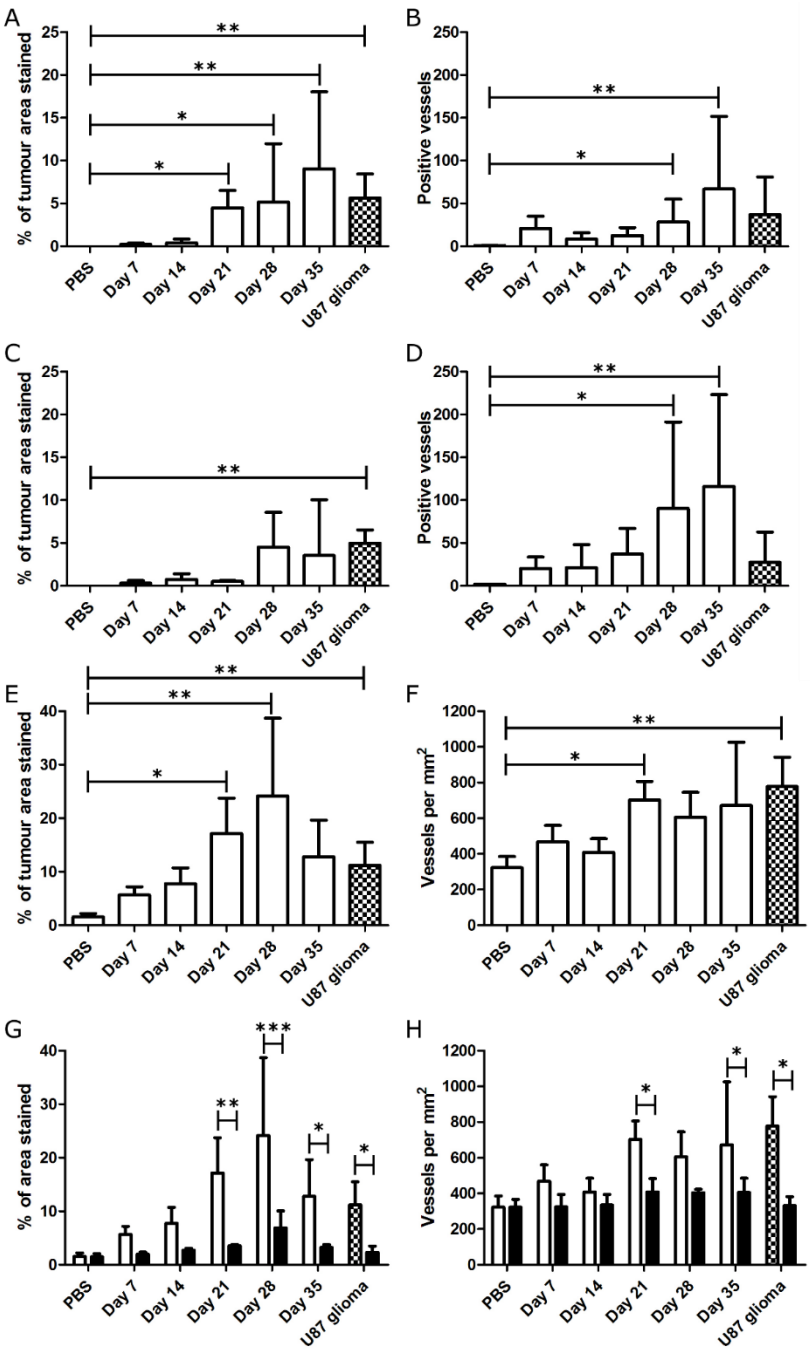


Figure 4.6: Analysis of angiogenic markers in 4T1-GFP and U87 tumours by immunohistochemistry. Quantification of (A) integrin $\alpha_v\beta_3$ and (C) TIE2 total stained area as a percentage of tumour area; and (B,D) as positively stained vessels, is shown for each timepoint. (E) Quantification of CD31 total stained area as a percentage of tumour area. (F) Microvessel density of the tumour at each timepoint. (G) Comparison of CD31 total stained area as a percentage of tumour area in the tumour (white bars) and the contralateral striatum (black bars). (H) Comparison of microvessel density in the tumour (white bars) and the contralateral striatum (black bars). PBS control (n = 3), day 7 (n = 4), 14 (n = 6), 21 (n = 3), 28 (n = 4), and 35 (n = 4) timepoints are shown, along with a day 28 timepoint for the U87 glioma (n = 3). Error bars represent standard deviation, *p < 0.05, **p < 0.01, ***p < 0.001.

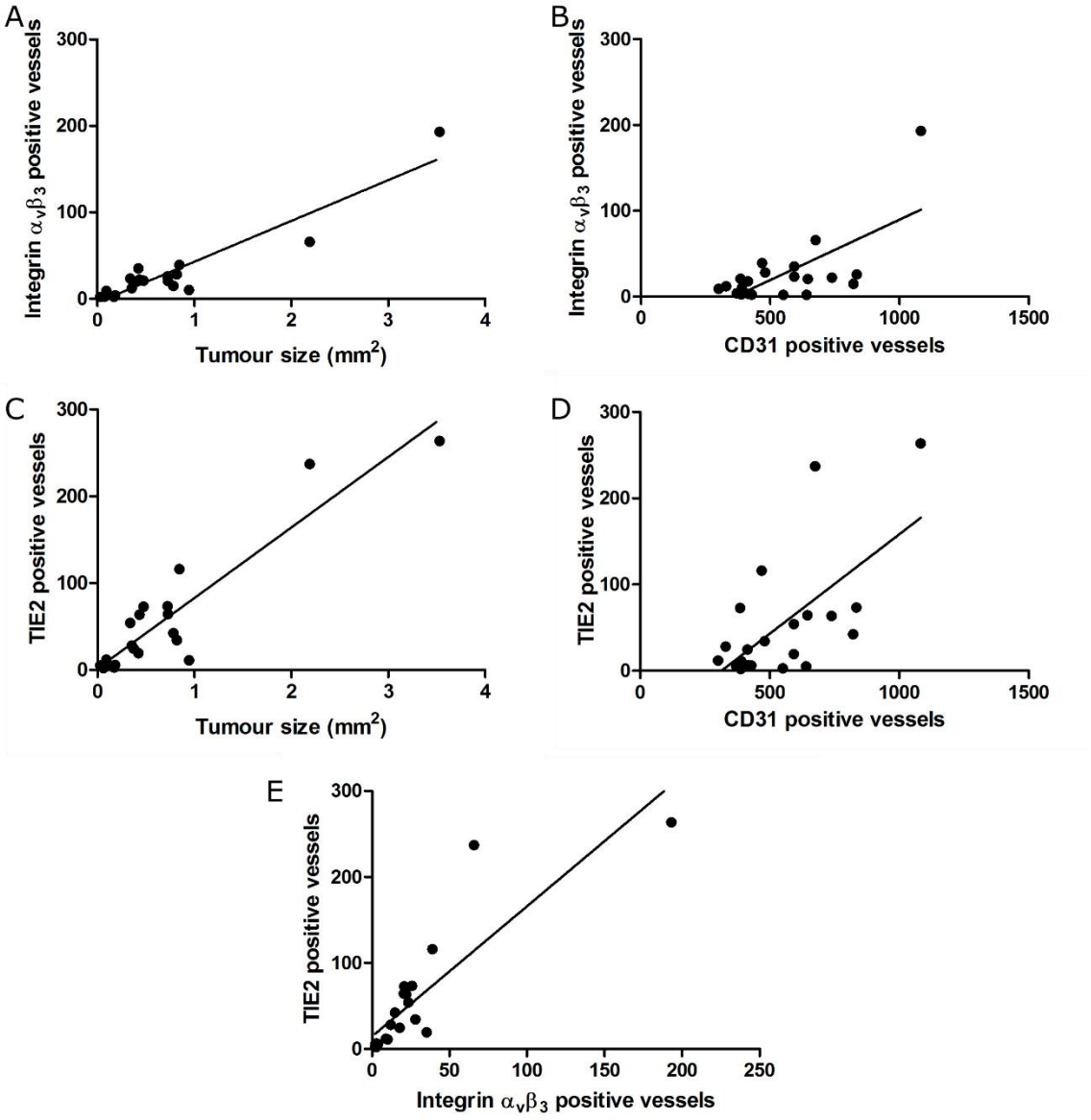


Figure 4.7: Correlation analysis for angiogenic marker expression. (A) Integrin $\alpha_v\beta_3$ positive vessels are positively correlated with tumour size (Pearson's coefficient $p < 0.0001$, $R^2 = 0.88$). (B) Integrin $\alpha_v\beta_3$ positive vessels are positively correlated with CD31 microvessel density (Pearson's coefficient $p < 0.001$, $R^2 = 0.46$). (C) TIE2 positive vessels are positively correlated with tumour size (Pearson's coefficient $p < 0.0001$, $R^2 = 0.85$). (D) TIE2 positive vessels are positively correlated with CD31 microvessel density (Pearson's coefficient $p < 0.005$, $R^2 = 0.41$). (E) Integrin $\alpha_v\beta_3$ positive vessels are positively correlated with TIE2 positive vessels (Pearson's coefficient $p < 0.0001$, $R^2 = 0.75$).

4.3.2 Co-localisation of angiogenic markers with blood vessels

In 4T1-GFP tumours, the number of pixels stained for angiogenic markers (integrin $\alpha_v\beta_3$ and TIE2) that co-localised with pixels stained for the blood vessel marker CD31 was analysed to provide a measure of the percentage of blood vessels that are angiogenic (Figure 4.8).

For integrin $\alpha_v\beta_3$, the percentage of co-localised pixels was 0.043 ± 0.068 for the PBS injected control group, 4.01 ± 1.60 at day 7, 0.99 ± 0.90 at day 14, 3.99 ± 1.61 at day 21, 2.00 ± 1.32 at day 28, and 4.09 ± 2.97 at day 35. A significant increase in co-localised pixels was found (Kruskal-Wallis test, $p < 0.01$, Figure 4.9A), and post-hoc tests showed significant differences at days 7, 21 and 35 compared to the PBS control group (post-hoc Dunn's test, $p < 0.05$). In U87 glioma, significant co-localisation (31.06 ± 22.07) was observed between integrin $\alpha_v\beta_3$ and CD31 when compared to the PBS control group (t-test, $p < 0.05$, Figure 4.9A)

For TIE2, the percentage of co-localised pixels was 0.45 ± 0.13 for the PBS injected control group, 3.18 ± .27 at day 7, 1.41 ± 0.73 at day 14, 6.92 ± 5.41 at day 21, 7.57 ± 5.76 at day 28, and 8.77 ± 6.67 at day 35. No significant differences between groups were found (Kruskal-Wallis test, $p = 0.06$, Figure 4.9B), although a trend towards increased co-localisation at later timepoints was observed. In the U87 glioma model, despite the presence of colocalised pixels and hence angiogenic vessels, this was again not statistically significant compared to PBS (t-test, $p = 0.055$, Figure 4.9B)

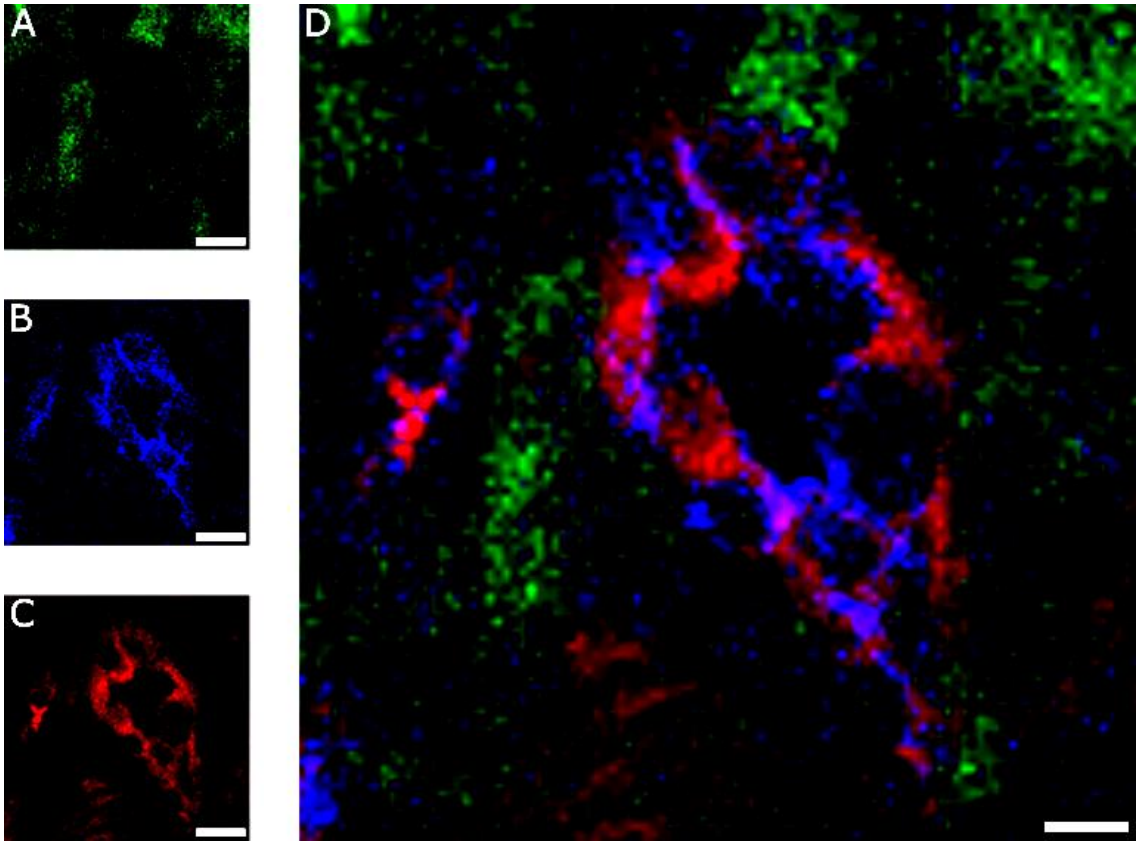


Figure 4.8: Fluorescent co-localisation of integrin $\alpha_v\beta_3$ and CD31 in a day 28 4T1-GFP tumour, showing (A) GFP positive 4T1 metastatic murine mammary carcinoma tumour cells in green, (B) CD31 staining of blood vessels in blue, (C) integrin $\alpha_v\beta_3$ in red, and (D) merged images. Scale bar represents 5 µm in all images.

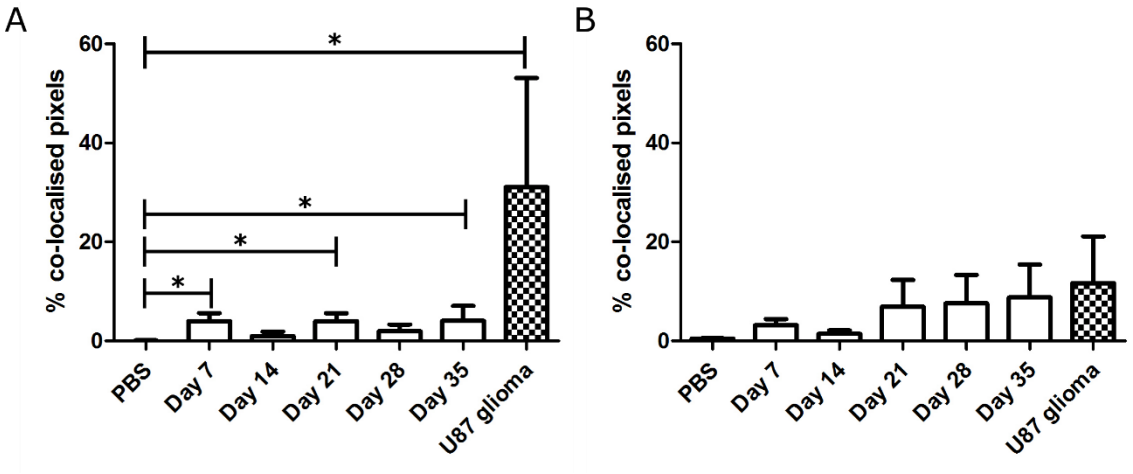


Figure 4.9: Analysis of angiogenic marker co-localisation with blood vessels in 4T1-GFP tumours at each timepoint. The percentage of blood vessels also expressing integrin $\alpha_v\beta_3$ (A) and TIE2 (B) are shown at each timepoint. Day 7 (n = 4), 14 (n = 6), 21 (n = 3), 28 (n = 4), and 35 (n = 4) timepoints are shown, along with a day 28 timepoint for the U87 glioma (n = 3). Error bars represent standard deviation, *p < 0.05.

4.3.3 *In vitro* binding of RGD-MPIO to integrin $\alpha_v\beta_3$

In order to determine binding efficacy of various RGD peptides to mouse integrin $\alpha_v\beta_3$, the number of binding events of RGD-MPIO to integrin $\alpha_v\beta_3$ per FOV in a glass capillary under flow conditions was measured. Each cyclic-RGD was tested in both integrin $\alpha_v\beta_3$ coated and negative control (BSA coated) capillaries (Figure 4.10). The cyclic-RGD PP785 showed the highest level of binding to integrin $\alpha_v\beta_3$ under flow conditions (flow rate 21.6 ± 1 µL/min).

Analysis of binding events across both capillaries showed an effect of both capillary (2-way ANOVA, $p < 0.0001$) and cyclic-RGD (2-way ANOVA, $p < 0.001$). Tukey's multiple comparison post-hoc tests showed significant differences between BSA and integrin $\alpha_v\beta_3$ coated capillaries for the PP001 ($p < 0.05$), PP785 ($p < 0.001$), and PP786 ($p < 0.001$) cyclic-RGD peptides (Figure 4.10). The control RDG peptide PP787 showed no significant difference in binding to BSA or integrin $\alpha_v\beta_3$ coated capillaries (Figure 4.10).

Analysis of binding events across the different peptides showed no significant differences between binding of the different RGD-MPIO to the BSA capillary (1-way ANOVA, $p > 0.05$). For the integrin $\alpha_v\beta_3$ capillary, the RGD peptide PP785 showed significantly higher binding compared to both the scrambled control RDG peptide PP787 (1 way ANOVA $p < 0.005$, Bonferroni's multiple comparison post-hoc test $p < 0.001$), and the other RGD-MPIO peptides PP001 (post-hoc $p < 0.01$) and PP786 (post-hoc test $p < 0.05$).

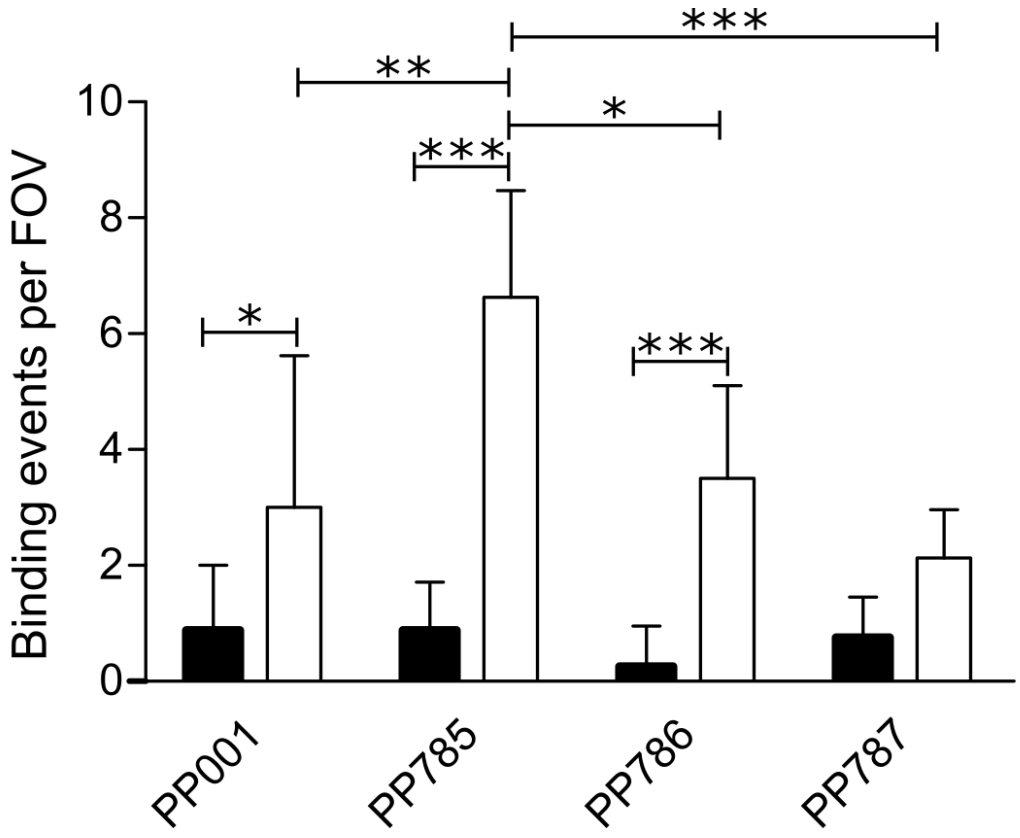


Figure 4.10: Binding of cyclic-RGD conjugated MPIO to integrin $\alpha_v\beta_3$ coated capillaries (white bars) under physiological flow conditions. Binding of MPIO to a BSA coated capillary (black bars) as a negative control was also measured. Error bars represent standard deviation (n = 8 FOVs per capillary and peptide), *p < 0.05, ***p < 0.001.

4.3.4 *In vivo* detection of angiogenic vessels using RGD-MPIO

Representative tumour images showing progression of MRI-detectable parameters in the 4T1-GFP model are shown for mice injected with RGD-MPIO in Figure 4.11, and in mice injected with control RDG-MPIO in Figure 4.12.

The noise level of the pre-contrast MGE3D imaging for detecting hypointense voxels was calculated. Analysis of the contralateral (non-tumour bearing) striatum in the pre-contrast images across all animals showed that 47 ± 31 voxels were more than 3 standard deviations below the mean of the striatum, and thus designated as hypointense (Figure 4.13). This is approximately 0.2% of the volume of the contralateral striatum. In the mice where more hypointense voxels were detected in the pre-contrast image than in the post-contrast image, the difference was within one standard deviation of the noise level, indicating that any differences lie within the noise range of this technique.

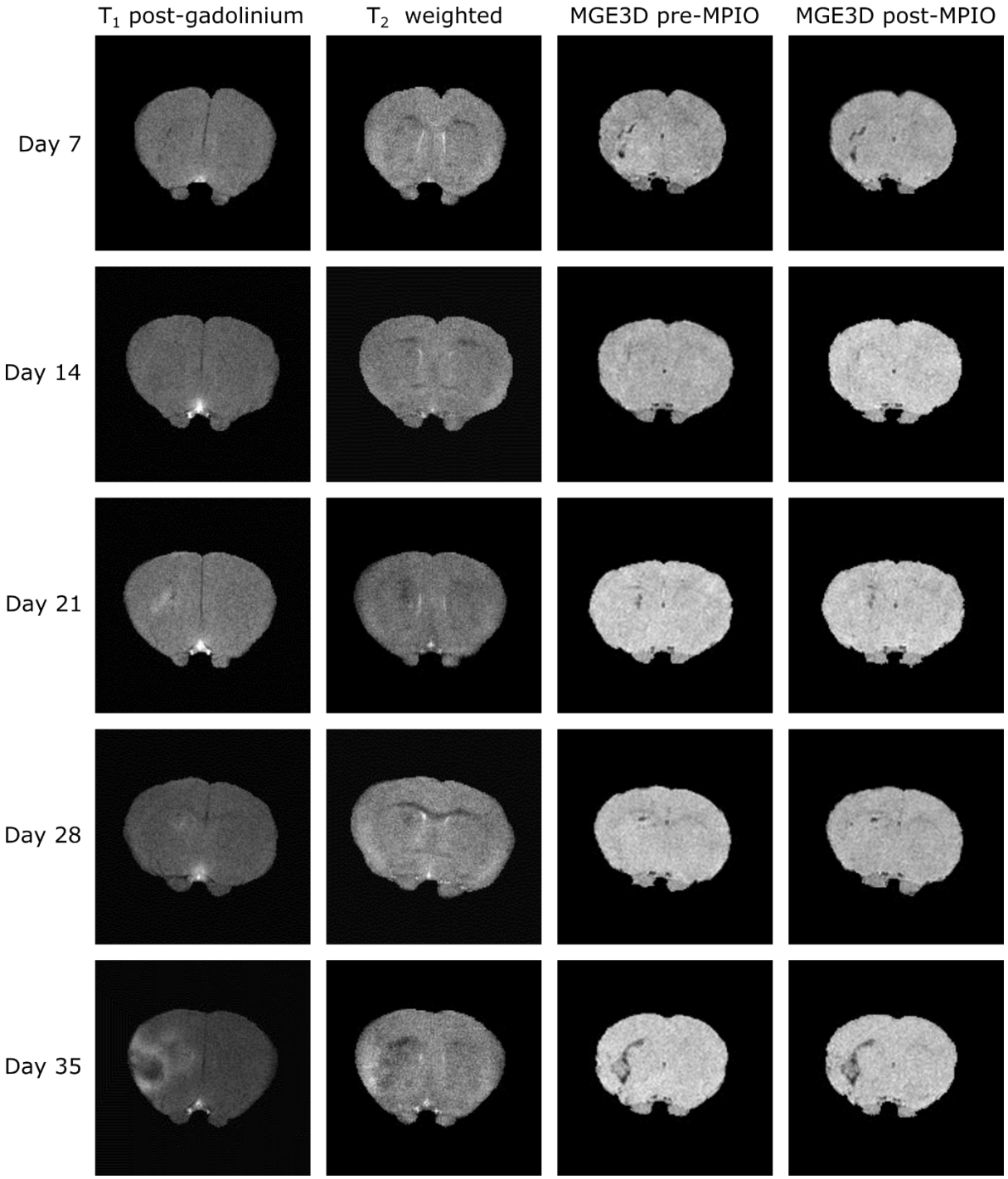


Figure 4.11: Representative images from animals for each timepoint in the 4T1-GFP model for mice injected with RGD-MPIO. Each column, from the left, shows T_1-weighted post-gadolinium images, T_2-weighted images, pre-RGD-MPIO MGE3D images, and post-RGD-MPIO contrast MGE3D images.

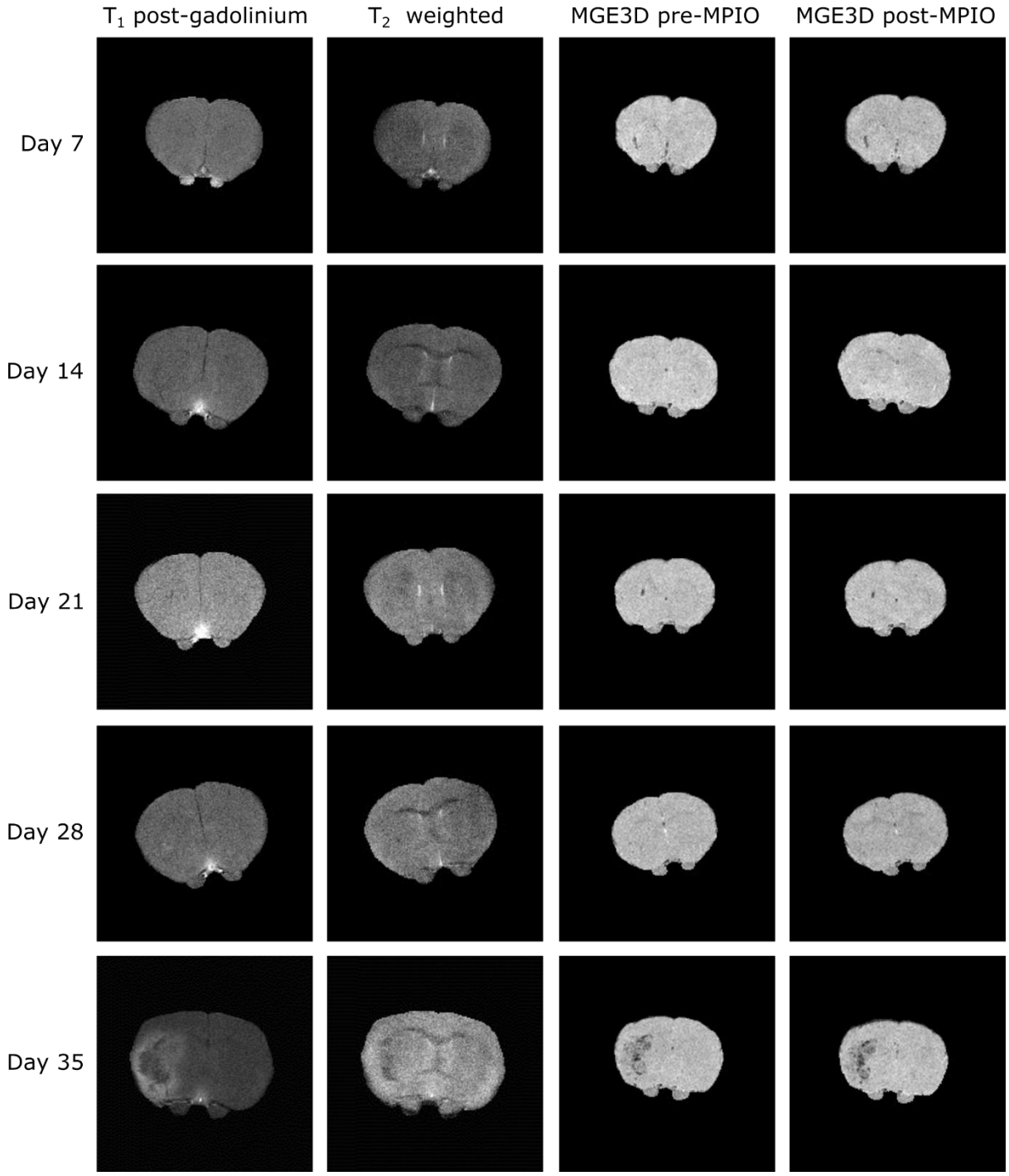


Figure 4.12: Representative images from animals for each timepoint in the 4T1-GFP model for mice injected with control RDG-MPIO. Each column, from the left, shows T_1-weighted post-gadolinium images, T_2-weighted images, pre-RDG-MPIO MGE3D images, and post-RDG-MPIO contrast MGE3D images.

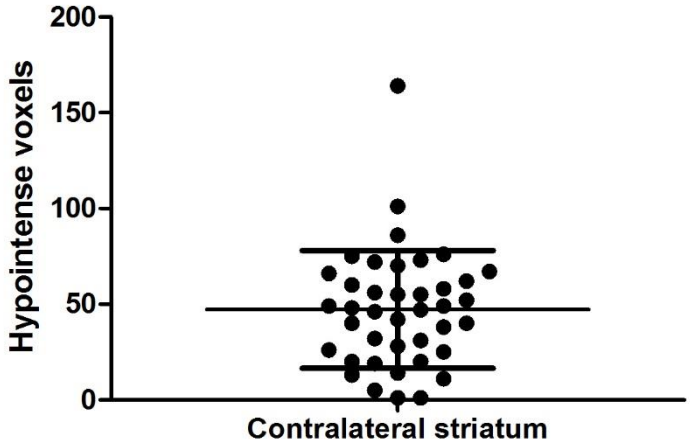


Figure 4.13: Graph showing the number of voxels designated as hypointense, in the pre-contrast MGE3D images of the normal, non-tumour bearing, contralateral striatum. The data is pooled from all animals across all timepoints, and is shown as individual data points, with lines indicating mean ± standard deviation. These data indicate the noise level of this technique in the normal striatum.

Overall, in mice injected with RGD-MPIO, MPIO induced hypointense voxels post-RGD-MPIO injection were evident at most time-points in the tumour-bearing striatum, but not in the contralateral striatum. A significant difference was found between the tumour-bearing and contralateral striatum at day 35 (2-way paired ANOVA $p < 0.05$; Post-hoc Bonferroni test $p < 0.05$; Figure 4.14A). In the animals injected with the control RDG-MPIO, a significant difference was also found between the tumour-bearing and contralateral striatum at day 35 (2-way paired ANOVA $p < 0.05$; Post-hoc Bonferroni test $p < 0.05$; Figure 4.14B). In mice receiving the PBS control injection, very few hypointense voxels were detected in mice receiving RGD-MPIO in both the ipsilateral (14 ± 23) and contralateral (10 ± 4) striatum (Figure 4.14A).

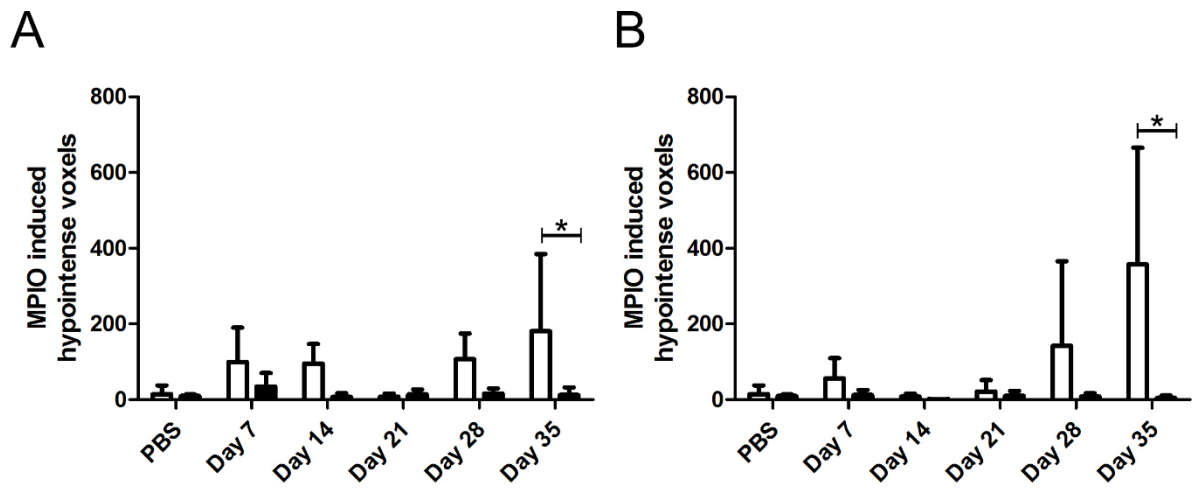


Figure 4.14 – Number of MPIO induced hypointense voxels, presented as post-contrast hypointense voxels minus pre-contrast hypointense voxels for all data, shown as mean ± standard deviation. (A) Significantly increased RGD-MPIO induced hypointense voxels were evident in the tumour-bearing striatum (white) compared to the contralateral striatum (black) at day 35 (2-way paired ANOVA $p < 0.05$, Bonferroni post-hoc test $p < 0.05$). (B) Significantly increased control RDG-MPIO induced hypointense voxels were also seen in the tumour-bearing striatum (white) compared to the contralateral striatum (black) at day 35 (2-way paired ANOVA $p < 0.05$, Bonferroni post-hoc test $p < 0.05$). *$p < 0.05$

Following whole group analysis, in order to determine why significant uptake of control RDG-MPIO was observed at the day 35 timepoint, gadolinium enhancing and non-enhancing tumours were separated for further analysis. Example images are shown in Figure 4.15. In the pooled group of non-enhancing tumours (n = 7 RGD-MPIO, n = 13 control RDG-MPIO), mice injected with RGD-MPIO showed higher levels of MPIO-induced hypointense voxels in the tumour-bearing hemisphere (1-way ANOVA $p < 0.005$, Figure 4.16A) than both the contralateral hemisphere (Bonferroni post-hoc test $p < 0.05$), and the mice injected with control RDG-MPIO in the tumour-bearing hemisphere (Bonferroni post-hoc test $p < 0.05$). No difference was observed between the tumour bearing and contralateral striatum in mice receiving control RDG-MPIO.

The gadolinium-enhancing tumours (n = 10 RGD-MPIO, n = 3 control RDG-MPIO, from days 21, 28 and 35) were pooled and analysed separately to determine whether higher levels of angiogenesis were present in these tumours. In mice injected with RGD-MPIO, significantly more MPIO-induced hypointense voxels were observed in the tumour-bearing striatum compared to the contralateral striatum (1-way ANOVA $p < 0.0001$, Bonferroni post-hoc test $p < 0.05$, Figure 4.16B). However, in mice receiving control RDG-MPIO the volume of hypointense voxels was also significantly greater in the tumour-bearing striatum than in the contralateral hemisphere (Bonferroni post-hoc test $p < 0.001$; Figure 4.16B), and additionally was greater than those injected with RGD-MPIO (Bonferroni post-hoc test $p < 0.001$; Figure 4.16B).

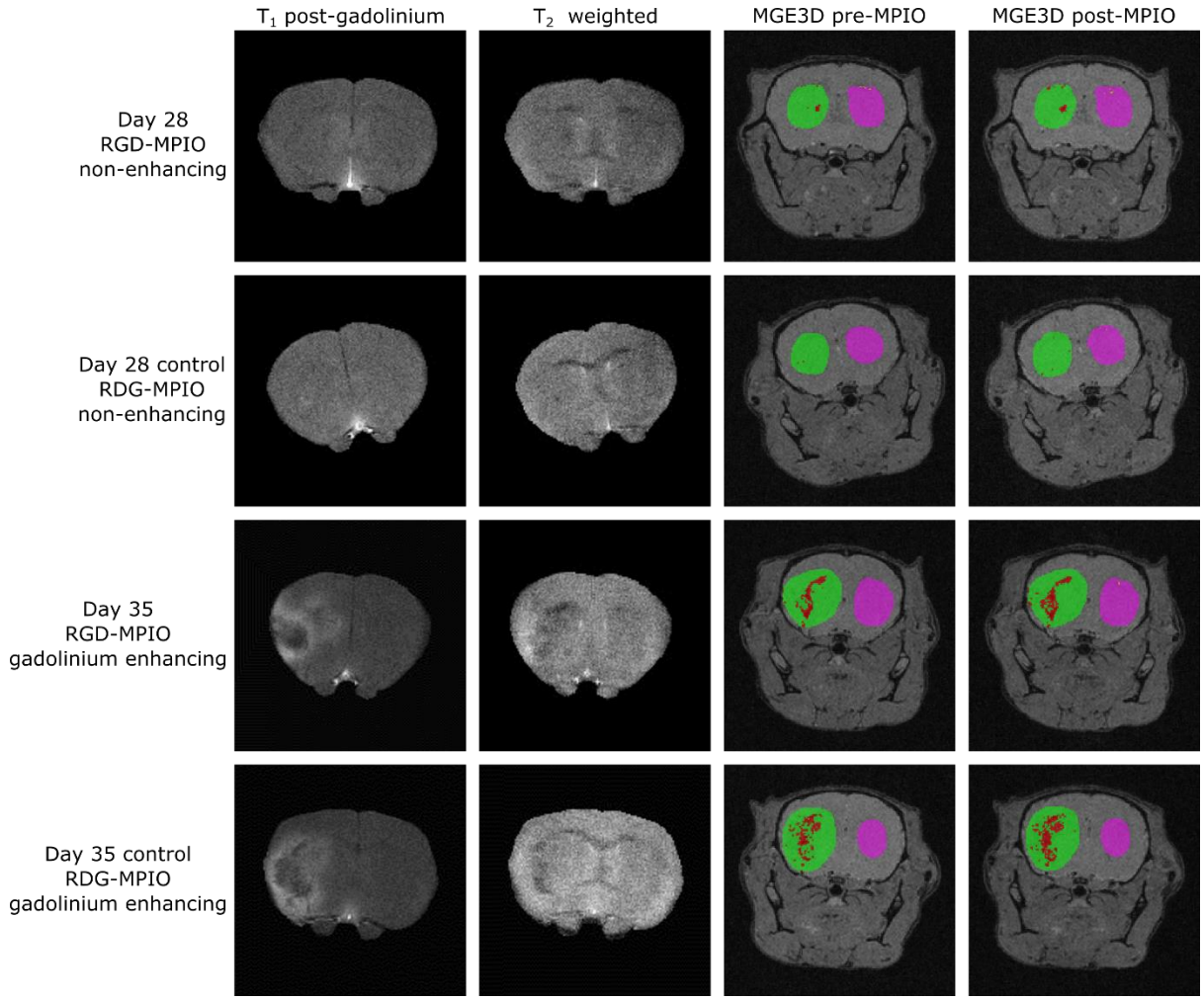


Figure 4.15: Representative images of both enhancing and non-enhancing 4T1-GFP metastatic tumours. Each column, from the left, shows T_1-weighted post-gadolinium images, T_2-weighted images, pre-MPIO MGE3D images, and post-MPIO contrast MGE3D images. For the MGE3D images, the tumour-bearing striatum is segmented in green, and the contralateral striatum segmented in pink. Hypointense voxels are shown in red.

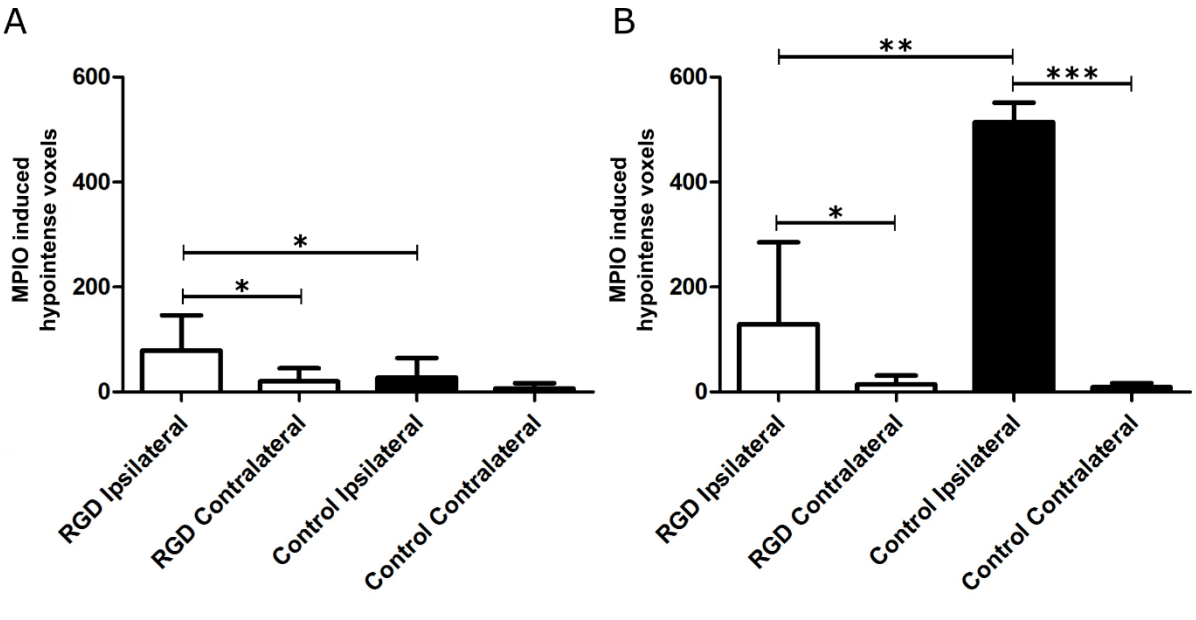


Figure 4.16: Number of MPIO induced hypointense voxels, presented as post-contrast hypointense voxels minus pre-contrast hypointense voxels for all data, and shown as mean ± standard deviation. Comparison of pooled data across all timepoints for (A) non-enhancing tumours, and (B) enhancing tumours. (A) Mice with non-enhancing tumours (n = 7 RGD-MPIO, n = 13 control RDG-MPIO) injected with RGD-MPIO showed higher levels of MPIO-induced hypointense voxels in the tumour-bearing hemisphere (1-way ANOVA $p < 0.005$) than both the contralateral hemisphere (Bonferroni post-hoc test $p < 0.05$) and the mice injected with control RDG-MPIO in the tumour-bearing hemisphere (Bonferroni post-hoc test $p < 0.05$). (B) In mice with gadolinium enhancing tumours (n = 10 RGD-MPIO, n = 3 control RDG-MPIO) significantly more MPIO-induced hypointense voxels were observed in the tumour-bearing striatum compared to the contralateral striatum (1-way ANOVA $p < 0.0001$, Bonferroni post-hoc test $p < 0.05$). However, in mice receiving control RDG-MPIO the volume of hypointense voxels was also significantly greater than the MPIO-induced hypointense voxels in the contralateral hemisphere (Bonferroni post-hoc test $p < 0.001$), and additionally was greater than those injected with RGD-MPIO (Bonferroni post-hoc test $p < 0.001$). Error bars represent standard deviation. *$p < 0.05$, **$p < 0.01$, ***$p < 0.001$.

To determine whether MPIO induced hypointensity numbers were related to the tumour size, the volume of the gadolinium enhancing region was also measured by manual segmentation of the post-gadolinium T_1-weighted images. In mice imaged with RGD-MPIO, the average enhancing region volume was 8.6 ± 10.4 mm^3, with range 1.3 – 22.4 mm^3. In mice imaged with control RDG-MPIO, the average enhancing region volume was 27.1 ± 12.8 mm^3, with range 13.3 – 38.7 mm^3. Mice were randomly assigned to be injected with either RGD-MPIO or control RDG-MPIO before the enhancing volume was known.

In the positive control glioma model, induced hypointense voxels (post- minus pre-contrast hypointense voxels) were observed in mice imaged with both RGD-MPIO (171 ± 284) and control RDG-MPIO (111 ± 191), as shown in Figure 4.17. Although there appeared to be more hypointense voxels in the tumour-bearing striatum for both groups, no significant differences were found between groups or between hemispheres (Figure 4.18). However, in this cohort, only two mice had gadolinium enhancing tumours, one in the RGD-MPIO group and one in the control RDG-MPIO group, with volumes of 8.9 mm^3 and 14.8 mm^3; respectively, as shown in Figure 4.17.

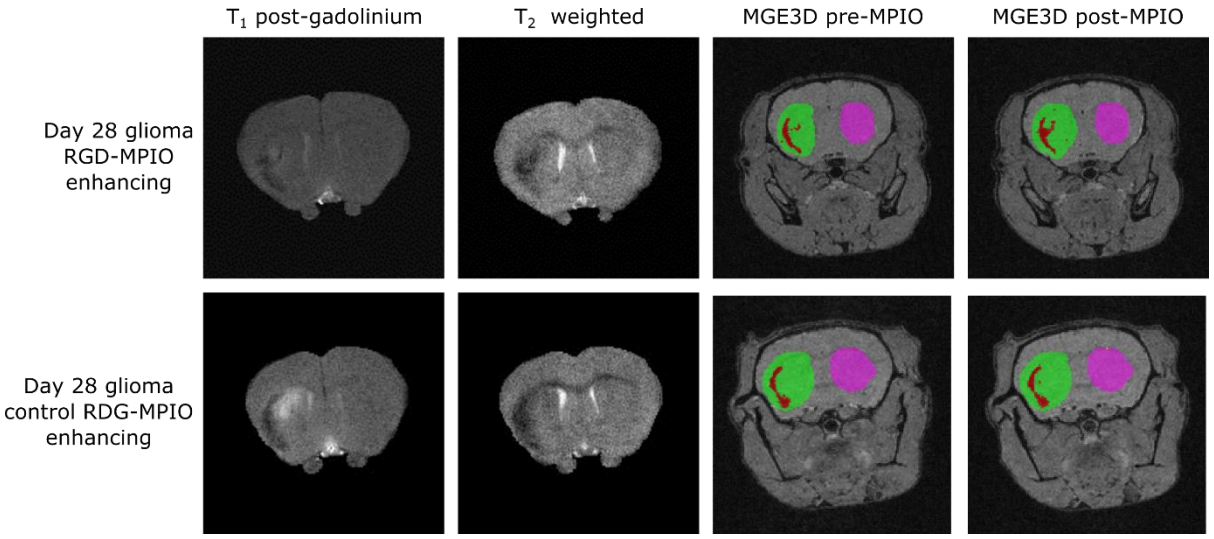


Figure 4.17: Representative images of both enhancing and non-enhancing U87 glioma tumours. Each column, from the left, shows T_1-weighted post-gadolinium images, T_2-weighted images, pre-MPIO MGE3D images, and post-MPIO contrast MGE3D images. For the MGE3D images, the tumour-bearing striatum is segmented in green, and the contralateral striatum segmented in pink. Hypointense voxels are shown in red.

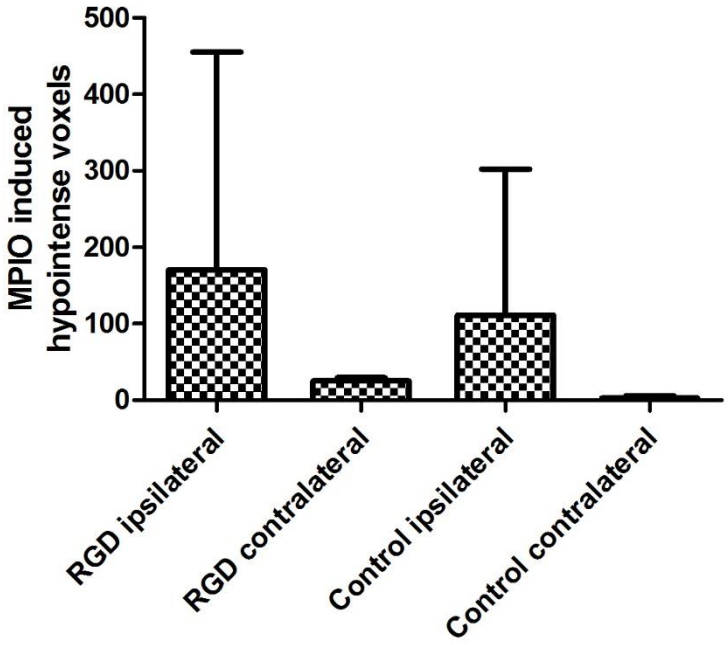


Figure 4.18: MPIO induced hypointense voxels in the U87 glioma model, presented as post-contrast hypointense voxels minus pre-contrast hypointense voxels for both RGD-MPIO (n = 3) and control RDG-MPIO (n = 3), and are shown as mean ± standard deviation. No significant differences in hypointense voxels were found between groups.

4.3.5 Histological examination of MPIO in the brain

Following Prussian blue staining to visualise MPIO in the tumour tissue, whilst individual MPIO were visible in the tumour tissue, large blue areas that appeared to be aggregations of MPIO were also visible in tissue sections at all timepoints (Figure 4.19). Spatially, the MPIO aggregations appeared to be clustered in close proximity to blood vessels.

These aggregations were observed in mice injected with both RGD-MPIO and control RDG-MPIO, across all timepoints, as shown in Figure 4.20A. A positive correlation was observed between tumour size and number of aggregations in mice injected with RGD-MPIO (linear regression, $p < 0.0005$, $R^2 = 0.64$, Figure 4.20B), and a trend towards an increased number of aggregations was observed in mice injected with scrambled-MPIO ($p = 0.09$).

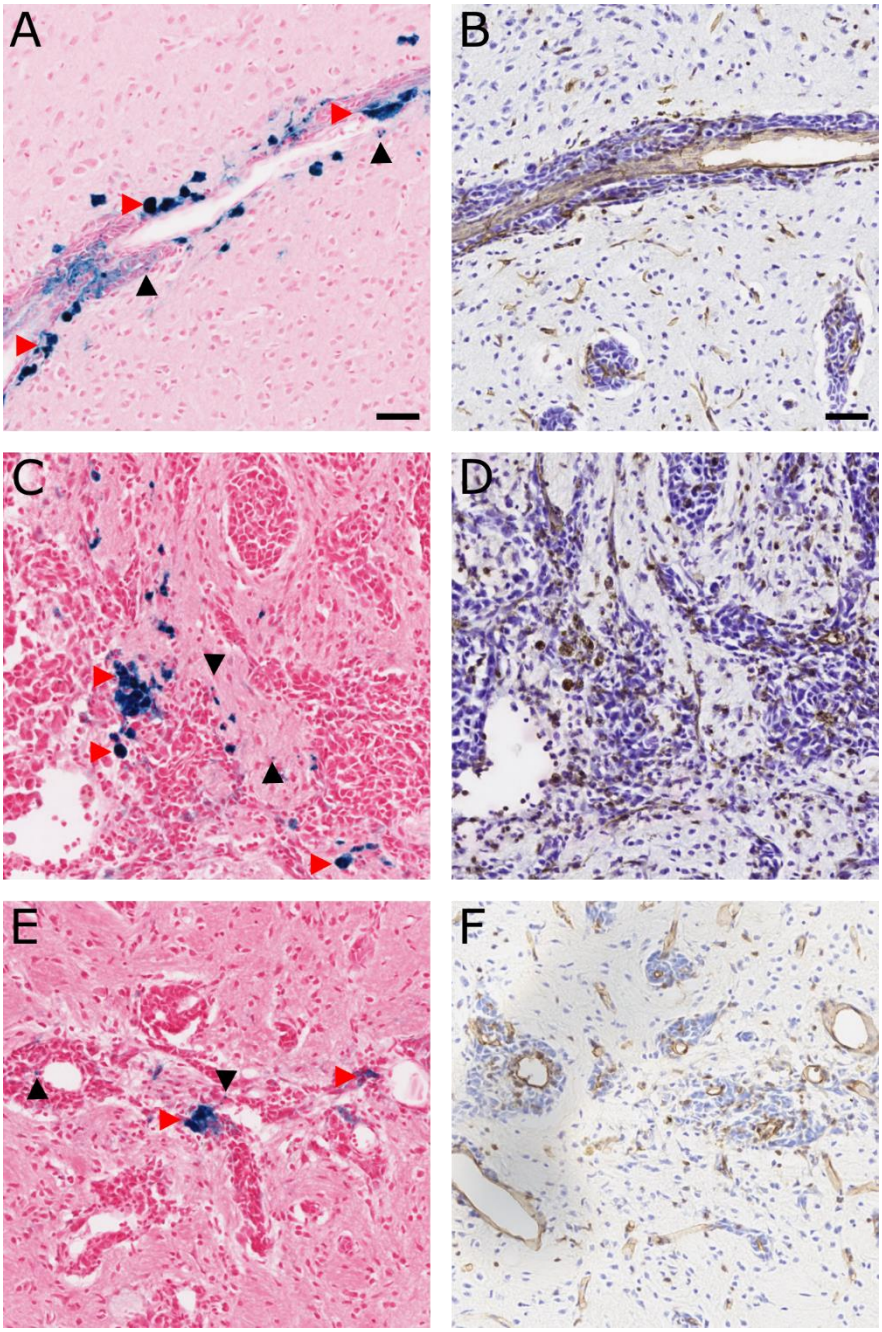


Figure 4.19: Aggregations of MPIO in tumour tissue. Representative sections stained for Perl's Prussian blue (A,C,E; MPIO, blue) and counterstained with nuclear fast red. Black arrowheads indicate examples of single MPIO, and red arrowheads indicate examples of aggregations. (B,D,E) Consecutive sections stained for blood vessel marker CD31 (brown), and counterstained with Cresyl violet. Scale bar represents 25 µm at 20x magnification in all images.

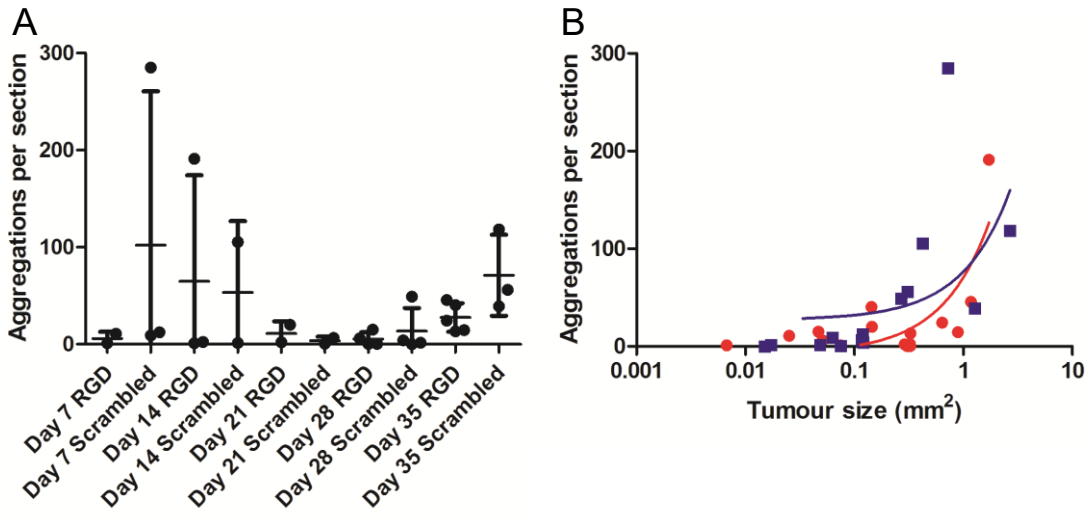


Figure 4.20: Aggregations of MPIO visible in Perl's Prussian blue stained tumour sections. (A) Distribution of aggregations across timepoints for both RGD-MPIO (red) and control RDG-MPIO (blue). (B) Comparison of aggregations with tumour size, for RGD-MPIO (red) and control RDG-MPIO (blue). Linear regression lines are fitted showing a positive correlation between number of aggregations and tumour size for mice injected with RGD-MPIO ($p < 0.0005$, $R^2 = 0.64$), and a trend towards a positive association for control RDG-MPIO. Error bars represent mean ± standard deviation.

4.4 Discussion

4.4.1 Expression of angiogenic markers in brain metastasis

The first aim of this study was to determine the potential for targeting integrin $\alpha_v\beta_3$ expression in brain metastasis in order to image angiogenesis. Integrin $\alpha_v\beta_3$ stained area increased significantly at days 21, 28 and 35 after tumour induction, whilst no expression was seen in the PBS control model or the normal contralateral striatum. This expression at later timepoints was associated with increased microvessel density, as measured by increased CD31 staining and vessel number. These findings suggest that integrin $\alpha_v\beta_3$ is a specific marker of tumour angiogenesis, and, hence, has potential for molecular imaging of angiogenesis. The presence of some integrin $\alpha_v\beta_3$ positive vessels at the day 7 timepoint, although not statistically significant, likely reflects the fact that integrin $\alpha_v\beta_3$, as with many pro-angiogenic factors, is also expressed during inflammatory processes. At later timepoints, the number of integrin $\alpha_v\beta_3$ positive vessels per mm^2 increased significancantly. This finding was also reflected in the fluorescent co-localisation experiments, where the proportion of integrin $\alpha_v\beta_3$ co-localised with vessels remained steady at approximately 10% throughout the time course. This steady proportion of vessels is consistent with an increased number of integrin $\alpha_v\beta_3$ positive vessels in larger tumours. Examination of histology has successfully demonstrated that integrin $\alpha_v\beta_3$ is expressed on the vasculature in a mouse model of brain metastasis, which suggests it is a potential target for molecular imaging of angiogenesis *in vivo*.

Increased TIE2 staining at later timepoints was also observed to correlate with increased CD31 expression, but this expression was not statistically significant.

Similar trends were seen in the fluorescent co-localisation, with integrin $\alpha_v\beta_3$ and TIE2 positive blood vessels increasing at later timepoints. However, in the U87 glioma model, a significant increase in TIE2 expression was observed. These data suggest that, whilst not statistically significant, TIE2 may also be an appropriate angiogenic marker for molecular imaging, particularly in glioma.

Increased staining of the blood vessel marker CD31 was also observed from day 21 onwards, indicating an increase in microvessel area fraction. Similarly, microvessel density was increased from the day 21 timepoint. There was some disparity between these two measures at the day 28 timepoint, with significantly increased staining, but not a significantly increased vessel count. This increased staining may reflect the enlargement and dilatation of angiogenic vessels, which would increase the stained area, but not the vessel count.

Despite a trend towards an increase in expression of angiogenic markers at later timepoints for all markers measured, few statistically significant changes were observed. This finding likely reflects the large variability of angiogenic marker expression within timepoints, which in turn is likely related to the variability seen in tumour sizes within timepoints. Owing to this variability, it is difficult to pinpoint the timing of the angiogenic switch in this tumour model, and it is likely that the angiogenic switch was not reached in many of these tumours. However, the gadolinium enhancement data from the imaging study suggest that vessel permeability rarely occurs before day 21, and is established in most tumours by day 28. These findings replicate the timecourse seen in other independent studies within our group[16,373]. This observation, since angiogenic vessels are more permeable than normal brain vessels, combined with integrin $\alpha_v\beta_3$ marker expression data, suggests that the angiogenic switch takes place at approximately

day 21 after tumour induction. In the context of this finding, it should be noted that vessel permeability is not restricted to de novo vessels, and can also reflect inflammatory processes. Owing to this variability in the timing of the angiogenic switch, the full range of timepoints was also used for the MPIO imaging study.

The U87 primary glioma was used as a positive control, as it is known to be highly angiogenic[64,181]. In the U87 glioma tumours, high levels of expression of the angiogenic markers integrin $\alpha_v\beta_3$ and TIE2 were found for both stained area and vessel counts, along with increased microvessel counts compared with the normal striatum. The histology of these tumours was also variable, with a large range of sizes observed, which again may contribute to the variability seen in the quantitation of angiogenic markers. Despite the use of a later day 28 timepoint, only 2 / 6 of these tumours were gadolinium enhancing, suggesting that despite the upregulation of angiogenic markers, BBB breakdown may occur later in this model. It is important to note that in our model, the U87 tumour grew diffusely and relatively slowly, with no defined margins. This slow growth is in contrast with many studies in the literature, which report aggressive growth and well-defined tumour margins[295,374-377]. Those studies reported high levels of angiogenic markers[374] together with gadolinium enhancement[295,375,376]. However, in many of those studies the tumour cell burden at the time of induction was orders of magnitude higher than in our model[295,375,377], and, hence, the tumours were much larger. The histology seen here is, however, similar to that seen by de Groot et al. in the U87 model following treatment with bevacizumab[374]. However, this model does have high levels of angiogenic vessels, based on integrin $\alpha_v\beta_3$ and TIE2 expression, and hence is useful as a positive control model for the imaging studies.

4.4.2 *In vitro* binding of RGD peptides to integrin $\alpha_v\beta_3$

Before *in vivo* studies commenced, the binding efficacy of various RGD peptides to integrin $\alpha_v\beta_3$ was measured. The results were used to determine the most appropriate peptide for RGD-MPIO imaging in mice. Analysis of RGD-MPIO binding *in vitro* under physiological flow conditions showed that RGD peptide 785 exhibited the highest level of binding efficacy out of the three peptides tested, and that binding was specific to integrin $\alpha_v\beta_3$. The scrambled control RDG peptide 787 showed no significant binding to integrin $\alpha_v\beta_3$ *in vitro,* compared to a BSA control. Therefore, these peptides were chosen as targeted and control peptides to produce imaging contrast agents to be used *in vivo*.

4.4.3 *In vivo* detection of angiogenic vessels using RGD-MPIO

The targeted contrast agents were then tested *in vivo* in the brain metastasis and glioma models. In all animals, hypointense voxels were apparent in the pre-contrast T_2*-weighted MGE3D images, in the tumour bearing striatum. In animals at the day 7 timepoint, the injection track was often visible. Pre-existing hypointense voxels have been observed in previous studies of intracerebral tumour models within our group, however these studies have had far fewer pre-existing hypointense voxels (unpublished results). It is important to note, however, that the previous imaging studies were conducted with a less sensitive T_2*-weighted sequence, and at 7.0 T compared to the current study at 9.4 T with an optimised sequence. It is possible that the increased sensitivity of this study has resulted in the detection of spurious pre-existing hypointense voxels that are unrelated to MPIO. There are a number of biological parameters that may result in these pre-existing hypointense voxels. These include iron deposition from micro-

haemorrhages, and deoxyhaemoglobin T_2* susceptibility effects[378]. It has been shown that giving normobaric oxygen therapy to mice with intracranial haemorrhage reduces the T_2* susceptibility artefacts, and restores the ability to perform molecular MRI without pre-existing hypointense voxels[379]. Other methods have also been described that use novel pulse sequences to produce a positive contrast from iron oxide based contrast agents[380-384]. Either of these methods could potentially be applied to help reduce this issue of pre-existing hypointense voxels.

These pre-existing hypointense voxels may confound the imaging results. In many animals, there were apparently more hypointense voxels in the pre-contrast image than in the post-contrast image. Those animals where banding artefacts affected the region of interest were excluded, but in most animals no significant artefacts or differences in SNR were apparent between the pre- and post-contrast images. In these cases, MPIO-induced hypointense voxels fall within the noise range of this technique. An optimised MGE3D sequence is available that has higher SNR and may, therefore, be more sensitive to small quantities of bound MPIO[193]. However, this sequence has a scan time of ~40 mins. If used in the current experimental protocol, its length is such that acquisition of pre- and post-contrast scans, together with anatomical scans, approaches the limits of anaesthesia duration that is possible in animals with a high tumour burden. For this reason, a sequence with identical parameters except for a reduced number of echoes was used, with a scan time of 20 mins per scan, and concomitantly lower SNR.

RGD-MPIO induced hypointense voxels were found to be significantly increased at day 35 after metastasis induction. However, this increase in apparent binding coincided with BBB breakdown. Analysis showed that large volumes of hypointense voxels were also detected in enhancing tumours using both control

RDG-MPIO and unconjugated-MPIO. This was an unexpected result, as the control RDG-MPIO had shown only very low levels of binding *in vitro*. Similarly, MPIO are an obligate blood pool agent, as they are too large to extravasate from the circulation. It is possible that in areas of frank BBB breakdown MPIO may be able to exit the circulation and enter the parenchyma, but this has not been demonstrated previously. Thus, it is an important consideration to investigate further (see Chapter 5).

However, at the day 7 and 14 time-points where no BBB breakdown was evident, a trend towards increased hypointense voxels was observed in RGD-MPIO injected mice compared to both the contralateral hemisphere and control RDG-MPIO injected mice. As integrin $\alpha_v\beta_3$ is upregulated in inflammatory processes as well as angiogenesis, this likely reflects successful and specific targeting of integrin $\alpha_v\beta_3$ at early time-points, but of inflamed rather than angiogenic vessels.

In the U87 glioma model that was used as a positive angiogenic model, high numbers of hypointense voxels were observed in the pre-injection scans. When compared to the post- RGD-MPIO injection scans, many more hypointense voxels were evident in the pre-contrast scan than in the post-contrast scan. This observation suggests that RGD-MPIO binding was within the noise level. However, histological analysis using Prussian blue stained slides to detect MPIO confirmed the clear presence of MPIO as aggregations in the tumour tissue. It is possible that regions of pre-existing hypointense signal may obscure the presence of bound RGD-MPIO in the same region.

It is generally thought that MPIO with a diameter of 1 µm are unable to cross the BBB, and are used in preference to iron oxide nanoparticles for this reason. In the

current study, in tumours with marked BBB breakdown, uptake of both control RDG-MPIO and RGD-MPIO was evident by MRI, with uptake of the control RDG-MPIO being significantly greater. However, those tumours also showed a much greater volume of gadolinium enhancement, and, hence, this may be related to tumour size. It is not clear whether MPIO are able to cross a permeable BBB, or whether they are retained by some other mechanism. These results suggest that imaging with MPIO may produce non-specific contrast in tumours with highly permeable blood vessels, and warrants further investigation.

4.4.4 Histological examination of MPIO in the brain

Analysis of the histology of these tumours showed a number of large aggregations of MPIO. These aggregations were found mostly in late timepoint tumours with frank BBB breakdown. However, there were a number of outliers showing a large number of aggregations in small tumours, at early timepoints where no BBB breakdown was evident. This finding may indicate that a retention mechanism other than the simple crossing of a permeable BBB is responsible. Similarly, the spatial localisation of these aggregations within the tumour showed no discernible pattern, as aggregations were observed clustered around blood vessels, and in both the periphery and core regions of the tumours at various timepoints. However, the shape and size of these aggregations indicates that they may be intracellular accumulations and, hence, it is postulated that the MPIO may be taken up by tumour associated macrophages. MPIO have been used successfully in many tumour models and inflammation studies in this group, and such aggregations have not been observed previously in any of those studies. Thus, it is important to

understand the mechanisms behind the formation of MPIO aggregations, and the circumstances in which they form (see Chapter 5).

4.5 Conclusion

The expression of integrin $\alpha_v\beta_3$ on the neovasculature in mouse models of brain metastasis and glioma was assessed, and it was determined that integrin $\alpha_v\beta_3$ expression was increased at later timepoints and in larger tumours. Thus, integrin $\alpha_v\beta_3$ is an appropriate target for molecular imaging of angiogenesis in brain metastasis.

The binding of various RGD peptide conjugated MPIO was assessed *in vitro*, and peptide 785 showed the highest specific binding to mouse integrin $\alpha_v\beta_3$. This peptide was taken forward for use in *in vivo* studies.

The imaging of angiogenesis in brain metastasis using RGD-MPIO has not been successful, as pre-existing hypointense voxels and retention of the control RDG-MPIO in large tumours are confounding factors. Application of molecularly targeted MRI using RGD-MPIO may be precluded once tumours reach later stages with overt pathological BBB breakdown, since retention is no longer target-specific. It is important to understand the mechanisms behind the formation of these MPIO aggregations, and the circumstances in which they form, and this will form the basis for the next chapter in this thesis.

Chapter 5 – Iron, macrophages, and the tumour microenvironment

5.1 Introduction

Chapter 4 of this thesis, which examined the use of targeted RGD-MPIO for the *in vivo* imaging of integrin $\alpha_v\beta_3$, yielded results that were not expected. In that study I found that not only targeted RGD-MPIO, but also control RDG-MPIO, were visible with imaging and were retained in the brain in the form of aggregations. I concluded that the application of molecularly targeted MRI using RGD-MPIO may be precluded once tumours reach later stages with overt pathological blood brain barrier (BBB) breakdown, since retention is not target-specific. This chapter seeks to investigate the identity and formation of these aggregations, and to elucidate whether MPIO cross the BBB, and how.

5.1.1 MPIO penetration of the blood-brain barrier

In Chapter 4, some single MPIO were found free in the tumour parenchyma in animals with frank BBB breakdown. It has been shown that even when the BBB is permeabilised, the pore sizes are only 50 nm, so MPIO should not be able to extravasate from the vasculature even under these conditions[385,386]. If MPIO are able to cross a permeabilised BBB, this would be an important consideration for clinical molecular imaging in pathologies where the BBB is not intact. Similarly, if MPIO are able to cross a permeabilised BBB, MPIO penetration into the parenchyma may also explain the aggregations observed in Chapter 4. As MPIO have not been observed in the tumour parenchyma in previous studies using antibody-targeted MPIO, the ability of both peptide- and antibody-targeted MPIO to cross the BBB was investigated. Thus, the first specific objective of this chapter was to determine whether MPIO can cross a permeabilised BBB *in vivo*.

5.1.2 Retention of MPIO by tumour associated macrophages

Under normal conditions, iron oxide particles, including both USPIO and MPIO, are cleared by the reticuloendothelial system (also known as the mononuclear phagocytic system or macrophage system), which consists of monocytes and tissue macrophages, mostly in the liver and spleen. A review of the function of the reticuloendothelial system in relation to iron metabolism has been written by Knutson and Wessling-Resnick[387]. MPIO are cleared rapidly from the bloodstream, with a half-life of approximately 0.5 - 2 min, whilst USPIO persist for approximately 3 - 21 hours[193,195,365,388,389]. One hour after intravenous injection in mice, unconjugated MPIO are found primarily in the liver and spleen, with small amounts present in the lungs and intestines[372]. In the case of USPIO, hypointense signal voids can be seen on MRI up to 1 month later in the liver, spleen, and bone marrow, indicating that iron is still present in the tissue at late timepoints[389].

Whilst the vast majority of the reticuloendothelial system is found in the liver, spleen, and bone marrow, macrophages and microglia are also found associated with brain metastases. It has previously been shown, in the mouse model of brain metastasis used in this study, that macrophage/microglia infiltration is present from the earliest timepoints[390]. Moreover, the volume of Iba-1 positive staining has been shown to correlate positively with tumour volume[390]. Amoeboid shaped Iba-1 positive cells were identified in close association with the metastatic foci, and could be either perivascular macrophages, or amoeboid microglia[390]. Macrophage infiltration has also been demonstrated in brain metastases where the BBB remains intact[391]. High numbers of tumour associated macrophages are associated with poor prognosis in many types of cancer[392], and have been

observed to congregate around blood vessels in regions where tissue invasion and vessel intravasation are occurring[393].

The uptake of nanoparticles by macrophages is often exploited for the imaging of inflammatory disease[394], including tumour-associated inflammation[395]. Ferumoxytol, a clinically approved, untargeted USPIO, has been shown to be taken up by macrophages, and has thus been used to image brain tumour-associated macrophages[396,397]. However, Ferumoxytol remains an intravascular agent for approximately 24 hours, owing to its long half-life in the blood[398,399], and is only taken up by macrophages after a number of days. A number of other studies have also used USPIO and other iron oxide nanoparticles for MRI of macrophages in a variety of disease settings including neuro-oncology[400-403], atherosclerosis[404,405], breast cancer models[406,407], lymph node metastasis staging[408-410], stroke[411], multiple sclerosis[412-414], epilepsy[415], and many other applications.

The contrast produced by USPIO uptake in macrophages, however, is generally only produced at late timepoints following injection (Figure 5.1), of hours to days. As the clearance rates of USPIO from the bloodstream differ dramatically from MPIO, it is difficult to compare the equivalent imaging timepoints. To our knowledge, no studies have used untargeted MPIO as a contrast agent to image macrophages, so this pattern of enhancement has not been demonstrated with MPIO. However, when peripheral macrophages are labelled with USPIO, they are usually detected in the brain 24 hours following intravenous injection[416,417]. Thus, the timescale of this study, whereby imaging occurs 20 minutes post-injection, and brain harvesting within a few hours, suggests that contrast is unlikely to be produced by peripheral macrophages which have taken up MPIO and migrated to the brain.

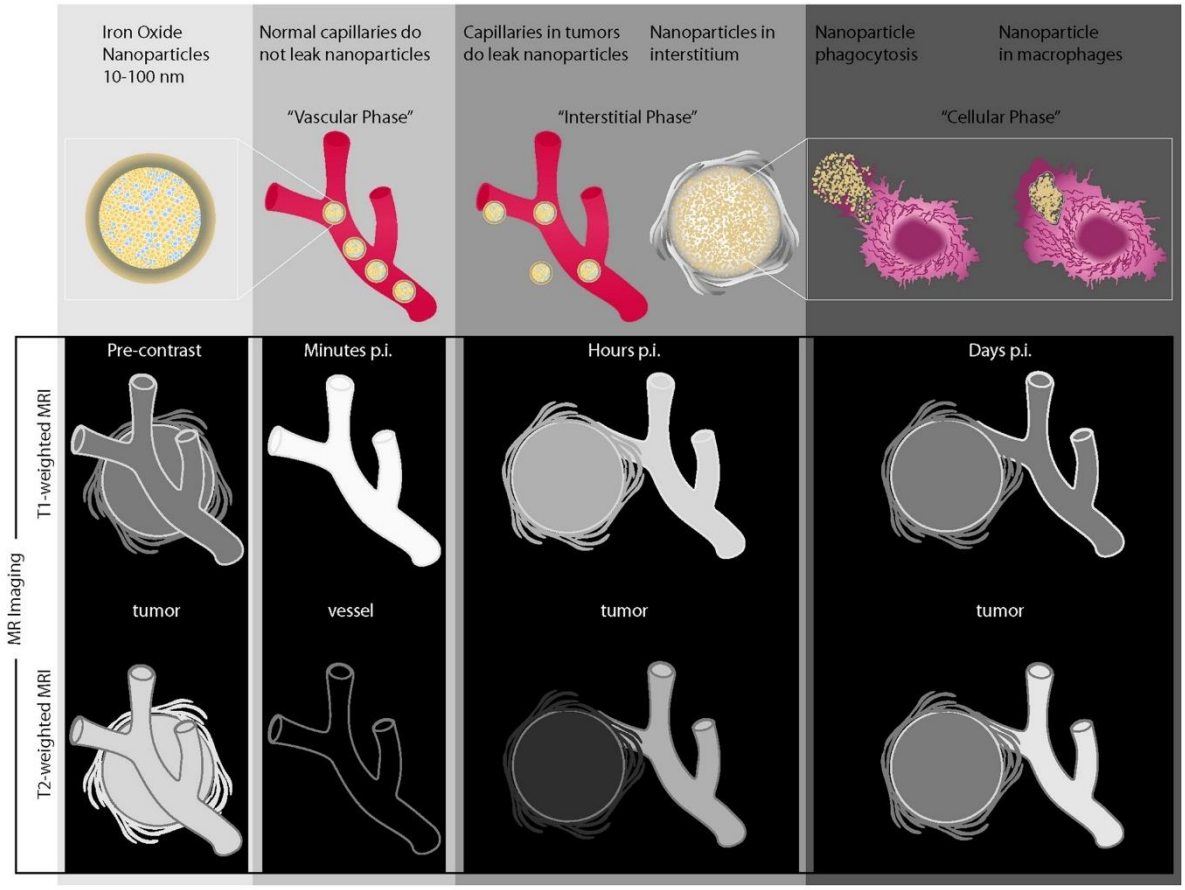


Figure 5.1: Mechanisms of USPIO enhancement kinetics. USPIO can be used with T_1- or T_2-weighted scans immediately following intravenous injection to produce dynamic vascular contrast. Hours post-injection, T_2-weighted scans can be used to observe extravasated particles in the tumour, and contrast produced by phagocytosed particles in macrophages can be seen days to weeks post-injection. Reproduced with permission from Daldrup-Link and Coussens[406].

Given the infiltration of tumours by macrophages, and the clearance pathway of MPIO by the reticulo-endothelial system, it is likely that macrophages may be involved in the apparent aggregations of MPIO seen in the brain tissue in the previous chapter. Because of this, histology from the tumour model in Chapter 4 was further investigated in order to identify the aggregations of MPIO and the conditions under which they occur, with the specific hypothesis being that the aggregations reflect macrophages that have taken up MPIO.

5.1.3 Effect of MPIO targeting moiety

In *in vitro* studies, uptake of RGD targeted iron oxide nanoparticles by human umbilical vein endothelial cells (HUVECs) can be blocked by prior injection of RGD peptide, suggesting that this uptake is receptor specific[355]. This same study also showed that injection of RGD peptide prior to RGD targeted iron oxide nanoparticle administration can block targeted binding in an intracerebral U87 glioma model[355]. This finding would also suggest that the *in vivo* nanoparticle targeting is specific. However, in the Prussian blue stained histology images presented in that paper (Figure 5.2), the iron staining appears to be in macrophage-like aggregations clustered around integrin β_3 positive vessels, rather than bound to the vessels themselves. These data would seem to suggest that the RGD peptide block actually prevents phagocytosis by macrophages, rather than blocking specific endothelial binding. For this reason, I aim to test the ability of macrophages and tumour cells to take up both peptide- and antibody-targeted MPIO, with and without receptor specific blocking.

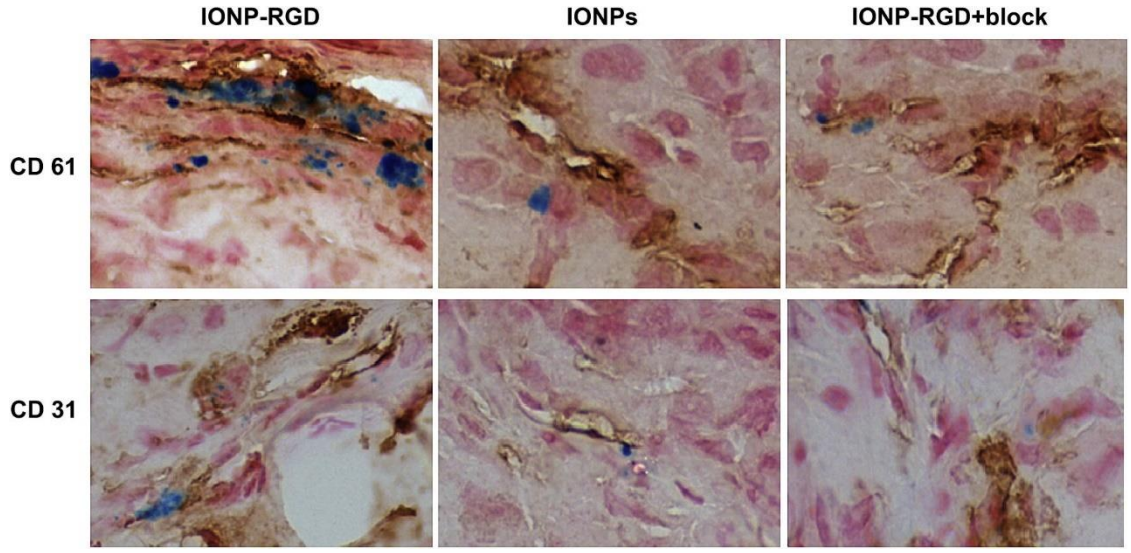


Figure 5.2: Uptake of RGD targeted iron oxide nanoparticles (IONP) in a U87 glioma model. The targeted IONP-RGD particles appear to have extravasated from the vasculature, and appear in macrophage-like aggregations surrounding integrin β_3 (CD61) positive blood vessels (CD31). Untargeted IONPs show less retention in the tissue, as do targeted IONP-RGD particles administered following pre-treatment with an RGD peptide block. Reproduced with permission from Zhang et al.[355]

It is important to note that whilst the normal clearance pathway of MPIO is via macrophages, aggregations of iron in the brain have not been observed before in any of the MPIO imaging studies performed in our laboratory group. This would suggest that the aggregations may be related to the MPIO targeting moiety, as peptide-targeted MPIO have not previously been used in brain pathology models. Thus, a specific objective of this chapter is to determine whether peptide-conjugated and antibody-conjugated MPIO behave differently *in vivo*, with regards to macrophage uptake and specific endothelial binding.

5.1.4 Endogenous iron-laden macrophages

Iron accumulation in macrophages is a normal physiological process associated with haem homeostasis[418]. It is also associated with macrophage polarisation, with pro-inflammatory polarised macrophages more able to accumulate and store intracellular iron, and anti-inflammatory polarised macrophages playing a role in the uptake and release of iron[419,420]. Moreover, the addition of extra iron to a system can drive macrophage polarisation towards the pro-inflammatory phenotype[421-423], including the addition of iron oxide nanoparticles[424]. Endogenous iron-laden macrophages have also been found to be associated with areas of tumour microhaemorrhage, as they play a role in recycling the iron from haemoglobin[425]. The iron content of the microhaemorrhages increased polarisation of the macrophages to the pro-inflammatory phenotype[425], as does an increase in iron following a co-injection of iron oxide nanoparticles with the tumour cells, and this resulted in anti-tumour effects[425,426]. Systemic delivery of Ferumoxytol also reduces the metastatic burden of liver and lung tumours through increased levels of pro-inflammatory macrophages[426].

Endogenous aggregations of Prussian blue positive staining have been observed in a number of other molecular imaging studies. Leftin and Koutcher recently reported that Prussian blue positive endogenous iron-laden macrophage aggregations were present in a prostate cancer model[427], and in a breast cancer model, both in the primary tumour and also in lung and brain metastasis[428], although less aggregations were present in the metastases. They also demonstrated in a separate study that endogenous iron-laden macrophages were present as MRI detectable hypointense voxels prior to molecular imaging, and that an increased number of macrophage clusters were present following USPIO

administration[429]. This finding may provide an explanation as to the identity of the pre-existing, pre-contrast hypointense voxels that were present in the intracerebral tumour models used in Chapter 4, and may also suggest an explanation for why macrophages take up MPIO.

However, in the previously mentioned study of intracerebral glioma by Zhang et al[355], although the tumours were large, there was no evidence of pre-existing pre-contrast hypointense voxels, which were seen in our both of our intracerebral tumour models. The results of the Zhang study, including RGD peptide blocking of RGD-USPIO binding by HUVECs and *in vivo* tumour cells, macrophage-like iron aggregations, and a lack of pre-contrast hypointense voxels, were also replicated in a model of nasopharyngeal carcinoma[353]. Hence, I plan to determine whether endogenous iron-laden macrophages can account for the presence and localisation of pre-existing hypointense voxels in the 4T1-GFP metastasis model, with the specific objective being to determine whether endogenous iron in tumour associated macrophages produces non-specific hypointense voxels in pre-contrast images.

5.1.5 Specific objectives

It is important to note that the vast majority of research into cellular and macrophage uptake of iron oxide particles for molecular imaging has been performed with nanometre sized particles. As micron sized particles behave differently both in circulation and in the tissue, it is not known whether they show the same pattern of uptake as USPIO. Thus, the overarching aim of this chapter was to investigate the retention of peptide- and antibody-conjugated microparticles of iron oxide by macrophages, both *in vitro* and *in vivo*. The specific objectives of this chapter were:

1. Determine whether MPIO can cross a permeabilised BBB *in vivo*.
2. Identify the aggregations of MPIO and the conditions under which they occur, with the specific hypothesis being that the aggregations reflect macrophages that have taken up MPIO.
3. Determine whether peptide-conjugated and antibody-conjugated MPIO behave differently *in vitro* and *in vivo*, with regards to macrophage uptake and specific endothelial binding.
4. Determine whether endogenous iron in tumour associated macrophages produces non-specific hypointense voxels in pre-contrast images.

5.2 Methods

5.2.1 MPIO penetration of the blood-brain barrier

5.2.1.1 Characterisation of an *in vivo* model of blood-brain barrier permeabilisation

To determine whether MPIO can cross a permeabilised BBB *in vivo,* cytokine-induced neutrophil chemoattractant 1 (CINC-1) was used to create a model of BBB breakdown in the absence of a tumour. First, a pilot study was conducted to test the appropriate dose for induction of BBB breakdown. Using the intracranial injection protocol described in Chapter 2.3.2, 0.5, 1 or 2 µg (n = 2 per dose) of CINC-1 protein (453-KC-050/CF, R&D systems, Abingdon, UK) was injected in a volume of 1 µL.

After 5 hours, T_1 weighted MRI images were acquired with the parameters described in Chapter 2.6.1. Subsequently, 30 µL of gadolinium (Omniscan, GE Healthcare) was injected in the tail vein, and after 5 mins a post-contrast T_1 weighted image was acquired. The enhancing volume was quantified by manual segmentation of the images.

Following imaging, mice underwent perfusion-fixation, and brains were harvested for histology as described in Chapter 2.3.3. Staining was conducted for Iba-1, integrin $\alpha_v\beta_3$, and VCAM-1 according to the protocols described in Chapter 2.5.1 and 2.5.2.

BBB breakdown was also confirmed histologically in separate animals (n = 3). Mice underwent intracranial injection of 1 µg CINC-1. To identify areas of BBB permeability, 5 hours after CINC-1 injection, mice were injected intravenously with 100 µl type II horseradish peroxidase (300 units; Sigma Aldrich, UK). 30 mins later mice were transcardially perfused under terminal anaesthesia with 50 ml 0.9% heparinised saline followed by 50 mL Karnovsky's fixative. Brains were cryoprotected and frozen according to the protocol described in Chapter 2.3.4. 20 µm sections were cut on the cryostat and collected free-floating in 0.1 M phosphate buffer. Sections were stained using a modified Hanker-Yates method. Hanker-Yates solution was prepared fresh for each experiment, and free-floating sections were washed in 0.1 M phosphate buffer, transferred into metal solution for 10 min, washed twice in 0.1 M phosphate buffer, exposed to developing solution for 10 min, and washed twice in 0.1 M phosphate buffer. Tissue sections were transferred to glass slides and allowed to air dry overnight. Slides were mounted and scanned as previously described in Chapter 2.5.1 and 2.5.4.

[Perfusion-fixation, Hanker-Yates staining, and image preparation were performed by Dr Mario Munoz Pinto.]

5.2.1.2 MPIO penetration of a permeabilised blood-brain barrier

To determine whether MPIO can cross a permeabilised BBB *in vivo,* a full study was conducted to test the ability of peptide- and antibody-conjugated MPIO to enter the brain parenchyma following CINC-1 BBB permeabilisation. Using intracranial micro-injection, 1 µg of CINC-1 protein was injected in a volume of 1 µL into the left striatum (n = 12). After 5 hours, an imaging session was conducted as per the

protocol described in Chapter 4.2.4. The imaging session consisted of (in order) T_1 and T_2 weighted anatomical imaging, pre- and post-MPIO injection MGE3D scans, and a gadolinium enhanced T_1 weighted scan.

A pre-injection MGE3D scan was performed as described in Chapter 2.6.3. During this time, the MPIO (RGD-MPIO n = 3, control RDG-MPIO n = 3, VCAM-MPIO n = 3, IgG-MPIO n = 3) were prepared for injection at a dose of 4 mg/kg Fe in 100 µL sterile saline. Immediately prior to injection, the MPIO were vortexed for 2 min and sonicated for 2 min to reduce particle clumping. The mouse was removed from the magnetic field, but remained anaesthetised and positioned inside the volume coil. The particles were injected via an indwelling tail vein cannula, and the mouse remained outside the magnetic field for 20 min. A 20 min dummy scan was run during this time to prevent field drift from gradient cooling. The mouse was then positioned back in the magnetic field, and a post-injection MGE3D scan carried out. Following this, with the mouse remaining inside the magnet, 30 µL of gadodiamide (Omniscan, GE Healthcare) was injected through the tail vein cannula, and after 5 min a T_1 weighted scan was carried out to assess BBB breakdown. Following the imaging session, brains were perfusion-fixed, and removed with tissue stored as described in Chapter 2.3.3. The MGE3D images were processed and analysed as described in Chapter 4.2.4.

To analyse whether retention of MPIO in the tissue was specific or macrophage associated, Prussian blue staining was performed as per the protocol described in Chapter 2.5.3. Separate tissue sections were also stained for Iba-1, integrin $\alpha_v\beta_3$, and VCAM-1 according to the protocols described in Chapter 2.5.1 and 2.5.2.

5.2.2 Retention of MPIO by tumour associated macrophages

5.2.2.1 Characterisation of Prussian blue localisation

In order to identify the aggregations of MPIO and the conditions under which they occur, consecutive tissue sections were stained for Perl's Prussian blue (as per Chapter 2.5.3), macrophage and microglia marker Iba-1, and blood vessel marker CD31 (as per Chapter 2.5.1).

Following this, double staining of Prussian blue with the macrophage and microglia marker Iba-1 was performed on tumour tissue that showed gadolinium enhancement on MRI. The standard immunohistochemistry staining protocol (described in Chapter 2.5.1) was performed with antibody combinations described in Chapter 2.4.1, as far as the DAB visualisation step. Following this, the Perl's Prussian blue protocol described in Chapter 2.5.3 was performed. Sections were then counterstained with nuclear fast red, dehydrated, cleared and coverslipped.

Double staining of Prussian blue with the blood vessel marker CD31 was performed as above, with the omission of the counterstaining step. Quantification of the aggregation distance from the vessels was performed by measuring the distance between the centre of the aggregation and the centre of the vessel lumen, where visible, or the centre of the vessel diameter where in profile. Quantification of single MPIO bound to vessels was also performed by manual counting of each section.

5.2.3 Effect of MPIO targeting moiety

5.2.3.1 *In vitro* uptake of MPIO

In order to determine whether peptide-conjugated and antibody-conjugated MPIO show different patterns of uptake *in vitro,* 4T1-GFP tumour cells and RAW-264.7 macrophages were seeded on 6 well plates following the procedures described in Chapter 2.2.3. When cells reached 80% confluency, 1 µg of RGD-MPIO, control RDG-MPIO, VCAM-MPIO and IgG MPIO were added to separate wells. Cells were incubated in a shaking incubator for 40 mins at 37° and 2500 rpm, then washed 5 times with PBS to remove any unbound MPIO. Cells were fixed with 4% paraformaldehyde for 20 minutes, then were examined under a Nikon Ti-E inverted microscope. Phase-contrast settings were used with a phase condenser at 20x magnification, and 0.33 µm resolution. Images were taken at random locations in each well, and MPIO were quantified by manual counting.

To analyse receptor-specific uptake in RAW264.7 macrophages, cells were seeded into 6 well plates as above. Cells were pre-treated with 0.1, 1 or 10 µL of 10 mM RGD or control RDG peptide; 0.1, 1 or 10 µg VCAM-1 or IgG antibody for 1 hour. Following this, 1 µg of the same MPIO as the blocking agent was administered. Cells were incubated in a shaking incubator for 40 mins at 37° and 2500 rpm, then washed 5 times with PBS to remove any unbound beads. Cells were fixed with 4% paraformaldehyde for 20 minutes, then were examined under a Nikon Ti-E inverted microscope, as above.

5.2.3.2 Antibody-targeted MPIO uptake *in vivo*

In order to determine whether peptide-conjugated and antibody-conjugated MPIO behave differently *in vivo,* tissue was sourced from previous studies in which antibody-targeted MPIO had been used in large tumour models, to enable comparison with macrophage uptake in tumours imaged with peptide-targeted MPIO. Frozen tissue sections from male RNU nude rats with primary (U87 human glioma) and secondary (MDA-231-Br metastatic human breast carcinoma) brain tumours were taken from animals that had been imaged with 4 mg/kg Fe in 100 µL sterile saline of either VCAM-MPIO (anti-VCAM-1 conjugated MPIO) or IgG-MPIO (isotype control non-specific antibody conjugated MPIO) at day 26 - 32. Tissue sections were stained with Perl's Prussian blue stain, as described in Chapter 2.5.3, and manual counting of blue aggregations was conducted. Low levels of pre-existing, pre-contrast hypointense voxels in the T_2*-weighted images were confirmed using historical imaging records, and animals with high levels of pre-existing hypointense voxels were excluded.

[Tumour tissue and corresponding imaging was donated by Dr Nick dePennington.]

Following this, antibody targeted VCAM-MPIO and IgG-MPIO were tested with the 4T1-GFP brain metastasis model. The brain metastasis model was established as described in Chapter 2.3.2. Imaging was undertaken using VCAM-MPIO at day 28 (n = 3); and with control IgG-MPIO at day 28 (n = 2). The imaging session consisted of (in order) T_1 and T_2 weighted anatomical imaging, pre- and post-MPIO injection MGE3D scans, and a gadolinium enhanced T_1 weighted scan, with the MPIO injection protocol described in Chapter 5.2.6 above. To analyse whether retention of MPIO in the tissue was specific or macrophage associated, Prussian blue staining was performed as per the protocol described in Chapter 2.5.3. Double

staining for Iba-1 combined with Prussian blue was also carried out, as was double staining for VCAM-1 and Prussian blue.

5.2.4 Endogenous iron-laden macrophages

In order to determine whether endogenous iron in tumour associated macrophages produces non-specific hypointense voxels in pre-contrast images, the 4T1-GFP tumour model was established as described in Chapter 2.3.2, and tumours grown to a single day 28 timepoint (n = 6). A gadolinium-enhanced T_1 weighted scan was carried out, along with a T_2* weighted MGE3D scan, but no MPIO were injected, in order to test for the presence of pre-existing hypointense voxels in the tumour, and whether these correspond with any pre-existing Prussian Blue positive aggregations. Tissue sections underwent staining for Prussian blue as described in Chapter 2.5.3, and iron-laden macrophages were manually counted. Double staining for Iba-1 combined with Prussian blue was then carried out.

Tissue was also sourced from previous studies in which immunocompetent mice grew intracerebral tumours, in order to quantify the presence of iron-laden macrophages across the tumour time-course. Remaining tissue from the 4T1-GFP histology study described in Chapter 4.2.1 was obtained, with timepoints of day 7 (n = 4), 14 (n = 4), 21 (n = 2), 28 (n = 4), and 35 (n = 3). These animals had no prior exposure to iron oxide contrast agents. Tissue sections underwent staining for Prussian blue as described in Chapter 2.5.3, and iron-laden macrophages were manually counted.

5.3 Results

5.3.1 MPIO penetration of the blood-brain barrier

5.3.1.1 Characterisation of an *in vivo* model of blood-brain barrier permeabilisation

In order to test whether in MPIO could cross a permeable BBB in the absence of a tumour, CINC-1 was used to create an *in vivo* model of BBB breakdown. A dose-response pattern was observed, with an increased dose of CINC-1 corresponding to an increased area of BBB breakdown, as measured by gadolinium enhancement. In the mice injected with the 2 µg dose, areas of haemorrhage were observed in both mice, as shown in Figure 5.3. As such, it was not possible to measure the enhancing lesion volume accurately, and the histology is obscured by large areas of haemorrhage. Although the mice displayed no outward signs of pain or brain injury, the 2 µg dose was excluded from further analysis, and is considered too high a dose for safe use in mice. The mean enhancing lesion volume was 6.1 ± 0.8 mm^3 for the 0.5 µg dose, and 10.2 ± 1.6 mm^3 for the 1 µg dose. The 1 µg dose more closely corresponded to the mean enhancing volume of the late stage tumour model, so it was chosen going forward into the main study.

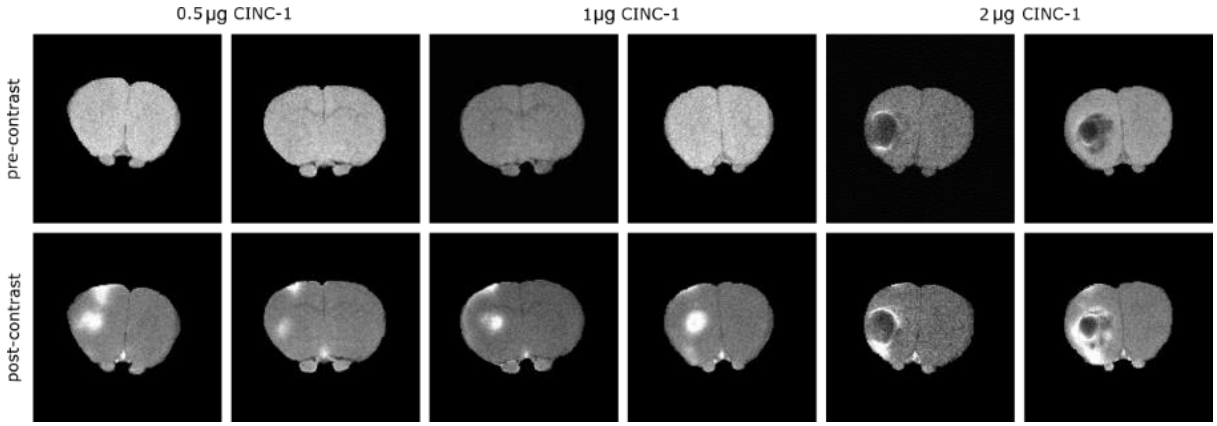


Figure 5.3: Frank BBB breakdown was induced by intracerebral injection of CINC-1. At the 0.5 µg and 1 µg doses, no obvious injury was seen to the brain in the pre-contrast T_1 weighted scans, but following gadolinium contrast injection, localised areas of BBB breakdown were evident in the striatum. At the 2 µg dose, haemorrhage (hypointense area) was evident in the pre-contrast scan, and hence this dose is considered not safe for use in mice.

BBB breakdown was also confirmed histologically in three mice receiving a 1 µg dose of CINC-1 using Hanker-Yates staining, as shown in Figure 5.4, and was localised to the ipsilateral striatum.



Figure 5.4: Histological confirmation of BBB breakdown in 3 independent mice injected with a 1 µg dose of CINC-1 in the left striatum. Dark brown areas indicate areas of BBB breakdown as demonstrated by HRP accumulation. [Staining and images provided by Dr Mario Munoz Pinto]

Histology showed increased expression of the macrophage/microglia marker Iba-1 at both doses of CINC-1 (Figure 5.5A,D), in the injected hemisphere but not the contralateral hemisphere. At the 0.5 µg dose, 0.18 - 0.85% of the injected striatum was positively stained, compared to 0.04 – 0.12% of the contralateral striatum. At the 1 µg dose, 0.71 – 1.2% of the injected striatum was positively stained, compared to 0.07 – 0.2% of the contralateral striatum (Figure 5.6A). Due to the small size of this pilot study (n = 2) statistical analysis was not carried out.

Analysis of the histology showed that integrin $\alpha_v\beta_3$ expression was upregulated at both doses of CINC-1 (Figure 5.5B,E), with 0.65 – 1.45 integrin $\alpha_v\beta_3$ positive vessels per mm^2 at the 0.5 µg dose, and 1.18 – 2.1 integrin $\alpha_v\beta_3$ positive vessels per mm^2 at the 1 µg dose (Figure 5.6B). VCAM-1 expression was also upregulated at both doses of CINC-1 (Figure 5.5C,F), with 8.5 – 11.5 VCAM-1 positive vessels per mm^2 at the 0.5 µg dose, and 10.6 – 11.8 VCAM-1 positive vessels per mm^2 at the 1 µg dose (Figure 5.6C). Neither integrin $\alpha_v\beta_3$ nor VCAM-1 positive vessels were observed in the hemisphere contralateral to the injection.

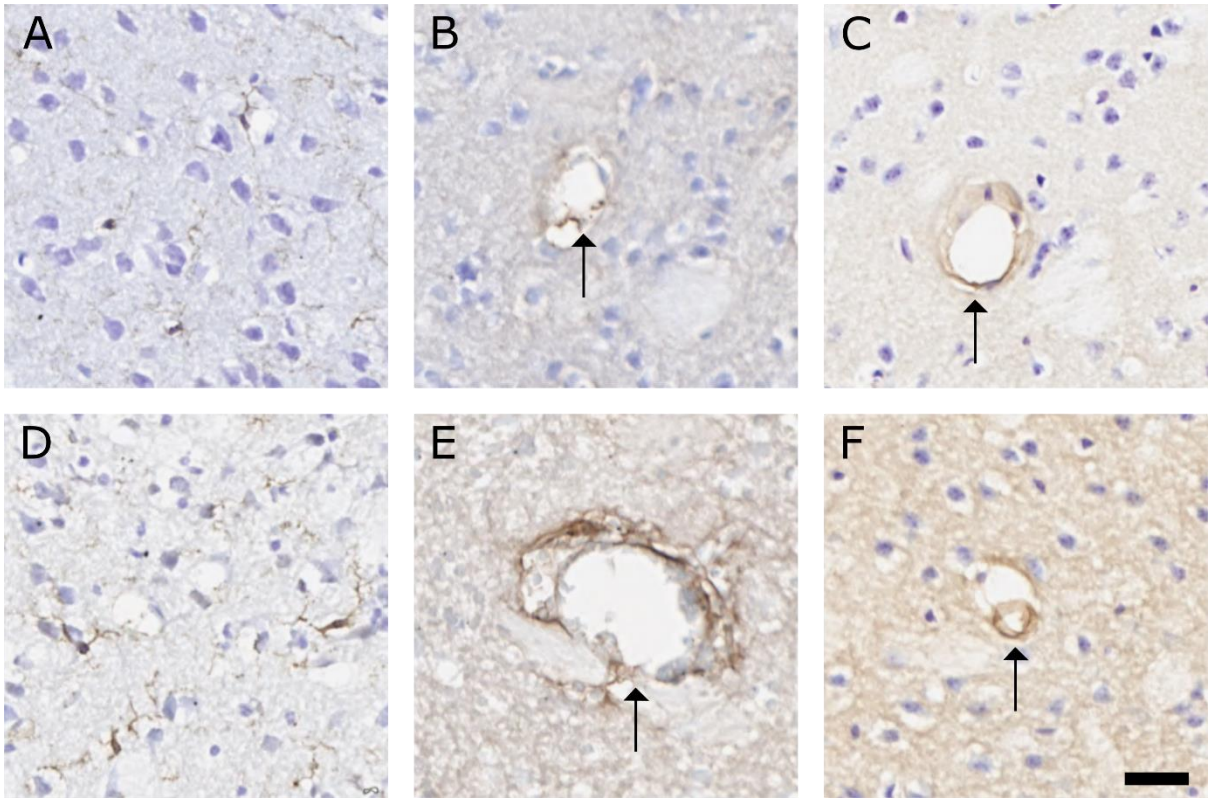


Figure 5.5: (A,D) Expression of Iba-1 (macrophages and microglia, brown staining). (B,E) Expression of integrin $\alpha_v\beta_3$ (brown staining). (C,F) Expression of VCAM-1 (brown staining) associated with frank BBB breakdown induced by 0.5 µg (A-C) or 1 µg (D-F) CINC-1. Arrows indicate positively stained blood vessels.

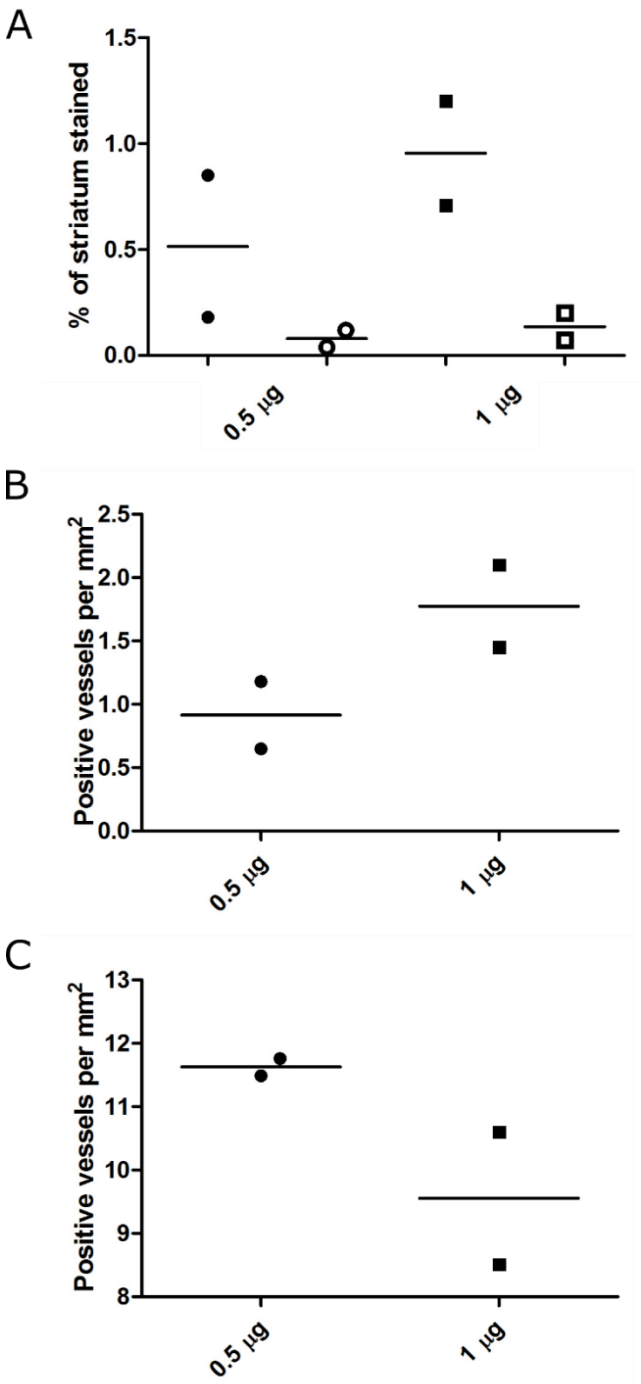


Figure 5.6: Graph showing expression of histological markers following intracerebral injection of CINC-1. (A) Expression of the macrophage/microglia marker Iba-1, in the CINC-1 injected (closed symbols) and contralateral (open symbols) hemispheres for 0.5 µg (circles) and 1 µg doses (squares). (B) Expression of VCAM-1 in the injected hemisphere for 0.5 µg (circles) and 1 µg doses (squares). No VCAM-1 expression was observed in the contralateral hemisphere. (C) Expression of integrin $\alpha_v\beta_3$ in the injected hemisphere for 0.5 µg (circles) and 1 µg doses (squares). No integrin $\alpha_v\beta_3$ expression was observed in the contralateral hemisphere. All data are presented as individual data points with a line representing the mean. N = 2.

5.3.1.2 MPIO penetration of a permeabilised blood-brain barrier

BBB breakdown was confirmed in all animals using gadolinium-enhanced imaging (Figure 5.7A). Across mice injected with 1 µg of CINC-1 and imaged with either RGD, control RDG, VCAM or IgG conjugated MPIO, the mean enhancing lesion volume did not differ between groups, and was 6.9 ± 4.6 mm^3 on average across all groups.

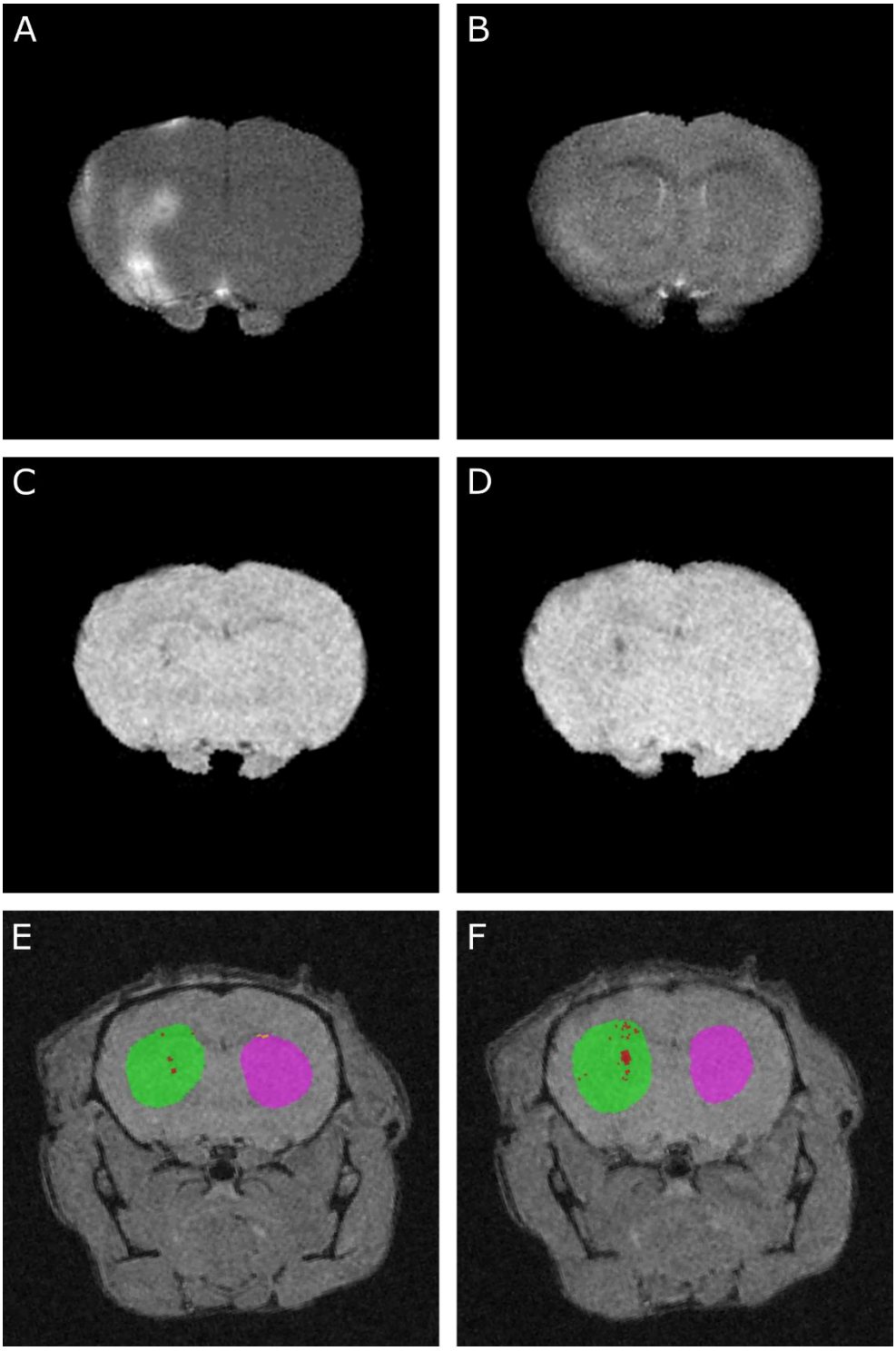


Figure 5.7: Example MR images following intracerebral injection of CINC-1, and imaging with RGD-MPIO. (A) Gadolinium enhanced T_1-weighted scan confirming areas of BBB breakdown. (B) T_2-weighted scan. (C) T_2*-weighted MGE3D scan before, and (D) after injection of RGD-MPIO. (E-F) In the pre- (E) and post-contrast (F) MGE3D images, the tumour-bearing striatum is segmented in green, and the contralateral striatum is segmented in pink. Hypointense voxels are shown in red.

In a number of mice (n = 1 RGD, n = 1 control RDG, n = 2 IgG), the hypointense voxels in the tumour-bearing striatum of the pre-contrast image were more numerous than those in the post-contrast image. This resulted in a negative difference in pre- minus post-contrast hypointense voxels. Images were inspected to ensure no artefacts were present that would affect image quality, nor any differences in SNR. As for the tumour model in Chapter 4, any MPIO-induced hypointense voxels in these mice fall within the noise range of this technique, and thus for further analysis those animals were assigned a value of zero MPIO-induced hypointense voxels instead of a negative value.

In mice across all groups, induced hypointense voxels post-MPIO injection were evident in the injected striatum, but not in the contralateral striatum (Figure 5.8). In the CINC-1 injected hemisphere, MPIO induced hypointense voxels were observed with RGD-MPIO (269 ± 232), control RDG-MPIO (147 ± 202), VCAM-MPIO (157 ± 108) and IgG-MPIO (71 ± 121). Analysis showed a trend towards increased MPIO induced hypointense voxels in the ipsilateral hemisphere for all MPIO types tested, but this effect was not statistically significant (paired t-test, $p > 0.05$).

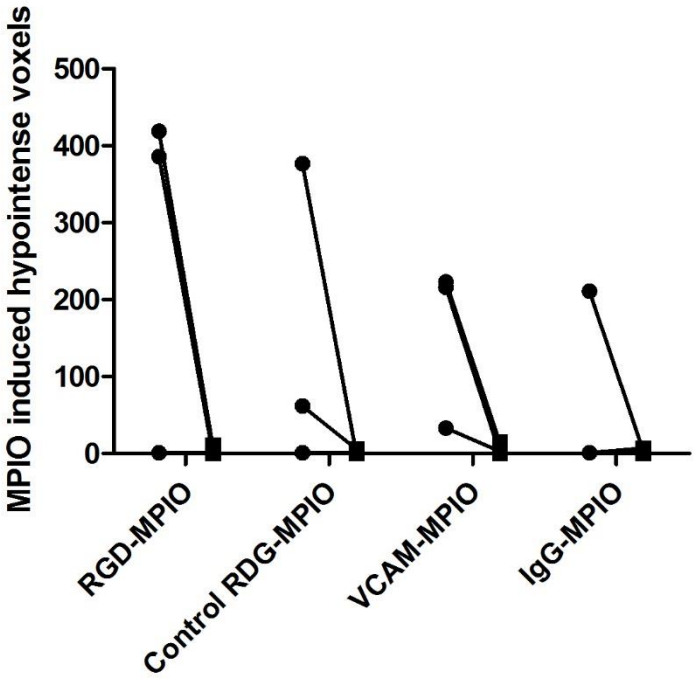


Figure 5.8: Graph showing MPIO induced hypointense voxels following BBB breakdown induced by intracerebral injection of 1 µg CINC-1. Analysis showed a trend towards increased MPIO induced hypointense voxels in the ipsilateral hemisphere (circles) compared to the contralateral hemisphere (squares) for all MPIO types tested, but this effect was not statistically significant (paired t-test, $p > 0.05$, $n = 3$ for all groups).

Following imaging, the brain tissue was examined histologically to determine whether MPIO-laden macrophage aggregations were present. Very few MPIO-laden macrophages were present in the injected hemisphere (Figure 5.9), and none were present in the contralateral hemisphere for any animal. Single MPIO were identified very rarely, and only in the injected hemisphere.

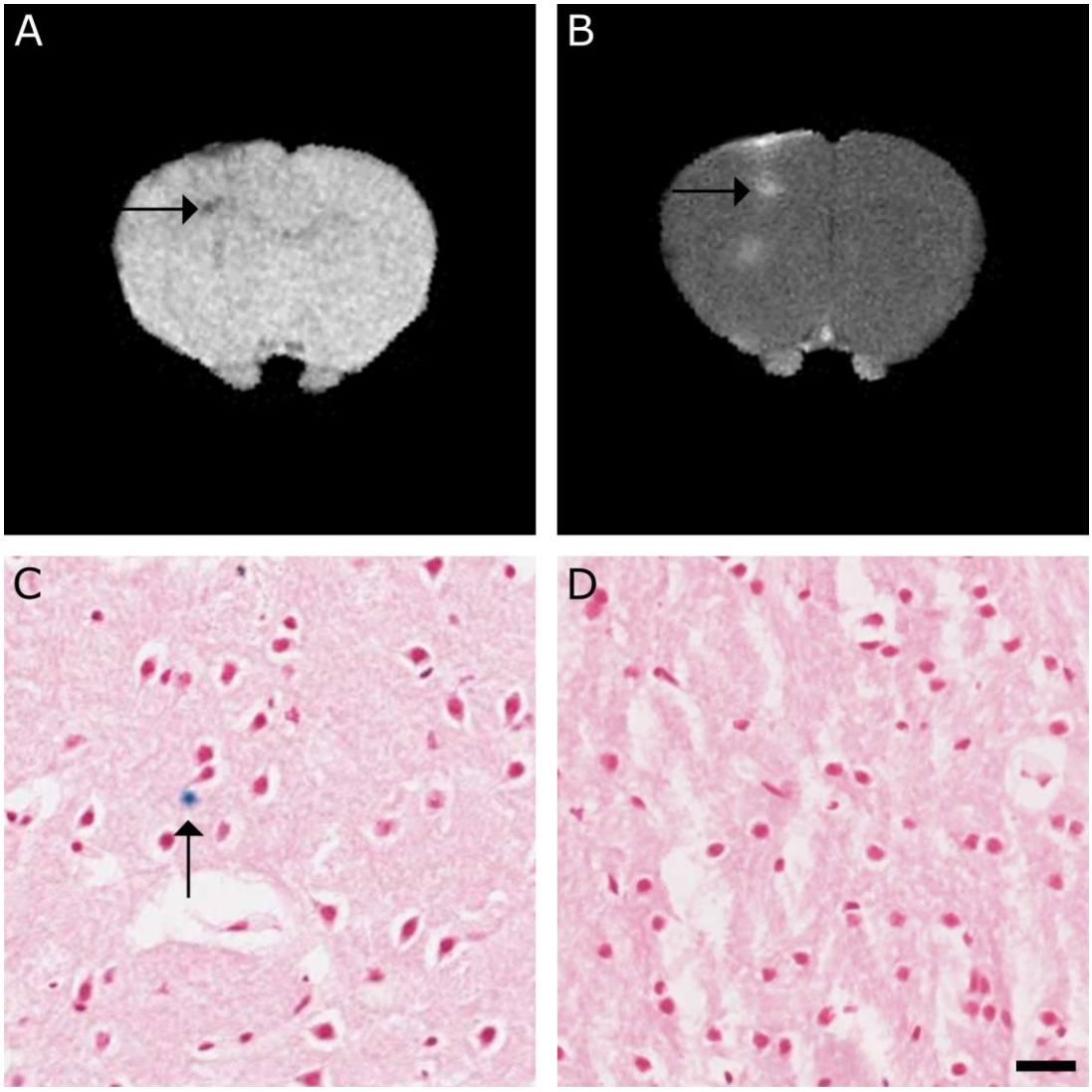


Figure 5.9: MPIO uptake in the brain following BBB breakdown induced by intracerebral injection of 1 µg CINC-1. (A) MPIO induced hypointense voxels in a post RGD-MPIO injection MGE3D scan are visible in the areas in which BBB breakdown has occurred (indicated by arrow). (B) Gadolinium enhanced T_1-weighted scan showing frank BBB breakdown (indicated by arrow). (C) Histological analysis shows no evidence of tissue damage, and only a single iron aggregation is present in the injected striatum (indicated by arrow). (D) No evidence of iron aggregations could be found in the contralateral striatum. Scale bar indicates 20 µm.

For mice imaged with RGD-MPIO, 0.89 ± 0.51 macrophage-like iron aggregations per tissue section were observed (Figure 5.10). 0.78 ± 0.51 macrophages per section were observed in mice imaged with control RDG-MPIO, 2.44 ± 0.77 macrophages per section were observed in mice imaged with VCAM-MPIO, and 0.78 ± 0.84 macrophages per section were observed in mice imaged with IgG-MPIO. No significant differences between groups were observed, although a trend towards increased aggregations in mice imaged with VCAM-MPIO was observed ($p = 0.06$). It should be noted, however, that these are still very small numbers of aggregations even in the VCAM-MPIO injected animals.

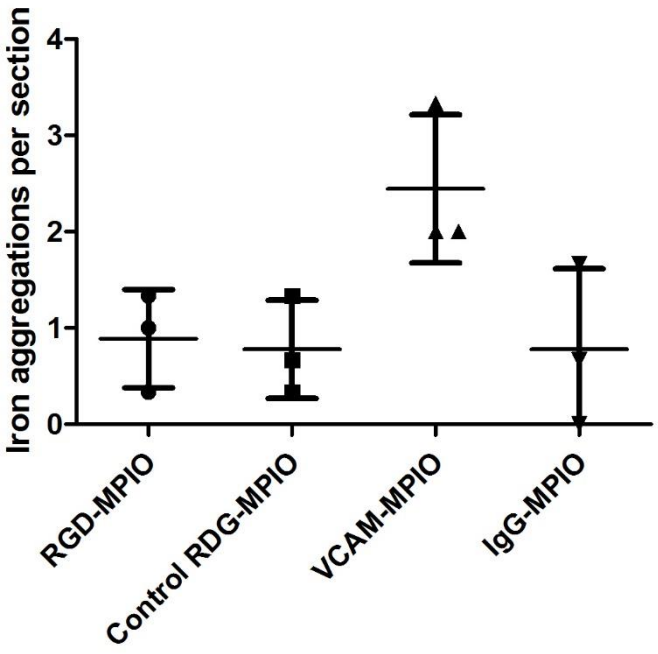


Figure 5.10: Graph showing quantification of iron aggregations in the injected hemisphere following BBB breakdown induced by intracerebral injection of 1 µg CINC-1, and imaged with RGD-MPIO, control RDG-MPIO, VCAM-MPIO, or IgG MPIO. No significant differences between groups were observed (1-way ANOVA, $p > 0.05$). Data are shown as individual data points, with error bars representing mean ± standard deviation.

5.3.2 Retention of MPIO by tumour associated macrophages

5.3.2.1 Characterisation of Prussian blue localisation

Initial staining of consecutive tumour sections from the enhancing 4T1-GFP tumours studied in Chapter 4, revealed that the apparent MPIO aggregations were located in similar spatial patterns to macrophages. The aggregations were in turn closely associated with blood vessels, as shown in Figure 5.11. In order to confirm this result, double staining of Perl's Prussian blue with the macrophage/microglia marker Iba-1 was carried out. These images showed that the aggregations of MPIO were present inside macrophages and/or microglia, as shown in Figure 5.12. Single MPIO were also occasionally visible outside of the macrophages in the tumour parenchyma.

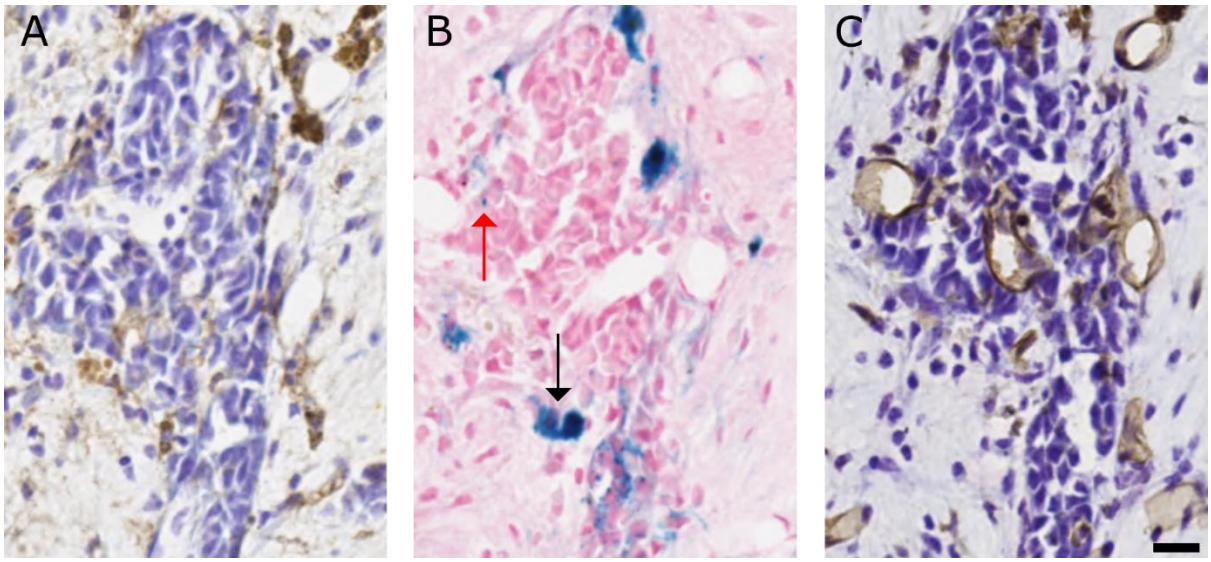


Figure 5.11: MPIO aggregations in the enhancing 4T1-GFP tumours from Chapter 4 appear to be macrophages associated with blood vessels. Consecutive sections stained for (A) Iba-1 (macrophages and microglia, brown staining), (B) Prussian Blue (iron) and (C) CD31 (blood vessels, brown staining) in a day 35 mouse injected with RGD-MPIO. Black arrow indicates macrophage-like aggregation, while red arrow indicates single MPIO. 20x magnification, scale bar indicates 10 µm.

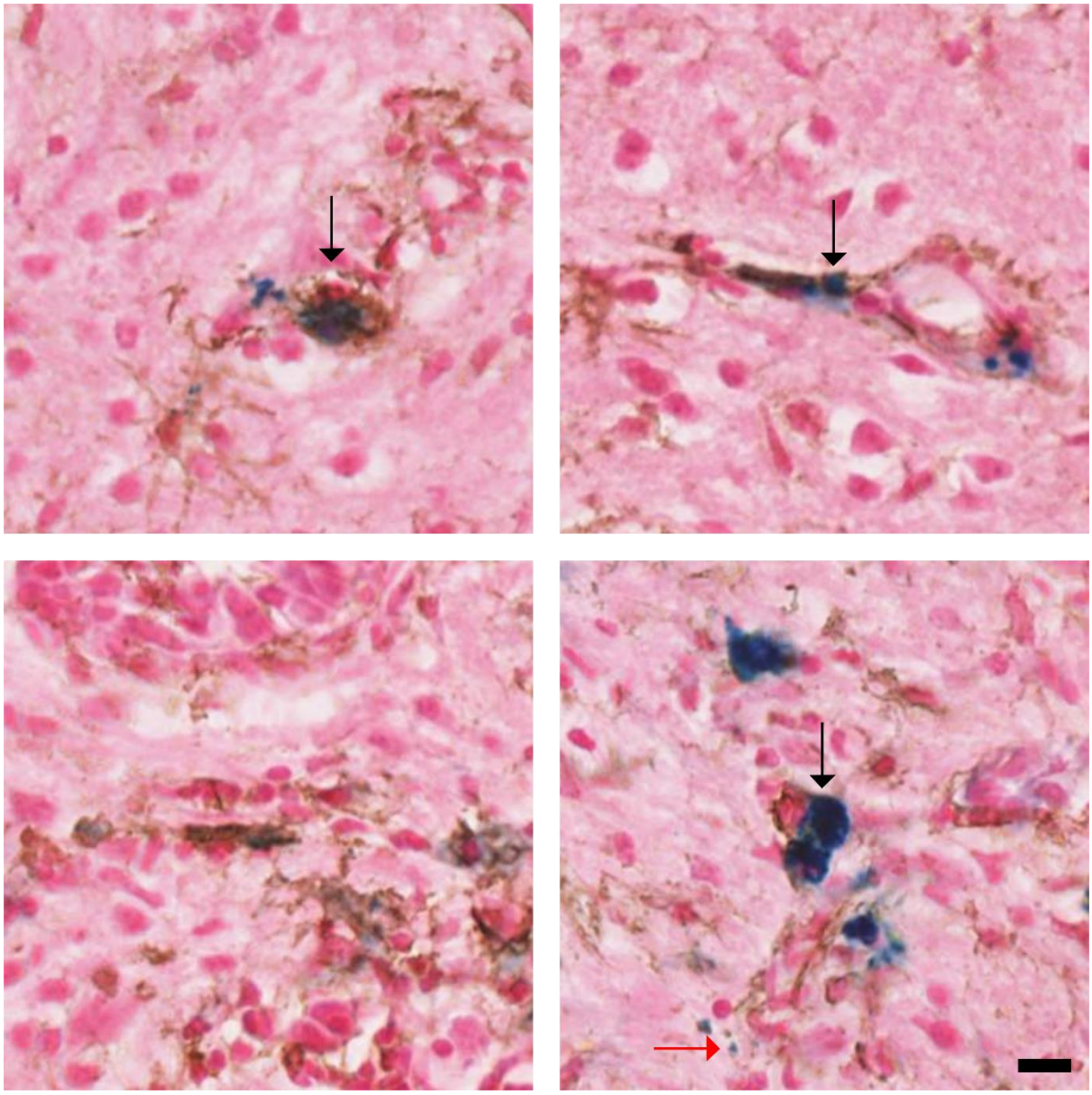


Figure 5.12: Aggregations are found inside macrophages and microglia. 4T1-GFP tumour tissue sections from a single mouse injected with RGD-MPIO at the day 35 timepoint is double stained for Prussian blue (iron) and macrophages/microglia (Iba-1, brown staining), and counterstained with nuclear fast red. Black arrows indicate macrophage-like aggregation, while red arrow indicates single MPIO. 40x magnification, scale bar indicates 10 µm.

In order to determine whether MPIO-laden macrophages were associated with tumour blood vessels, double staining for CD31 and Prussian blue was carried out. MPIO-laden macrophages were closely associated with blood vessels (Figure 5.13A), with a median value of 11 µm from the blood vessel lumen. Over 92% of MPIO-laden macrophages were within 25 µm of the blood vessel lumen, as shown in Figure 5.13B.

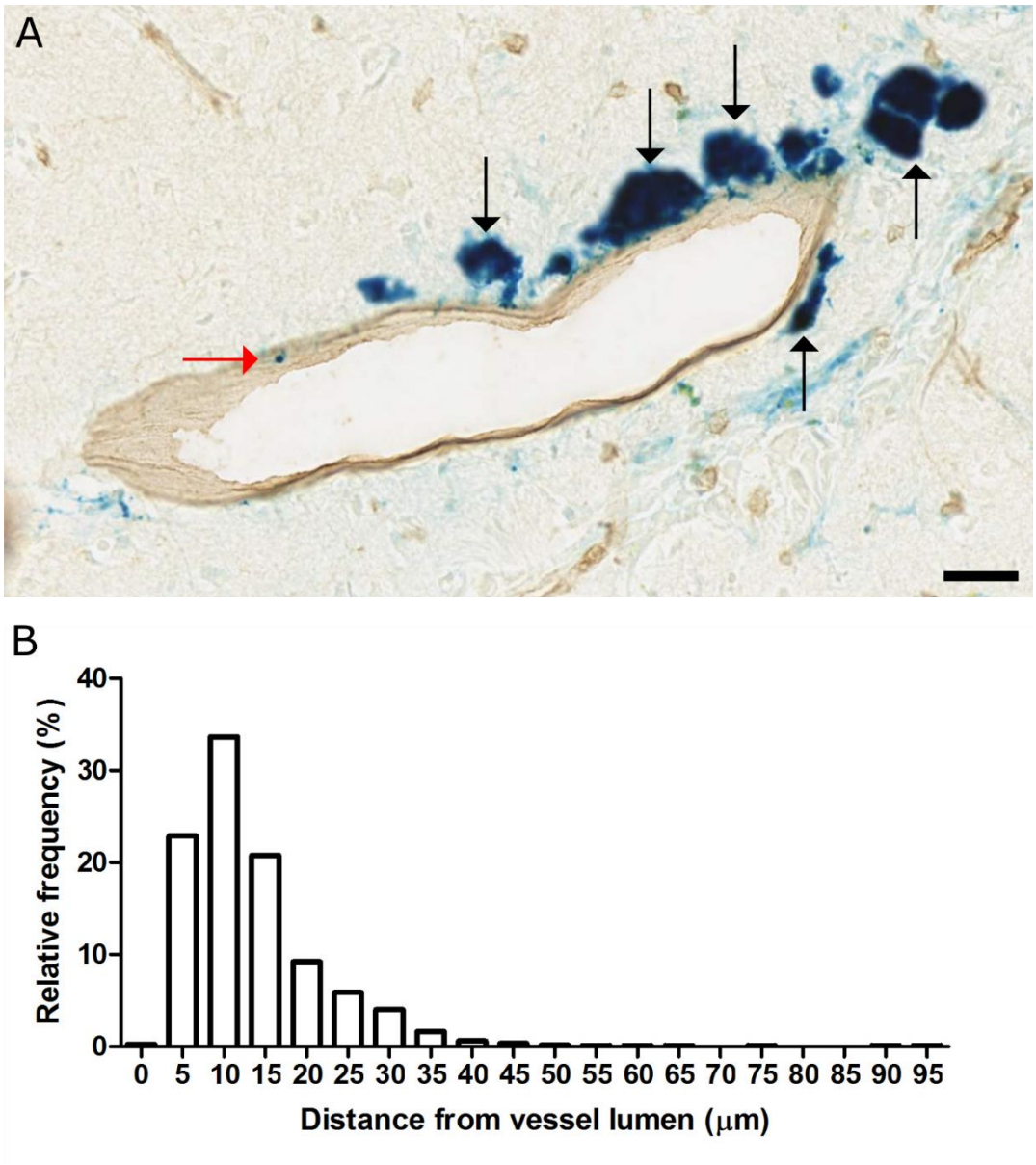


Figure 5.13: MPIO-laden macrophages are closely associated with blood vessels. (A) Tumour tissue from a mouse injected with RGD-MPIO at the day 35 timepoint is double stained for Prussian blue (iron) and CD31 (blood vessels, brown staining). Black arrows indicate macrophage-like aggregation, while the red arrow indicates single MPIO. 40x magnification, scale bar indicates 20 µm. (B) Histogram showing the relative frequency of the measured distance between the centre of the MPIO-laden macrophage and the centre of the blood vessel lumen. The median distance is 11 µm, and more than 90% of macrophages are within 25 µm of the blood vessel lumen.

In the enhancing 4T1-GFP tumours from Chapter 4, single MPIO were also observed bound to the endothelium in the enhancing tumour tissue sections, as shown in Figure 5.14. Single MPIO that were associated with blood vessels were manually counted, for both RGD-MPIO and control RDG-MPIO injected mice, as shown in Figure 5.15. In mice injected with RGD-MPIO, significantly more MPIO were bound per mm^2 of endothelium (943 ± 346 single MPIO), compared to 192 ± 62 single MPIO in mice injected with control RDG-MPIO (Figure 5.15, t-test, $p < 0.01$).

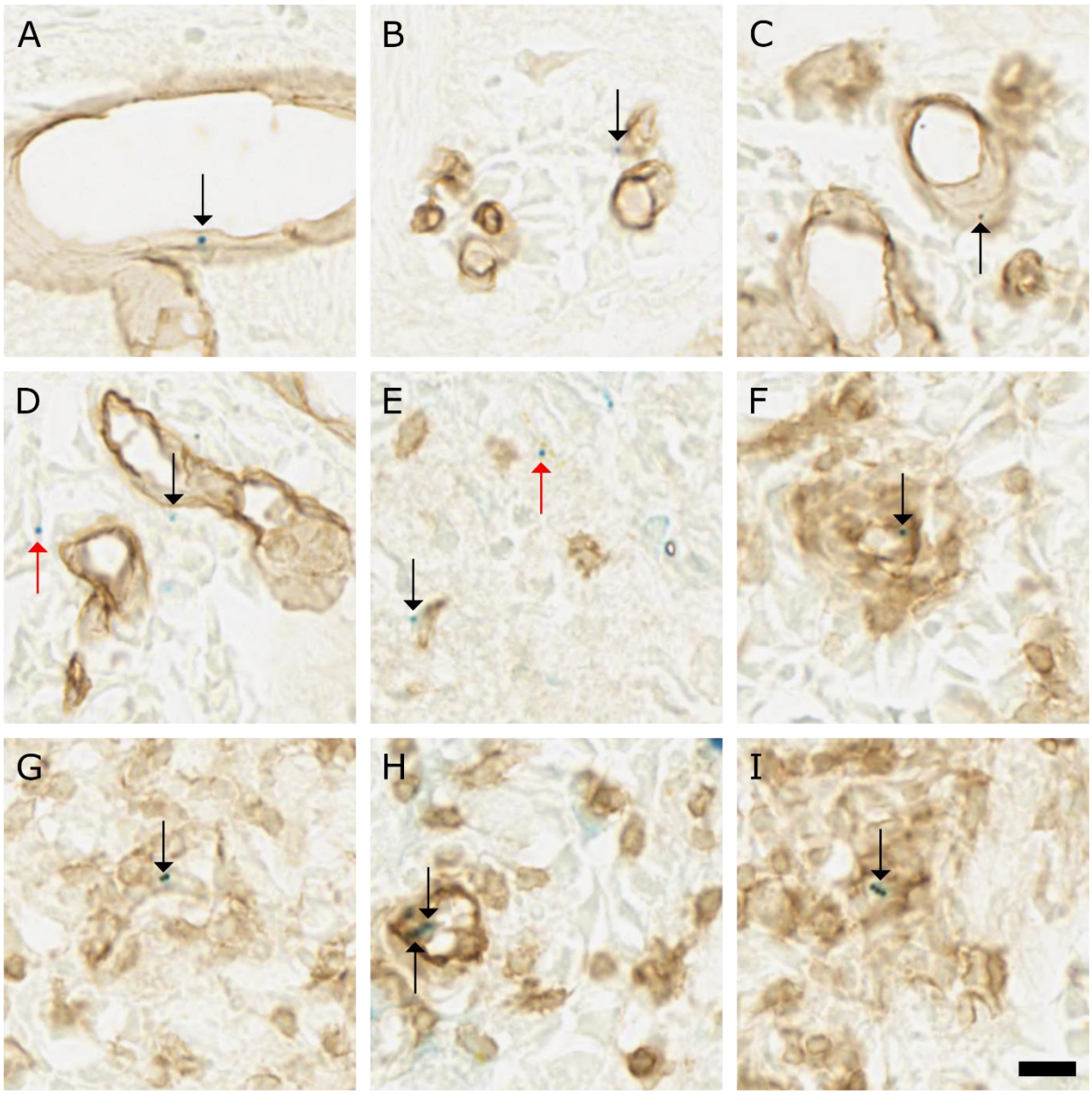


Figure 5.14: In the enhancing 4T1-GFP tumours from Chapter 4, single MPIO were found bound to blood vessels. Double staining for Prussian Blue (MPIO) and CD31 (brown, blood vessels) reveals single MPIO bound to blood vessels in mice injected with RGD-MPIO at the day 21 (A-B), 28 (C-E) and 35 (F-I) timepoints, as highlighted by black arrows. Single MPIO were occasionally observed in the tumour parenchyma (red arrows). Images taken at 40x magnification. Scale bar indicates 10 µm.

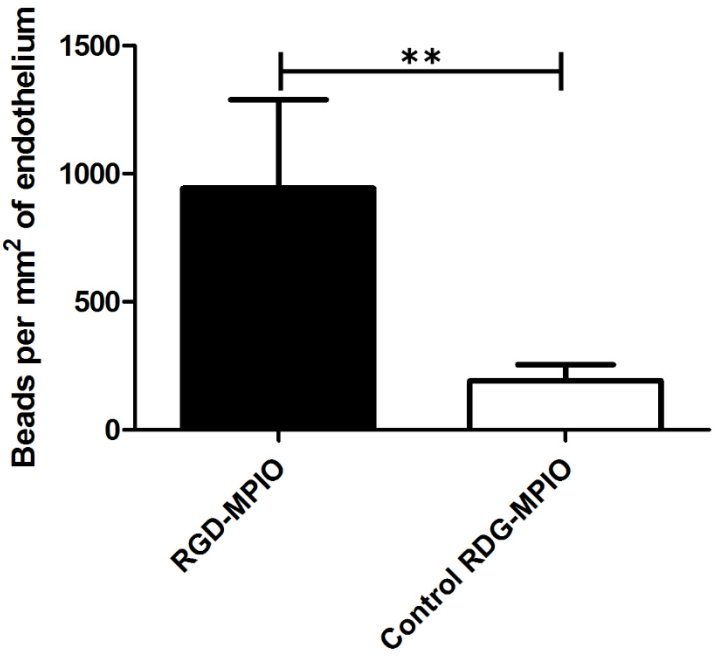


Figure 5.15: In the enhancing 4T1-GFP tumours from Chapter 4, single MPIO bound to the endothelium are observed more often in mice with enhancing tumours injected with RGD-MPIO (n = 10) than in those injected with control RDG-MPIO (n = 3, t-test, **p < 0.01).

5.3.3 Effect of MPIO targeting moiety

5.3.3.1 *In vitro* uptake of MPIO

The uptake of various types of MPIO by cells in culture was measured. Significantly fewer MPIO were taken up by 4T1-GFP tumour cells than by RAW 264.7 macrophages for all four MPIO types tested (Figure 5.16 and Figure 5.17A-B; 2 way ANOVA, $p < 0.001$).

In order to determine whether MPIO uptake in macrophages was receptor specific, the above experiment was repeated following 1 hour of blocking with either RGD or control RDG peptides (Figure 5.17C-D). No significant differences were found between treated and untreated groups. Receptor specificity testing was also repeated following 1 hour of blocking with either VCAM-1 or IgG antibodies (Figure 5.17E-F). No significant differences were found between treated and untreated groups.

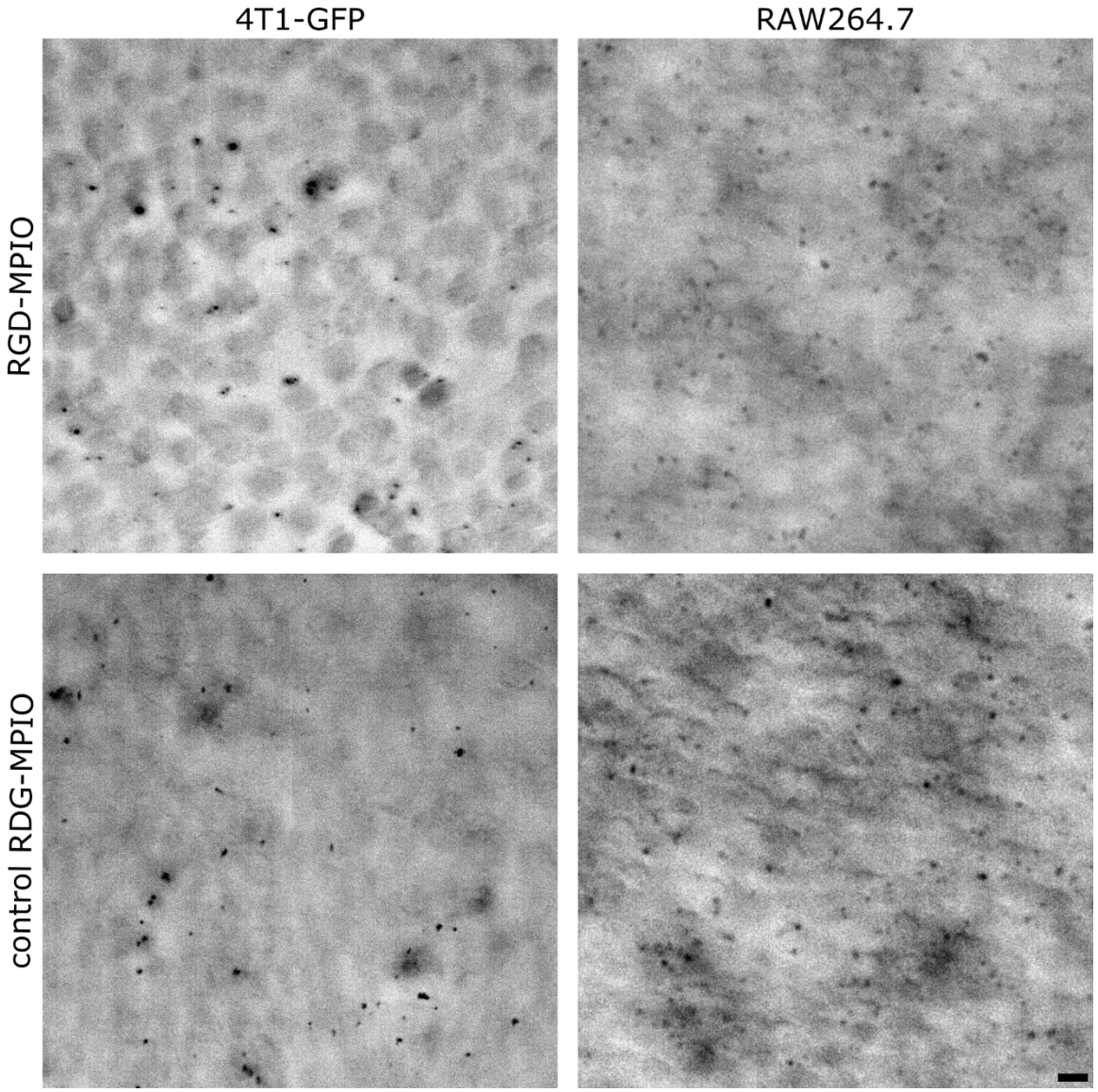


Figure 5.16: Phase contrast microscopy images showing *in vitro* uptake of MPIO by 4T1-GFP tumour cells and RAW264.7 macrophages. Significantly higher uptake of both RGD-MPIO and control RDG-MPIO was observed in the RAW264.7 macrophages (2-way ANOVA, $p < 0.001$). 20x magnification, scale bar indicates 10 µm.

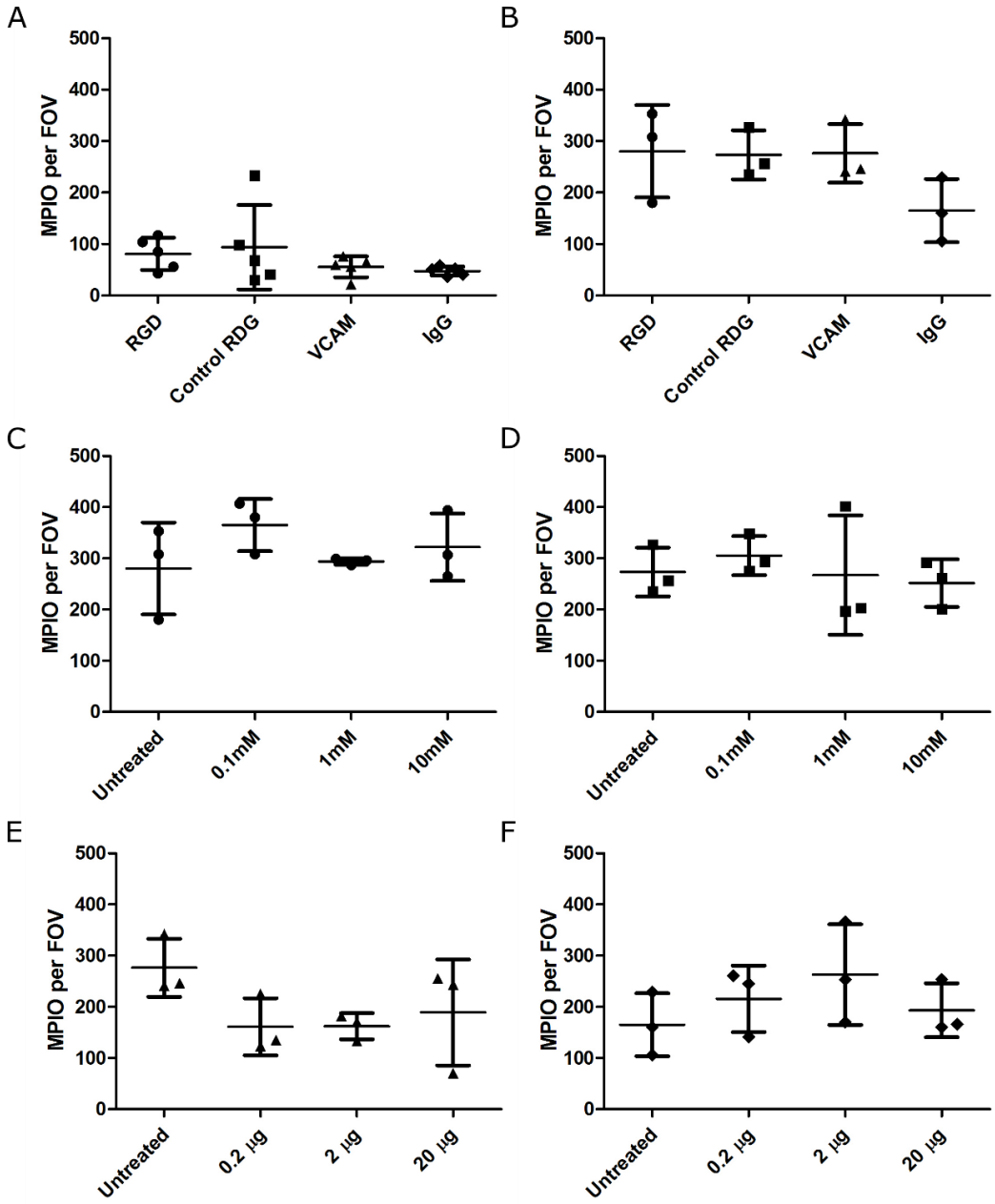


Figure 5.17: Uptake of MPIO by macrophages. (A) Uptake of all four types of MPIO (RGD, control RDG, VCAM, IgG) by 4T1-GFP tumour cells. (B) Uptake of all four types of MPIO by RAW 264.7 macrophages. Uptake was significantly higher in macrophages than for 4T1-GFP cells (2-way ANOVA, $p < 0.001$) for all MPIO types (Bonferroni post-hoc tests $p < 0.05$). (C) Uptake of RGD-MPIO by RAW264.7 macrophages following pre-treatment with increasing concentrations of RGD peptide. (D) Uptake of control RDG-MPIO by RAW264.7 macrophages following pre-treatment with increasing concentrations of control RDG peptide. (E) Uptake of VCAM-MPIO by RAW264.7 macrophages following pre-treatment with increasing concentrations of VCAM-1 antibody. (F) Uptake of IgG-MPIO by RAW264.7 macrophages following pre-treatment with increasing concentrations of IgG antibody. Data are shown as individual data points, with lines representing mean ± standard deviation.

5.3.3.2 Antibody-targeted MPIO uptake *in vivo*

Donated tissue and images from rats bearing MDA-231-Br breast cancer brain metastases, or U87 glioma tumours, which had been imaged with antibody-conjugated MPIO were analysed for evidence of MPIO-laden macrophages (Figure 5.18).

Analysis of T_2* weighted imaging revealed that MPIO induced hypointense voxels were present in all rats imaged with VCAM-MPIO (post- minus pre-contrast hypointense voxels as a percentage of the tumour bearing hemisphere, 1.59 ± 1.15% for U87 tumours, and 0.25 ± 0.09% for MDA-231-Br tumours, Figure 5.19). MPIO induced hypointense voxels were only present at very low levels in rats imaged with control IgG-MPIO (0.055 ± 0.07% for U87 tumours, and 0.028 ± 0.019% for MDA-231-Br tumours). Significantly more MPIO induced hypointense voxels were observed in the rats imaged with VCAM-MPIO than with IgG MPIO for both U87 (t-test, $p < 0.05$) and MDA-231-Br tumours (t-test, $p < 0.001$).

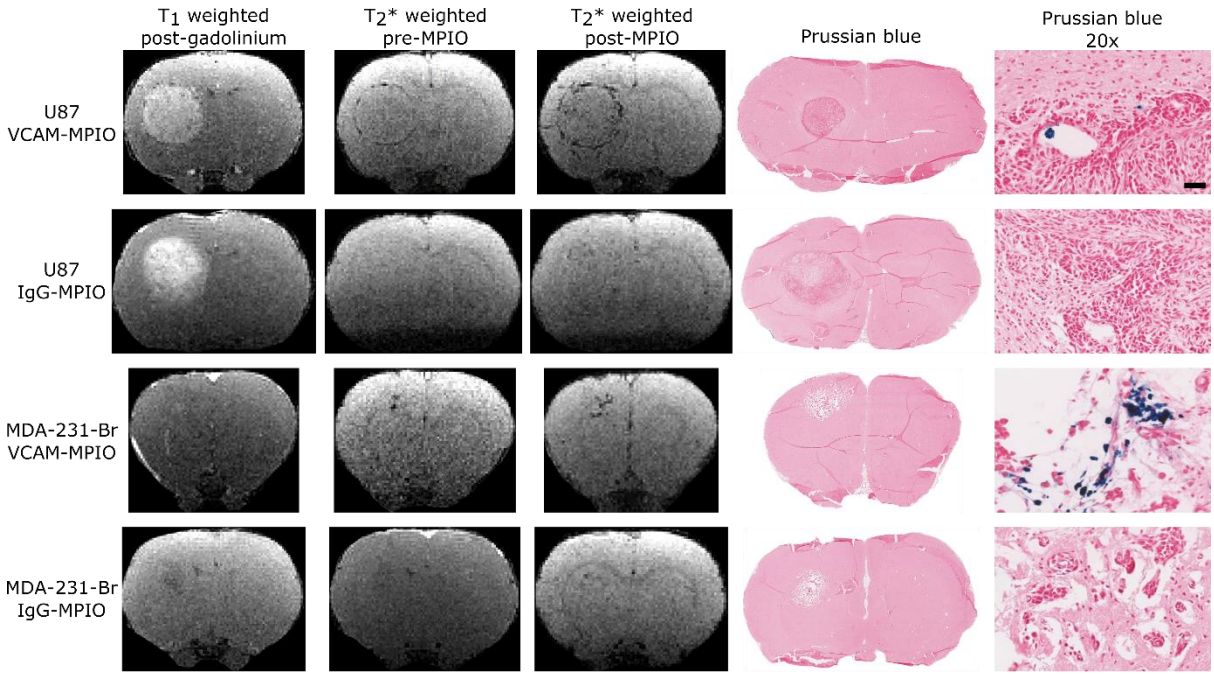


Figure 5.18: Example MRI and histology images from rats with U87 glioma or MDA-231-Br breast cancer brain metastases. Histology images are stained for Prussian blue (iron – blue) and counterstained with nuclear fast red (nuclei – pink). Scale bar indicates 25 µm for all 20x histology images. [MRI images and tumour tissue donated by Mr Nick De Pennington]

Analysis of the histology using Prussian blue staining showed that only low levels of MPIO-laden macrophages were observed in all animals, except one that showed substantially higher numbers (MDA-231-Br, VCAM-MPIO, shown in Figure 5.18). No significant differences were evident between groups (Figure 5.19). For the U87 tumours, in those imaged with targeted VCAM-MPIO 9.25 ± 12.99 MPIO-laden macrophages per section were observed, and in those imaged with control IgG-MPIO 7.58 ± 7.19 MPIO-laden macrophages per section were observed. For the MDA-231-Br tumours, in those imaged with targeted VCAM-MPIO 19.0 ± 38.2 MPIO-laden macrophages per section were observed, and in those imaged with control IgG-MPIO 2.73 ± 2.25 MPIO-laden macrophages per section were observed.

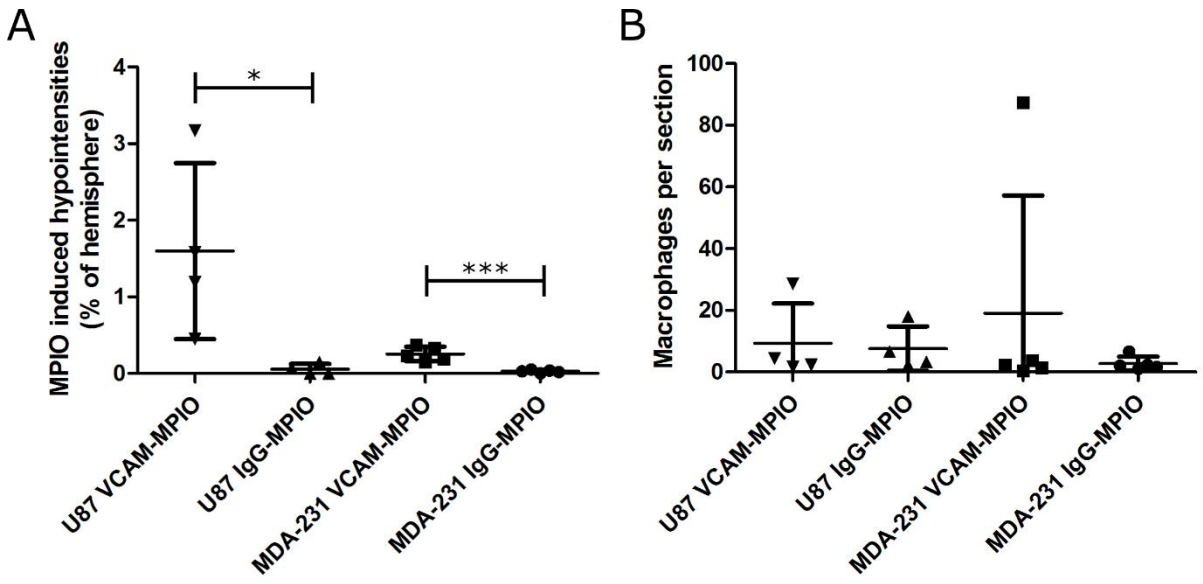


Figure 5.19: Quantification of imaging and histology parameters in rat models of U87 glioma and MDA-231-Br breast cancer brain metastases. (A) Graph showing MPIO induced hypointense voxels, reported as post- minus pre-contrast hypointense voxels as a percentage of the tumour bearing hemisphere. Significantly more MPIO induced hypointense voxels were present in the U87 tumours imaged with VCAM-MPIO compared to the control IgG-MPIO (t-test $p < 0.05$, $n = 4$). Significantly more MPIO induced hypointense voxels were also present in the MDA-231-Br tumours imaged with VCAM-MPIO compared to the control IgG-MPIO (t-test $p < 0.001$, $n = 5$). (B) Graph showing the number of MPIO-laden macrophages per tissue section. Only one animal with an MDA-231-Br tumour and imaged with VCAM-MPIO showed a high number of MPIO-laden macrophages. No significant differences were evident between groups. $*p < 0.05$, $***p < 0.001$. [MRI images and tumour tissue donated by Mr Nick De Pennington]

The above studies were conducted in rat models; to determine whether antibody-conjugated MPIO would have the same effects in mice, the 4T1-GFP tumour model was also analysed. Mice bearing 4T1-GFP tumours were imaged at the day 28 timepoint with either targeted VCAM-MPIO, or control IgG-MPIO. In the mice receiving VCAM-MPIO, MPIO induced hypointense voxels (post-contrast minus pre-contrast hypointense voxels) were observed in the tumour bearing striatum (Figure 5.20, 1993 ± 2621 MPIO induced hypointense voxels). In the contralateral striatum, the hypointense voxels in the pre-contrast image were more numerous than those in the post-contrast image for each animal. This resulted in a negative difference in post-contrast minus pre-contrast hypointense voxels. Images were inspected to ensure no artefacts were present that would affect image quality, or any differences in SNR. In the absence of any technical basis for this observation, it was concluded that MPIO-induced hypointense voxels in these mice fall within the noise range of this technique and, thus, were allocated a result of zero MPIO induced hypointense voxels for further analysis. The differences between the tumour-bearing and contralateral striatum, whilst large, are not statistically significant, possibly due to the small sample size of this pilot study.

Similarly, in mice receiving the control IgG-MPIO, in the tumour-bearing striatum, the hypointense voxels in the pre-contrast image were more numerous than those in the post-contrast image, and thus were allocated a result of zero MPIO induced hypointense voxels for further analysis. In the contralateral striatum, very few MPIO induced hypointense voxels were observed (18 ± 2), which are within the noise range of this technique.

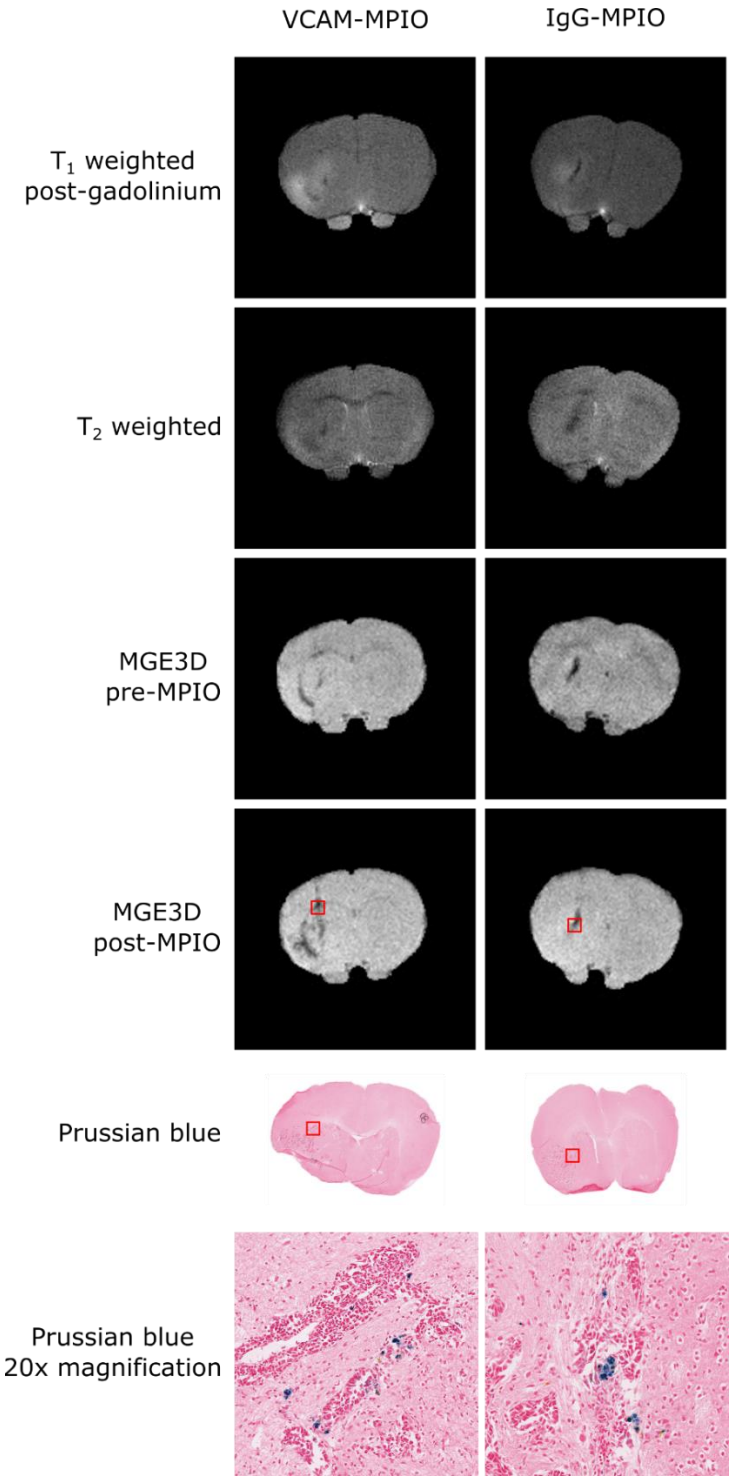


Figure 5.20: Example MRI and histology images from mice with 4T1-GFP brain metastases. Significantly more hypointense voxels were seen in the post-MPIO MGE3D images than in the pre-MPIO MGE3D images in mice imaged with VCAM-MPIO, but not in mice imaged with IgG-MPIO. Insets at 20x magnification correspond to red highlighted regions. The location of apparent MPIO-laden macrophages corresponds to hypointense regions in the pre-contrast MGE3D images. In mice imaged with VCAM-MPIO, hypointense voxels induced by specific endothelial binding can be seen in the post-contrast MGE3D images.

Analysis of the histology using Prussian blue staining showed similar levels of apparent MPIO-laden macrophages between mice imaged with VCAM-MPIO (40.9 ± 52.4) and IgG-MPIO (50.2 ± 64.8), with no significant differences between groups (Figure 5.21). Two mice, one imaged with VCAM-MPIO and one imaged with IgG-MPIO, showed markedly higher levels of MPIO-laden macrophages. These were both large, gadolinium-enhancing tumours

A correlation analysis was performed to determine whether the apparent MPIO-laden macrophages correlated with the quantity of pre-existing pre-contrast hypointense voxels in the MGE3D imaging (Figure 5.21). A significant correlation was found using linear regression ($p < 0.05$, $R^2 = 0.86$).

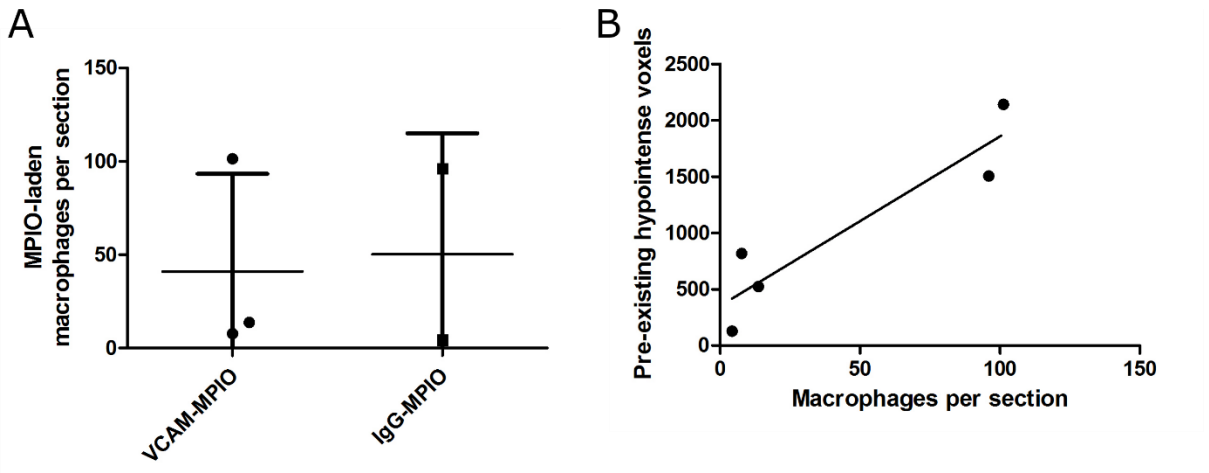


Figure 5.21: Quantification of imaging and histology in the 4T1-GFP metastasis model at day 28, imaged with antibody-conjugated MPIO. (A) Graph showing the number of apparent MPIO-laden macrophages per tissue section. In each group, one animal showed large numbers of MPIO-laden macrophages. No significant differences were found between groups. Bars represent mean ± standard deviation. (B) Graph showing a significant correlation between the number of apparent MPIO-laden macrophages per section and the number of pre-existing pre-contrast hypointense voxels in the MGE3D images ($p < 0.05$, $R^2 = 0.86$).

Double staining for both Prussian blue and VCAM-1 revealed that in addition to apparent MPIO-laden macrophages, single MPIO were present bound to VCAM-1 positive blood vessels in mice imaged with VCAM-MPIO, but not in mice imaged with control IgG-MPIO (Figure 5.22).

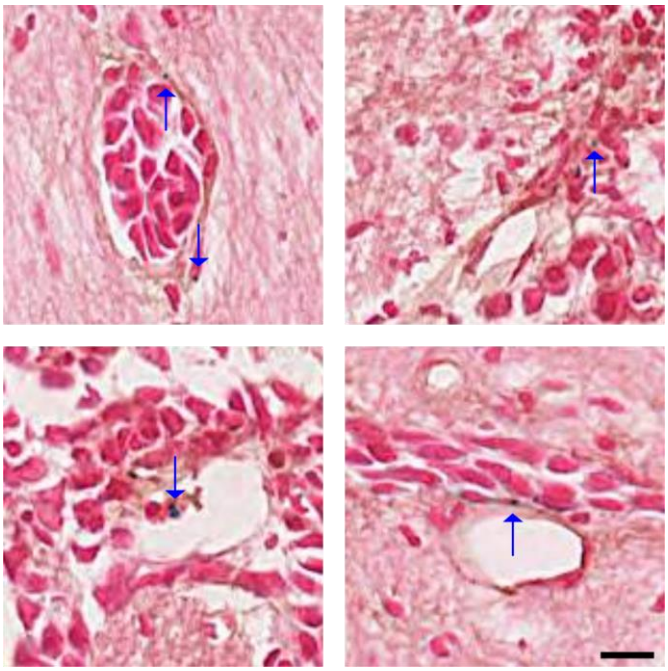


Figure 5.22: Histology sections from 4T1-GFP tumours imaged with VCAM-MPIO, double stained for VCAM-1 (brown), Prussian blue (iron, blue), and counterstained for nuclear fast red (nuclei, pink). Images show single VCAM-MPIO bound to VCAM-1 positive blood vessels, highlighted by blue arrows. Scale bar indicates 10 µm in all images.

5.3.4 Endogenous iron-laden macrophages

Data shown in the previous section raised the question of whether iron-laden macrophages observed in the tumour model were in fact MPIO-laden macrophages, or were endogenous iron-laden macrophages, owing to their spatial correlation with pre-existing hypointense voxels. In mice with 4T1-GFP tumours, and with no exposure to iron oxide contrast agents, levels of endogenous iron-laden macrophages in the tumour tissue were quantified across the tumour timecourse.

Low levels of endogenous iron-laden macrophages were observed in the tumour tissue across all timepoints (Figure 5.23), and were histologically indistinguishable from the apparent MPIO-laden macrophages observed in the previous section. At day 7, on average 11.3 ± 10.9 macrophages per tissue section were observed, with 1.9 ± 2.7 at day 14, 9.2 ± 13.0 at day 21, 19.6 ± 27.4 at day 28, and 3.3 ± 1.2 at day 35 (Figure 5.23). No statistically significant differences were evident between groups (Kruskal-Wallis test, $p > 0.05$). When endogenous iron-laden macrophage levels were compared to tumour size, no significant correlation was found (Figure 5.23, $R^2 = 0.08$, linear regression $p > 0.2$).

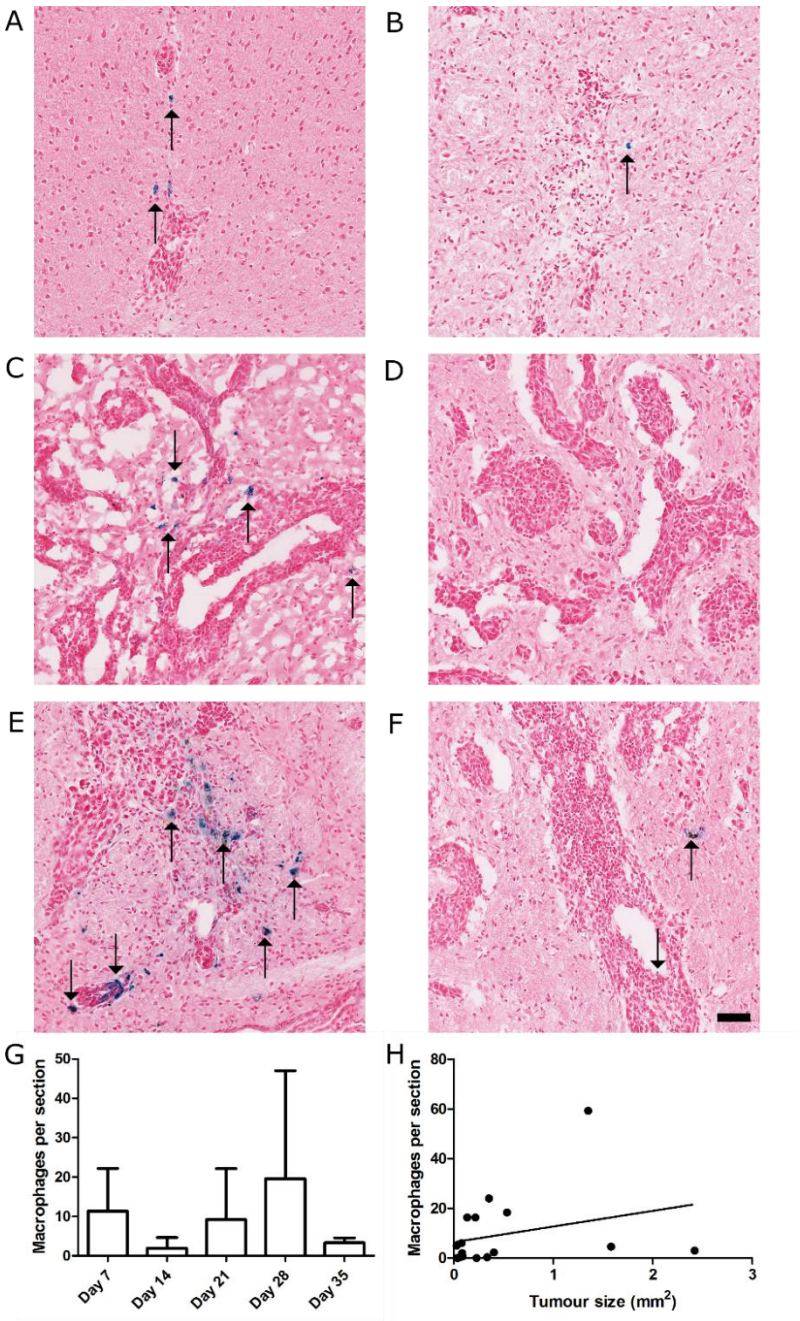


Figure 5.23: Quantitation of endogenous iron-laden macrophages in the 4T1-GFP model across the tumour timecourse, in mice with no exposure to iron oxide contrast agents. (A-F) Histology sections stained for Prussian blue (iron, blue), and counterstained with nuclear fast red (nuclei, pink). Scale bar indicates 40 µm in all images, arrows show iron-laden macrophages. Representative images from (A) day 7, (B) day 14, (C) day 21, (D) a day 28 tumour with low levels of endogenous iron-laden macrophages, (E) a day 28 tumour of a similar size with high levels of endogenous iron-laden macrophages, and (F) day 35. (G) Graph showing numbers of endogenous iron-laden macrophages per tissue section. Endogenous iron-laden macrophages are present at all timepoints, but no significant differences were found between timepoints. (H) Graph showing relationship between the number of endogenous iron-laden macrophages per section and the tumour size. Numbers of endogenous iron-laden macrophages show no significant correlation with tumour size ($R^2 = 0.08$, $p > 0.2$, $n = 17$)

In order to determine whether these tumour-associated, endogenous iron-laden macrophages are a cause of pre-existing hypointense voxels seen in the MGE3D imaging in the previous chapter, 4T1-GFP tumours at the day 28 timepoint were imaged using the T_2* weighted MGE3D sequence (Figure 5.24). These data were compared with Prussian blue stained histological sections (Figure 5.25). The tumours had varying levels of pre-existing hypointense voxels in the tumour bearing striatum (720 ± 570; Figure 5.26). In contrast, the contralateral striatum had very few pre-existing hypointense voxels (57 ± 21). In all cases, significantly more pre-existing hypointense voxels were evident in the tumour-bearing striatum than in the contralateral striatum (paired t-test, $p < 0.05$, Figure 5.26). The levels of pre-existing hypointense voxels in this study are similar to the levels of pre-contrast hypointense voxels observed in the 4T1-GFP tumour model in Chapter 4.

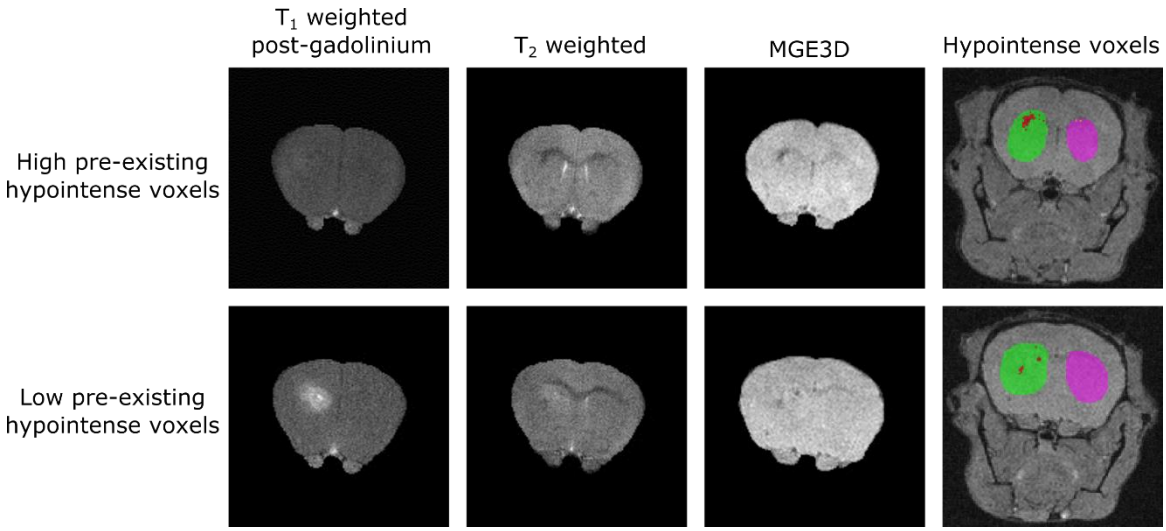


Figure 5.24: Representative MRI images showing pre-existing hypointense voxels in mice with day 28 4T1-GFP tumours and no exposure to iron oxide contrast agents. Mice with high (top row, >1000) and low (bottom row, <400) levels of pre-existing hypointense voxels are shown. Hypointense voxels in the tumour bearing striatum (green) are shown in red, and hypointense voxels in the contralateral striatum (pink) are shown in yellow.

Analysis of the histology from these mice showed that, despite no exposure to iron oxide contrast agents, endogenous iron-laden macrophages were present in the tumour tissue, and closely matched the location of the pre-existing hypointense voxels in the MGE3D images (Figure 5.25). Double staining for Prussian blue and the macrophage/microglia marker Iba-1 showed that the iron aggregations were co-localised with the Iba-1 staining (Figure 5.25).

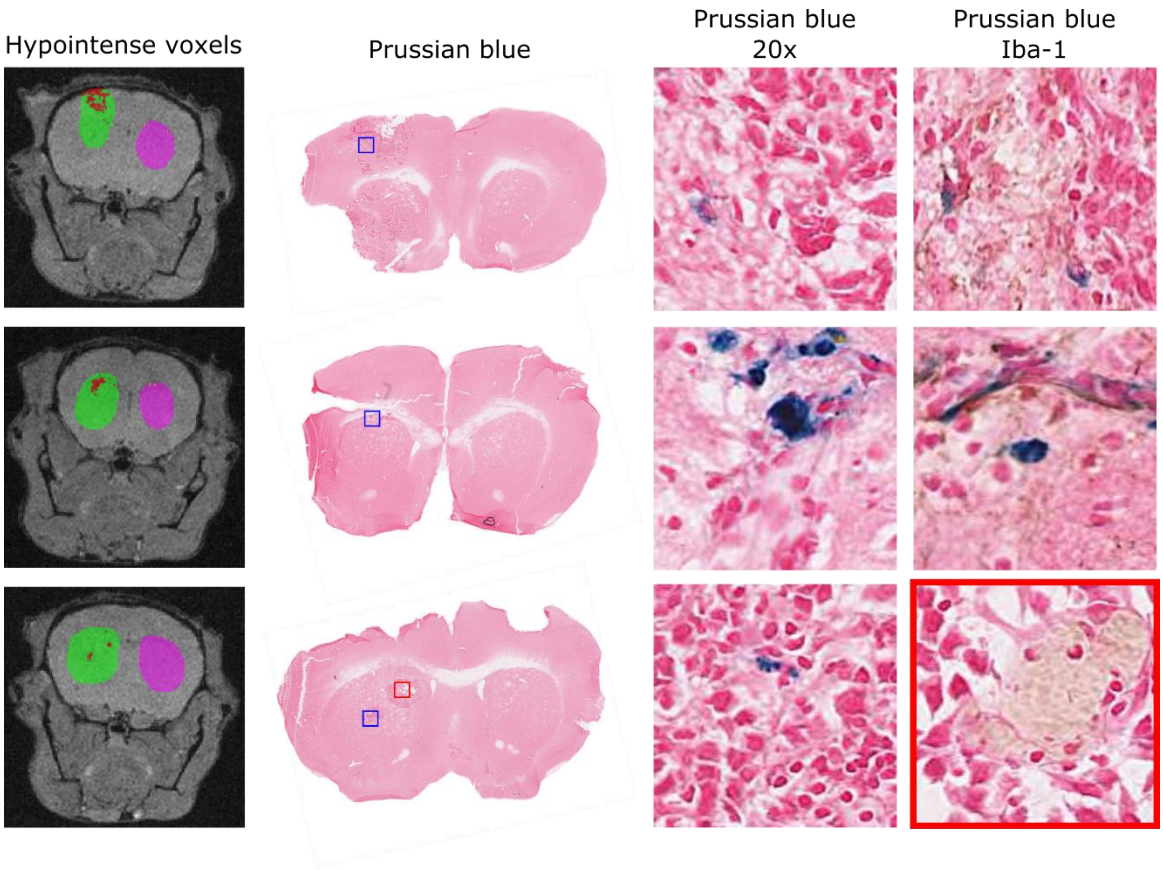


Figure 5.25: Representative images showing pre-existing hypointense voxels in mice with day 28 4T1-GFP tumours and no exposure to iron oxide contrast agents. Hypointense voxels in the tumour bearing striatum (green) are shown in red, the contralateral striatum is shown in pink. Histology sections stained for Prussian blue (iron, blue) and counterstained with nuclear fast red (nuclei, pink) are shown. Insets show 20x magnification of the areas indicated by blue boxes. In the bottom row, areas of micro-haemorrhage are shown in the inset indicated by a red box. The location of endogenous iron-laden macrophages correspond to hypointense voxels in the MGE3D images. An inset of Prussian blue staining at 20x magnification is also shown. A second inset in the far right column shows section double stained for Prussian blue and the macrophage/microglia marker Iba-1.

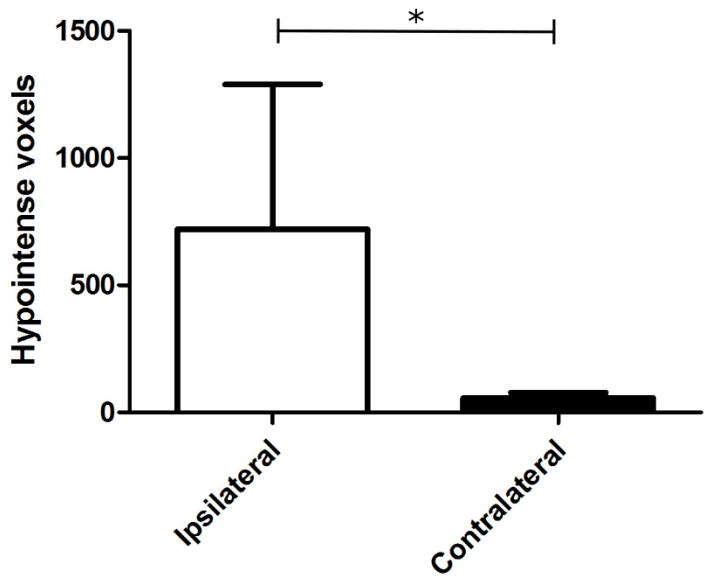


Figure 5.26: Graph showing pre-existing hypointense voxels in 4T1-GFP tumours at the day 28 timepoint, in mice with no exposure to MPIO. Significantly more hypointense voxels are present in the tumour bearing ipsilateral striatum than the contralateral striatum ($p < 0.05$, paired t-test, $n = 6$). Bars represent mean ± standard deviation. *$p < 0.05$

5.4 Discussion

The main aim of this chapter was to investigate the retention of peptide- and antibody-conjugated microparticles of iron oxide by macrophages, both *in vitro* and *in vivo*. The specific objectives of this chapter were to determine whether MPIO can cross a permeabilised BBB *in vivo*, to identify the aggregations of MPIO observed in the brain parenchyma and the conditions under which they occur, to determine whether peptide-conjugated and antibody-conjugated MPIO behave differently *in vitro* and *in vivo*, and to determine whether endogenous iron in tumour associated macrophages produces non-specific hypointense voxels in pre-contrast images.

5.4.1 MPIO penetration of the blood-brain barrier

In Chapter 4, MPIO appeared to be retained in the brain in a non-specific manner in tumours with frank BBB breakdown. Data suggested that both targeted RGD-MPIO and control RDG-MPIO were retained, and histology showed that most iron observed in the tissue parenchyma was present in tumour associated aggregations. The retention of MPIO within the brain parenchyma had not been observed before, and, thus, the first specific objective of this chapter was to determine whether MPIO can cross a permeabilised BBB. In order to test whether the non-specific retention of MPIO was associated primarily with the tumour microenvironment, or whether BBB breakdown alone was sufficient to produce this effect, an *in vivo* model of BBB breakdown was used. A number of chemokines are able to induce BBB breakdown *in vivo*. One such agent, tumour necrosis factor (TNF), is known to induce integrin $\alpha_v\beta_3$ activation[430], which would lead to specific binding of RGD-MPIO. As the aim of this experiment was to measure non-specific

retention, this approach was not used. TNF also induces a subtle, widespread breakdown of the BBB which does not mimic the frank breakdown seen in late stage metastases. IL-1beta is also commonly used to induce BBB breakdown. However, intracerebral injection of IL-1beta has been shown to produce only low levels of BBB breakdown in adult rodents compared to juveniles[431]. The effects of IL-1beta have been shown to be potentiated by chemokine-induced neutrophil chemoattractant 1 (CINC-1, also known as CXCL1), and this cytokine can induce BBB breakdown in adult rodents when injected intracerebrally[432]. For this reason, intracerebral CINC-1 injection was used as an *in vivo* model of non-tumour associated BBB breakdown.

A pilot study to determine the appropriate dosage of CINC-1 was carried out. The highest dose of 2 µg, when injected intracerebrally, caused intracerebral haemorrhage visible on MRI, although no clinical signs of brain injury or pain were observed. The 2 µg dose was excluded from further analysis, and is considered too high a dose for safe use in mice. Both the 0.5 and 1 µg doses resulted in frank BBB breakdown, localised to the injected striatum, with no damage visible in the brain on the pre-contrast MR images. The 1 µg dose more closely corresponded to the mean enhancing volume of the late stage tumour model. Hence, this dose was used going forward into the main study. Histological examination confirmed BBB breakdown, and that breakdown was localised to the striatum. Thus, the results of the imaging and histology have shown that a 1 µg dose of CINC-1 injected intracerebrally is an appropriate *in vivo* model for frank BBB breakdown in the absence of tumour.

The 1 µg dose of CINC-1 was taken forward to study whether MPIO could cross a permeable BBB, in the absence of the tumour microenvironment. Gadolinium

enhanced imaging confirmed frank BBB breakdown in all animals, and MPIO induced hypointense voxels were observed in the injected hemisphere, but not the contralateral hemisphere. Interestingly, although the effects were not statistically significant, a trend towards reduced MPIO induced hypointense voxels was seen in both the control peptide (RDG) and the control antibody (IgG) conjugated MPIO groups, compared to the corresponding targeted peptide (RGD) or antibody (VCAM) conjugated MPIO. In the pilot study, low levels of VCAM-1 and integrin $\alpha_v\beta_3$ upregulation was observed on vessels in the injected striatum, together with increased expression of the macrophage/microglia marker Iba-1 in the injected hemisphere, but not the contralateral hemisphere. These findings suggest that some specific endothelial binding of VCAM-MPIO and RGD-MPIO may be taking place.

Histology results found single MPIO and MPIO-laden macrophages observed only in the injected hemisphere. However, MPIO-laden macrophages were observed only in very low levels, with on average 0-4 macrophages per tissue section, compared to hundreds of apparent MPIO-laden macrophages per section observed in the 4T1-GFP tumour model in Chapter 4.

However, small numbers of MPIO induced hypointense voxels were also seen in the control RDG-MPIO and IgG-MPIO groups, despite no evidence of single MPIO or macrophage aggregations in the tissue. Systemic CINC-1 administration is known to cause cutaneous vasoconstriction[433], so it is possible that acute intracerebral administration can cause vasoconstriction and reduced blood flow. This would potentially cause transient MPIO induced hypointense voxels to be visible in areas of low blood flow, and could explain why few MPIO were detected using histology. Another possibility is that increased shear stress during perfusion-

fixation caused detachment of bound MPIO from the endothelium. Future studies using CINC-1 to permeabilise the BBB should measure CBF using the MP pCASL sequence in order to determine whether any effects on blood flow are present.

These data suggest that the high levels of apparent MPIO-laden macrophages seen in the 4T1-GFP tumour model are related to the tumour microenvironment, as opposed to BBB breakdown alone. It is proposed that factors in the tumour microenvironment may prime macrophages and microglia in such a way that increased uptake of MPIO occurs.

5.4.2 Retention of MPIO by tumour associated macrophages

The second specific objective of this chapter was to identify the apparent aggregations of MPIO observed in the tumour model in Chapter 4, having previously determined that they were likely to be tumour microenvironment related as opposed to being mediated by simple BBB breakdown. Histological examination of the aggregations revealed that they were apparent MPIO-laden macrophages and/or microglia. Single marker staining on consecutive sections showed that the aggregations were spatially localised with tumour-associated Iba-1 positive macrophages/microglia. Subsequently, double-staining for Prussian blue and Iba-1 confirmed that the aggregations of MPIO were present inside macrophages and microglia. Interestingly, previous studies by Leftin and Koutcher, showed the presence of iron-laden macrophages in breast cancer brain metastases[428], and further characterised them as pro-inflammatory polarised macrophages. These endogenous iron-laden macrophages were also characterised as being in close proximity to blood vessels. In many cases iron-laden macrophages were closely associated with the endothelium, and may represent perivascular macrophages.

These findings suggest a propensity for pro-inflammatory polarised macrophages in the tumour microenvironment to take up iron. One possibility, therefore, is that pro-inflammatory polarised macrophages with access to the blood through close association with the BBB may be predisposed to take up MPIO in this tumour model. It has also been shown that peripheral macrophages labelled either *ex vivo* with MPIO, or *in vivo* through USPIO injection, can home to intracerebral tumours[434], so it is possible that peripheral macrophages may also be involved. However, as peripheral labelling of macrophages and migration to the brain usually occurs after 24 hours, it is unlikely that in the timeframe of this experiment that peripheral macrophages would be able to migrate to the tumour. Thus, the specific hypothesis tested was that the iron aggregations observed in the tumour model of Chapter 4 represent MPIO-laden tumour-associated macrophages.

Whilst the majority of iron detected was visible inside macrophages, double staining for iron and the blood vessel marker CD31 showed that single endothelium-bound MPIO were also present in the tumour. Significantly more endothelium-bound MPIO were present in mice injected with RGD-MPIO compared to those injected with control RDG-MPIO. This finding suggests that some specific binding of angiogenic blood vessels did occur with the targeted RGD-MPIO. Thus, imaging of the angiogenic endothelium may be possible using RGD-MPIO if confounding factors including pre-existing hypointense voxels and macrophage uptake can be overcome. Single MPIO were also detected in the tumour parenchyma, distant from blood vessels. MPIO entering the tumour parenchyma is an important concern for the clinical translation of targeted MPIO. However, it should be noted that MPIO were never observed in the contralateral hemisphere, nor in the normal brain tissue surrounding metastatic foci. Thus, MPIO

entering the tumour parenchyma may not be a clinical problem in tumour tissue that is due to be resected. Similarly, the entry of MPIO into the tumour parenchyma may open the door to the possibility of theranostic MPIO, with theranostic RGD-targeted iron oxide nanoparticles having already been used successfully in a pre-clinical model of glioma[435]. This study suggests that the iron aggregations observed in the tumour model may be MPIO-laden macrophages, but specific targeting of RGD-MPIO on vessels was also achieved.

5.4.3 Effect of MPIO targeting moiety

MPIO-laden macrophages have not been observed in any previous studies using MPIO to study brain pathology, however, all previous studies have used an antibody as a targeting moiety compared to the peptides used in this study. Thus, the third objective of this chapter was to determine whether peptide-conjugated and antibody-conjugated MPIO behave differently *in vitro* and *in vivo*.

In vitro studies showed that both peptide- and antibody-conjugated MPIO were taken up by macrophages and 4T1-GFP tumour cells, with macrophages taking up significantly more MPIO than the 4T1-GFP cells. These results are consistent with previous studies showing cellular uptake of peptide-conjugated[353] and antibody-conjugated[436] IONPs and MPIO[434,437] by macrophages *in vitro*.

It has previously been shown that pre-treatment with RGD peptide blocks binding of RGD-IONPs both *in vitro*[353,438] and *in vivo*[355]. However, the data from the *in vivo* paper[355] also appear to show iron-laden macrophage-like aggregations, which are reduced by the RGD peptide block. To determine whether this method might reduce macrophage uptake in our model, we tested the ability of macrophages to take up peptide- and antibody-conjugated MPIO *in vitro* following blocking with the

appropriate peptide/antibody. Contrary to the previous *in vivo* results from Zhang *et al*[355], pre-treatment with RGD peptide did not reduce the uptake of RGD-MPIO, and this finding was replicated with control RGD-MPIO, VCAM-MPIO, and IgG-MPIO following appropriate pre-treatment. It appears, therefore, that in our *in vitro* model, macrophage uptake is not mediated by a specific receptor, and may instead occur by simple phagocytosis. It is possible that this uptake may reflect the increased size of MPIO, as all previously mentioned studies have used nanometre sized particles. It has been shown that larger particles are taken up at higher rates by macrophages, in both nanometre sized[439,440] and micron sized particles[437].

Studies in both glioma[355] and nasopharyngeal carcinoma[353] have found that RGD peptide injection prior to administration of RGD targeted iron oxide nanoparticles can block specific binding. Although we have shown no difference in macrophage uptake following an RGD block, a future avenue for this study would be to test the ability of the RGD peptide to block specific and non-specific retention of RGD-MPIO *in vivo*.

Peptide- and antibody-conjugated MPIO were also tested *in vivo* in tumour models to determine whether MPIO with different targeting moieties behave differently *in vivo*. Peptides and antibodies have different sizes, shapes, and charge. It has been shown that antibody coated iron oxide nanoparticles are larger and stay in the circulation longer than peptide targeted nanoparticles, which home to the target more quickly[441]. Antibody coated MPIO will also be larger than peptide coated MPIO, however given the iron oxide core is an order of magnitude larger in these particles than nanoparticles, the size effect of antibodies compared to peptides may be somewhat diminished. The pharmacokinetic properties of antibodies compared to peptides have not been measured using micron sized particles, but it

can be expected that they will likely follow the same patterns. As retention of control antibody-conjugated MPIO have not been observed in any other early stage tumour models used within the group, a study of large tumours imaged with antibody-conjugated MPIO was carried out, in order to compare uptake of antibody-conjugated MPIO with peptide-conjugated MPIO.

In rat models of brain metastasis and glioma, which had been imaged using either VCAM-MPIO or control IgG-MPIO, significantly more MPIO induced hypointense voxels were present in the rats imaged with VCAM-MPIO than with IgG-MPIO. Examination of the histology showed that only low levels of MPIO-laden macrophages were present in the tissue. In the single animal where a large number of MPIO-laden macrophages were observed in the tumour, a large number of pre-existing hypointense voxels were also present, which may suggest the presence of endogenous iron-laden macrophages in the tumour prior to contrast administration. These data, when taken together, lead to the conclusion that the antibody-conjugated MPIO were capable of sensitive and specific imaging of VCAM-1 positive blood vessels in these tumour models, and that these results were not affected by macrophage uptake of VCAM-MPIO.

However, these glioma and metastatic tumours were both orthotopically grown in immunocompromised RNU nude rats. Whilst these rats are athymic[442], they generally have normal macrophage numbers and function[443]. It is unknown, however, whether iron-laden macrophages are observed more or less frequently in these rats because the tumours are xenografts in immunocompromised animals. Because of this question, it was decided to test the uptake of antibody-conjugated MPIO in BALB/c mice with syngeneic 4T1-GFP tumours to see if the above results hold true in immunocompetent animals. The genetic background of mice and rats

also affects iron metabolism as a whole[444], so it is important to confirm these results in our model of interest, the 4T1-GFP brain metastasis model.

MPIO induced hypointense voxels were observed in the tumour bearing striatum in mice imaged with VCAM-MPIO. MPIO induced hypointense voxels were not observed in the contralateral striatum, or in mice imaged with control IgG-MPIO. Similarly, analysis of the histology showed single MPIO bound to VCAM-1 positive blood vessels. Thus, the imaging data alone would suggest that the antibody-conjugated MPIO were capable of sensitive and specific imaging of VCAM-1 positive blood vessels in the 4T1-GFP tumour model. These results are in contrast to the results seen in Chapter 4, where both RGD-MPIO and control RDG-MPIO appeared to be retained non-specifically in larger tumours.

However, in two mice, one imaged with VCAM-MPIO and one with control IgG-MPIO, relatively large numbers of endogenous iron-laden macrophages were observed as pre-existing hypointense voxels in the pre-contrast MGE3D images. Consequently, it was not possible to determine whether further antibody-targeted MPIO were retained by those macrophages in addition to their endogenous iron content. Since this was a small study, it is possible that in larger, gadolinium enhancing tumours, or those where higher numbers of pre-existing hypointense voxels and, hence, a higher number of endogenous iron-laden macrophages are present, non-specific uptake of antibody targeted MPIO may also be observed. It has been shown that tumour associated iron-laden macrophages can take up further iron upon administration of USPIO[428,429], and it is possible, therefore, that they may also be able to take up further antibody-targeted MPIO.

Even if ways to prevent MPIO uptake by macrophages are developed, this pre-existing iron deposition could be a confounding factor for molecular MRI of large tumours. It is recommended, therefore, that studies performed with iron oxide contrast agents should include both pre- and post-contrast imaging in order to assess for any pre-existing iron deposits. Also, where experimental outcomes allow, histological analysis should take place to check for the presence of endogenous iron-laden macrophages, which may reduce the specificity of the results.

However, it is important to note that the tumours in this study are large, late-stage tumours. The VCAM-MPIO have been designed to detect brain metastases at a very early stage, when endogenous iron-laden macrophages are unlikely to be present[166]. Hence, VCAM-MPIO, and potentially other such targeted contrast agents can still be used for sensitive and specific imaging of early stage brain metastases, but care must be taken in the development of iron oxide contrast agents for use in larger tumours.

5.4.4 Endogenous iron-laden macrophages

Although the previous chapter, and the sections above, suggest that perivascular macrophages may take up peptide-targeted MPIO, the observation of endogenous iron-laden macrophages raises questions. It has previously been reported that brain metastases may contain endogenous iron-laden macrophages, and our hypothesis was that these macrophages were responsible for the pre-existing, pre-contrast hypointense voxels observed in the T_2* weighted imaging. In order to assess the levels of endogenous iron-laden macrophages resident in tumour tissue prior to iron oxide contrast agent exposure, 4T1-GFP tumour tissue was analysed.

In mice with no exposure to MPIO, endogenous iron-laden macrophages were observed at all timepoints, and there was no correlation with tumour size. This suggests that tumour associated macrophages involved in iron homeostasis are ordinarily resident in this tumour model, and that they contain large iron stores even in the absence of exogenous contrast agent administration. As this model uses an intracerebral injection to induce macromestastases, it is possible that tumour models using intra-cardiac injection to seed micrometastases may not show the presence of endogenous iron-laden macrophages until large macrometastatic tumours are observed.

The levels of pre-existing hypointense voxels observed in this study are similar to the levels of pre-contrast hypointense voxels observed in the 4T1-GFP tumour model in Chapter 4, suggesting levels of endogenous iron-laden macrophages are similar. However, in the mice in Chapter 4, further non-specific MPIO induced hypointense voxels were observed, in addition to the pre-existing pre-contrast hypointense voxels, when mice were imaged with control RDG-MPIO. These data suggest that, where endogenous iron-laden macrophages are present in the tissue, they may be able to take up further iron in the form of MPIO, and thus cause non-specific signal voids. Given that non-specific uptake was much higher when using the peptide-conjugated MPIO compared to the antibody-conjugated MPIO, endogenous iron-laden macrophages may be predisposed to take up peptide-conjugated MPIO due to particle charge, size, or other factors.

In the mice that underwent MRI without contrast agent administration prior to histology, the location of the endogenous iron-laden macrophages correlated closely with the location of the pre-existing hypointense voxels in the MGE3D images. In one animal, micro-haemorrhage was observed which also correlated

with areas of pre-existing hypointense voxels. This finding suggests that pre-existing hypointense voxels visible with MGE3D imaging could be used to quantify the levels of endogenous iron-laden macrophages in the tumour microenvironment. This finding is also supported by the results of Leftin *et al*, who have previously used T_2* weighted imaging to quantify macrophages in a mouse model of brain metastasis[428]. However, they suggest that T_2* weighted imaging can be used to quantify the total tumour macrophage burden, whereas our observations suggest that only a minority of tumour associated macrophages contain iron deposits.

It is likely that endogenous iron-laden macrophages will be present at some level in most, if not all, tumour models. Thus, for any study using iron oxide based contrast agents, it will be important to quantify any pre-existing hypointense voxels using pre-contrast imaging, in order to distinguish between pre-existing iron and specific binding effects. Nevertheless, the endogenous iron-laden macrophages are only present within the tumour and not in the normal brain parenchyma, so even the non-specific contrast will still indicate areas of tumour burden, and thus may still be useful in a clinical setting. In human breast carcinoma, macrophages have been found to accumulate at areas of tumour angiogenesis[445,446]. Given this, along with the presence of BBB breakdown, which is also indicative of angiogenesis, the iron-laden macrophages found in this study may still provide an imaging readout of areas of active tumour angiogenesis. Additionally, as long as pre-contrast imaging is carried out, since the targeted RGD-MPIO have shown specific endothelial binding, RGD-MPIO can still be used to detect angiogenesis in vivo. The background endogenous iron will reduce the specificity of this method, but will not preclude it.

5.5 Conclusion

Owing to the unexpected results of Chapter 4, the overarching aim of this chapter was to investigate the retention of peptide- and antibody-conjugated microparticles of iron oxide by macrophages, both *in vitro* and *in vivo*. The first specific objective of this chapter was to determine whether MPIO can cross a permeabilised BBB *in vivo*. It was shown that there was no evidence of iron retention in the brain parenchyma, either in macrophages or as bound MPIO, in areas of frank BBB breakdown induced by CINC-1 in the absence of a tumour.

The second objective of this chapter was to identify the apparent aggregations of MPIO and the conditions under which they occur, with the specific hypothesis being that the aggregations reflect macrophages that have taken up MPIO. The aggregations of MPIO described in Chapter 4 have been positively characterised as MPIO-laden macrophages. These MPIO-laden macrophages are closely associated with blood vessels, and are present at all timepoints and in all tumour sizes. Single, endothelium bound MPIO were also observed in the mice imaged with RGD-MPIO, suggesting that some specific binding has occurred alongside the macrophage uptake.

The third specific objective of this chapter was to determine whether peptide-conjugated and antibody-conjugated MPIO behave differently *in vivo*. It was shown that whilst low levels of endogenous iron-laden macrophages do confound the molecular MRI results, antibody conjugated MPIO demonstrate sensitive and specific imaging of the tumour vasculature, whilst peptide conjugated MPIO show non-specific uptake in larger tumours.

Finally, the fourth objective of this chapter was to determine whether endogenous iron in tumour associated macrophages produces non-specific hypointense voxels

in pre-contrast images. It was found that endogenous iron-laden macrophages are present in the 4T1-GFP tumour model in animals with no prior iron oxide contrast agent exposure at all timepoints and sizes. These endogenous iron-laden macrophages are detectable using T_2* weighted imaging as pre-existing hypointense voxels in the pre-contrast images.

To conclude, peptide-conjugated MPIO are retained by tumour-associated macrophages, while antibody-conjugated MPIO are not. Endogenous iron-laden macrophages are also present in the tumour, and may represent a confounding factor for molecular imaging with iron oxide contrast agents.

Chapter 6 – Discussion and future work

6.1 Limitations and further work

6.1.1 Arterial spin labelling to measure brain and tumour blood flow in mice

The primary aim of Chapter 3 was to develop and validate arterial spin labelling for quantitative measurement of tumour blood flow in a mouse model of brain metastasis. The implementation of MP pCASL has been successful in measuring CBF in both naïve mice, and in mouse models of primary and secondary brain tumours. Given the successful implementation of this method, there are many avenues that could be explored in future studies.

The first objective, to optimise ASL for use in mice, has been achieved to the degree that is possible on our pre-clinical system using the current hardware. There are further improvements to the MP pCASL sequence that could potentially be made in order to bring the sequence fully into line with the recommendations for clinical imaging in the white paper[292]. These improvements include the use of background suppression to improve the SNR of the imaging readout, and 3D imaging to cover the whole brain. These would be valid improvements to the sequence that may well improve its sensitivity further. However, both are difficult to implement on the preclinical hardware available to our group. A 3D readout, in particular, is difficult to acquire in a reasonable timeframe. In the future, the use of parallel acquisition or compressed sensing could speed up the 3D acquisition. Similarly, background suppression could also be used to help improve the sequence, however it is difficult to implement in multislice sequences.

The second objective, to validate quantitative ASL measurements against gold-standard autoradiography measurements, has been achieved in the naïve mouse

brain. However, in order to fully validate the MP pCASL method, measurements in each disease state would also need to be validated using the current gold-standard – autoradiography. In this study we have not validated the CBF measurements in tumour bearing mice, and it is entirely possible that confounds exist that may impact on the accuracy of the MP pCASL sequence in tumours. It would be advisable for this study to be carried out in the future, along with validation for any other pre-clinical disease models to be assessed. Similarly, the intracerebral model of brain metastasis used in this study produces a single macrometastatic tumour, which does not replicate all radiological features of clinical breast cancer brain metastasis. MP pCASL should also be assessed in a model using intracardiac or intracarotid seeding to ensure the method is sensitive enough to measure changes in CBF in tumours resulting from vascular dissemination.

One of the most pressing studies that could be carried out in the future, would be to use the MP pCASL method to measure the response of both primary and metastatic brain tumours to either anti-angiogenic treatment or vascular normalisation. It is anticipated that early changes in CBF would predict treatment response in these tumours, and perhaps would mitigate some of the issues such as pseudo-progression that affect response prediction using gadolinium-enhanced MRI. MP pCASL could of course also be applied in any number of pre-clinical disease models outside the oncology sphere where CBF is affected, including stroke, traumatic brain injury and Alzheimer's disease. An optimised, validated and standardised ASL sequence would be of great utility in pre-clinical testing of many therapies for the above conditions.

To conclude, the aim of developing and validating arterial spin labelling for quantitative measurement of tumour blood flow in a mouse model of brain

metastasis has been achieved. These results represent an important advance in the field, as the first implementation of a multiphase pCASL sequence in mice. There is great potential in this technique, however this study was run in parallel with the molecular imaging study. As a result of the molecular imaging results requiring further investigation, application of the MP pCASL sequence to disease models was not able to be taken further during the timecourse of this thesis.

6.1.2 Targeting integrin $\alpha_v\beta_3$ for *in vivo* imaging of brain metastasis

The primary aim of chapter 4 was to develop and validate targeted MPIO for visualisation of angiogenesis by MRI. This chapter yielded mixed results, and whilst the overall aim was not fully met, many of the individual objectives were achieved.

The first objective of the study was to assess the expression of integrin $\alpha_v\beta_3$ in a mouse model of brain metastasis, and to determine the extent of expression on the neovasculature. This study has successfully established that angiogenic markers are expressed on angiogenic neovasculature in a mouse model of brain metastasis, and that integrin $\alpha_v\beta_3$ expression is increased at later timepoints and in larger tumours. TIE2 also showed high levels of expression in the U87 tumour model, and may also be a good target for imaging angiogenic vasculature in some tumour models. However, although TIE2 is expressed on the luminal surface of blood vessels, targeting antibodies with sufficient *in vivo* binding capability are not currently available[447]. It may be possible to develop a suitable anti-TIE2 antibody for *in vivo* use if RGD-MPIO, or MPIO targeted with antibodies to integrin $\alpha_v\beta_3$, are shown to be ineffective for imaging of brain metastases. VEGFR2, which was not investigated in this study, can also now be targeted with high specificity *in vivo* with

the lipoprotein BR55 as used in ultrasonography studies[221,229], and as such would also be a viable target for future studies.

The third objective of this study was to determine whether RGD-MPIO enable detection of the switch from co-optive to angiogenic tumour growth in brain metastasis *in vivo*. This objective was not achieved owing to two major confounds.

The primary confound, and a major limitation of the study, was the accumulation of MPIO, both RGD-targeted and control RDG-MPIO, in tumour-associated macrophages. This accumulation resulted in overwhelming non-specific contrast, and as such the angiogenic vessels could not be visualised specifically using MRI. If the issue of aggregation in macrophages could be solved, perhaps using an antibody-conjugated MPIO instead of the RGD peptide, integrin $\alpha_v\beta_3$ may still be an appropriate marker for the molecular imaging of angiogenesis. However, antibodies to mouse integrin $\alpha_v\beta_3$ and TIE2 which are suitable for in vivo use are not widely available.

Another confound of this study which could be improved for future work is the presence of large hypo-intense areas in the pre-contrast scans. Whilst the majority of these hypointense voxels are likely to be caused by iron-laden macrophages resident in the tissue, they may also be caused by micro-haemorrhage, or by BOLD effects caused by tumour hypoxia. It has been demonstrated in previous studies that normobaric oxygen reduces T_2* susceptibility effects following intracranial haemorrhage, and allows molecular imaging with iron oxide to be used[379,448]. This method could be tested prior to molecular imaging of large tumour models, to see whether it could reduce pre-existing hypointense regions and, thus, increase the sensitivity and specificity of the technique. Measurement of T_2*/R_2* values in the

tumour-bearing striatum may also allow the identification of relaxivity changes induced by MPIO, and could be derived from the existing MGE3D data. Importantly, this would allow for the development of a quantitative biomarker alongside the qualitative identification of MPIO induced hypointense voxels.

If it is possible to fix these issues, it should be possible to produce sensitive and specific molecular imaging of angiogenesis in mouse models of brain tumours using molecular MRI. However, with the current data available, it is not possible to draw firm conclusions about the ability of RGD-MPIO to image angiogenesis in an *in vivo* mouse model of brain metastasis. As this chapter produced results that were important to investigate further, it was decided to focus the final thesis chapter on molecular imaging, rather than the successful ASL imaging that was developed in parallel to this study.

6.1.3 Iron, macrophages and the tumour microenvironment

Due to the results observed in Chapter 4, the primary aim of chapter 5 was investigate the retention of peptide- and antibody-conjugated microparticles of iron oxide by macrophages, both *in vitro* and *in vivo*. The first specific objective of this chapter was to determine whether MPIO can cross a permeabilised BBB *in vivo*. We found no evidence that MPIO were able to cross a permeabilised BBB, and nor did they accumulate in aggregations. Thus, it was determined that the iron aggregations observed in Chapter 4 were likely related to factors in the tumour microenvironment as opposed to BBB permeability.

The second objective of this chapter was to identify the aggregations of MPIO observed in the tumour model. Histological examination of the aggregations revealed that they were MPIO-laden macrophages and/or microglia.

Following this, the targeting moiety of the MPIO was examined as the third specific objective of this chapter. Fewer MPIO-laden macrophages were observed in animals imaged with antibody-targeted MPIO compared to peptide-targeted MPIO. Given that issues with macrophage uptake have not been seen previously with antibody targeted MPIO, it is likely that any future molecular imaging studies involving targeted MPIO will be performed with antibody conjugation. Antibodies against mouse integrin $\alpha_v\beta_3$ and mouse TIE2 could be used to target the angiogenic vasculature in future studies, if sensitive and specific antibodies suitable for *in vivo* use are developed. If used in conjunction with methods to reduce confounds from pre-existing hypointense voxels, antibody targeted MPIO may potentially be used to successfully image the neovasculature.

The final objective for this chapter was to determine whether endogenous iron in tumour associated macrophages produces non-specific hypointense voxels in pre-contrast images. In mice with no prior iron oxide exposure, endogenous iron-laden macrophages were identified which spatially localised with pre-existing hypointense voxels, and were present throughout the tumour timecourse. These endogenous iron-laden macrophages present a challenge to the use of targeted iron oxide contrast agents for specific molecular MRI of tumours, regardless of the particle size or target used.

A potential avenue for future studies is the application of MRI sequences for detection of MPIO as a 'positive contrast' agent, which may help reduce the present confound of pre-existing hypointense voxels. A number of sequences for detecting

USPIO as a positive contrast exist[449-451], however they suffer from low sensitivity. It is possible that owing to the higher iron content of MPIO, they may be more easily detected than USPIO by these sequences. If developed further, these sequences may be useful for molecular MRI. This of course comes with the major limitation that if endogenous iron-laden macrophages are present in the tumour, these may cause pre-existing bright, or hyperintense, regions. Studies will need to be undertaken to determine whether the contribution of additional positive contrast from targeted MPIO can be distinguished from pre-existing hyperintense regions.

Alternatively, changes in relaxivity induced by MPIO may be able to be quantified using R_2* measurements, and differentiated from background endogenous iron signal. Changes in R_2* values have been observed following the administration of ferumoxytol in glioblastoma patients, and these changes correlated with the amount of iron-laden CD163-positive macrophages found in the tumour tissue[452]. These changes in relaxivity following USPIO uptake by tumour-associated macrophages have also been demonstrated extensively pre-clinically[406], but it remains to be seen whether they can successfully differentiate the contributions of endogenous iron-laden macrophages compared to targeted MPIO.

It may be possible to engineer MPIO or USPIO to reduce uptake by macrophages and, thus, increase specificity. It has been shown that encapsulating USPIO within a liposome reduces uptake by macrophages[453]. However, this reduced the change in relaxivity induced by the USPIO, so a three stage targeting system of an IV injection of biotinylated integrin $\alpha_v\beta_3$ antibody, followed by injection of avidin and streptavidin for signal amplification, and finally followed by biotinylated magnetoliposomes was required for adequate signal-to-noise[453]. Whilst this strategy may be successful in a pre-clinical setting, it is unlikely to be easily

translatable into the clinic, and hence other options for reducing macrophage uptake should be explored. The shape of iron oxide nanoparticles also affects uptake by macrophages, and could be used as another strategy to increase specificity[454]. However, none of these strategies have been explored with MPIO or other larger particles, so it is not currently known whether these strategies would be effective. Additionally, these approaches would not address the confounding factor of endogenous iron-laden macrophages already resident in the tumour tissue.

6.2 Conclusions

The data from this thesis have shown the need for different types of molecularly targeted MPIO to be validated in each specific disease model used to ensure no non-specific retention is present. The results would suggest that caution is used in studies using peptides or charged small molecules as the targeting molecule, as they may have undesirable non-specific retention. We have, however, observed no such effects using antibody targeted MPIO, although careful validation of both imaging and histology should be undertaken before any new imaging agent moves into the clinic.

It was originally intended for this project to compare the ability of MP pCASL, RGD-MPIO, and the integrin $\alpha_v\beta_3$ targeted SPECT tracer Maraciclatide, to visualise angiogenesis *in vivo* in mouse models of brain metastasis. It was also intended to use these modalities to measure the response to anti-angiogenic treatment, and to compare the sensitivity and specificity of each imaging modality for this purpose. As the RGD-MPIO imaging was unsuccessful, these studies could not be carried out. However, it remains a viable future avenue of work to compare and contrast different modalities for the imaging of anti-angiogenic treatment response. Thus, the clinical question of how best to image angiogenesis and the response to anti-angiogenic treatment remains unanswered, although progress has been made towards unravelling the methods with which to study this important question.

To conclude, this thesis suggests that multiphase pseudo-continuous arterial spin labelling can be used successfully to image angiogenesis in brain metastasis, and, with future improvements, antibody targeted microparticles of iron oxide may also be used to image tumour angiogenesis.

References

1 World Health Organisation. *World Cancer Report 2014*. (International Agency for Research on Cancer, 2014).

2 Cancer Research UK. *Cancer statistics for the UK*, <http://www.cancerresearchuk.org/health-professional/cancer-statistics-for-the-uk> (2014).

3 Cancer Research UK. *Cancer incidence for common cancers*, <http://www.cancerresearchuk.org/health-professional/cancer-statistics/incidence/common-cancers-compared> (2014).

4 Cancer Research UK. *Brain, other CNS and intracranial tumours incidence statistics*, <http://www.cancerresearchuk.org/health-professional/cancer-statistics/statistics-by-cancer-type/brain-other-cns-and-intracranial-tumours/incidence> (2014).

5 Langley, R. R. & Fidler, I. J. The Biology of Brain Metastasis. *Clinical Chemistry* **59**, 180-189, doi:10.1373/clinchem.2012.193342 (2013).

6 Davis, F. G., Dolecek, T. A., McCarthy, B. J. & Villano, J. L. Toward determining the lifetime occurrence of metastatic brain tumors estimated from 2007 United States cancer incidence data. *Neuro-Oncology* **14**, 1171-1177, doi:10.1093/neuonc/nos152 (2012).

7 Hanahan, D. & Weinberg, R. A. The Hallmarks of Cancer. *Cell* **100**, 57-70, doi:http://dx.doi.org/10.1016/S0092-8674(00)81683-9 (2000).

8 Hanahan, D. & Weinberg, Robert A. Hallmarks of Cancer: The Next Generation. *Cell* **144**, 646-674, doi:10.1016/j.cell.2011.02.013 (2011).

9 Folkman, J., Long, D. M. & Becker, F. F. Growth and metastasis of tumor in organ culture. *Cancer* **16**, 453-467, doi:10.1002/1097-0142(196304)16:4<453::aid-cncr2820160407>3.0.co;2-y (1963).

10 Patel-Hett, S. & D'Amore, P. A. Signal Transduction in Vasculogenesis and Developmental Angiogenesis. *The International journal of developmental biology* **55**, 353-363, doi:10.1387/ijdb.103213sp (2011).

11 Carmeliet, P. Angiogenesis in health and disease. *Nature Medicine* **9**, 653, doi:10.1038/nm0603-653 (2003).

12 Ausprunk, D. H. & Folkman, J. Migration and proliferation of endothelial cells in preformed and newly formed blood vessels during tumor angiogenesis. *Microvascular Research* **14**, 53-65, doi:https://doi.org/10.1016/0026-2862(77)90141-8 (1977).

13 Gerhardt, H. *et al.* VEGF guides angiogenic sprouting utilizing endothelial tip cell filopodia. *The Journal of Cell Biology* **161**, 1163-1177, doi:10.1083/jcb.200302047 (2003).

14 Makanya, A. N., Hlushchuk, R. & Djonov, V. G. Intussusceptive angiogenesis and its role in vascular morphogenesis, patterning, and remodeling. *Angiogenesis* **12**, 113, doi:10.1007/s10456-009-9129-5 (2009).

15 Folkman , J. Tumor Angiogenesis: Therapeutic Implications. *New England Journal of Medicine* **285**, 1182-1186, doi:10.1056/nejm197111182852108 (1971).

16 Carbonell, W. S., Ansorge, O., Sibson, N. & Muschel, R. The Vascular Basement Membrane as “Soil” in Brain Metastasis. *PLoS ONE* **4**, e5857, doi:10.1371/journal.pone.0005857 (2009).
17 Knighton, D., Ausprunk, D., Tapper, D. & Folkman, J. Avascular and vascular phases of tumour growth in the chick embryo. *British Journal of Cancer* **35**, 347-356 (1977).
18 Folkman, J. Role of angiogenesis in tumor growth and metastasis. *Seminars in Oncology* **29**, 15-18, doi:http://dx.doi.org/10.1016/S0093-7754(02)70065-1 (2002).
19 Holash, J. *et al.* Vessel Cooption, Regression, and Growth in Tumors Mediated by Angiopoietins and VEGF. *Science* **284**, 1994-1998, doi:10.1126/science.284.5422.1994 (1999).
20 Pezzella, F. *et al.* Non-small-cell lung carcinoma tumor growth without morphological evidence of neo-angiogenesis. *The American Journal of Pathology* **151**, 1417-1423 (1997).
21 Nagano, N., Sasaki, H., Aoyagi, M. & Hirakawa, K. Invasion of experimental rat brain tumor: early morphological changes following microinjection of C6 glioma cells. *Acta Neuropathologica* **86**, 117-125, doi:10.1007/bf00334878 (1993).
22 Rogers, M. S. *et al.* Spontaneous Reversion of the Angiogenic Phenotype to a Nonangiogenic and Dormant State in Human Tumors. *Molecular Cancer Research* **12**, 754-764, doi:10.1158/1541-7786.mcr-13-0532-t (2014).
23 Bergers, G. & Benjamin, L. E. Tumorigenesis and the angiogenic switch. *Nature Reviews Cancer* **3**, 401, doi:10.1038/nrc1093 (2003).
24 Greenblatt, M. S. & Shubi, P. Tumour angiogenesis: transfilter diffusion studies in the hamster by the transparent chamber technique. *Journal of the National Cancer Institute* **41**, 111-124 (1968).
25 Ehrmann, R. L. & Knoth, M. Choriocarcinoma. Transfilter stimulation of vasoproliferation in the hamster cheek pouch. Studied by light and electron microscopy. *Journal of the National Cancer Institute* **41**, 1329-1341 (1968).
26 Gimbrone, J. M. A., Cotran, R. S., Leapman, S. B. & Folkman, J. Tumor Growth and Neovascularization: An Experimental Model Using the Rabbit Cornea2. *JNCI: Journal of the National Cancer Institute* **52**, 413-427, doi:10.1093/jnci/52.2.413 (1974).
27 Shing, Y. *et al.* Heparin-affinity: purification of a tumour-derived capillary endothelial growth factor. *Science* **223**, 1296-1299 (1984).
28 Senger, D. R. *et al.* Tumour cells secrete a vascular permeability factor that promotes accumulation of ascites fluid. *Science* **219**, 983-985 (1983).
29 Ferrara, N. & Henzel, W. J. Pituitary follicular cells secrete a novel heparin-binding growth factor specific for vascular endothelial cells. *Biochemical and Biophysical Research Communications* **161**, 851-858, doi:https://doi.org/10.1016/0006-291X(89)92678-8 (1989).
30 Leung, D., Cachianes, G., Kuang, W., Goeddel, D. & Ferrara, N. Vascular endothelial growth factor is a secreted angiogenic mitogen. *Science* **246**, 1306-1309, doi:10.1126/science.2479986 (1989).
31 Kut, C., Mac Gabhann, F. & Popel, A. S. Where is VEGF in the body? A meta-analysis of VEGF distribution in cancer. *British Journal Of Cancer* **97**, 978, doi:10.1038/sj.bjc.6603923

https://www.nature.com/articles/6603923#supplementary-information (2007).
32 Plouet, J., Schilling, J. & Gospodarowicz, D. Isolation and characterisation of a newly identified endothelial cell mitogen produced by AtT-20 cells. *EMBO J* **8**, 3801-3806 (1989).
33 Conn, G. *et al.* Amino acid and cDNA sequences of a vascular endothelial cell mitogen that is homologous to platelet-derived growth factor. *Proceedings of the National Academy of Sciences* **87**, 2628-2632 (1990).
34 Senger, D. R., Connolly, D. T., Van De Water, L., Feder, J. & Dvorak, H. F. Purification and NH2-Terminal Amino Acid Sequence of Guinea Pig Tumor-secreted Vascular Permeability Factor. *Cancer Research* **50**, 1774-1778 (1990).
35 Plate, K. H., Breier, G., Weich, H. A. & Risau, W. Vascular endothelial growth factor is a potential tumour angiogenesis factor in human gliomas in vivo. *Nature* **359**, 845, doi:10.1038/359845a0 (1992).
36 Shweiki, D., Itin, A., Soffer, D. & Keshet, E. Vascular endothelial growth factor induced by hypoxia may mediate hypoxia-initiated angiogenesis. *Nature* **359**, 843, doi:10.1038/359843a0 (1992).
37 Vaisman, N., Gospodarowicz, D. & Neufeld, G. Characterisation of the receptors for vascular endothelial growth factor. *J Biol Chem.* **265**, 19461 (1990).
38 Terman, B. I. *et al.* Identification of the KDR tyrosine kinase as a receptor for vascular endothelial cell growth factor. *Biochemical and Biophysical Research Communications* **187**, 1579-1586, doi:https://doi.org/10.1016/0006-291X(92)90483-2 (1992).
39 Waltenberger, J., Claessonwelsh, L., Siegbahn, A., Shibuya, M. & Heldin, C. H. Different signal tranduction properties of KDR and Flt1, two receptors for vascular endothelial growth factor. *J Biol Chem.* **269**, 26988-26995 (1994).
40 Zhuang, G. *et al.* Phosphoproteomic Analysis Implicates the mTORC2-FoxO1 Axis in VEGF Signaling and Feedback Activation of Receptor Tyrosine Kinases. *Science Signaling* **6**, ra25-ra25, doi:10.1126/scisignal.2003572 (2013).
41 Koukourakis, M. I. *et al.* Vascular Endothelial Growth Factor/KDR Activated Microvessel Density versus CD31 Standard Microvessel Density in Non-Small Cell Lung Cancer. *Cancer Research* **60**, 3088-3095 (2000).
42 Vajkoczy, P. *et al.* Microtumor growth initiates angiogenic sprouting with simultaneous expression of VEGF, VEGF receptor-2, and angiopoietin-2. *The Journal of Clinical Investigation* **109**, 777-785, doi:10.1172/jci14105 (2002).
43 Smith, N. R. *et al.* Vascular Endothelial Growth Factor Receptors VEGFR-2 and VEGFR-3 Are Localized Primarily to the Vasculature in Human Primary Solid Cancers. *Clinical Cancer Research* **16**, 3548-3561, doi:10.1158/1078-0432.Ccr-09-2797 (2010).
44 Huang, H., Held-Feindt, J., Buhl, R., Mehdorn, H. M. & Mentlein, R. Expression of VEGF and its receptors in different brain tumors. *Neurological Research* **27**, 371-377, doi:10.1179/016164105x39833 (2005).
45 Inoue, K., Ozeki, Y., Suganuma, T., Sugiura, Y. & Tanaka, S. Vascular endothelial growth factor expression in primary esophageal squamous cell

carcinoma. Association with angiogenesis and tumour progression. *Cancer* **79**, 206-213 (1997).
46 Anan, K. *et al.* Vascular endothelial growth factor and platelet-derived growth factor are potential angiogenic and metastatic factors in human breast cancer. *Surgery* **119**, 333-339, doi:https://doi.org/10.1016/S0039-6060(96)80120-6 (1996).
47 Takahashi, Y., Kitadai, Y., Bucana, C. D., Cleary, K. R. & Ellis, L. M. Expression of Vascular Endothelial Growth Factor and Its Receptor, KDR, Correlates with Vascularity, Metastasis, and Proliferation of Human Colon Cancer. *Cancer Research* **55**, 3964-3968 (1995).
48 Weidner , N., Semple , J. P., Welch , W. R. & Folkman , J. Tumor Angiogenesis and Metastasis — Correlation in Invasive Breast Carcinoma. *New England Journal of Medicine* **324**, 1-8, doi:10.1056/nejm199101033240101 (1991).
49 Salven, P., HeikkilÃ¤, P. & Joensuu, H. Enhanced expression of vascular endothelial growth factor in metastatic melanoma. *British Journal of Cancer* **76**, 930-934 (1997).
50 Yamamoto, S. *et al.* Expression of vascular endothelial growth factor (VEGF) in epithelial ovarian neoplasms: correlation with clinicopathology and patient survival, and analysis of serum VEGF levels. *British Journal of Cancer* **76**, 1221-1227 (1997).
51 Maeda, K. *et al.* Prognostic value of vascular endothelial growth factor expression in gastric carcinoma. *Cancer* **77**, 858-863, doi:10.1002/(sici)1097-0142(19960301)77:5<858::aid-cncr8>3.0.co;2-a (1996).
52 Gasparini, G. *et al.* Prognostic significance of vascular endothelial growth factor protein in node-negative breast carcinoma. *J Natl Cancer Inst.* **89**, 139-147 (1997).
53 Imoto, H. *et al.* Vascular endothelial growth factor expression in non-small-cell lung cancer: Prognostic significance in squamous cell carcinoma. *The Journal of Thoracic and Cardiovascular Surgery* **115**, 1007-1014, doi:https://doi.org/10.1016/S0022-5223(98)70398-8 (1998).
54 Millauer, B., Shawver, L. K., Plate, K. H., Risaui, W. & Ullrich, A. Glioblastoma growth inhibited in vivo by a dominant-negative Flk-1 mutant. *Nature* **367**, 576, doi:10.1038/367576a0 (1994).
55 Kim, K. J. *et al.* Inhibition of vascular endothelial growth factor-induced angiogenesis suppresses tumour growth in vivo. *Nature* **362**, 841, doi:10.1038/362841a0 (1993).
56 Rubenstein, J. L. *et al.* Anti-VEGF Antibody Treatment of Glioblastoma Prolongs Survival But Results in Increased Vascular Cooption. *Neoplasia* **2**, 306-314, doi:https://doi.org/10.1038/sj.neo.7900102 (2000).
57 Ferrara, N., Hillan, K. J., Gerber, H.-P. & Novotny, W. Discovery and development of bevacizumab, an anti-VEGF antibody for treating cancer. *Nature Reviews Drug Discovery* **3**, 391, doi:10.1038/nrd1381 (2004).
58 Presta, L. G. *et al.* Humanization of an Anti-Vascular Endothelial Growth Factor Monoclonal Antibody for the Therapy of Solid Tumors and Other Disorders. *Cancer Research* **57**, 4593-4599 (1997).
59 Jayson, G. C., Kerbel, R., Ellis, L. M. & Harris, A. L. Antiangiogenic therapy in oncology: current status and future directions. *The Lancet* **388**, 518-529, doi:https://doi.org/10.1016/S0140-6736(15)01088-0 (2016).

60 Silva, R., D'Amico, G., Hodivala-Dilke, K. M. & Reynolds, L. E. Integrins. *The Keys to Unlocking Angiogenesis* **28**, 1703-1713, doi:10.1161/atvbaha.108.172015 (2008).
61 Christofidou-Solomidou, M., Bridges, M., Murphy, G. F., Albelda, S. M. & DeLisser, H. M. Expression and function of endothelial cell alpha v integrin receptors in wound-induced human angiogenesis in human skin/SCID mice chimeras. *The American Journal of Pathology* **151**, 975-983 (1997).
62 Max, R. *et al.* Immunohistochemical analysis of integrin αvβ3 expression on tumor-associated vessels of human carcinomas. *International Journal of Cancer* **71**, 320-324, doi:doi:10.1002/(SICI)1097-0215(19970502)71:3<320::AID-IJC2>3.0.CO;2-# (1997).
63 Horton, M. A. The αvβ3 integrin "vitronectin receptor". *The International Journal of Biochemistry & Cell Biology* **29**, 721-725, doi:https://doi.org/10.1016/S1357-2725(96)00155-0 (1997).
64 Benedetto, S. *et al.* Quantification of the expression level of integrin receptor avb3 in cell lines and MR imaging with antibody-coated iron oxide particles. *Magnetic Resonance in Medicine* **56**, 711-716 (2006).
65 Seguin, J., Nicolazzi, C., Mignet, N., Scherman, D. & Chabot, G. Vascular density and endothelial cell expression of integrin alpha v beta 3 and E-selectin in murine tumours. *Tumour Biology* **33**, 1709-1717, doi:10.1007/s13277-012-0428-x (2012).
66 Huang, S., Endo, R. I. & Nemerow, G. R. Upregulation of integrins alpha v beta 3 and alpha v beta 5 on human monocytes and T lymphocytes facilitates adenovirus-mediated gene delivery. *Journal of Virology* **69**, 2257-2263 (1995).
67 Pierschbacher, M. D. & Ruoslahti, E. Cell attachment activity of fibronectin can be duplicated by small synthetic fragments of the molecule. *Nature* **309**, 30, doi:10.1038/309030a0 (1984).
68 Suzuki, S., Oldberg, A., Hayman, E. G., Pierschbacher, M. D. & Ruoslahti, E. Complete amino acid sequence of human vitronectin deduced from cDNA. Similarity of cell attachment sites in vitronectin and fibronectin. *The EMBO Journal* **4**, 2519-2524, doi:doi:10.1002/j.1460-2075.1985.tb03965.x (1985).
69 Pytela, R., Pierschbacher, M. D. & Ruoslahti, E. A 125/115-kDa cell surface receptor specific for vitronectin interacts with the arginine-glycine-aspartic acid adhesion sequence derived from fibronectin. *Proceedings of the National Academy of Sciences* **82**, 5766-5770, doi:10.1073/pnas.82.17.5766 (1985).
70 Ruoslahti, E. RGD AND OTHER RECOGNITION SEQUENCES FOR INTEGRINS. *Annual Review of Cell and Developmental Biology* **12**, 697-715, doi:10.1146/annurev.cellbio.12.1.697 (1996).
71 Sulyok, G. A. G. *et al.* Solid-Phase Synthesis of a Nonpeptide RGD Mimetic Library: New Selective αvβ3 Integrin Antagonists. *Journal of Medicinal Chemistry* **44**, 1938-1950, doi:10.1021/jm0004953 (2001).
72 Kapp, T. G. *et al.* A Comprehensive Evaluation of the Activity and Selectivity Profile of Ligands for RGD-binding Integrins. *Scientific Reports* **7**, 39805, doi:10.1038/srep39805

https://www.nature.com/articles/srep39805#supplementary-information (2017).

73 Bader, B. L., Rayburn, H., Crowley, D. & Hynes, R. O. Extensive Vasculogenesis, Angiogenesis, and Organogenesis Precede Lethality in Mice Lacking All αv Integrins. *Cell* **95**, 507-519, doi:https://doi.org/10.1016/S0092-8674(00)81618-9 (1998).
74 McCarty, J. H. *et al.* Defective Associations between Blood Vessels and Brain Parenchyma Lead to Cerebral Hemorrhage in Mice Lacking αv Integrins. *Molecular and Cellular Biology* **22**, 7667-7677, doi:10.1128/mcb.22.21.7667-7677.2002 (2002).
75 McCarty, J. H. *et al.* Selective ablation of αv integrins in the central nervous system leads to cerebral hemorrhage, seizures, axonal degeneration and premature death. *Development* **132**, 165-176, doi:10.1242/dev.01551 (2005).
76 van der Horst, G. *et al.* Targeting of alpha-v integrins reduces malignancy of bladder carcinoma. *PloS one* **9**, e108464-e108464, doi:10.1371/journal.pone.0108464 (2014).
77 Cruet-Hennequart, S. *et al.* αv integrins regulate cell proliferation through integrin-linked kinase (ILK) in ovarian cancer cells. *Oncogene* **22**, 1688, doi:10.1038/sj.onc.1206347 (2003).
78 Reynolds, L. E. *et al.* Enhanced pathological angiogenesis in mice lacking β3 integrin or β3 and β5 integrins. *Nature Medicine* **8**, 27, doi:10.1038/nm0102-27 (2002).
79 Hodivala-Dilke, K. M. *et al.* β3-integrin–deficient mice are a model for Glanzmann thrombasthenia showing placental defects and reduced survival. *Journal of Clinical Investigation* **103**, 229-238 (1999).
80 Mahabeleshwar, G. H., Feng, W., Phillips, D. R. & Byzova, T. V. Integrin signaling is critical for pathological angiogenesis. *The Journal of Experimental Medicine* **203**, 2495-2507, doi:10.1084/jem.20060807 (2006).
81 Brooks, P. C. *et al.* Antiintegrin alpha v beta 3 blocks human breast cancer growth and angiogenesis in human skin. *The Journal of clinical investigation* **96**, 1815-1822, doi:10.1172/jci118227 (1995).
82 Rader, C., Popkov, M., Neves, J. A. & III, C. F. B. Integrin αvβ3 targeted therapy for Kaposi's sarcoma with an in vitro evolved antibody. *The FASEB Journal* **16**, 2000-2002, doi:10.1096/fj.02-0281fje (2002).
83 Kumar, C. C. *et al.* Inhibition of Angiogenesis and Tumor Growth by SCH221153, a Dual αvβ3 and αvβ5 Integrin Receptor Antagonist. *Cancer Research* **61**, 2232-2238 (2001).
84 Trikha, M. *et al.* CNTO 95, a fully human monoclonal antibody that inhibits αv integrins, has antitumor and antiangiogenic activity in vivo. *International Journal of Cancer* **110**, 326-335, doi:doi:10.1002/ijc.20116 (2004).
85 MacDonald, T. J. *et al.* Preferential susceptibility of brain tumors to the antiangiogenic effects of an alpha(v) integrin antagonist. *Neurosurgery* **48**, 151-157 (2001).
86 Taga, T. *et al.* αv-Integrin antagonist EMD 121974 induces apoptosis in brain tumor cells growing on vitronectin and tenascin. *International Journal of Cancer* **98**, 690-697, doi:doi:10.1002/ijc.10265 (2002).
87 Gasparini, G. *et al.* Vascular integrin alpha(v)beta3: a new prognostic indicator in breast cancer. *Clinical Cancer Research* **4**, 2625-2634 (1998).

88 Brooks, P. C. *et al.* Integrin αvβ3 antagonists promote tumor regression by inducing apoptosis of angiogenic blood vessels. *Cell* **79**, 1157-1164, doi:10.1016/0092-8674(94)90007-8 (1994).
89 Brooks, P. C. *et al.* Antiintegrin alpha v beta 3 blocks human breast cancer growth and angiogenesis in human skin. *Journal of Clinical Investigation* **96**, 1815-1822 (1995).
90 Riecke, B. *et al.* Topical Application of Integrin Antagonists Inhibits Proliferative Retinopathy. *Horm Metab Res* **33**, 307-311, doi:10.1055/s-2001-15279 (2001).
91 Hammes, H.-P., Brownlee, M., Jonczyk, A., Sutter, A. & Preissner, K. T. Subcutaneous injection of a cyclic peptide antagonist of vitronectin receptor–type integrins inhibits retinal neovascularization. *Nature Medicine* **2**, 529, doi:10.1038/nm0596-529 (1996).
92 Chavakis, E. *et al.* Kinetics of integrin expression in the mouse model of proliferative retinopathy and success of secondary intervention with cyclic RGD peptides. *Diabetologia* **45**, 262-267, doi:10.1007/s00125-001-0727-z (2002).
93 Soldi, R. *et al.* Role of αvβ3 integrin in the activation of vascular endothelial growth factor receptor 2. *The EMBO Journal* **18**, 882-892, doi:10.1093/emboj/18.4.882 (1999).
94 Reynolds, A. R. *et al.* Elevated Flk1 (Vascular Endothelial Growth Factor Receptor 2) Signaling Mediates Enhanced Angiogenesis in β3-Integrin–Deficient Mice. *Cancer Research* **64**, 8643-8650, doi:10.1158/0008-5472.can-04-2760 (2004).
95 Mahabeleshwar, G. H., Feng, W., Reddy, K., Plow, E. F. & Byzova, T. V. Mechanisms of Integrin–Vascular Endothelial Growth Factor Receptor Cross-Activation in Angiogenesis. *Circulation Research* **101**, 570-580, doi:10.1161/circresaha.107.155655 (2007).
96 De, S. *et al.* VEGF–integrin interplay controls tumor growth and vascularization. *Proceedings of the National Academy of Sciences of the United States of America* **102**, 7589-7594, doi:10.1073/pnas.0502935102 (2005).
97 Robinson, S. D., Reynolds, L. E., Wyder, L., Hicklin, D. J. & Hodivala-Dilke, K. M. β3-Integrin Regulates Vascular Endothelial Growth Factor-A–Dependent Permeability. *Arteriosclerosis, Thrombosis, and Vascular Biology* **24**, 2108-2114, doi:10.1161/01.ATV.0000143857.27408.de (2004).
98 Saiki, I. *et al.* Inhibition of Tumor Angiogenesis by a Synthetic Cell-adhesive Polypeptide Containing the Arg-Gly-Asp (RGD) Sequence of Fibronectin, Poly(RGD). *Japanese Journal of Cancer Research* **81**, 668-675, doi:doi:10.1111/j.1349-7006.1990.tb02625.x (1990).
99 Nicosia, R. F. & Bonanno, E. Inhibition of angiogenesis in vitro by Arg-Gly-Asp-containing synthetic peptide. *The American Journal of Pathology* **138**, 829-833 (1991).
100 Mitjans, F. *et al.* In vivo therapy of malignant melanoma by means of antagonists of αv integrins. *International Journal of Cancer* **87**, 716-723, doi:doi:10.1002/1097-0215(20000901)87:5<716::AID-IJC14>3.0.CO;2-R (2000).
101 Eskens, F. A. L. M. *et al.* Phase I and pharmacokinetic study of continuous twice weekly intravenous administration of Cilengitide (EMD 121974), a

novel inhibitor of the integrins alphavbeta3 and alphavbeta5 in patients with advanced solid tumours. *European Journal of Cancer* **39**, 917-926, doi:10.1016/S0959-8049(03)00057-1 (2003).

102 Hariharan, S. *et al.* Assessment of the biological and pharmacological effects of the αvβ3 and αvβ5 integrin receptor antagonist, cilengitide (EMD 121974), in patients with advanced solid tumors. *Annals of Oncology* **18**, 1400-1407, doi:10.1093/annonc/mdm140 (2007).

103 Raguse, J.-D., Gath, H. J., Bier, J., Riess, H. & Oettle, H. Cilengitide (EMD 121974) arrests the growth of a heavily pretreated highly vascularised head and neck tumour. *Oral Oncology* **40**, 228-230, doi:https://doi.org/10.1016/j.oraloncology.2003.08.003 (2004).

104 Nabors, L. B. *et al.* Phase I and Correlative Biology Study of Cilengitide in Patients With Recurrent Malignant Glioma. *Journal of Clinical Oncology* **25**, 1651-1657, doi:10.1200/jco.2006.06.6514 (2007).

105 Stupp, R. *et al.* Phase I/IIa Study of Cilengitide and Temozolomide With Concomitant Radiotherapy Followed by Cilengitide and Temozolomide Maintenance Therapy in Patients With Newly Diagnosed Glioblastoma. *Journal of Clinical Oncology* **28**, 2712-2718, doi:10.1200/jco.2009.26.6650 (2010).

106 Reardon, D. A. *et al.* Randomized Phase II Study of Cilengitide, an Integrin-Targeting Arginine-Glycine-Aspartic Acid Peptide, in Recurrent Glioblastoma Multiforme. *Journal of Clinical Oncology* **26**, 5610-5617, doi:10.1200/jco.2008.16.7510 (2008).

107 Nabors, L. B. *et al.* NABTT 0306: A randomized phase II trial of EMD 121974 in conjunction with concomitant and adjuvant temozolomide with radiation therapy in patients with newly diagnosed glioblastoma multiforme (GBM). *Journal of Clinical Oncology* **27**, 2001-2001, doi:10.1200/jco.2009.27.15_suppl.2001 (2009).

108 Friess, H. *et al.* A randomized multi-center phase II trial of the angiogenesis inhibitor Cilengitide (EMD 121974) and gemcitabine compared with gemcitabine alone in advanced unresectable pancreatic cancer. *BMC Cancer* **6**, 285-285, doi:10.1186/1471-2407-6-285 (2006).

109 Nabors, L. B. *et al.* Two cilengitide regimens in combination with standard treatment for patients with newly diagnosed glioblastoma and unmethylated MGMT gene promoter: results of the open-label, controlled, randomized phase II CORE study. *Neuro-Oncology* **17**, 708-717, doi:10.1093/neuonc/nou356 (2015).

110 Stupp, R. *et al.* Cilengitide combined with standard treatment for patients with newly diagnosed glioblastoma with methylated MGMT promoter (CENTRIC EORTC 26071-22072 study): a multicentre, randomised, open-label, phase 3 trial. *The Lancet Oncology* **15**, 1100-1108, doi:http://dx.doi.org/10.1016/S1470-2045(14)70379-1 (2014).

111 Reynolds, A. R. *et al.* Stimulation of tumor growth and angiogenesis by low concentrations of RGD-mimetic integrin inhibitors. *Nature Medicine* **15**, 392, doi:10.1038/nm.1941

https://www.nature.com/articles/nm.1941#supplementary-information (2009).

112 Wong, P.-P. *et al.* Dual-Action Combination Therapy Enhances Angiogenesis while Reducing Tumor Growth and Spread. *Cancer Cell* **27**, 123-137, doi:10.1016/j.ccell.2014.10.015 (2015).

113 Mas-Moruno, C., Rechenmacher, F. & Kessler, H. Cilengitide: The First Anti-Angiogenic Small Molecule Drug Candidate. Design, Synthesis and Clinical Evaluation. *Anti-Cancer Agents in Medicinal Chemistry* **10**, 753-768, doi:10.2174/187152010794728639 (2010).
114 Albert, J. M. *et al.* Integrin alpha v beta 3 antagonist Cilengitide enhances efficacy of radiotherapy in endothelial cell and non small-cell lung cancer models. *International Journal of Radiation Oncology • Biology • Physics* **65**, 1536-1543, doi:10.1016/j.ijrobp.2006.04.036 (2006).
115 Abdollahi, A. *et al.* Inhibition of αvβ3 Integrin Survival Signaling Enhances Antiangiogenic and Antitumor Effects of Radiotherapy. *Clinical Cancer Research* **11**, 6270-6279, doi:10.1158/1078-0432.Ccr-04-1223 (2005).
116 Wu, H. *et al.* Stepwise in vitro affinity maturation of Vitaxin, an α(v)β(3)-specific humanized mAb. *Proceedings of the National Academy of Sciences of the United States of America* **95**, 6037-6042 (1998).
117 Gutheil, J. C. *et al.* Targeted Antiangiogenic Therapy for Cancer Using Vitaxin: A Humanized Monoclonal Antibody to the Integrin αvβ3. *Clinical Cancer Research* **6**, 3056-3061 (2000).
118 Posey, J. A. *et al.* A Pilot Trial of Vitaxin, A Humanized Anti-Vitronectin Receptor (anti αvβ3) Antibody in Patients with Metastatic Cancer. *Cancer Biotherapy and Radiopharmaceuticals* **16**, 125-132, doi:10.1089/108497801300189218 (2001).
119 Hersey, P. *et al.* A randomized phase 2 study of etaracizumab, a monoclonal antibody against integrin αvβ3, ± dacarbazine in patients with stage IV metastatic melanoma. *Cancer* **116**, 1526-1534, doi:doi:10.1002/cncr.24821 (2010).
120 Patel, S. R. *et al.* Pilot study of vitaxin—an angiogenesis inhibitor—in patients with advanced leiomyosarcomas. *Cancer* **92**, 1347-1348, doi:doi:10.1002/1097-0142(20010901)92:5<1347::AID-CNCR1456>3.0.CO;2-0 (2001).
121 Davis, S. *et al.* Isolation of Angiopoietin-1, a Ligand for the TIE2 Receptor, by Secretion-Trap Expression Cloning. *Cell* **87**, 1161-1169, doi:https://doi.org/10.1016/S0092-8674(00)81812-7 (1996).
122 Maisonpierre, P. C. *et al.* Angiopoietin-2, a Natural Antagonist for Tie2 That Disrupts in vivo Angiogenesis. *Science* **277**, 55-60, doi:10.1126/science.277.5322.55 (1997).
123 Yuan, H. T., Khankin, E. V., Karumanchi, S. A. & Parikh, S. M. Angiopoietin 2 Is a Partial Agonist/Antagonist of Tie2 Signaling in the Endothelium. *Molecular and Cellular Biology* **29**, 2011-2022, doi:10.1128/mcb.01472-08 (2009).
124 Helfrich, I. *et al.* Angiopoietin-2 Levels Are Associated with Disease Progression in Metastatic Malignant Melanoma. *Clinical Cancer Research* **15**, 1384-1392, doi:10.1158/1078-0432.Ccr-08-1615 (2009).
125 Murdoch, C., Tazzyman, S., Webster, S. & Lewis, C. E. Expression of Tie-2 by Human Monocytes and Their Responses to Angiopoietin-2. *The Journal of Immunology* **178**, 7405-7411, doi:10.4049/jimmunol.178.11.7405 (2007).
126 Chen, L. *et al.* Tie2 expression on macrophages is required for blood vessel reconstruction and tumor relapse after chemotherapy. *Cancer Research*, doi:10.1158/0008-5472.Can-16-1114 (2016).

127 De Palma, M. *et al.* Tie2 identifies a hematopoietic lineage of proangiogenic monocytes required for tumor vessel formation and a mesenchymal population of pericyte progenitors. *Cancer Cell* **8**, 211-226, doi:10.1016/j.ccr.2005.08.002 (2005).
128 Sfiligoi, C. *et al.* Angiopoietin-2 expression in breast cancer correlates with lymph node invasion and short survival. *International Journal of Cancer* **103**, 466-474, doi:doi:10.1002/ijc.10851 (2003).
129 Ahmad, S. A. *et al.* The Effects of Angiopoietin-1 and -2 on Tumor Growth and Angiogenesis in Human Colon Cancer. *Cancer Research* **61**, 1255-1259 (2001).
130 Imanishi, Y. *et al.* Angiopoietin-2 Stimulates Breast Cancer Metastasis through the α5β1 Integrin-Mediated Pathway. *Cancer Research* **67**, 4254-4263, doi:10.1158/0008-5472.Can-06-4100 (2007).
131 Nasarre, P. *et al.* Host-Derived Angiopoietin-2 Affects Early Stages of Tumor Development and Vessel Maturation but Is Dispensable for Later Stages of Tumor Growth. *Cancer Research* **69**, 1324-1333, doi:10.1158/0008-5472.Can-08-3030 (2009).
132 Huang, Y. *et al.* Pulmonary Vascular Destabilization in the Premetastatic Phase Facilitates Lung Metastasis. *Cancer Research* **69**, 7529-7537, doi:10.1158/0008-5472.Can-08-4382 (2009).
133 Oliner, J. *et al.* Suppression of angiogenesis and tumor growth by selective inhibition of angiopoietin-2. *Cancer Cell* **6**, 507-516, doi:10.1016/j.ccr.2004.09.030 (2004).
134 Huang, H. *et al.* Specifically Targeting Angiopoietin-2 Inhibits Angiogenesis, Tie2-Expressing Monocyte Infiltration, and Tumor Growth. *Clinical Cancer Research* **17**, 1001-1011, doi:10.1158/1078-0432.Ccr-10-2317 (2011).
135 Brown, J. L. *et al.* A Human Monoclonal Anti-ANG2 Antibody Leads to Broad Antitumor Activity in Combination with VEGF Inhibitors and Chemotherapy Agents in Preclinical Models. *Molecular Cancer Therapeutics* **9**, 145-156, doi:10.1158/1535-7163.Mct-09-0554 (2010).
136 Hashizume, H. *et al.* Complementary Actions of Inhibitors of Angiopoietin-2 and VEGF on Tumor Angiogenesis and Growth. *Cancer research* **70**, 2213-2223, doi:10.1158/0008-5472.CAN-09-1977 (2010).
137 Lin, P. *et al.* Antiangiogenic gene therapy targeting the endothelium-specific receptor tyrosine kinase Tie2. *Proceedings of the National Academy of Sciences* **95**, 8829-8834, doi:10.1073/pnas.95.15.8829 (1998).
138 Herbst, R. S. *et al.* Safety, Pharmacokinetics, and Antitumor Activity of AMG 386, a Selective Angiopoietin Inhibitor, in Adult Patients With Advanced Solid Tumors. *Journal of Clinical Oncology* **27**, 3557-3565, doi:10.1200/jco.2008.19.6683 (2009).
139 Tait, C. R. & Jones, P. F. Angiopoietins in tumours: the angiogenic switch. *The Journal of Pathology* **204**, 1-10, doi:doi:10.1002/path.1618 (2004).
140 Geiger, T. R. & Peeper, D. S. Metastasis mechanisms. *Biochimica et Biophysica Acta (BBA) - Reviews on Cancer* **1796**, 293-308, doi:http://dx.doi.org/10.1016/j.bbcan.2009.07.006 (2009).
141 Steeg, P. S. Metastasis suppressors alter the signal transduction of cancer cells. *Nature Reviews Cancer* **3**, 55, doi:10.1038/nrc967 (2003).

142 Munshi, H. G. & Stack, M. S. Reciprocal interactions between adhesion receptor signaling and MMP regulation. *Cancer and Metastasis Reviews* **25**, 45-56, doi:10.1007/s10555-006-7888-7 (2006).
143 Baum, O. *et al.* Increased invasive potential and up-regulation of MMP-2 in MDA-MB-231 breast cancer cells expressing the β3 integrin subunit. *International Journal of Oncology* **30**, 325-332 (2007).
144 Attieh, Y. *et al.* Cancer-associated fibroblasts lead tumor invasion through integrin-β3–dependent fibronectin assembly. *The Journal of Cell Biology* **216**, 3509-3520, doi:10.1083/jcb.201702033 (2017).
145 Roman, J., Ritzenthaler, J. D., Roser-Page, S., Sun, X. & Han, S. α5β1-Integrin Expression Is Essential for Tumor Progression in Experimental Lung Cancer. *American Journal of Respiratory Cell and Molecular Biology* **43**, 684-691, doi:10.1165/rcmb.2009-0375OC (2010).
146 Desgrosellier, J. S. *et al.* Integrin αvβ3/c-src "Oncogenic Unit" Promotes Anchorage-independence and Tumor Progression. *Nature medicine* **15**, 1163-1169, doi:10.1038/nm.2009 (2009).
147 Alanko, J. *et al.* Integrin endosomal signalling suppresses anoikis. *Nature Cell Biology* **17**, 1412, doi:10.1038/ncb3250

https://www.nature.com/articles/ncb3250#supplementary-information (2015).
148 Knowles, L. M. *et al.* Integrin αvβ3 and Fibronectin Upregulate Slug in Cancer Cells to Promote Clot Invasion and Metastasis. *Cancer Research* **73**, 6175-6184, doi:10.1158/0008-5472.Can-13-0602 (2013).
149 Murphy, E. A. *et al.* Nanoparticle-mediated drug delivery to tumor vasculature suppresses metastasis. *Proceedings of the National Academy of Sciences* **105**, 9343-9348, doi:10.1073/pnas.0803728105 (2008).
150 Arap, W., Pasqualini, R. & Ruoslahti, E. Cancer Treatment by Targeted Drug Delivery to Tumor Vasculature in a Mouse Model. *Science* **279**, 377-380, doi:10.1126/science.279.5349.377 (1998).
151 Hakanpaa, L. *et al.* Endothelial destabilization by angiopoietin-2 via integrin β1 activation. *Nature Communications* **6**, 5962, doi:10.1038/ncomms6962 (2015).
152 Stoletov, K. *et al.* Visualizing extravasation dynamics of metastatic tumor cells. *Journal of Cell Science* **123**, 2332-2341, doi:10.1242/jcs.069443 (2010).
153 Hamidi, H. & Ivaska, J. Every step of the way: integrins in cancer progression and metastasis. *Nature Reviews Cancer* **18**, 533-548, doi:10.1038/s41568-018-0038-z (2018).
154 Lorger, M., Krueger, J. S., O'Neal, M., Staflin, K. & Felding-Habermann, B. Activation of tumor cell integrin αvβ3 controls angiogenesis and metastatic growth in the brain. *Proceedings of the National Academy of Sciences* **106**, 10666-10671, doi:10.1073/pnas.0903035106 (2009).
155 Vogetseder, A. *et al.* αv-Integrin isoform expression in primary human tumors and brain metastases. *International Journal of Cancer* **133**, 2362-2371, doi:doi:10.1002/ijc.28267 (2013).
156 Bäuerle, T. *et al.* Cilengitide inhibits progression of experimental breast cancer bone metastases as imaged noninvasively using VCT, MRI and DCE-MRI in a longitudinal in vivo study. *International Journal of Cancer* **128**, 2453-2462, doi:doi:10.1002/ijc.25563 (2011).

157 Sloan, E. K. *et al.* Tumor-specific expression of αvβ3 integrin promotes spontaneous metastasis of breast cancer to bone. *Breast Cancer Research* **8**, R20, doi:10.1186/bcr1398 (2006).
158 Barney, L. E. *et al.* A cell–ECM screening method to predict breast cancer metastasis. *Integrative biology : quantitative biosciences from nano to macro* **7**, 198-212, doi:10.1039/c4ib00218k (2015).
159 Achrol, A. S. *et al.* Brain metastases. *Nature Reviews Disease Primers* **5**, 5, doi:10.1038/s41572-018-0055-y (2019).
160 Nomoto, Y., Miyamoto, T. & Yamaguchi, Y. Brain Metastasis of Small Cell Lung Carcinoma: Comparison of Gd-DTPA Enhanced Magnetic Resonance Imaging and Enhanced Computerized Tomography. *Japanese Journal of Clinical Oncology* **24**, 258-262, doi:10.1093/oxfordjournals.jjco.a039718 (1994).
161 Mehndiratta, A., Tee, Y., Payne, S., Chappell, M. & Giesel, F. in *Tumors of the Central Nervous System, Volume 11* Vol. 11 *Tumors of the Central Nervous System* (ed M. A. Hayat) Ch. 1, 3-20 (Springer Netherlands, 2014).
162 Katakami, N. *et al.* Magnetic Resonance Evaluation of Brain Metastases From Systemic Malignances With Two Doses of Gadobutrol 1.0 M Compared With Gadoteridol: A Multicenter, Phase II/III Study in Patients With Known or Suspected Brain Metastases. *Investigative Radiology* **46**, 411-418, doi:10.1097/RLI.0b013e3182145a6c (2011).
163 Lockman, P. R. *et al.* Heterogeneous Blood–Tumor Barrier Permeability Determines Drug Efficacy in Experimental Brain Metastases of Breast Cancer. *Clinical Cancer Research* **16**, 5664-5678, doi:10.1158/1078-0432.Ccr-10-1564 (2010).
164 Zhang, R. D., Price, J. E., Fujimaki, T., Bucana, C. D. & Fidler, I. J. Differential permeability of the blood-brain barrier in experimental brain metastases produced by human neoplasms implanted into nude mice. *American Journal of Pathology* **141**, 1115-1124 (1992).
165 Fidler, I. J., Yano, S., Zhang, R.-d., Fujimaki, T. & Bucana, C. D. The seed and soil hypothesis: vascularisation and brain metastases. *The Lancet Oncology* **3**, 53-57, doi:https://doi.org/10.1016/S1470-2045(01)00622-2 (2002).
166 Serres, S. *et al.* Molecular MRI enables early and sensitive detection of brain metastases. *Proceedings of the National Academy of Sciences* **109**, 6674-6679, doi:10.1073/pnas.1117412109 (2012).
167 Zhang, R. D., Price, J. E., Fujimaki, T., Bucana, C. D. & Fidler, I. J. Differential permeability of the blood-brain barrier in experimental brain metastases produced by human neoplasms implanted into nude mice. *The American Journal of Pathology* **141**, 1115-1124 (1992).
168 Weissleder, R. & Pittet, M. J. Imaging in the era of molecular oncology. *Nature* **452**, 580-589 (2008).
169 Sala, E., Vargas, H., Donati, O., Weber, W. & Hricak, H. in *Functional Imaging in Oncology* (eds Antonio Luna, Joan C. Vilanova, L. Celso Hygino da Cruz Jr, & Santiago E. Rossi) Ch. 3, 43-58 (Springer Berlin Heidelberg, 2014).
170 Kienast, Y. *et al.* Real-time imaging reveals the single steps of brain metastasis formation. *Nature Medicine* **16**, 116, doi:10.1038/nm.2072

https://www.nature.com/articles/nm.2072#supplementary-information (2009).
171 Fitzgerald, D. P. *et al.* Reactive glia are recruited by highly proliferative brain metastases of breast cancer and promote tumor cell colonization. *Clinical & Experimental Metastasis* **25**, 799-810, doi:10.1007/s10585-008-9193-z (2008).
172 Küsters, B. *et al.* Vascular Endothelial Growth Factor-A165 Induces Progression of Melanoma Brain Metastases without Induction of Sprouting Angiogenesis. *Cancer Research* **62**, 341-345 (2002).
173 Leenders, W. P. J. *et al.* Antiangiogenic Therapy of Cerebral Melanoma Metastases Results in Sustained Tumor Progression via Vessel Co-Option. *Clinical Cancer Research* **10**, 6222-6230, doi:10.1158/1078-0432.Ccr-04-0823 (2004).
174 Eichler, A. F. *et al.* The biology of brain metastases - translation to new therapies. *Nat Rev Clin Oncol* **8**, 344-356 (2011).
175 Pulaski, B. A. & Ostrand-Rosenberg, S. Mouse 4T1 Breast Tumor Model. *Current Protocols in Immunology* **39**, 20.22.21-20.22.16, doi:doi:10.1002/0471142735.im2002s39 (2000).
176 Balathasan, L., Beech, J. S. & Muschel, R. J. Ultrasonography-Guided Intracardiac Injection. *The American Journal of Pathology* **183**, 26-34, doi:10.1016/j.ajpath.2013.03.003 (2013).
177 Aslakson, C. J. & Miller, F. R. Selective Events in the Metastatic Process Defined by Analysis of the Sequential Dissemination of Subpopulations of a Mouse Mammary Tumor. *Cancer Research* **52**, 1399-1405 (1992).
178 Laakmann, E. *et al.* Radiological Patterns of Brain Metastases in Breast Cancer Patients: A Subproject of the German Brain Metastases in Breast Cancer (BMBC) Registry. *International journal of molecular sciences* **17**, 1615, doi:10.3390/ijms17101615 (2016).
179 Lekanidi, K. *et al.* Pattern of brain metastatic disease according to HER-2 and ER receptor status in breast cancer patients. *Clinical Radiology* **68**, 1070-1073, doi:https://doi.org/10.1016/j.crad.2013.05.091 (2013).
180 Niwińska, A., Rudnicka, H. & Murawska, M. Breast cancer leptomeningeal metastasis: propensity of breast cancer subtypes for leptomeninges and the analysis of factors influencing survival. *Medical Oncology* **30**, 408, doi:10.1007/s12032-012-0408-4 (2013).
181 Candolfi, M. *et al.* Intracranial glioblastoma models in preclinical neuro-oncology: neuropathological characterization and tumor progression. *Journal of neuro-oncology* **85**, 133-148, doi:10.1007/s11060-007-9400-9 (2007).
182 Soffietti, R. *et al.* Diagnosis and treatment of brain metastases from solid tumors: guidelines from the European Association of Neuro-Oncology (EANO). *Neuro-Oncology* **19**, 162-174, doi:10.1093/neuonc/now241 (2017).
183 National Institute for Health and Care Excellence. *NICE guideline [NG99] Brain tumours (primary) and brain metastases in adults*. (NICE, 2018).
184 Fernandes, C. *et al.* in *Glioblastoma* (ed S De Vleeschouwer) (Codon Publications, 2017).
185 Weller, M. *et al.* EANO guideline for the diagnosis and treatment of anaplastic gliomas and glioblastoma. *The Lancet Oncology* **15**, e395-e403, doi:10.1016/S1470-2045(14)70011-7 (2014).

186 Weller, M., Cloughesy, T., Perry, J. R. & Wick, W. Standards of care for treatment of recurrent glioblastoma—are we there yet? *Neuro-Oncology* **15**, 4-27, doi:10.1093/neuonc/nos273 (2013).
187 Hygino da Cruz, L. C., Rodriguez, I., Domingues, R. C., Gasparetto, E. L. & Sorensen, A. G. Pseudoprogression and Pseudoresponse: Imaging Challenges in the Assessment of Posttreatment Glioma. *American Journal of Neuroradiology* **32**, 1978-1985, doi:10.3174/ajnr.A2397 (2011).
188 Abdulla, S., Saada, J., Johnson, G., Jefferies, S. & Ajithkumar, T. Tumour progression or pseudoprogression? A review of post-treatment radiological appearances of glioblastoma. *Clinical Radiology* **70**, 1299-1312, doi:10.1016/j.crad.2015.06.096 (2015).
189 Wen, P. Y. *et al.* Updated Response Assessment Criteria for High-Grade Gliomas: Response Assessment in Neuro-Oncology Working Group. *Journal of Clinical Oncology* **28**, 1963-1972, doi:10.1200/jco.2009.26.3541 (2010).
190 O'Connor, J. P. B. *et al.* Imaging biomarker roadmap for cancer studies. *Nature Reviews Clinical Oncology* **14**, 169, doi:10.1038/nrclinonc.2016.162

https://www.nature.com/articles/nrclinonc.2016.162#supplementary-information (2016).
191 Kiessling, F. *et al.* Recent Advances in Molecular, Multimodal and Theranostic Ultrasound Imaging. *Advanced drug delivery reviews* **0**, 15-27, doi:10.1016/j.addr.2013.11.013 (2014).
192 Abou-Elkacem, L., Bachawal, S. V. & Willmann, J. K. Ultrasound Molecular Imaging: Moving Towards Clinical Translation. *European journal of radiology* **84**, 1685-1693, doi:10.1016/j.ejrad.2015.03.016 (2015).
193 Zarghami, N. *et al.* Optimization of molecularly targeted MRI in the brain: empirical comparison of sequences and particles. *International journal of nanomedicine* **13**, 4345-4359, doi:10.2147/IJN.S158071 (2018).
194 Cheng, V. W. T. *et al.* VCAM-1 targeted magnetic resonance imaging enables detection of brain micrometastases from different primary tumours. *Clinical Cancer Research*, clincanres.1889.2018, doi:10.1158/1078-0432.Ccr-18-1889 (2018).
195 Melemenidis, S. *et al.* Molecular magnetic resonance imaging of angiogenesis in vivo using polyvalent cyclic RGD-iron oxide microparticle conjugates. *Theranostics* **5**, 515-529, doi:10.7150/thno.10319 (2015).
196 Hengerer, A. & Grimm, J. Molecular magnetic resonance imaging. *Biomedical Imaging and Intervention Journal* **2**, e8, doi:10.2349/biij.2.2.e8 (2006).
197 Ray, K. J. *et al.* Determination of an optimally sensitive and specific chemical exchange saturation transfer MRI quantification metric in relevant biological phantoms. *NMR in Biomedicine* **29**, 1624-1633, doi:doi:10.1002/nbm.3614 (2016).
198 Sipkins, D. A. *et al.* Detection of tumor angiogenesis in vivo by [alpha]v[beta]3-targeted magnetic resonance imaging. *Nat Med* **4**, 623-626 (1998).
199 Weis, S. M. & Cheresh, D. A. Tumor angiogenesis: molecular pathways and therapeutic targets. *Nat Med* **17**, 1359-1370 (2011).

200 Wesseling, P., van der Laak, J. A. W. M., de Leeuw, H., Ruiter, D. J. & Burger, P. C. Quantitative immunohistological analysis of the microvasculature in untreated human glioblastoma multiforme. *Journal of Neurosurgery* **81**, 902-909, doi:10.3171/jns.1994.81.6.0902 (1994).
201 Giatromanolaki, A. *et al.* 'Invading edge vs. inner' (edvin) patterns of vascularization: an interplay between angiogenic and vascular survival factors defines the clinical behaviour of non-small cell lung cancer. *The Journal of Pathology* **192**, 140-149, doi:10.1002/1096-9896(2000)9999:9999<::aid-path693>3.0.co;2-r (2000).
202 Gladson, C. L. & Cheresh, D. A. Glioblastoma expression of vitronectin and the alpha v beta 3 integrin. Adhesion mechanism for transformed glial cells. *The Journal of Clinical Investigation* **88**, 1924-1932, doi:10.1172/jci115516 (1991).
203 Brooks, P., Clark, R. & Cheresh, D. Requirement of vascular integrin alpha v beta 3 for angiogenesis. *Science* **264**, 569-571, doi:10.1126/science.7512751 (1994).
204 Gladson, C. L. Expression of Integrin avb3 in Small Blood Vessels of Glioblastoma Tumors. *Journal of Neuropathology & Experimental Neurology* **55**, 1143-1149 (1996).
205 Zitzmann, S., Ehemann, V. & Schwab, M. Arginine-Glycine-Aspartic Acid (RGD)-Peptide Binds to Both Tumor and Tumor-Endothelial Cells in Vivo. *Cancer Research* **62**, 5139-5143 (2002).
206 Pierschbacher, M. D. & Ruoslahti, E. Cell attachment activity of fibronectin can be duplicated by small synthetic fragments of the molecule. *Nature* **309**, 30-33 (1984).
207 Haubner, R. *et al.* Noninvasive Imaging of αvβ3 Integrin Expression Using 18F-labeled RGD-containing Glycopeptide and Positron Emission Tomography. *Cancer Research* **61**, 1781-1785 (2001).
208 Haubner, R. *et al.* Radiolabeled αvβ3 Integrin Antagonists: A New Class of Tracers for Tumor Targeting. *Journal of Nuclear Medicine* **40**, 1061-1071 (1999).
209 van Hagen, P. M. *et al.* Evaluation of a radiolabelled cyclic DTPA-RGD analogue for tumour imaging and radionuclide therapy. *International Journal of Cancer* **90**, 186-198, doi:10.1002/1097-0215(20000820)90:4<186::aid-ijc2>3.0.co;2-p (2000).
210 Sivolapenko, G. B. *et al.* Imaging of metastatic melanoma utilising a technetium-99m labelled RGD-containing synthetic peptide. *Eur J Nucl Med* **25**, 1383-1389, doi:10.1007/s002590050312 (1998).
211 Wu, Y. *et al.* microPET Imaging of Glioma Integrin αvβ3 Expression Using 64Cu-Labeled Tetrameric RGD Peptide. *Journal of Nuclear Medicine* **46**, 1707-1718 (2005).
212 Benezra, M. *et al.* Multimodal silica nanoparticles are effective cancer-targeted probes in a model of human melanoma. *The Journal of Clinical Investigation* **121**, 2768-2780, doi:10.1172/jci45600 (2011).
213 Mulder, W. J. M. *et al.* Molecular imaging of tumor angiogenesis using αvβ3-integrin targeted multimodal quantum dots. *Angiogenesis* **12**, 17-24, doi:10.1007/s10456-008-9124-2 (2009).
214 Carbary-Ganz, J. L., Welge, W. A., Barton, J. K. & Utzinger, U. In vivo molecular imaging of colorectal cancer using quantum dots targeted to vascular endothelial growth factor receptor 2 and optical coherence

tomography/laser-induced fluorescence dual-modality imaging. *Journal of Biomedical Optics* **20**, 096015, doi:10.1117/1.jbo.20.9.096015 (2015).
215 Backer, M. V. *et al.* Molecular imaging of VEGF receptors in angiogenic vasculature with single-chain VEGF-based probes. *Nature Medicine* **13**, 504, doi:10.1038/nm1522

https://www.nature.com/articles/nm1522#supplementary-information (2007).
216 Cai, W. *et al.* PET of Vascular Endothelial Growth Factor Receptor Expression. *Journal of Nuclear Medicine* **47**, 2048-2056 (2006).
217 Luo, H. *et al.* PET Imaging of VEGFR-2 Expression in Lung Cancer with (64)Cu-Labeled Ramucirumab. *Journal of nuclear medicine : official publication, Society of Nuclear Medicine* **57**, 285-290, doi:10.2967/jnumed.115.166462 (2016).
218 Meyer, J.-P. *et al.* Selective Imaging of VEGFR-1 and VEGFR-2 Using (89)Zr-Labeled Single-Chain VEGF Mutants. *Journal of Nuclear Medicine* **57**, 1811-1816, doi:10.2967/jnumed.116.173237 (2016).
219 Chen, K., Cai, W., Li, Z.-B., Wang, H. & Chen, X. Quantitative PET imaging of VEGF receptor expression. *Journal of Nuclear Medicine* **49**, 103P (2008).
220 Nagengast, W. B. *et al.* VEGF-PET Imaging Is a Noninvasive Biomarker Showing Differential Changes in the Tumor during Sunitinib Treatment. *Cancer Research* **71**, 143-153, doi:10.1158/0008-5472.Can-10-1088 (2011).
221 Pochon, S. *et al.* BR55: A Lipopeptide-Based VEGFR2-Targeted Ultrasound Contrast Agent for Molecular Imaging of Angiogenesis. *Investigative Radiology* **45**, 89-95, doi:10.1097/RLI.0b013e3181c5927c (2010).
222 Tardy, I. *et al.* Ultrasound Molecular Imaging of VEGFR2 in a Rat Prostate Tumor Model Using BR55. *Investigative Radiology* **45**, 573-578, doi:10.1097/RLI.0b013e3181ee8b83 (2010).
223 Wang, H., Kaneko, O. F., Tian, L., Hristov, D. & Willmann, J. K. Three-dimensional Ultrasound Molecular Imaging of Angiogenesis in Colon Cancer using a Clinical Matrix Array Ultrasound Transducer. *Investigative radiology* **50**, 322-329, doi:10.1097/RLI.0000000000000128 (2015).
224 Wang, S. *et al.* Ultra-low-dose Ultrasound Molecular Imaging for the Detection of Angiogenesis in a Mouse Murine Tumor Model: How Little Can We See? *Investigative radiology* **51**, 758-766, doi:10.1097/RLI.0000000000000310 (2016).
225 Deshpande, N., Ren, Y., Foygel, K., Rosenberg, J. & Willmann, J. K. Tumor Angiogenic Marker Expression Levels during Tumor Growth: Longitudinal Assessment with Molecularly Targeted Microbubbles and US Imaging. *Radiology* **258**, 804-811, doi:10.1148/radiol.10101079 (2011).
226 Rychak, J. J. *et al.* Microultrasound Molecular Imaging of Vascular Endothelial Growth Factor Receptor 2 in a Mouse Model of Tumor Angiogenesis. *Molecular Imaging* **6**, 7290.2007.00024, doi:10.2310/7290.2007.00024 (2007).
227 Rojas, J. D. *et al.* Ultrasound molecular imaging of VEGFR-2 in clear-cell renal carcinoma tracks disease response to angiogenic and notch-inhibition therapy. *Theranostics* **8**, 141-155 (2018).

228 Baetke, S. C. *et al.* Squamous Cell Carcinoma Xenografts: Use of VEGFR2-targeted Microbubbles for Combined Functional and Molecular US to Monitor Antiangiogenic Therapy Effects. *Radiology* **278**, 430-440, doi:10.1148/radiol.2015142899 (2016).
229 Willmann, J. K. *et al.* Ultrasound Molecular Imaging With BR55 in Patients With Breast and Ovarian Lesions: First-in-Human Results. *J Clin Oncol* **35**, 2133-2140, doi:10.1200/JCO.2016.70.8594 (2017).
230 Smeenge, M. *et al.* First-in-Human Ultrasound Molecular Imaging With a VEGFR2-Specific Ultrasound Molecular Contrast Agent (BR55) in Prostate Cancer: A Safety and Feasibility Pilot Study. *Investigative Radiology* **52**, 419-427, doi:10.1097/rli.0000000000000362 (2017).
231 O'Connor, M. K. *et al.* Comparison of Tc-99m maraciclatide and Tc-99m sestamibi molecular breast imaging in patients with suspected breast cancer. *EJNMMI Research* **7**, 5, doi:10.1186/s13550-017-0255-6 (2017).
232 O'Connor, M. *et al.* Relative uptake of the αvβ3 radiopharmaceutical Tc-99m maraciclatide and Tc-99m sestamibi in the breast tissue of patients with suspected breast cancer. *Journal of Nuclear Medicine* **55**, 1547 (2014).
233 Cook, G. J. R. *et al.* Imaging αvβ3 integrin expression in skeletal metastases with 99mTc-maraciclatide single-photon emission computed tomography: detection and therapy response assessment. *European Journal of Nuclear Medicine and Molecular Imaging* **45**, 898-903, doi:10.1007/s00259-017-3926-7 (2018).
234 Dearling, J. *et al.* Specific tumor targeting with the αvβ3 radiopharmaceutical 99mTc-NC100692 (Maraciclatide). *Journal of Nuclear Medicine* **52**, 476 (2011).
235 Dearling, J. L. J. *et al.* Specific uptake of 99mTc-NC100692, an αvβ3-targeted imaging probe, in subcutaneous and orthotopic tumors. *Nuclear Medicine and Biology* **40**, 788-794, doi:https://doi.org/10.1016/j.nucmedbio.2013.04.006 (2013).
236 Reardon, D. A. & Cheresh, D. Cilengitide: A Prototypic Integrin Inhibitor for the Treatment of Glioblastoma and Other Malignancies. *Genes & Cancer* **2**, 1159-1165, doi:10.1177/1947601912450586 (2011).
237 Ellegala, D. B. *et al.* Imaging tumour angiogenesis with contrast ultrasound and microbubbles targeted to alpha-v beta-3. *Circulation* **108**, 336-341 (2003).
238 Willmann, J. K. *et al.* Targeted Contrast-Enhanced Ultrasound Imaging of Tumor Angiogenesis with Contrast Microbubbles Conjugated to Integrin-Binding Knottin Peptides. *Journal of nuclear medicine : official publication, Society of Nuclear Medicine* **51**, 433-440, doi:10.2967/jnumed.109.068007 (2010).
239 Willmann, J. K. *et al.* Dual-targeted Contrast Agent for US Assessment of Tumor Angiogenesis in Vivo. *Radiology* **248**, 936-944, doi:10.1148/radiol.2483072231 (2008).
240 Anderson, C. R. *et al.* Ultrasound Molecular Imaging of Tumor Angiogenesis with an Integrin Targeted Microbubble Contrast Agent. *Investigative radiology* **46**, 215-224, doi:10.1097/RLI.0b013e3182034fed (2011).
241 Warram, J. M. *et al.* A Triple-Targeted Ultrasound Contrast Agent Provides Improved Localization to Tumor Vasculature. *Journal of ultrasound in*

medicine : official journal of the American Institute of Ultrasound in Medicine **30**, 921-931 (2011).
242 Sorace, A. G., Saini, R., Mahoney, M. & Hoyt, K. Molecular Ultrasound Imaging Using a Targeted Contrast Agent for Assessing Early Tumor Response to Antiangiogenic Therapy. *Journal of ultrasound in medicine : official journal of the American Institute of Ultrasound in Medicine* **31**, 1543-1550 (2012).
243 Fink, K. R. & Fink, J. R. Imaging of brain metastasis. *Surgical Neurology International* **4**, S209-S219 (2013).
244 Bhujwalla, Z. M., Artemov, D., Natarajan, K., Ackerstaff, E. & Solaiyappan, M. Vascular Differences Detected by MRI for Metastatic Versus Nonmetastatic Breast and Prostate Cancer Xenografts. *Neoplasia* **3**, 143-153, doi:https://doi.org/10.1038/sj.neo.7900129 (2001).
245 Tofts, P. S. *et al.* Estimating kinetic parameters from dynamic contrast-enhanced t1-weighted MRI of a diffusable tracer: Standardized quantities and symbols. *Journal of Magnetic Resonance Imaging* **10**, 223-232, doi:10.1002/(sici)1522-2586(199909)10:3<223::aid-jmri2>3.0.co;2-s (1999).
246 Perkiö, J. *et al.* Evaluation of four postprocessing methods for determination of cerebral blood volume and mean transit time by dynamic susceptibility contrast imaging. *Magnetic Resonance in Medicine* **47**, 973-981, doi:10.1002/mrm.10126 (2002).
247 Turetschek, K. *et al.* MR Imaging Characterization of Microvessels in Experimental Breast Tumors by Using a Particulate Contrast Agent with Histopathologic Correlation. *Radiology* **218**, 562-569, doi:10.1148/radiology.218.2.r01fe37562 (2001).
248 Turetschek, K. *et al.* Assessment of a rapid clearance blood pool MR contrast medium (P792) for assays of microvascular characteristics in experimental breast tumors with correlations to histopathology. *Magnetic Resonance in Medicine* **45**, 880-886, doi:10.1002/mrm.1117 (2001).
249 Buadu, L. D. *et al.* Breast lesions: correlation of contrast medium enhancement patterns on MR images with histopathologic findings and tumor angiogenesis. *Radiology* **200**, 639-649, doi:10.1148/radiology.200.3.8756909 (1996).
250 O'Connor, J. P. B., Jackson, A., Parker, G. J. M. & Jayson, G. C. DCE-MRI biomarkers in the clinical evaluation of antiangiogenic and vascular disrupting agents. *British Journal Of Cancer* **96**, 189-195 (2007).
251 Evelhoch, J. L. *et al.* Magnetic Resonance Imaging Measurements of the Response of Murine and Human Tumors to the Vascular-Targeting Agent ZD6126. *Clinical Cancer Research* **10**, 3650-3657, doi:10.1158/1078-0432.Ccr-03-0417 (2004).
252 Zhu, W., Kato, Y. & Artemov, D. Heterogeneity of Tumor Vasculature and Antiangiogenic Intervention: Insights from MR Angiography and DCE-MRI. *PLOS ONE* **9**, e86583, doi:10.1371/journal.pone.0086583 (2014).
253 Jalali, S. *et al.* MRI biomarkers identify the differential response of glioblastoma multiforme to anti-angiogenic therapy. *Neuro-Oncology* **16**, 868-879, doi:10.1093/neuonc/nou040 (2014).
254 Boult, J. K. R. *et al.* Evaluation of the Response of Intracranial Xenografts to VEGF Signaling Inhibition Using Multiparametric MRI. *Neoplasia* **19**, 684-694, doi:https://doi.org/10.1016/j.neo.2017.05.007 (2017).

255 Leenders, W. *et al.* Vascular endothelial growth factor-A determines detectability of experimental melanoma brain metastasis in GD-DTPA-enhanced MRI. *International Journal of Cancer* **105**, 437-443, doi:10.1002/ijc.11102 (2003).
256 TABOURET, E. *et al.* Recent Trends in Epidemiology of Brain Metastases: An Overview. *Anticancer Research* **32**, 4655-4662 (2012).
257 Cagney, D. N. *et al.* Incidence and prognosis of patients with brain metastases at diagnosis of systemic malignancy: a population-based study. *Neuro-Oncology* **19**, 1511-1521, doi:10.1093/neuonc/nox077 (2017).
258 Dunn, J. F. *et al.* Changes in oxygenation of intracranial tumors with carbogen: A BOLD MRI and EPR oximetry study. *Journal of Magnetic Resonance Imaging* **16**, 511-521, doi:10.1002/jmri.10192 (2002).
259 Packard, S. D. *et al.* Functional Response of Tumor Vasculature to PaCO2: Determination of Total and Microvascular Blood Volume by MRI. *Neoplasia* **5**, 330-338, doi:https://doi.org/10.1016/S1476-5586(03)80026-X (2003).
260 Abramovitch, R., Dafni, H., Smouha, E., Benjamin, L. E. & Neeman, M. In Vivo Prediction of Vascular Susceptibility to Vascular Endothelial Growth Factor Withdrawal. *Magnetic Resonance Imaging of C6 Rat Glioma in Nude Mice* **59**, 5012-5016 (1999).
261 Neeman, M., Dafni, H., Bukhari, O., Braun, R. D. & Dewhirst, M. W. In vivo BOLD contrast MRI mapping of subcutaneous vascular function and maturation: Validation by intravital microscopy. *Magnetic Resonance in Medicine* **45**, 887-898, doi:10.1002/mrm.1118 (2001).
262 O'Connor, J., Robinson, S. & Waterton, J. Imaging tumour hypoxia with oxygen-enhanced MRI and BOLD MRI. *The British Journal of Radiology*, 20180642, doi:10.1259/bjr.20180642 (2018).
263 Dennie, J. *et al.* NMR imaging of changes in vascular morphology due to tumor angiogenesis. *Magnetic Resonance in Medicine* **40**, 793-799, doi:10.1002/mrm.1910400602 (1998).
264 Rydland, J. *et al.* New Intravascular Contrast Agent Applied to Dynamic Contrast Enhanced Mr imaging of Human Breast Cancer. *Acta Radiologica* **44**, 275-283, doi:10.1034/j.1600-0455.2003.00068.x (2003).
265 Enochs, W. S., Harsh, G., Hochberg, F. & Weissleder, R. Improved delineation of human brain tumors on MR images using a long-circulating, superparamagnetic iron oxide agent. *Journal of Magnetic Resonance Imaging* **9**, 228-232, doi:10.1002/(sici)1522-2586(199902)9:2<228::aid-jmri12>3.0.co;2-k (1999).
266 Bremer, C. *et al.* Steady-State Blood Volume Measurements in Experimental Tumors with Different Angiogenic Burdens—A Study in Mice. *Radiology* **226**, 214-220, doi:10.1148/radiol.2261012140 (2003).
267 Robinson, S. P., Boult, J. K. R., Vasudev, N. S. & Reynolds, A. R. Monitoring the Vascular Response and Resistance to Sunitinib in Renal Cell Carcinoma In Vivo with Susceptibility Contrast MRI. *Cancer Research*, doi:10.1158/0008-5472.can-17-0248 (2017).
268 Gauberti, M., Montagne, A., Quenault, A. & Vivien, D. Molecular magnetic resonance imaging of brain–immune interactions. *Frontiers in Cellular Neuroscience* **8**, doi:10.3389/fncel.2014.00389 (2014).

269 Thorek, D. L. J., Chen, A. K., Czupryna, J. & Tsourkas, A. Superparamagnetic Iron Oxide Nanoparticle Probes for Molecular Imaging. *Annals of Biomedical Engineering* **34**, 23-38, doi:10.1007/s10439-005-9002-7 (2006).
270 von zur Muhlen, C. *et al.* A contrast agent recognizing activated platelets reveals murine cerebral malaria pathology undetectable by conventional MRI. *The Journal of Clinical Investigation* **118**, 1198-1207, doi:10.1172/JCI33314 (2008).
271 Deddens, L. H. *et al.* MRI of ICAM-1 Upregulation After Stroke: the Importance of Choosing the Appropriate Target-Specific Particulate Contrast Agent. *Molecular Imaging and Biology* **15**, 411-422, doi:10.1007/s11307-013-0617-z (2013).
272 Hoyte, L. C. *et al.* Molecular magnetic resonance imaging of acute vascular cell adhesion molecule-1 expression in a mouse model of cerebral ischemia. *Journal of Cerebral Blood Flow and Metabolism: Official Journal of the International Society of Cerebral Blood Flow and Metabolism* **30**, 1178-1187, doi:10.1038/jcbfm.2009.287 (2010).
273 Quenault, A. *et al.* Molecular magnetic resonance imaging discloses endothelial activation after transient ischaemic attack. *Brain* **140**, 146-157, doi:10.1093/brain/aww260 (2017).
274 McAteer, M. A. *et al.* In vivo magnetic resonance imaging of acute brain inflammation using microparticles of iron oxide. *Nature Medicine* **13**, 1253, doi:10.1038/nm1631

https://www.nature.com/articles/nm1631#supplementary-information (2007).
275 Serres, S. *et al.* VCAM-1-targeted magnetic resonance imaging reveals subclinical disease in a mouse model of multiple sclerosis. *FASEB journal : official publication of the Federation of American Societies for Experimental Biology* **25**, 4415-4422, doi:10.1096/fj.11-183772 (2011).
276 Montagne, A. *et al.* Ultra-sensitive molecular MRI of cerebrovascular cell activation enables early detection of chronic central nervous system disorders. *NeuroImage* **63**, 760-770, doi:https://doi.org/10.1016/j.neuroimage.2012.07.018 (2012).
277 Kaluzova, M., Bouras, A., Machaidze, R. & Hadjipanayis, C. G. Targeted therapy of glioblastoma stem-like cells and tumor non-stem cells using cetuximab-conjugated iron-oxide nanoparticles. *Oncotarget* **6**, 8788-8806 (2015).
278 Wen, P. Y. *et al.* Response Assessment in Neuro-Oncology Clinical Trials. *Journal of Clinical Oncology* **35**, 2439-2449, doi:10.1200/jco.2017.72.7511 (2017).
279 Lin, N. U. *et al.* Response assessment criteria for brain metastases: proposal from the RANO group. *The Lancet Oncology* **16**, e270-e278, doi:https://doi.org/10.1016/S1470-2045(15)70057-4 (2015).
280 Davis, D. W., McConkey, D. J., Abbruzzese, J. L. & Herbst, R. S. Surrogate markers in antiangiogenesis clinical trials. *British Journal of Cancer* **89**, 8, doi:10.1038/sj.bjc.6601035 (2003).
281 Miles, K. A. Tumour angiogenesis and its relation to contrast enhancement on computed tomography: a review. *European Journal of Radiology* **30**, 198-205, doi:https://doi.org/10.1016/S0720-048X(99)00012-1 (1999).

282 Dexter, D. L. *et al.* Heterogeneity of Tumor Cells from a Single Mouse Mammary Tumor. *Cancer Research* **38**, 3174-3181 (1978).
283 Cormack, B. P., Valdivia, R. H. & Falkow, S. FACS-optimized mutants of the green fluorescent protein (GFP). *Gene* **173**, 33-38, doi:https://doi.org/10.1016/0378-1119(95)00685-0 (1996).
284 Allen, M., Bjerke, M., Edlund, H., Nelander, S. & Westermark, B. Origin of the U87MG glioma cell line: Good news and bad news. *Science Translational Medicine* **8**, 354re353-354re353, doi:10.1126/scitranslmed.aaf6853 (2016).
285 Ponten, J. A. N. & Macintyre, E. H. Long term culture of normal and neoplastic human glia. *Acta Pathologica Microbiologica Scandinavica* **74**, 465-486, doi:10.1111/j.1699-0463.1968.tb03502.x (1968).
286 Raschke, W. C., Baird, S., Ralph, P. & Nakoinz, I. Functional macrophage cell lines transformed by abelson leukemia virus. *Cell* **15**, 261-267, doi:https://doi.org/10.1016/0092-8674(78)90101-0 (1978).
287 Paxinos, G. & Franklin, K. *The Mouse Brain In Stereotaxic Coordinates 4th Edition*. (Academic Press, 2012).
288 Colliez, F., Gallez, B. & Jordan, B. F. Assessing Tumor Oxygenation for Predicting Outcome in Radiation Oncology: A Review of Studies Correlating Tumor Hypoxic Status and Outcome in the Preclinical and Clinical Settings. *Frontiers in Oncology* **7**, 10, doi:10.3389/fonc.2017.00010 (2017).
289 Pang, R. W. C. & Poon, R. T. P. Clinical Implications of Angiogenesis in Cancers. *Vascular Health and Risk Management* **2**, 97-108 (2006).
290 Vaupel, P. & Mayer, A. Hypoxia in cancer: significance and impact on clinical outcome. *Cancer and Metastasis Reviews* **26**, 225-239, doi:10.1007/s10555-007-9055-1 (2007).
291 Nishida, N., Yano, H., Nishida, T., Kamura, T. & Kojiro, M. Angiogenesis in Cancer. *Vascular Health and Risk Management* **2**, 213-219 (2006).
292 Alsop, D. C. *et al.* Recommended implementation of arterial spin-labeled perfusion MRI for clinical applications: A consensus of the ISMRM perfusion study group and the European consortium for ASL in dementia. *Magnetic Resonance in Medicine* **73**, 102-116, doi:10.1002/mrm.25197 (2015).
293 Williams, D. S., Detre, J. A., Leigh, J. S. & Koretsky, A. P. Magnetic resonance imaging of perfusion using spin inversion of arterial water. *Proceedings of the National Academy of Sciences* **89**, 212-216 (1992).
294 Detre, J. A., Leigh, J. S., Williams, D. S. & Koretsky, A. P. Perfusion imaging. *Magnetic Resonance in Medicine* **23**, 37-45, doi:10.1002/mrm.1910230106 (1992).
295 Sun, Y. *et al.* Perfusion MRI of U87 brain tumors in a mouse model. *Magnetic Resonance in Medicine* **51**, 893-899, doi:10.1002/mrm.20029 (2004).
296 Vallatos, A., Gilmour, L., Chalmers, A. J. & Holmes, W. M. Multiple boli arterial spin labeling for high signal-to-noise rodent brain perfusion imaging. *Magnetic Resonance in Medicine* **79**, 1020-1030, doi:10.1002/mrm.26706 (2018).
297 Coutinho de Souza, P. *et al.* Inhibition of Pediatric Glioblastoma Tumor Growth by the Anti-Cancer Agent OKN-007 in Orthotopic Mouse

Xenografts. *PLOS ONE* **10**, e0134276, doi:10.1371/journal.pone.0134276 (2015).
298 Zheng, B., Lee, P. T. H. & Golay, X. High-sensitivity cerebral perfusion mapping in mice by kbGRASE-FAIR at 9.4 T. *NMR in Biomedicine* **23**, 1061-1070, doi:10.1002/nbm.1533 (2010).
299 Kober, F., Duhamel, G. & Cozzone, P. J. Experimental comparison of four FAIR arterial spin labeling techniques for quantification of mouse cerebral blood flow at 4.7 T. *NMR in Biomedicine* **21**, 781-792, doi:10.1002/nbm.1253 (2008).
300 Duhamel, G., Callot, V., Tachrount, M., Alsop, D. C. & Cozzone, P. J. Pseudo-continuous arterial spin labeling at very high magnetic field (11.75 T) for high-resolution mouse brain perfusion imaging. *Magnetic Resonance in Medicine* **67**, 1225-1236, doi:10.1002/mrm.23096 (2012).
301 Hirschler, L. *et al.* Transit time mapping in the mouse brain using time-encoded pCASL. *NMR in Biomedicine* **31**, e3855-n/a, doi:10.1002/nbm.3855 (2018).
302 Foley, L. M. *et al.* Murine orthostatic response during prolonged vertical studies: Effect on cerebral blood flow measured by arterial spin-labeled MRI. *Magnetic Resonance in Medicine* **54**, 798-806, doi:10.1002/mrm.20621 (2005).
303 Hirschler, L., Uszynski, I., Warnking, J. M. & Barbier, E. L. in *Proceedings of the International Society for Magnetic Resonance in Medicine.*
304 Uszynski, I. *et al.* in *Proceedings of the International Society for Magnetic Resonance in Medicine.*
305 Sicard, K. *et al.* Regional Cerebral Blood Flow and BOLD Responses in Conscious and Anesthetized Rats under Basal and Hypercapnic Conditions: Implications for Functional MRI Studies. *Journal of Cerebral Blood Flow & Metabolism* **23**, 472-481, doi:10.1097/01.wcb.0000054755.93668.20 (2003).
306 Li, C.-X., Patel, S., Wang, D. J. J. & Zhang, X. Effect of high dose isoflurane on cerebral blood flow in macaque monkeys. *Magnetic Resonance Imaging* **32**, 956-960, doi:https://doi.org/10.1016/j.mri.2014.04.019 (2014).
307 Xu, J. *et al.* Steady pulsed imaging and labeling scheme for noninvasive perfusion imaging. *Magnetic Resonance in Medicine* **75**, 238-248, doi:10.1002/mrm.25641 (2016).
308 Gao, Y. *et al.* Arterial spin labeling-fast imaging with steady-state free precession (ASL-FISP): a rapid and quantitative perfusion technique for high-field MRI. *NMR in Biomedicine* **27**, 996-1004, doi:10.1002/nbm.3143 (2014).
309 Chugh, B. P. *et al.* Robust method for 3D arterial spin labeling in mice. *Magnetic Resonance in Medicine* **68**, 98-106, doi:10.1002/mrm.23209 (2012).
310 Engel, D. C. *et al.* Changes of Cerebral Blood Flow during the Secondary Expansion of a Cortical Contusion Assessed by 14C-Iodoantipyrine Autoradiography in Mice Using a Non-Invasive Protocol. *Journal of Neurotrauma* **25**, 739-753, doi:10.1089/neu.2007.0480 (2008).
311 Maeda, K., Mies, G., Oláh, L. & Hossmann, K.-A. Quantitative Measurement of Local Cerebral Blood Flow in the Anesthetized Mouse Using Intraperitoneal [14C]Iodoantipyrine Injection and Final Arterial Heart

Blood Sampling. *Journal of Cerebral Blood Flow & Metabolism* **20**, 10-14, doi:doi:10.1097/00004647-200001000-00003 (2000).

312 Jiang, W., Gu, W., Hossmann, K.-A., Mies, G. & Wester, P. Establishing a Photothrombotic 'ring' Stroke Model in Adult Mice with Late Spontaneous Reperfusion: Quantitative Measurements of Cerebral Blood Flow and Cerebral Protein Synthesis. *Journal of Cerebral Blood Flow & Metabolism* **26**, 927-936, doi:doi:10.1038/sj.jcbfm.9600245 (2006).

313 Jay, T. M., Lucignani, G., Crane, A. M., Jehle, J. & Sokoloff, L. Measurement of Local Cerebral Blood Flow with [14C]Iodoantipyrine in the Mouse. *Journal of Cerebral Blood Flow & Metabolism* **8**, 121-129, doi:10.1038/jcbfm.1988.16 (1988).

314 Leithner, C. *et al.* A flow sensitive alternating inversion recovery (FAIR)-MRI protocol to measure hemispheric cerebral blood flow in a mouse stroke model. *Experimental Neurology* **210**, 118-127, doi:https://doi.org/10.1016/j.expneurol.2007.10.003 (2008).

315 Baskerville, T. A., McCabe, C., Weir, C. J., Macrae, I. M. & Holmes, W. M. Noninvasive MRI Measurement of CBF: Evaluating An Arterial Spin Labelling Sequence with 99mTc-HMPAO CBF Autoradiography in a Rat Stroke Model. *Journal of Cerebral Blood Flow & Metabolism* **32**, 973-977, doi:10.1038/jcbfm.2012.19 (2012).

316 Ewing, J. R., Cao, Y., Knight, R. A. & Fenstermacher, J. D. Arterial spin labeling: Validity testing and comparison studies. *Journal of Magnetic Resonance Imaging* **22**, 737-740, doi:doi:10.1002/jmri.20451 (2005).

317 Larkin, J. R. *et al.* Quantitative blood flow measurement in rat brain with multiphase arterial spin labelling magnetic resonance imaging. *Journal of Cerebral Blood Flow & Metabolism*, Epub ahead of print, doi:10.1177/0271678x18756218 (2018).

318 Artz, N. S. *et al.* Comparing Kidney Perfusion Using Noncontrast Arterial Spin Labeling MRI and Microsphere Methods in an Interventional Swine Model. *Investigative Radiology* **46**, 124-131, doi:10.1097/RLI.0b013e3181f5e101 (2011).

319 Jung, Y., Wong, E. C. & Liu, T. T. Multiphase pseudocontinuous arterial spin labeling (MP-PCASL) for robust quantification of cerebral blood flow. *Magnetic Resonance in Medicine* **64**, 799-810, doi:10.1002/mrm.22465 (2010).

320 Okell, T. W. *Assessment of Collateral Blood Flow in the Brain using Magnetic Resonance Imaging* Doctor of Philosophy Thesis thesis, University of Oxford, (2011).

321 Larkin, J. R. *et al.* Quantitative blood flow measurement in rat brain with multiphase arterial spin labelling magnetic resonance imaging. *Journal of Cerebral Blood Flow & Metabolism* **0**, 0271678X18756218, doi:10.1177/0271678x18756218.

322 Irving, B. *et al.* maskSLIC: Regional Superpixel Generation with Application to Local Pathology Characterisation in Medical Images. *CoRR*, doi:https://arxiv.org/pdf/1606.09518.pdf (2016).

323 Buxton, R. B. *et al.* A general kinetic model for quantitative perfusion imaging with arterial spin labeling. *Magnetic Resonance in Medicine* **40**, 383-396, doi:10.1002/mrm.1910400308 (1998).

324 Chappell, M. A., Groves, A. R., Whitcher, B. & Woolrich, M. W. Variational Bayesian Inference for a Nonlinear Forward Model. *IEEE Transactions on Signal Processing* **57**, 223-236, doi:10.1109/TSP.2008.2005752 (2009).
325 Sakurada, O. *et al.* Measurement of local cerebral blood flow with iodo [14C] antipyrine. *American Journal of Physiology - Heart and Circulatory Physiology* **234**, H59-H66 (1978).
326 Thomas, D. L. Arterial spin labeling in small animals: Methods and applications to experimental cerebral ischemia. *Journal of Magnetic Resonance Imaging* **22**, 741-744, doi:doi:10.1002/jmri.20453 (2005).
327 Lydiane, H. *et al.* Interpulse phase corrections for unbalanced pseudo-continuous arterial spin labeling at high magnetic field. *Magnetic Resonance in Medicine* **79**, 1314-1324, doi:doi:10.1002/mrm.26767 (2018).
328 Hirschler, L. *et al.* Interpulse phase corrections for unbalanced pseudo-continuous arterial spin labeling at high magnetic field. *Magnetic Resonance in Medicine* **79**, 1314-1324, doi:10.1002/mrm.26767 (2018).
329 Frietsch, T. *et al.* Reduced Cerebral Blood Flow but Elevated Cerebral Glucose Metabolic Rate in Erythropoietin Overexpressing Transgenic Mice with Excessive Erythrocytosis. *Journal of Cerebral Blood Flow & Metabolism* **27**, 469-476, doi:10.1038/sj.jcbfm.9600360 (2007).
330 Vallatos, A. *et al.* Quantitative histopathologic assessment of perfusion MRI as a marker of glioblastoma cell infiltration in and beyond the peritumoral edema region. *Journal of Magnetic Resonance Imaging* **0**, doi:10.1002/jmri.26580 (2018).
331 Silva, A. C., Kim, S.-G. & Garwood, M. Imaging blood flow in brain tumors using arterial spin labeling. *Magnetic Resonance in Medicine* **44**, 169-173, doi:10.1002/1522-2594(200008)44:2<169::AID-MRM1>3.0.CO;2-U (2000).
332 Weber, M. A. *et al.* Diagnostic performance of spectroscopic and perfusion MRI for distinction of brain tumors. *Neurology* **66**, 1899-1906, doi:10.1212/01.wnl.0000219767.49705.9c (2006).
333 Hong, X. *et al.* Quantitative multiparametric MRI assessment of glioma response to radiotherapy in a rat model. *Neuro-Oncology* **16**, 856-867, doi:10.1093/neuonc/not245 (2014).
334 Schor-Bardach, R. *et al.* Does Arterial Spin-labeling MR Imaging–measured Tumor Perfusion Correlate with Renal Cell Cancer Response to Antiangiogenic Therapy in a Mouse Model? *Radiology* **251**, 731-742, doi:10.1148/radiol.2521081059 (2009).
335 Nagy, J. A., Chang, S. H., Dvorak, A. M. & Dvorak, H. F. Why are tumour blood vessels abnormal and why is it important to know? *British Journal of Cancer* **100**, 865-869, doi:10.1038/sj.bjc.6604929 (2009).
336 Morikawa, S. *et al.* Abnormalities in Pericytes on Blood Vessels and Endothelial Sprouts in Tumors. *The American Journal of Pathology* **160**, 985-1000, doi:https://doi.org/10.1016/S0002-9440(10)64920-6 (2002).
337 Vajkoczy, P. & Menger, M. D. Vascular Microenvironment in Gliomas. *Journal of Neuro-Oncology* **50**, 99-108, doi:10.1023/A:1006474832189 (2000).
338 Alsop, D. C. *et al.* Recommended implementation of arterial spin-labeled perfusion MRI for clinical applications: A consensus of the ISMRM perfusion study group and the European consortium for ASL in dementia.

Magnetic Resonance in Medicine **73**, 102-116, doi:doi:10.1002/mrm.25197 (2015).
339 Liu, Y., Yang, Y. & Zhang, C. A concise review of magnetic resonance molecular imaging of tumor angiogenesis by targeting integrin αvβ3 with magnetic probes. *International Journal of Nanomedicine* **8**, 1083-1093, doi:10.2147/ijn.s39880 (2013).
340 Li, K. C. P., Guccione, S. & Bednarski, M. D. Combined vascular targeted imaging and therapy: A paradigm for personalized treatment. *Journal of Cellular Biochemistry* **87**, 65-71, doi:doi:10.1002/jcb.10401 (2002).
341 Mulder, W. J. M. *et al.* MR molecular imaging and fluorescence microscopy for identification of activated tumor endothelium using a bimodal lipidic nanoparticle. *The FASEB Journal* **19**, 2008-2010, doi:10.1096/fj.05-4145fje (2005).
342 Mulder, W. J. M. *et al.* Early in vivo assessment of angiostatic therapy efficacy by molecular MRI. *The FASEB Journal* **21**, 378-383, doi:10.1096/fj.06-6791com (2007).
343 Kluza, E. *et al.* Synergistic Targeting of αvβ3 Integrin and Galectin-1 with Heteromultivalent Paramagnetic Liposomes for Combined MR Imaging and Treatment of Angiogenesis. *Nano Letters* **10**, 52-58, doi:10.1021/nl902659g (2010).
344 Anderson, S. A. *et al.* Magnetic resonance contrast enhancement of neovasculature with αvβ3-targeted nanoparticles. *Magnetic Resonance in Medicine* **44**, 433-439, doi:doi:10.1002/1522-2594(200009)44:3<433::AID-MRM14>3.0.CO;2-9 (2000).
345 Schmieder, A. H. *et al.* Molecular MR imaging of melanoma angiogenesis with αvβ3-targeted paramagnetic nanoparticles. *Magnetic Resonance in Medicine* **53**, 621-627, doi:doi:10.1002/mrm.20391 (2005).
346 Ke, T. *et al.* RGD targeted poly(L-glutamic acid)-cystamine-(Gd-DO3A) conjugate for detecting angiogenesis biomarker α(v)β(3) integrin with MR T(1) mapping. *International Journal of Nanomedicine* **2**, 191-199 (2007).
347 Winter, P. M. *et al.* Molecular Imaging of Angiogenesis in Nascent Vx-2 Rabbit Tumors Using a Novel αvβ3-targeted Nanoparticle and 1.5 Tesla Magnetic Resonance Imaging. *Cancer Research* **63**, 5838-5843 (2003).
348 Chen, W. *et al.* RGD peptide functionalized and reconstituted high-density lipoprotein nanoparticles as a versatile and multimodal tumor targeting molecular imaging probe. *The FASEB Journal* **24**, 1689-1699, doi:10.1096/fj.09-139865 (2010).
349 Wang, Y.-X. J. Superparamagnetic iron oxide based MRI contrast agents: Current status of clinical application. *Quantitative Imaging in Medicine and Surgery* **1**, 35-40, doi:10.3978/j.issn.2223-4292.2011.08.03 (2011).
350 Beaumont, M. *et al.* Characterization of Tumor Angiogenesis in Rat Brain Using Iron-Based Vessel Size Index MRI in Combination with Gadolinium-Based Dynamic Contrast-Enhanced MRI. *Journal of Cerebral Blood Flow & Metabolism* **29**, 1714-1726, doi:10.1038/jcbfm.2009.86 (2009).
351 Turetschek, K. *et al.* Tumor microvascular characterization using ultrasmall superparamagnetic iron oxide particles (USPIO) in an experimental breast cancer model. *Journal of Magnetic Resonance Imaging* **13**, 882-888, doi:doi:10.1002/jmri.1126 (2001).
352 Boult, J. K. R. *et al.* Investigating intracranial tumour growth patterns with multiparametric MRI incorporating Gd-DTPA and USPIO-enhanced

imaging. *NMR in Biomedicine* **29**, 1608-1617, doi:10.1002/nbm.3594 (2016).
353 Cui, Y. *et al.* Noninvasive monitoring of early antiangiogenic therapy response in human nasopharyngeal carcinoma xenograft model using MRI with RGD-conjugated ultrasmall superparamagnetic iron oxide nanoparticles. *International Journal of Nanomedicine* **11**, 5671-5682, doi:10.2147/ijn.s115357 (2016).
354 Lim, E.-K. *et al.* Aptamer-conjugated magnetic nanoparticles enable efficient targeted detection of integrin αvβ3 via magnetic resonance imaging. *Journal of Biomedical Materials Research Part A* **102**, 49-59, doi:doi:10.1002/jbm.a.34678 (2014).
355 Zhang, F. *et al.* Noninvasive monitoring of orthotopic glioblastoma therapy response using RGD-conjugated iron oxide nanoparticles. *Biomaterials* **33**, 5414-5422, doi:https://doi.org/10.1016/j.biomaterials.2012.04.032 (2012).
356 Kazmierczak, P. M. *et al.* αvß3-Integrin–Targeted Magnetic Resonance Imaging for the Assessment of Early Antiangiogenic Therapy Effects in Orthotopic Breast Cancer Xenografts. *Investigative Radiology* **51**, 746-755, doi:10.1097/rli.0000000000000278 (2016).
357 de Oliveira, E. A. *et al.* Evaluation of Magnetonanoparticles Conjugated with New Angiogenesis Peptides in Intracranial Glioma Tumors by MRI. *Applied Biochemistry and Biotechnology* **183**, 265-279, doi:10.1007/s12010-017-2443-2 (2017).
358 Zhang, C. *et al.* Specific Targeting of Tumor Angiogenesis by RGD-Conjugated Ultrasmall Superparamagnetic Iron Oxide Particles Using a Clinical 1.5-T Magnetic Resonance Scanner. *Cancer Research* **67**, 1555-1562, doi:10.1158/0008-5472.can-06-1668 (2007).
359 Jiang, T. *et al.* Noninvasively characterizing the different αvβ3 expression patterns in lung cancers with RGD-USPIO using a clinical 3.0T MR scanner. *International Journal of Nanomedicine* **4**, 241-249 (2009).
360 Persigehl, T. *et al.* Prediction of Antiangiogenic Treatment Efficacy by Iron Oxide Enhanced Parametric Magnetic Resonance Imaging. *Investigative Radiology* **42**, 791-796 710.1097/RLI.1090b1013e3180d1095cbd1099 (2007).
361 Boucher, M. *et al.* Genetically tailored magnetosomes used as MRI probe for molecular imaging of brain tumor. *Biomaterials* **121**, 167-178, doi:https://doi.org/10.1016/j.biomaterials.2016.12.013 (2017).
362 Weissleder, R. *et al.* Ultrasmall superparamagnetic iron oxide: characterization of a new class of contrast agents for MR imaging. *Radiology* **175**, 489-493, doi:10.1148/radiology.175.2.2326474 (1990).
363 Xie, J. *et al.* Ultrasmall c(RGDyK)-Coated Fe(3)O(4) Nanoparticles and Their Specific Targeting to Integrin α(v)β(3)-Rich Tumor Cells. *Journal of the American Chemical Society* **130**, 7542-7543, doi:10.1021/ja802003h (2008).
364 Liu, D.-F. *et al.* Magnetic resonance imaging of post-ischemic blood–brain barrier damage with PEGylated iron oxide nanoparticles. *Nanoscale* **6**, 15161-15167, doi:10.1039/c4nr03942d (2014).
365 Yang, Y., Yang, Y., Yanasak, N., Schumacher, A. & Hu, T. C.-C. Temporal and noninvasive monitoring of inflammatory-cell infiltration to myocardial infarction sites using micrometer-sized iron oxide particles. *Magnetic Resonance in Medicine* **63**, 33-40, doi:doi:10.1002/mrm.22175 (2010).

366 McAteer, M. A. *et al.* In vivo magnetic resonance imaging of acute brain inflammation using microparticles of iron oxide. *Nature medicine* **13**, 1253-1258, doi:10.1038/nm1631 (2007).
367 McAteer, M. A. *et al.* A leukocyte-mimetic MRI contrast agent homes rapidly to activated endothelium and tracks with atherosclerotic lesion macrophage content. *Arteriosclerosis, Thrombosis, and Vascular Biology* **32**, 1427-1435, doi:10.1161/atvbaha.111.241844 (2012).
368 McAteer, M. A. *et al.* Magnetic Resonance Imaging of endothelial adhesion molecules in mouse atherosclerosis using dual-targeted microparticles of iron oxide. *Atherosclerosis, Thrombosis, and Vascular Biology* **28**, 77-83 (2007).
369 Fournier, A. P. *et al.* Prediction of disease activity in models of multiple sclerosis by molecular magnetic resonance imaging of P-selectin. *Proceedings of the National Academy of Sciences of the United States of America* **114**, 6116-6121, doi:10.1073/pnas.1619424114 (2017).
370 Shapiro, E. M. *et al.* MRI detection of single particles for cellular imaging. *Proceedings of the National Academy of Sciences of the United States of America* **101**, 10901-10906, doi:10.1073/pnas.0403918101 (2004).
371 Shapiro, E. M., Sharer, K., Skrtic, S. & Koretsky, A. P. In vivo detection of single cells by MRI. *Magnetic Resonance in Medicine* **55**, 242-249, doi:10.1002/mrm.20718 (2006).
372 Perez-Balderas, F. *et al.* Covalent assembly of nanoparticles as a peptidase-degradable platform for molecular MRI. *Nature Communications* **8**, 14254, doi:10.1038/ncomms14254

https://www.nature.com/articles/ncomms14254#supplementary-information (2017).
373 Larkin, J. R. *et al.* Early Diagnosis of Brain Metastases Using a Biofluids-Metabolomics Approach in Mice. *Theranostics* **6**, 2161-2169, doi:10.7150/thno.16538 (2016).
374 de Groot, J. F. *et al.* Tumor invasion after treatment of glioblastoma with bevacizumab: radiographic and pathologic correlation in humans and mice. *Neuro-Oncology* **12**, 233-242, doi:10.1093/neuonc/nop027 (2010).
375 Wong, K. *et al.* Characterization of a human tumorsphere glioma orthotopic model using magnetic resonance imaging. *Journal of neuro-oncology* **104**, 473-481, doi:10.1007/s11060-010-0517-x (2011).
376 Gambarota, G. *et al.* Characterisation of tumour vasculature in mouse brain by USPIO contrast-enhanced MRI. *British Journal of Cancer* **98**, 1784, doi:10.1038/sj.bjc.6604389 (2008).
377 Claes, A. *et al.* Magnetic resonance imaging-based detection of glial brain tumors in mice after antiangiogenic treatment. *International journal of cancer* **122**, 1981-1986, doi:doi:10.1002/ijc.23306 (2008).
378 Gauberti, M., Montagne, A., Quenault, A. & Vivien, D. Molecular magnetic resonance imaging of brain–immune interactions. *Frontiers in Cellular Neuroscience* **8**, 389, doi:10.3389/fncel.2014.00389 (2014).
379 Gaberel, T. *et al.* Intracerebral Hematomas Disappear on T2*-Weighted Images During Normobaric Oxygen Therapy. *Stroke* **44**, 3482-3489 (2013).

380 Wolters, M. *et al.* Efficacy of positive contrast imaging techniques for molecular MRI of tumor angiogenesis. *Contrast Media & Molecular Imaging* **7**, 130-139, doi:doi:10.1002/cmmi.471 (2012).
381 Delangre, S. *et al.* Bottom-up study of the MRI positive contrast created by the Off-Resonance Saturation sequence. *Journal of Magnetic Resonance* **254**, 98-109, doi:https://doi.org/10.1016/j.jmr.2015.02.014 (2015).
382 Liu, W., Dahnke, H., Jordan, E. K., Schaeffter, T. & Frank, J. A. In vivo MRI using positive-contrast techniques in detection of cells labeled with superparamagnetic iron oxide nanoparticles. *NMR in Biomedicine* **21**, 242-250, doi:doi:10.1002/nbm.1187 (2008).
383 Vonken, E.-j. P. A., Schär, M., Yu, J., Bakker, C. J. G. & Stuber, M. Direct in vitro comparison of six three-dimensional positive contrast methods for susceptibility marker imaging. *Journal of Magnetic Resonance Imaging* **38**, 344-357, doi:doi:10.1002/jmri.23976 (2013).
384 Delangre, S. *et al.* Theoretical and experimental study of ON-Resonance Saturation, an MRI sequence for positive contrast with superparamagnetic nanoparticles. *Journal of Magnetic Resonance* **252**, 151-162, doi:https://doi.org/10.1016/j.jmr.2015.01.007 (2015).
385 Robinson, P. J. & Rapoport, S. I. Size selectivity of blood-brain barrier permeability at various times after osmotic opening. *American Journal of Physiology-Regulatory, Integrative and Comparative Physiology* **253**, R459-R466, doi:10.1152/ajpregu.1987.253.3.R459 (1987).
386 Gauberti, M., Fournier, A. P., Docagne, F., Vivien, D. & Martinez de Lizarrondo, S. Molecular Magnetic Resonance Imaging of Endothelial Activation in the Central Nervous System. *Theranostics* **8**, 1195-1212, doi:10.7150/thno.22662 (2018).
387 Knutson, M. & Wessling-Resnick, M. Iron Metabolism in the Reticuloendothelial System. *Critical Reviews in Biochemistry and Molecular Biology* **38**, 61-88, doi:10.1080/713609210 (2003).
388 McLachlan, S. J. *et al.* Phase I clinical evaluation of a new iron oxide MR contrast agent. *Journal of Magnetic Resonance Imaging* **4**, 301-307, doi:doi:10.1002/jmri.1880040313 (1994).
389 Toth, G. B. *et al.* Current and potential imaging applications of ferumoxytol for magnetic resonance imaging. *Kidney international* **92**, 47-66, doi:10.1016/j.kint.2016.12.037 (2017).
390 Andreou, K. E. *et al.* Anti-inflammatory Microglia/Macrophages As a Potential Therapeutic Target in Brain Metastasis. *Frontiers in Oncology* **7**, 251, doi:10.3389/fonc.2017.00251 (2017).
391 Schackert, G., Simmons, R. D., Buzbee, T. M., Hume, D. A. & Fidler, I. J. Macrophage Infiltration Into Experimental Brain Metastases: Occurrence Through an Intact Blood-Brain Barrier2. *JNCI: Journal of the National Cancer Institute* **80**, 1027-1034, doi:10.1093/jnci/80.13.1027 (1988).
392 Bingle, L., Brown, N. J. & Lewis, C. E. The role of tumour-associated macrophages in tumour progression: implications for new anticancer therapies. *The Journal of Pathology* **196**, 254-265, doi:doi:10.1002/path.1027 (2002).
393 Yamaguchi, H., Pixley, F. & Condeelis, J. Invadopodia and podosomes in tumor invasion. *European Journal of Cell Biology* **85**, 213-218, doi:https://doi.org/10.1016/j.ejcb.2005.10.004 (2006).

394 Neuwelt, A. *et al.* Iron-Based Superparamagnetic Nanoparticle Contrast Agents for MRI of Infection and Inflammation. *American Journal of Roentgenology* **204**, W302-W313, doi:10.2214/AJR.14.12733 (2015).
395 Weissleder, R., Nahrendorf, M. & Pittet, M. J. Imaging macrophages with nanoparticles. *Nature Materials* **13**, 125, doi:10.1038/nmat3780 (2014).
396 Dósa, E. *et al.* Magnetic resonance imaging of intracranial tumors: intra-patient comparison of gadoteridol and ferumoxytol. *Neuro-Oncology* **13**, 251-260, doi:10.1093/neuonc/noq172 (2011).
397 Hamilton, B. E. *et al.* Comparative analysis of ferumoxytol and gadoteridol enhancement using T1- and T2-weighted MRI in neuroimaging. *AJR. American journal of roentgenology* **197**, 981-988, doi:10.2214/AJR.10.5992 (2011).
398 Bashir, M. R., Bhatti, L., Marin, D. & Nelson, R. C. Emerging applications for ferumoxytol as a contrast agent in MRI. *Journal of Magnetic Resonance Imaging* **41**, 884-898, doi:doi:10.1002/jmri.24691 (2015).
399 McCullough, B. J., Kolokythas, O., Maki, J. H. & Green, D. E. Ferumoxytol in clinical practice: Implications for MRI. *Journal of Magnetic Resonance Imaging* **37**, 1476-1479, doi:doi:10.1002/jmri.23879 (2013).
400 Weinstein, J. S. *et al.* Superparamagnetic Iron Oxide Nanoparticles: Diagnostic Magnetic Resonance Imaging and Potential Therapeutic Applications in Neurooncology and Central Nervous System Inflammatory Pathologies, a Review. *Journal of Cerebral Blood Flow & Metabolism* **30**, 15-35, doi:10.1038/jcbfm.2009.192 (2009).
401 Muldoon, L. L., Sàndor, M., Pinkston, K. E. & Neuwelt, E. A. Imaging, Distribution, and Toxicity of Superparamagnetic Iron Oxide Magnetic Resonance Nanoparticles in the Rat Brain and Intracerebral Tumor. *Neurosurgery* **57**, 785-796, doi:10.1227/01.NEU.0000175731.25414.4c (2005).
402 Varallyay, P. *et al.* Comparison of Two Superparamagnetic Viral-Sized Iron Oxide Particles Ferumoxides and Ferumoxtran-10 with a Gadolinium Chelate in Imaging Intracranial Tumors. *American Journal of Neuroradiology* **23**, 510-519 (2002).
403 Neuwelt, E. A. *et al.* The potential of ferumoxytol nanoparticle magnetic resonance imaging, perfusion, and angiography in central nervous system malignancy: a pilot study. *Neurosurgery* **60**, 601-612, doi:10.1227/01.neu.0000255350.71700.37 (2007).
404 Ruehm, S. G., Corot, C., Vogt, P., Cristina, H. & Debatin, J. F. Ultrasmall Superparamagnetic Iron Oxide–enhanced MR Imaging of Atherosclerotic Plaque in Hyperlipidemic Rabbits. *Academic Radiology* **9**, S143-S144, doi:10.1016/s1076-6332(03)80422-1 (2002).
405 SCHMITZ, S. A. *et al.* Superparamagnetic Iron Oxide–Enhanced MRI of Atherosclerotic Plaques in Watanabe Hereditable Hyperlipidemic Rabbits. *Investigative Radiology* **35**, 460-471 (2000).
406 Daldrup-Link, H. & Coussens, L. M. MR imaging of tumor-associated macrophages. *OncoImmunology* **1**, 507-509, doi:10.4161/onci.19456 (2012).
407 Daldrup-Link, H. E. *et al.* MRI of Tumor-Associated Macrophages with Clinically Applicable Iron Oxide Nanoparticles. *Clinical Cancer Research* **17**, 5695-5704, doi:10.1158/1078-0432.Ccr-10-3420 (2011).

408 Anzai, Y. *et al.* Evaluation of Neck and Body Metastases to Nodes with Ferumoxtran 10–enhanced MR Imaging: Phase III Safety and Efficacy Study. *Radiology* **228**, 777-788, doi:10.1148/radiol.2283020872 (2003).
409 Harisinghani, M., Ross, R. W., Guimaraes, A. R. & Weissleder, R. Utility of a New Bolus-injectable Nanoparticle for Clinical Cancer Staging. *Neoplasia* **9**, 1160-1165, doi:https://doi.org/10.1593/neo.07940 (2007).
410 Harisinghani, M. G., Saini, S., Slater, G. J., Schnall, M. D. & Rifkin, M. D. MR imaging of pelvic lymph nodes in primary pelvic carcinoma with ultrasmall superparamagnetic iron oxide (combidex): Preliminary observations. *Journal of Magnetic Resonance Imaging* **7**, 161-163, doi:doi:10.1002/jmri.1880070124 (1997).
411 Rausch, M. *et al.* Dynamic patterns of USPIO enhancement can be observed in macrophages after ischemic brain damage. *Magnetic Resonance in Medicine* **46**, 1018-1022, doi:doi:10.1002/mrm.1290 (2001).
412 Floris, S. *et al.* Blood–brain barrier permeability and monocyte infiltration in experimental allergic encephalomyelitisA quantitative MRI study. *Brain* **127**, 616-627, doi:10.1093/brain/awh068 (2004).
413 Rausch, M., Hiestand, P., Baumann, D., Cannet, C. & Rudin, M. MRI-based monitoring of inflammation and tissue damage in acute and chronic relapsing EAE. *Magnetic Resonance in Medicine* **50**, 309-314, doi:doi:10.1002/mrm.10541 (2003).
414 Vellinga, M. M. *et al.* Pluriformity of inflammation in multiple sclerosis shown by ultra-small iron oxide particle enhancement. *Brain* **131**, 800-807, doi:10.1093/brain/awn009 (2008).
415 Akhtari, M. *et al.* Functionalized magnetonanoparticles for MRI diagnosis and localization in epilepsy. *Epilepsia* **49**, 1419-1430, doi:doi:10.1111/j.1528-1167.2008.01615.x (2008).
416 Serres, S. *et al.* Systemic Inflammatory Response Reactivates Immune-Mediated Lesions in Rat Brain. *The Journal of Neuroscience* **29**, 4820-4828, doi:10.1523/jneurosci.0406-09.2009 (2009).
417 Weissleder, R. *et al.* Ultrasmall superparamagnetic iron oxide: an intravenous contrast agent for assessing lymph nodes with MR imaging. *Radiology* **175**, 494-498, doi:10.1148/radiology.175.2.2326475 (1990).
418 Gammella, E., Buratti, P., Cairo, G. & Recalcati, S. Macrophages: central regulators of iron balance. *Metallomics* **6**, 1336-1345, doi:10.1039/C4MT00104D (2014).
419 Corna, G. *et al.* Polarization dictates iron handling by inflammatory and alternatively activated macrophages. *Haematologica* **95**, 1814-1822, doi:10.3324/haematol.2010.023879 (2010).
420 Recalcati, S., Locati, M., Gammella, E., Invernizzi, P. & Cairo, G. Iron levels in polarized macrophages: Regulation of immunity and autoimmunity. *Autoimmunity Reviews* **11**, 883-889, doi:https://doi.org/10.1016/j.autrev.2012.03.003 (2012).
421 Vinchi, F. *et al.* Hemopexin therapy reverts heme-induced proinflammatory phenotypic switching of macrophages in a mouse model of sickle cell disease. *Blood* **127**, 473-486, doi:10.1182/blood-2015-08-663245 (2016).
422 Sindrilaru, A. *et al.* An unrestrained proinflammatory M1 macrophage population induced by iron impairs wound healing in humans and mice. *The Journal of Clinical Investigation* **121**, 985-997, doi:10.1172/JCI44490 (2011).

423 Kroner, A. *et al.* TNF and Increased Intracellular Iron Alter Macrophage Polarization to a Detrimental M1 Phenotype in the Injured Spinal Cord. *Neuron* **83**, 1098-1116, doi:https://doi.org/10.1016/j.neuron.2014.07.027 (2014).
424 Laskar, A., Eilertsen, J., Li, W. & Yuan, X.-M. SPION primes THP1 derived M2 macrophages towards M1-like macrophages. *Biochemical and Biophysical Research Communications* **441**, 737-742, doi:https://doi.org/10.1016/j.bbrc.2013.10.115 (2013).
425 Costa da Silva, M. *et al.* Iron Induces Anti-tumor Activity in Tumor-Associated Macrophages. *Frontiers in Immunology* **8**, doi:10.3389/fimmu.2017.01479 (2017).
426 Zanganeh, S. *et al.* Iron oxide nanoparticles inhibit tumour growth by inducing pro-inflammatory macrophage polarization in tumour tissues. *Nature Nanotechnology* **11**, 986, doi:10.1038/nnano.2016.168

https://www.nature.com/articles/nnano.2016.168#supplementary-information (2016).
427 Leftin, A. *et al.* Iron deposition is associated with differential macrophage infiltration and therapeutic response to iron chelation in prostate cancer. *Scientific Reports* **7**, 11632, doi:10.1038/s41598-017-11899-2 (2017).
428 Leftin, A., Ben-Chetrit, N., Klemm, F., Joyce, J. A. & Koutcher, J. A. Iron imaging reveals tumor and metastasis macrophage hemosiderin deposits in breast cancer. *PLOS ONE* **12**, e0184765, doi:10.1371/journal.pone.0184765 (2017).
429 Leftin, A. & Koutcher, J. A. Quantification of Nanoparticle Enhancement in Polarized Breast Tumor Macrophage Deposits by Spatial Analysis of MRI and Histological Iron Contrast Using Computer Vision. *Contrast Media & Molecular Imaging* **2018**, 9, doi:10.1155/2018/3526438 (2018).
430 Friedlander, M. *et al.* Definition of Two Angiogenic Pathways by Distinct α_v Integrins. *Science* **270**, 1500-1502, doi:10.1126/science.270.5241.1500 (1995).
431 Anthony, D. C., Bolton, S. J., Fearn, S. & Perry, V. H. Age-related effects of interleukin-1 beta on polymorphonuclear neutrophil-dependent increases in blood-brain barrier permeability in rats. *Brain* **120**, 435-444, doi:10.1093/brain/120.3.435 (1997).
432 Anthony, D. *et al.* CXC chemokines generate age-related increases in neutrophil-mediated brain inflammation and blood–brain barrier breakdown. *Current Biology* **8**, 923-927, doi:https://doi.org/10.1016/S0960-9822(07)00373-9 (1998).
433 Soares, D. M., Machado, R. R., Yamashiro, L. H., Melo, M. C. C. & Souza, G. E. P. Cytokine-induced neutrophil chemoattractant (CINC)-1 induces fever by a prostaglandin-dependent mechanism in rats. *Brain Research* **1233**, 79-88, doi:https://doi.org/10.1016/j.brainres.2008.07.069 (2008).
434 Wu, Y. L. *et al.* In situ labeling of immune cells with iron oxide particles: An approach to detect organ rejection by cellular MRI. *Proceedings of the National Academy of Sciences of the United States of America* **103**, 1852-1857, doi:10.1073/pnas.0507198103 (2006).
435 Shen, Z. *et al.* Multifunctional Theranostic Nanoparticles Based on Exceedingly Small Magnetic Iron Oxide Nanoparticles for T1-Weighted

Magnetic Resonance Imaging and Chemotherapy. *ACS Nano* **11**, 10992-11004, doi:10.1021/acsnano.7b04924 (2017).
436 Beduneau, A. *et al.* Facilitated Monocyte-Macrophage Uptake and Tissue Distribution of Superparmagnetic Iron-Oxide Nanoparticles. *PLOS ONE* **4**, e4343, doi:10.1371/journal.pone.0004343 (2009).
437 Williams, J. B., Ye, Q., Hitchens, T. K., Kaufman, C. L. & Ho, C. MRI detection of macrophages labeled using micrometer-sized iron oxide particles. *Journal of Magnetic Resonance Imaging* **25**, 1210-1218, doi:doi:10.1002/jmri.20930 (2007).
438 Deng, S. *et al.* Radiolabeled cyclic arginine-glycine-aspartic (RGD)-conjugated iron oxide nanoparticles as single-photon emission computed tomography (SPECT) and magnetic resonance imaging (MRI) dual-modality agents for imaging of breast cancer. *Journal of Nanoparticle Research* **17**, 19, doi:10.1007/s11051-014-2845-9 (2015).
439 Saito, S. *et al.* Impact of surface coating and particle size on the uptake of small and ultrasmall superparamagnetic iron oxide nanoparticles by macrophages. *International Journal of Nanomedicine* **7**, 5415-5421, doi:10.2147/ijn.s33709 (2012).
440 Engberink, R. D. O., Pol, S. M. A. v. d., Döpp, E. A., Vries, H. E. d. & Blezer, E. L. A. Comparison of SPIO and USPIO for in Vitro Labeling of Human Monocytes: MR Detection and Cell Function. *Radiology* **243**, 467-474, doi:10.1148/radiol.2432060120 (2007).
441 Cai, W., Gambhir, S. S. & Chen, X. Multimodality tumor imaging targeting integrin αvβ3. *BioTechniques* **39**, S14-S25, doi:10.2144/000112091 (2005).
442 Festing, M. F. W., Lovell, D., Sparrow, S., May, D. & Connors, T. A. An athymic nude mutation in the rat. *Nature* **274**, 365, doi:10.1038/274365a0 (1978).
443 Benestad, H. B., Hersleth, I. B. & Rolstad, B. Thymus and T cells are not essential for rat leucopoiesis. *European Journal of Haematology* **43**, 150-157, doi:doi:10.1111/j.1600-0609.1989.tb00271.x (1989).
444 Cavey, T. *et al.* Mouse genetic background impacts both on iron and non-iron metals parameters and on their relationships. *BioMetals* **28**, 733-743, doi:10.1007/s10534-015-9862-8 (2015).
445 Leek, R. D. *et al.* Association of Macrophage Infiltration with Angiogenesis and Prognosis in Invasive Breast Carcinoma. *Cancer Research* **56**, 4625-4629 (1996).
446 Leek, R. D., Landers, R. J., Harris, A. L. & Lewis, C. E. Necrosis correlates with high vascular density and focal macrophage infiltration in invasive carcinoma of the breast. *British Journal Of Cancer* **79**, 991, doi:10.1038/sj.bjc.6690158 (1999).
447 Suero-Abreu, G. A. *et al.* Multimodal Genetic Approach for Molecular Imaging of Vasculature in a Mouse Model of Melanoma. *Molecular Imaging and Biology*, 1-12, doi:10.1007/s11307-016-1006-1 (2016).
448 Goulay, R. *et al.* Modification of apparent intracerebral hematoma volume on T2∗-weighted images during normobaric oxygen therapy may contribute to false diagnosis. *Journal of Clinical Neuroscience* **52**, 105-108, doi:https://doi.org/10.1016/j.jocn.2018.01.046 (2018).
449 Chambon, C., Clement, O., Le Blanche, A., Schouman-Claeys, E. & Frija, G. Superparamagnetic iron oxides as positive MR contrast agents: In vitro

and in vivo evidence. *Magnetic Resonance Imaging* **11**, 509-519, doi:https://doi.org/10.1016/0730-725X(93)90470-X (1993).
450 Wei, H. *et al.* Exceedingly small iron oxide nanoparticles as positive MRI contrast agents. *Proceedings of the National Academy of Sciences* **114**, 2325-2330, doi:10.1073/pnas.1620145114 (2017).
451 Eibofner, F., Steidle, G., Kehlbach, R., Bantleon, R. & Schick, F. Positive contrast imaging of iron oxide nanoparticles with susceptibility-weighted imaging. *Magnetic Resonance in Medicine* **64**, 1027-1038, doi:doi:10.1002/mrm.22498 (2010).
452 Iv, M. *et al.* Quantification of macrophages in high-grade gliomas by using ferumoxytol-enhanced MRI: a pilot study. *Radiology* **290** (2018).
453 Yan, C. *et al.* Anti-αvβ3 antibody guided three-step pretargeting approach using magnetoliposomes for molecular magnetic resonance imaging of breast cancer angiogenesis. *International Journal of Nanomedicine* **8**, 245-255, doi:10.2147/ijn.s38678 (2013).
454 Naumenko, V. *et al.* Biodistribution and Tumors MRI Contrast Enhancement of Magnetic Nanocubes, Nanoclusters, and Nanorods in Multiple Mice Models. *Contrast Media & Molecular Imaging* **2018**, 12, doi:10.1155/2018/8264208 (2018).